Magneto-optical characterization of magnetic thin films and interface structures

eman ta zabal zazu

Universidad del País Vasco

Euskal Herriko Unibertsitatea

Patricia Riego Saavedra

- Ph. D. Thesis –

2019

Supervised by:

Dr. Andreas Berger

Dr. Jose Maria Pitarke de la Torre

Que no, que no, que el pensamiento
no puede tomar asiento,
que el pensamiento es estar
siempre de paso, de paso, de paso...

Luis E. Aute

Resumen

La tendencia hacia la miniaturización de los dispositivos electrónicos y la mejora constante de sus capacidades constituyen un importante reto tecnológico. Con transistores cuyas dimensiones son cada vez menores, del orden de unos pocos nanómetros, y discos duros con densidades de almacenamiento magnético superiores a 200 Gbits/cm^2, la importancia del estudio de las propiedades de los materiales en la nanoescala es más que evidente. Asimismo, en las últimas décadas se ha propuesto explotar diferentes fenómenos para optimizar circuitos lógicos y memorias. Por ejemplo, para una nueva generación de dispositivos, se ha planteado beneficiarse no sólo de la carga de los electrones sino también de su espín para transportar información, dando lugar al ámbito de la espintrónica. En este sentido se podría utilizar el efecto Hall de spin (SHE), el cual convierte corrientes eléctricas en corrientes de espín. Además, se ha propuesto sacar provecho de interacciones magnéticas poco empleadas hasta ahora como la interacción de Dzyaloshinskii-Moriya (DMI, por sus siglas en inglés)[1] que da lugar a skyrmions, texturas magnéticas que podrían utilizarse en memorias. La DMI ha sido poco estudiada históricamente ya que ocurre principalmente en interfases de láminas finas, es decir, en una escala nanoscópica. Cabe destacar también que, para satisfacer la cada vez mayor velocidad de los dispositivos demandada por los consumidores, es necesario investigar la dinámica de los sistemas bajo la influencia de excitaciones externas con dependencia temporal.

Más allá de la relevancia tecnológica que puedan tener el SHE, la DMI y la respuesta dinámica de sistemas tales como materiales ferromagnéticos, es importante subrayar que aún hay mucha investigación básica por llevar a cabo en tales ámbitos. El objetivo de esta tesis es estudiar estos fenómenos en capas finas e interfases de materiales específicos por medio de métodos magneto-ópticos, que destacan por su versatilidad. En particular, el efecto magneto-óptico Kerr (MOKE), que consiste en el cambio de polarización de un haz de luz al reflejarse en la superficie de una muestra magnetizada, es el fundamento de los métodos de caracterización comunes a los diferentes estudios presentados aquí.

El cambio en la luz reflejada producido por MOKE puede ser detectado por medio de sistemas ópticos, lo cual permite acceder a ciertas propiedades magnéticas de manera rápida y no

---

[1] En lo que sigue, las siglas se referirán a las siglas en inglés.

destructiva. Además, el método utilizado en esta tesis, la elipsometría magneto-óptica generalizada (GME), logra separar efectos puramente ópticos de efectos magneto-ópticos gracias a que unos y otros tienen diferentes simetrías con respecto al ángulo de polarización de la luz incidente y reflejada, los cuales se cambian en GME por medio de sendos polarizadores lineales giratorios colocados inmediatamente antes y después de la reflexión en la muestra. Por otro lado, GME es capaz de separar entre sí los efectos magneto-ópticos producidos por las diferentes componentes del vector de la magnetización, debido a que también presentan diferentes simetrías.

En esta tesis, la técnica GME ha sido optimizada y se han incorporado modificaciones en la configuración experimental y el sistema de análisis de datos para llevar a cabo las medidas que se presentan. La tesis también contribuye al desarrollo de un método de fabricación de muestras en las que capas ultrafinas de un material metálico son depositadas en forma de cuña gracias a una alineación oblicua del sistema de deposición con el objetivo de crear muestras con un gradiente espacial en el espesor de una de sus capas. Este sistema de deposición se ha combinado con el crecimiento epitaxial de capas de Co en las que el eje fácil de magnetización está en el plano de la muestra.

Las muestras, además de por medio de MOKE, han sido caracterizadas magnética, óptica y estructuralmente mediante reflexión y difracción de rayos X, elipsometría espectroscópica y magnetometría de muestra vibrante, técnicas explicadas en el Capítulo 2. La combinación de fabricación y caracterización de muestras con métodos de modelización basados en Hamiltonianos de espín ha servido para realizar investigaciones cuyos resultados se exponen en los Capítulos 3, 4 y 5 de la tesis, tras una introducción general al magnetismo, el SHE y la magneto-óptica en el capítulo 1.

En el Capítulo 3 se estudia la posibilidad de detectar el SHE en metales por medio de MOKE. En este efecto, los electrones con espín opuesto se desvían en sentidos opuestos al aplicar una corriente eléctrica a un material con acoplamiento espín-órbita, y en la superficie se genera un desequilibrio entre los espines de una polarización y la opuesta, dando lugar a una polarización de espín. En semiconductores esta acumulación de espines debida al SHE ha sido detectada mediante MOKE pero, hasta muy recientemente, este método no se ha usado en metales ya que, debido a su mayor número de electrones libres, el MOKE generado por los electrones polarizados es mucho menor que el efecto óptico de todos los electrones que interaccionan con la luz. Una

investigación publicada en 2014 detectó una señal MOKE debida al SHE en metales como Pt o W; de hecho, el artículo comunicaba una señal extraordinariamente grande, solo unas cinco veces menor que la de un material ferromagnético como Fe. En el Capítulo 3 se estudia este fenómeno por medio de GME y se separan las señales ópticas de las magneto-ópticas, gracias a que estos dos tipos de señales poseen simetrías con respecto a la polarización incidente y detectada que son diferentes entre sí. Esto permite observar que la señal relacionada con MOKE es prácticamente nula dentro de los márgenes de error, los cuales son muy pequeños y constituyen un límite superior de la señal que es mucho menor que los valores comunicados anteriormente. Las señales observadas en trabajos previos son catalogadas como "falsos positivos" ya que, según las pruebas realizadas aquí, publicaciones anteriores probablemente malinterpretaran señales puramente ópticas o espurias como señales MOKE y se concluye que GME es un método que evita estos "falsos positivos".

El Capítulo 4 se centra en la investigación por medio de GME de las propiedades de la interfase entre Co y Ru en muestras que, como se ha descrito arriba, se han fabricado con el recubrimiento de Ru en forma de cuña, como se ve en la Figura R.1 (a). Tras la caracterización estructural de las muestras, se ha utilizado GME para realizar magnetometría tridimensional y detectar todas las componentes de la magnetización. Pese a aplicar un campo magnético a lo largo del eje x (ver Figura R.1 (b) para la definición de los ejes) y pese a que la energía magnetocristalina del Co favorece la magnetización en el plano, se observa una componente de la magnetización fuera del plano que depende del espesor de Ru, como se representa en la Figura R.1 (a), donde las flechas azules representan la magnetización local. En muestras sin recubrimiento de Ru esta rotación de la magnetización no se observa, por lo que se concluye que este efecto se debe a la interfase Co/Ru y así, se asume que la distribución de la magnetización es la mostrada esquemáticamente en la Figura R.1 (a), estando en el plano lejos de la interfase y rotando gradualmente fuera del plano al acercarse a la interfase. Además, si se inserta una capa de SiO_2 de 1.2 nm de espesor entre el Co y el Ru, la rotación fuera del plano de la magnetización se suprime. Curiosamente, tampoco se observa tal rotación en muestras donde el recubrimiento de Ru es homogéneo, como se muestra en la Figura R.1 (b).

Esto podría explicarse por medio de una diferente disposición de los átomos de Ru sobre la superficie de Co al ser depositados de forma oblicua u homogénea. Como es sabido, los átomos de elementos con acoplamiento espín-órbita pueden mediar DMI entre espines, la cual favorece

que los dos espines que interaccionan no se alineen de forma paralela, sino perpendicular. Así, los átomos de Ru mediarían una DMI entre los espines del Co que sería heterogénea en el caso de la Figura R. 1 (a) y homogénea en el de R. 1 (b). Se han realizado cálculos numéricos basados en modelos de espín diseñados para representar ambas circunstancias y se ha observado que la DMI modulada espacialmente da lugar a una rotación neta de la magnetización fuera del plano, mientras que la DMI homogénea no, reproduciendo los resultados experimentales. Además, el modelo propuesto también reproduce las dependencias con el campo magnético y con la orientación del eje cristalográfico uniaxial con respecto al campo aplicado observadas por medio de GME. Estos resultados contribuyen a la comprensión de los efectos a los que la DMI puede dar lugar y podrían abrir un camino a explotar faltas de homogeneidad en los materiales para diseñar estructuras de espín específicas.
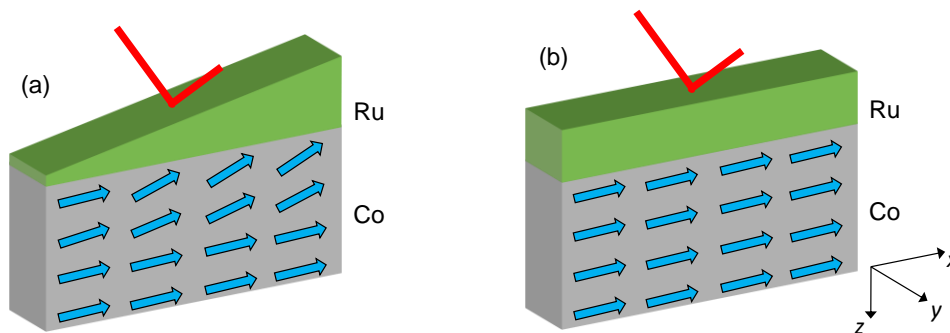

Figura R.1 Esquema de dos muestra alargadas con una capa homogénea de Co y un recubrimiento de Ru en forma de cuña en (a) y homogéneo en (b). Las líneas rojas representan el haz de luz, que incide en un punto específico de la muestra y permite realizar medidas locales. Las flechas azules representan la magnetización localmente. En (a) la capa de Ru en forma de cuña induce una rotación fuera del plano cerca de la interfase que es mayor según aumenta el espesor del Ru. En (b) la magnetización permanece en el plano. El eje de coordenadas en (b) corresponde a los esquemas (a) y (b).

Por último, en el Capítulo 5, se ha estudiado por medio de MOKE y de cálculos numéricos la respuesta dinámica de un sistema ferromagnético con anisotropía uniaxial a un campo magnético oscilatorio de periodo P y amplitud h_0 aplicado a lo largo del eje fácil de magnetización. El sistema experimenta una transición de fase dinámica (DPT) en un valor crítico del periodo P_c entre una fase dinámicamente desordenada para valores grandes de P, donde la magnetización puede seguir al campo y oscila alrededor del cero, dando lugar a un valor medio a lo largo de un periodo de oscilación $Q = 0$, y una fase dinámicamente ordenada donde el sistema no puede seguir al campo, la magnetización no logra invertirse y $Q \neq 0$. El parámetro de orden de la DPT es precisamente Q, que cumple el mismo rol que la magnetización M en la transición de fase termodinámica (TPT)

8

convencional, en la cual un material ferromagnético pasa a una fase paramagnética al aumentar la temperatura T por encima de T_C. DPTs y TPTs pertenecen a la misma clase de universalidad y décadas de investigaciones habían concluido que sus diagramas de fase eran equivalentes, incluyendo la dependencia de los parámetros de orden Q y M con P y T respectivamente, así como con un campo magnético externo constante, llamado h_b en el caso de la DPT y h en el caso de la TPT. No obstante, el trabajo llevado a cabo en esta tesis ha demostrado que la equivalencia entre DPT y TPT no es total y que depende crucialmente de la amplitud del campo oscilatorio que da lugar a la DPT. Como se muestra en las Figura R.2 (b) y (c), para h_0 grandes, $Q(P, h_b)$ y $M(T, h)$ tienen un comportamiento similar mientras que para h_0 pequeñas, como se muestra en la Figura R.2 (a), $Q(P, h_b)$ muestra a valores h_b simétricos con respecto a $h_b = 0$ cambios abruptos que son señal de tendencias metamagnéticas, las cuales están ausentes en la TPT de modelos de espín convencionales como el modelo de Ising. Por todo ello, se infiere que la equivalencia entre DPT y TPT no es universal, ya que a valores de h_0 diferentes, se dan diferencias cualitativas en la DPT.
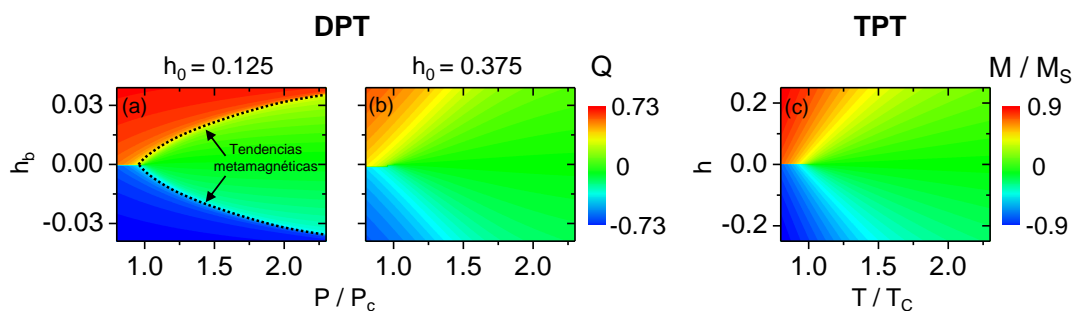

Figura R.2 (a) y (b) diagramas del parámetro de orden de la DPT, Q, en función del periodo del campo oscilatorio P y de la intensidad de un campo constante adicional h_b, para dos valores de la amplitud del campo oscilatorio h_0. La escala de color se sitúa a la derecha de (b). (c) Magnetización en función de la temperatura T y la intensidad de un campo magnético externo constante h.

Abstract

This thesis explores different phenomena in spintronics and magnetism by utilizing magneto-optics as the main characterization technique. On the one hand, the spin Hall effect (SHE) is studied in non-ferromagnetic metals with high spin-orbit coupling upon the application of a charge current. On the other hand, the magnetization state of ferromagnets and its reversal under externally applied magnetic fields is investigated in two specific systems: first, the effects of a non-ferromagnetic metallic overcoat onto the magnetic behavior of a thin ferromagnetic film are investigated; second, the effect of a field that oscillates at periods comparable to the characteristic time in which the magnetization of the system is reversed is studied in uniaxial ferromagnets.

Those three different materials systems have been studied in this thesis by means of the magneto-optical Kerr effect (MOKE), a phenomenon that produces magnetization-related changes in polarized light upon reflection from a magnetized sample. In order to separate changes in the reflected light that are related to the magnetic state of the sample from those which are not, a MOKE-based ellipsometry technique has been utilized, namely, the so-called generalized magneto-optical ellipsometry (GME) method. GME has also been utilized to perform three-dimensional vector magnetometry, taking advantage of the fact that different components of the magnetization vector, as defined by the geometry of the reflection experiment, give rise to different types of changes in the reflected light. Those differences can be picked up by GME by changing the experimental illumination and detection conditions.

After an introduction of the basic concepts of ferromagnetism, SHE, and MOKE in Chapter 1, the experimental and modeling techniques utilized throughout the thesis are described in Chapter 2. Then, Chapters 3, 4, and 5 present the main results of the thesis.

In Chapter 3, the detectability of the SHE in Pt, W, and Ta metals utilizing MOKE has been studied by means of GME, and the large SHE-related MOKE signals reported previously in literature for metals could not be reproduced. Most likely, the reported large MOKE was caused by a misinterpretation of the detected signals that can occur if no ellipsometric data analysis is done. Chapter 3 concludes that, even if SHE-induced spin polarization could give rise to MOKE, such effect is extremely small because, even with the very high sensitivity of the GME system utilized here it was not possible to detect it. Instead, an upper limit of the effect was identified.

Chapter 4 is devoted to the study of the effect of a Ru overcoat onto the magnetic properties of a Co thin film with in-plane magneto-crystalline anisotropy. Details about the fabrication of the samples, as well as their structural characterization are given. GME is utilized to perform three-dimensional vector magnetometry, and the dependence of the three Cartesian components of the magnetization with the applied field strength and the sample orientation is evaluated. The key result is that, even in the absence of an external field, the Co/Ru interface induces a polar MOKE component related to an out-of-plane rotation of the magnetization away from the crystallographic easy axis, which has not been detected previously. However, this magnetization rotation only occurs if the Ru overcoat is deposited obliquely with a thickness gradient, while the magnetization remains in-plan if the Ru overcoat is homogeneous. These findings are compared to an atomistic spin model and the results are interpreted on the basis of a spatially modulated Dzyaloshinskii-Moriya interaction at the Co/Ru interface that produces the *a priori* unexpected rotation of the magnetization only if the Ru overcoat is deposited in a specific way.

In Chapter 5 MOKE is utilized to measure the response of a ferromagnet to an external oscillating magnetic field of varying frequency. A dynamic phase transition (DPT) is observed between a phase where the magnetization can follow the field when its frequency is low, and a phase at sufficiently high frequencies of the external field, where it cannot. Experiments performed on a sample with uniaxial anisotropy are combined with a kinetic Ising model to investigate the phenomenon of the DPT and to compare it to conventional thermodynamic phase transitions (TPTs) in ferromagnets, where a phase transition from a ferromagnetic to a paramagnetic phase occurs upon increasing the temperature. While the consensus for decades was that DPTs and TPTs have equivalent behaviors, the results presented here demonstrate that this is not the case, and that the equivalency between both phenomena is limited and not universal.

Finally, the conclusions of the thesis are summarized in Chapter 6 and an outlook is provided.

List of abbreviations

Abbreviations are not listed here if they occur only in the immediate context of a statement

AC	alternating current
CPL	circularly polarized light
DC	direct current
DFM	dynamic ferromagnetic
DMI	Dzyaloshinskii-Moriya interaction
DOS	density of states
DPM	dynamic paramagnetic
DPT	dynamic phase transition
EA	easy axis
FM	ferromagnetic
GME	generalized magneto-optical ellipsometry
hcp	hexagonal close packed
L-MOKE	longitudinal magneto-optical Kerr effect
LTS	linear translation stage
MCA	magneto-crystalline anisotropy
MFA	mean field approximation
MO	magneto-optical
MOKE	magneto-optical Kerr effect
NM	non-magnetic (non-ferromagnetic)
PBC	periodic boundary conditions
PM	paramagnetic
P-MOKE	polar magneto-optical Kerr effect
QWP	quarter wave-plate
SE	spectroscopic ellipsometry
SHE	spin Hall effect
SOC	spin-orbit coupling
T-MOKE	transverse magneto-optical Kerr effect
TPT	thermodynamic phase transition
VSM	vibrating sample magnetometer
XRD	x-ray diffraction
XRR	x-ray reflectivity

List of variables

Variables are not listed here if they occur only in the immediate context of a statement

Bold symbols represent vectors, bold symbols with a curved line or two lines on top represent tensors

B_i	fitting parameters of GME related to reflection matrix elements
$\boldsymbol{D}_{ij}$	Dzyaloshinskii-Moriya vector between spins i and j with units of energy
d	thickness of a layer or distance between crystallographic planes
$\hat{\boldsymbol{e}}$	unit vector giving the orientation of the EA
$\mathcal{E}$	energy of a system
$\mathcal{F}$	Helmholtz free energy of a system
$\boldsymbol{H}$	external magnetic field
h_0	normalized amplitude of oscillating field driving the DPT
h_b	normalized bias field of the DPT
h_b^m	bias field value at which metamagnetic tendencies occur in the DPT
$\hbar$	external magnetic field with energy units
$\hbar_0$	amplitude of oscillating field driving the DPT with energy units
$\hbar_b$	bias field in the DPT with energy units
$\mathcal{H}$	Hamiltonian of a system
I	averaged intensity detected for a magnetic state and the reversed one
I_0	fitting parameter of GME describing noise in the light intensity
I_D	light intensity at the detector in a MOKE experiment
$\mathfrak{I}$	DC current
J	exchange constant between neighboring spins
$\boldsymbol{j}_c$	charge current density
$\boldsymbol{j}_s$	spin current density
K_d	effective shape anisotropy constant with units of energy per volume
K_i	MCA constants of ith order in a macrospin model with units of energy per volume
k_B	Boltzmann constant
k_i	MCA constants of ith order with energy units
$\boldsymbol{M}$	magnetization vector
M_H	projection of the magnetization along the field axis
M_s	saturation magnetization
$\hat{\boldsymbol{m}}$	unit vector of the magnetization $\boldsymbol{M}/|\boldsymbol{M}|$
m_l	magnetic quantum number
m_ν	Cartesian components of normalized magnetization vector ($\nu = x, y, z$)
N	refractive index of a material
N_s	number of spins / local magnetic moments in a system
P	period of the oscillating field driving the DPT
P_c	critical period
Q	order parameter of DPT
Q_{MO}	magneto-optical coupling constant
$\overline{\overline{\boldsymbol{R}}}$	reflection matrix
$\widetilde{\boldsymbol{R}}$	reflection matrix normalized to r_p
$r_{ss}, r_{sp}, r_{ps}, r_{pp}$	generic reflection matrix elements
$\boldsymbol{S}_i$	unit vector of a localized magnetic moment i
T	temperature
T_C	Curie temperature
t_{Ru}	Ru overcoat thickness

α	element in reflection matrix related to L-MOKE
β	element in reflection matrix related to T-MOKE
β_D	critical exponent in the DPT at $H_b = 0$ and $P \rightarrow P_C$
β_T	critical exponent in the TPT at $H = 0$ and $T \rightarrow T_C$
γ	element in reflection matrix related to P-MOKE
$\Delta\theta_i$	experimental correction for angle of polarizers in GME setup, $i = 1, 2$.
δI	change of light intensity upon magnetization reversal in a MOKE experiment
$\bar{\bar{\varepsilon}}$	dielectric tensor
ϵ_K	Kerr ellipticity
θ^X	x-ray detector angle with respect to the surface plane
θ_i	angle of polarizers in the laboratory reference frame in GME setup, $i = 1, 2$
$\tilde{\theta}_i$	angle of polarizers with respect to s polarization direction in GME setup, $i = 1, 2$
θ_K	Kerr rotation
θ_{tilt}	angle of sputter gun with respect to the vertical
Λ	modulus of DMI vector
λ	wavelength of electromagnetic radiation
$\boldsymbol{\mu}$	magnetic moment vector
μ_0	magnetic permeability of vacuum
μ_B	Bohr magneton
μ_s	spin accumulation
σ^D	fluctuations in the DPT
$\boldsymbol{\sigma}_s$	polarization of the spins in the SHE
τ	intrinsic relaxation time of ferromagnet
Φ_0	angle between EA and projection of the applied field axis on to the sample plane
Φ_i	azimuthal angle of an individual spin i
Φ_M	angle between $\boldsymbol{M}$ and projection of the applied field axis on to the sample plane
φ	rotation angle with respect to surface normal in XRD measurements
χ	magnetic susceptibility
χ_D	dynamic magnetic susceptibility in the DPT
Ψ	x-ray scattering wave vector angle with respect to the surface normal
Ψ_0	angle between the EA and the sample plane
Ψ_i	polar angle of an individual spin i
Ψ_H	angle between the applied field axis and the L-MOKE axis in a GME experiment
Ψ_M	angle between $\boldsymbol{M}$ and the sample plane
Ω	angle of incidence in a reflection experiment
ω	frequency of electromagnetic wave
ω^X	x-ray incidence angle respect to the surface plane

Table of contents

Chapter 1

Fundamental concepts

This chapter provides a theoretical basis of the concepts that will be utilized along the thesis. The origin of ferromagnetism and the energy contributions determining the energy landscape of ferromagnets are explained in Section 1.1. Section 1.2 describes the behavior of ferromagnets under an applied magnetic field and presents a simple model, namely the macrospin model, to explain the reversal of a single-domain ferromagnetic system. Section 1.3 presents the fundamentals of the spin Hall effect. Finally, basic concepts of magneto-optics and, in particular, of the magneto-optical Kerr effect, are explained in Section 1.4.

1.1 Types of magnetism and energy contributions

1.1.1 Forms of magnetism

In order to study the magnetism of solids, it is first important to understand how magnetism arises in atoms[2]. Electrons in an atom have a given spin and orbital angular momentum state that give rise to a magnetic moment μ related to the total angular momentum of the electron. In atoms with filled electronic shells μ amounts to zero, while atoms with partially filled shells possess a nonzero μ. An external magnetic field H can induce or modify μ. If $\mu = 0$ in the absence of field, an external H induces a μ antiparallel to H, a phenomenon that is called diamagnetism. If $\mu \neq 0$ in the absence of field, when H is applied, μ tries to align parallel to it to minimize the energy, an effect called paramagnetism.

The magnitude utilized for the description of magnetism in the solid state is the magnetization M, which is the magnetic moment per volume unit. In diamagnetic materials, the individual magnetic moments are zero and M is zero if $H = 0$. In paramagnetic materials, the interaction between individual magnetic moments is only dipolar, which is very weak to induce significant ordering at room temperature. Thus, due to thermal disorder, the magnetic moments are

---

[2] Electronic magnetism is considered in this thesis, neglecting the effects of nuclear magnetism, which is much weaker.

randomly oriented and lead to M = 0 in the absence of field. At room temperature, in diamagnetic and paramagnetic materials M is linearly related to H by

$$M = \chi H, \tag{1.1}$$

where χ is the magnetic susceptibility. In the diamagnetic case[3], $\chi < 0$, and in the paramagnetic case $\chi > 0$ [1].

In other types of materials individual magnetic moments interact strongly with each other giving rise to long-range magnetic order. This thesis focuses on ferromagnets, where the interactions among the magnetic moments favor a parallel alignment that leads to a net spontaneous magnetization at a macroscopic level even in the absence of an external magnetic field[4]. The long-range order of the magnetic moments and the observation of a ferromagnetic (FM) state with net magnetization without applying a field is nevertheless only possible below a certain temperature T. As T increases, disorder is induced in the system and M decreases, as shown in Fig. 1.1. At a given T called Curie temperature T_C, marked as a red circle in Fig. 1.1, the long-range order of the magnetic moments is lost and the system undergoes a thermodynamic phase transition (TPT) from a FM to a paramagnetic (PM) phase with M = 0 in the absence of field. $T = T_C$ is the critical point of the TPT. Approaching T_C from lower temperatures, M follows a power law behavior in the vicinity of the critical point [2] with M being proportional to $(T_C - T)^{\beta_T}$, as shown in Fig. 1.1. A lower estimate of the order of magnitude of the interaction energy between the magnetic moments is given by $k_B T_C$, where k_B is the Boltzmann constant. With the typical T_C values for elementary ferromagnets as Fe, Ni, and Co, the interaction energy between two magnetic moments is larger than 10^{-20} J, much higher than the magnetostatic interaction between two atomic magnetic moments separated by 10^{-10} m, which is of the order of 10^{-23} J and would be overcome by thermal energy with a temperature of just 1 K. Therefore, the origin of ferromagnetic interaction cannot be related to magnetostatics [3].

---

[3] The diamagnetic contribution is present in all materials, but is very small compared to paramagnetism, so if paramagnetism is present, the diamagnetic effect can be neglected. The χ related to paramagnetism is positive and much larger in absolute value than the diamagnetic χ.

[4] Many other types of magnetic order are possible, such as antiferromagnetic order, where magnetic moments of the same magnitude align in an antiparallel fashion yielding a zero net magnetization but long range order, or ferrimagnetic order, where magnetic moments are antiparallel to each other but the moments that point in opposite directions have different magnitudes, resulting in a net magnetization. Other types of more complex arrangement and non-collinear order are possible depending on the interaction between the magnetic moments.
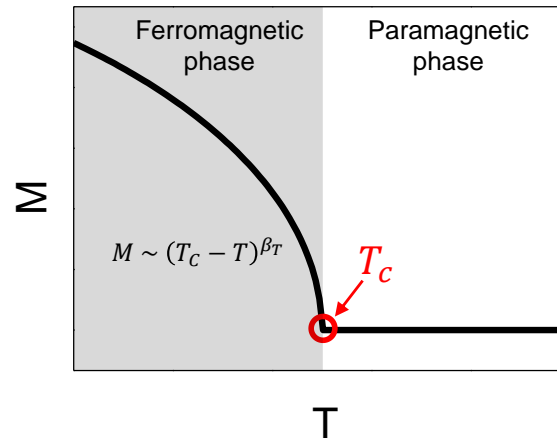
Figure 1.1 Schematics of the dependence of the magnetization of a ferromagnet as a function of temperature, in the absence of an external magnetic field. The critical temperature T_C is signaled with a red circle. The power law behavior of M in the vicinity of T_C is also shown. The shadowed region at $T < T_C$ delimits the ferromagnetic phase.

1.1.2 Origin of magnetic order: exchange interaction

1.1.2.1 Basic principle

The interaction among electronic magnetic moments giving rise to magnetic order is of quantum mechanical nature and is called exchange interaction. Exchange interaction arises as a consequence of the Coulomb repulsion and the Pauli exclusion principle between electrons. On the one hand, the electronic Hamiltonian, which includes Coulomb repulsion between electrons, determines the spatial part of the ground state wavefunction, which will be either symmetric or antisymmetric with respect to the exchange of two electrons. On the other hand, because electrons are indistinguishable fermions, the Pauli exclusion principle determines that the total electronic wavefunction (spatial part times spin part) of the system has to be antisymmetric and therefore, the spatial part, which is determined by the electronic Hamiltonian, will determine the symmetry of the spin part of the ground state. Thus, despite the fact that, neglecting relativistic effects, the Hamiltonian of the system is independent of the spin of the electrons, the energy will be different for different spin states.

In the simplest case of a two-electron system the spin state can be either a triplet or a singlet, the former with a spin quantum number 1 and being symmetric with respect to the exchange of electrons, and the latter with spin quantum number 0 and being antisymmetric. The spatial part of the wavefunction will be different in each case, antisymmetric or symmetric, respectively, giving rise to a different energy, E_t and E_s respectively. The electronic Hamiltonian can thus be

mapped onto a spin Hamiltonian with the same eigenvalue spectrum up to a constant shift in the energy of the form

$$\mathcal{H} = -J\,\widehat{\boldsymbol{S}}_1 \cdot \widehat{\boldsymbol{S}}_2 \tag{1.2}$$

where the exchange constant $J = E_s - E_t$ has units of energy and $\widehat{\boldsymbol{S}}_1$ and $\widehat{\boldsymbol{S}}_2$ are dimensionless vector spin operators of the electrons [4].

1.1.2.2 Heisenberg Hamiltonian

After some approximations, a generalization of the spin Hamiltonian in Eq. (1.2) can be performed for systems with N_s spins[5] to arrive to the so-called Heisenberg Hamiltonian

$$\mathcal{H}_{ex} = -\frac{1}{2}\sum_{\substack{i=1 \\ i \neq j}}^{N_s}\sum_{j=1}^{N_s} J_{ij}\,\widehat{\boldsymbol{S}}_i \cdot \widehat{\boldsymbol{S}}_j\,. \tag{1.3}$$

J_{ij} is the exchange integral between electron i and j and has units of energy [4]. If $J_{ij} > 0$ a state where all spins are parallel, *i.e.*, a FM state, is favored. In most common applications of the Hamiltonian in Eq. (1.3) spins are envisioned to be located at lattice sites and, given that exchange interaction is short ranged and falls off very quickly with the distance, the sum in Eq. (1.3) is typically restricted to the nearest neighbors. A simplification of this model, which was actually proposed and studied earlier than the Heisenberg model itself by Lenz and Ising in the 1920s [6, 7], assumes one-dimensional spins, which can only take values of +1 or -1. Due to its formal simplicity, this so-called Ising model is widely used in statistical physics to study a broad variety of phenomena [2] and will be utilized in Chapter 5. In the rest of this chapter, however, the discussion will focus on the Heisenberg model, where the spins can be oriented in any direction.

A simplifying step can be performed to transition from a quantum mechanical Heisenberg model with a spin operator picture as in Eq. (1.3) to a classical picture with localized magnetic moments as vectors. To do so $\widehat{\boldsymbol{S}}_i$ and $\widehat{\boldsymbol{S}}_j$ in Eq. (1.3) are commonly substituted by $\boldsymbol{S}_i$ and $\boldsymbol{S}_j$, the unit vectors of the magnetic moments ascribed to the atoms i and j, in such way that $\boldsymbol{S}_i = \boldsymbol{\mu}_i/\mu_i$, where $\boldsymbol{\mu}_i$ is the magnetic moment vector and μ_i is its modulus. $\boldsymbol{S}_i$ and $\boldsymbol{S}_j$ are commonly referred to as *spins*,

---

[5] In general, one should consider the total angular momentum, which is the sum of the orbital and the spin momenta. However, the orbital momentum is very often quenched, in particular for the materials of concern in this thesis, so the Heisenberg Hamiltonian will be written as depending only on the spin [5].

not to be confused with the spin of an electron, and can take any direction in the three-dimensional space. In that case, N_s in the sum in Eq. (1.3) is the number of magnetic moments. Plus, the double sum in Eq. (1.3) is only performed between nearest neighbor spins. Another aspect to consider is that the most general form of bilinear coupling between two spins is mediated by a tensor $\overline{\overline{\mathcal{J}}}_{ij}$ [8], and not by a scalar as J_{ij} in Eq. (1.3). So, while transitioning to a classical vector picture, but allowing for the most general bilinear pair interaction, the exchange Hamiltonian can be written as

$$\mathcal{H}_{ex} = -\frac{1}{2}\sum_{i=1}^{N_s}\sum_{j\in\mathcal{N}_1(i)} \boldsymbol{S}_i^T\, \overline{\overline{\mathcal{J}}}_{ij}\, \boldsymbol{S}_j, \tag{1.4}$$

where $\boldsymbol{S}_i^T$ is the transposed unit vector of spin i and $\mathcal{N}_1(i)$ represents the ensemble of nearest neighbors of spin i. $\overline{\overline{\mathcal{J}}}_{ij}$ is a tensor that can be decomposed as

$$\overline{\overline{\mathcal{J}}}_{ij} = J_{ij}\mathbb{1}_{3\times3} + \overline{\overline{\mathcal{J}}}_{ij}^{S} + \overline{\overline{\mathcal{J}}}_{ij}^{A}, \tag{1.5}$$

where $J_{ij} = \frac{1}{3}\mathrm{Tr}[\overline{\overline{\mathcal{J}}}_{ij}] = J_{ji}$ is the term that is typically used as the exchange constant, $\overline{\overline{\mathcal{J}}}_{ij}^{S} = \frac{1}{2}(\overline{\overline{\mathcal{J}}}_{ij} + \overline{\overline{\mathcal{J}}}_{ij}^{T}) - J_{ij}\mathbb{1}_{3\times3}$ is the traceless symmetric part, and $\overline{\overline{\mathcal{J}}}_{ij}^{A} = \frac{1}{2}(\overline{\overline{\mathcal{J}}}_{ij} - \overline{\overline{\mathcal{J}}}_{ij}^{T})$ is the antisymmetric part. $\mathbb{1}_{3\times3}$ is the 3×3 identity matrix. With those definitions Eq. (1.4) can be rewritten as

$$\mathcal{H}_{ex} = -\frac{1}{2}\sum_{i=1}^{N_s}\sum_{j\in\mathcal{N}_1(i)} \left(J_{ij}\,\boldsymbol{S}_i\cdot\boldsymbol{S}_j + \boldsymbol{S}_i^T\,\overline{\overline{\mathcal{J}}}_{ij}^{S}\,\boldsymbol{S}_j + \boldsymbol{D}_{ij}\cdot\left(\boldsymbol{S}_i\times\boldsymbol{S}_j\right) \right), \tag{1.6}$$

given that the term related to $\overline{\overline{\mathcal{J}}}_{ij}^{A}$ can be rewritten as a vector product in the last term in Eq. (1.6), where $\boldsymbol{D}_{ij} = -\boldsymbol{D}_{ji}$ is the so-called Dzyaloshinskii-Moriya vector with the following components

$$\begin{pmatrix} D_{ij}^x & D_{ij}^y & D_{ij}^z \end{pmatrix} = \begin{pmatrix} \mathcal{J}_{ij}^{A\,yz} & -\mathcal{J}_{ij}^{A\,xz} & \mathcal{J}_{ij}^{A\,xy} \end{pmatrix}. \tag{1.7}$$

The first term in Eq. (1.6) is the conventional isotropic symmetric exchange. The second term in Eq (1.6) is the so-called symmetric anisotropic exchange, which will not be discussed further in this thesis because it is typically a small correction to isotropic exchange [9] and for most observational aspects it can be incorporated into the magneto-crystalline anisotropy (Section 1.1.3.2). Finally, the last term is the asymmetric exchange, also called Dzyaloshinskii-Moriya interaction (DMI).

1.1.2.3 Dzyaloshinskii-Moriya interaction

Contrary to symmetric exchange, DMI favors a perpendicular alignment of the neighboring spins, as it tends to maximize the vector product $\boldsymbol{S}_i \times \boldsymbol{S}_j$. Furthermore, it induces a chirality, because $\boldsymbol{S}_i \times \boldsymbol{S}_j$ depends on the sign of the angle formed by the two spins, and thus clockwise or counterclockwise rotations are not identical, and one of them will be energetically favored depending on the DMI vector $\boldsymbol{D}_{ij}$. DMI is only present in systems without inversion symmetry, which can occur in materials with non-centrosymmetric crystal structures but also at surfaces and interfaces. The competition between symmetric exchange, which favors parallel alignment of the spins, and DMI, which disfavors it, can lead to non-collinear spin structures and to weak ferromagnetism in antiferromagnets [10]. Moriya found that DMI arises due to spin-orbit coupling (SOC) and that $\boldsymbol{D}_{ij}$ is constrained by the symmetry of the system [11].

The first studies of DMI focused on bulk compounds that lack inversion symmetry, such as spin glasses or materials with specific symmetries, [12-18]. The observation of skyrmions, *i.e.*, vortex-like magnetic objects [19], in bulk B20 compounds [20-22] sparked the interest in DMI from a technological perspective, given that skyrmions are topologically protected objects that are potentially applicable in high-density information storage and logic devices [23]. In such bulk materials, however, DMI is quite small and skyrmions are only found in a relatively narrow window of temperatures and applied magnetic fields, which is impractical for applications. On the other hand, bilayers or multilayers combining ferromagnetic and high SOC nonmagnetic metals may give rise to large interfacial DMI [24-27], which can substantially affect magnetic configurations in nanomagnetic systems [28], as will become apparent in Chapter 4, where the interface between Co and Ru is explored.

1.1.2.4   Itinerant ferromagnetism

While the Hamiltonian in Eq. (1.6) is related to local magnetic moments, in transition metal ferromagnets as Co, Fe, and Ni, the electrons responsible for the magnetism are delocalized in d bands. Their itinerant character explains, for instance, why in such materials the magnetic moment per atom is not an integer multiple of the Bohr magneton μ_B, *i.e.*, the magnetic moment of one electron. In this kind of materials ferromagnetism is explained on the basis of band theory [3]. A spontaneous splitting of the spin up and spin down bands occurs if it produces a

sufficient reduction of Coulomb energy that overcomes the increase in kinetic energy and, upon filling the bands up to the Fermi energy E_F, such splitting creates an imbalance of the number of spin up and spin down electrons, giving rise to a net spontaneous magnetization.

Despite the Hamiltonian in Eq. (1.6) being related to local magnetic moments, atomistic magnetic simulations typically utilize it also for the description of itinerant ferromagnets. To do so, experiments or ab initio calculations are utilized to obtain the exchange coupling terms (J_{ij} and $\boldsymbol{D}_{ij}$) as well as the values of magnetic moment per atom that allows one to map the exchange-related full Hamiltonian of the itinerant system onto Eq. (1.6) [29].

1.1.3 Additional energy contributions in ferromagnets

While exchange interaction is the key ingredient for the rise of a spontaneous magnetization in the absence of an external field, the behavior of a ferromagnet is affected by additional energy terms.

1.1.3.1 Magnetostatic energy

Once ferromagnetic order is established by exchange interactions, magnetostatics plays a crucial role in the determination of the arrangement of the magnetic dipole moments associated with the spins in the material. In contrast to exchange interaction, dipole-dipole interaction is longer range and can be written as

$$\mathcal{H}_{dip} = -\frac{\mu_0}{2} \sum_{\substack{i=1 \\ i \neq j}}^{N_s} \sum_{j=1}^{N_s} \boldsymbol{\mu_i} \cdot \boldsymbol{H}_{dip}^{j(i)}, \tag{1.8}$$

where μ_0 is the vacuum permeability and $\boldsymbol{H}_{dip}^{j(i)}$ is the dipole field, also called demagnetizing or stray field, created by a magnetic moment $\boldsymbol{\mu}_j$ at the position of moment i

$$\boldsymbol{H}_{dip}^{j(i)} = \frac{1}{4\pi} \frac{3\boldsymbol{r}_{ij}(\boldsymbol{\mu}_j \cdot \boldsymbol{r}_{ij}) - \boldsymbol{\mu}_j |\boldsymbol{r}_{ij}|^2}{|\boldsymbol{r}_{ij}|^5}. \tag{1.9}$$

$\boldsymbol{r}_{ij} = \boldsymbol{r}_i - \boldsymbol{r}_j$, with $\boldsymbol{r}_i$ being the position of the ith magnetic moment and $\boldsymbol{r}_j$ that of the jth [30]. Due to the dependence of $\boldsymbol{H}_{dip}^{j(i)}$ on the distance vector (and not only on its modulus) between magnetic moments, the shape of the sample will affect the magnetostatic energy contribution

caused by dipole-dipole interaction and thus this term effectively creates a shape anisotropy for all non-spherical bodies.

Following Eqs. (1.8) and (1.9), the magnetostatic energy is minimized when the magnetic moments are parallel to the vector connecting them. In thin films, which are the focus of this thesis, the thickness is much smaller than the other two dimensions and thus magnetostatic energy tends to align the magnetic moments parallel to each other in the plane of the sample. Within that plane, the magnetostatic energy does not depend relevantly on the azimuthal orientation of the magnetization. It turns out that for a uniformly magnetized infinite thin film with a saturation magnetization M_s the demagnetizing field is constant [1] and magnetostatic energy can be rewritten as

$$\mathcal{H}_{dip} = \frac{\mu_0}{2} V M_s^2 (1 - \cos^2 \Psi_M), \tag{1.10}$$

where V is the volume of the system and Ψ_M is the angle between the magnetization and the plane of the sample, in such way that $\mathcal{H}_{dip}$ is minimized if the magnetization is contained in the plane of the sample.
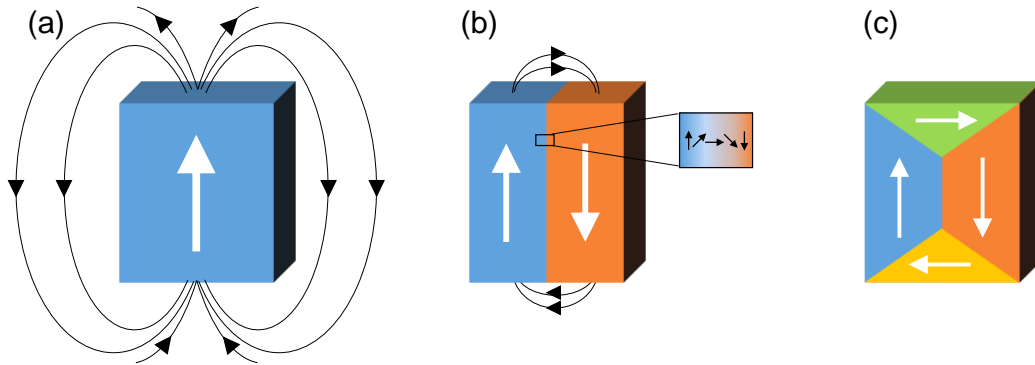

Figure 1.2 Schematic illustration of domain formation in a ferromagnet: (a) uniform magnetic state with the corresponding stray field lines shown by black lines, (b) two magnetic domains with the reduced stray field and (c) closure domains with the absence of relevant stray field. The zoom-in in (b) shows the transition region between the two domains with inverse magnetization, where the exchange energy between neighboring spins is not minimized.

Dipolar interactions are responsible for domain formation inside a ferromagnet. If all spins are parallel to each other to satisfy the ferromagnetic exchange interaction, the stray field generated in the environment by such magnetization distribution in an arbitrarily shaped magnetic sample may be very large. Hence, the sample may break into magnetic domains with different orientations of the magnetization, as shown in Fig. 1.2, even at the expense of forming domain

walls within which the exchange energy is not minimized, as shown in the inset in Fig. 1.2 (b) [31]. As will become clear later, the samples explored in this thesis have a single magnetic domain, a fact that facilitates the interpretation of the observed results.

1.1.3.2 Magneto-crystalline anisotropy energy

Another source of anisotropy in ferromagnets is related to the crystal structure of the materials and is called magneto-crystalline anisotropy (MCA). MCA arises due to the combination of crystal field splitting and SOC. The crystal field created by the lattice of the material quenches the orbital angular momentum and some particular orbitals of the electrons, depending on the symmetry of the crystal, are stabilized [32]. On top of that, SOC[6] relates those stabilized orbital momentum states with the spin of electrons [33] and, as a consequence, the alignment of the magnetization is favored along certain crystallographic directions [1] and the Hamiltonian related to MCA reflects the symmetry of the crystal. Here, only ferromagnetic materials with uniaxial MCA are studied. For such cases, the MCA Hamiltonian can be given as a power series expansion in terms of the polar and azimuthal angles of the magnetization with respect to the uniaxial symmetry axis. In the case of a hexagonal crystal:

$$\mathcal{H}_K = \sum_{i=1}^{N_s} \left(k_1 (1 - (\boldsymbol{S}_i \cdot \hat{\boldsymbol{e}})^2) + k_2 (1 - (\boldsymbol{S}_i \cdot \hat{\boldsymbol{e}})^2)^2 + \mathcal{O}((1 - (\boldsymbol{S}_i \cdot \hat{\boldsymbol{e}})^2)^3) \right)$$

$$= \sum_{i=1}^{N_s} \left(k_1 \sin^2 \Phi_i + k_2 \sin^4 \Phi_i + \mathcal{O}(\sin^6 \Phi_i) \right), \tag{1.11}$$

where $\hat{\boldsymbol{e}}$ is the unit vector or the uniaxial anisotropy axis, Φ_i is the polar angle between $\boldsymbol{S}_i$ and $\hat{\boldsymbol{e}}$, and k_1 and k_2 are anisotropy constants that have units of energy. Only even terms in $\sin \Phi_i$ are present in the expression because odd terms vanish due to time-inversion symmetry. Terms of order $\sin^6 \Phi_i$ and higher also depend on the azimuthal angle of the spin, but the anisotropy constants decrease with the order and it is typically sufficient to consider first and second order anisotropy. For the case of interest in this thesis, $k_1 > 0$ and $(k_1 + k_2) > 0$, the magnetization is energetically favored to lie along the uniaxial symmetry axis, which is called the easy axis (EA). In

---

[6] SOC is a relativistic effect that describes the interaction of the spin state and the orbital moment state. In a semi-classical picture can be understood as arising from the interaction between the electron spin and the magnetic field felt by the electron in its own frame of reference during its orbital motion in the Coulomb potential of the crystal.

the particular case of Co, at room temperature it displays a hexagonal close packed (hcp) structure, for which the EA is the c axis of the crystal. The MCA energy per atom can take a broad range of values depending on the material and typically ranges from 10^{-28} to 10^{-22} J [3], so it is at least two orders of magnitude smaller than the exchange interaction for the most common ferromagnetic materials.

1.1.3.3 Zeeman energy

Upon the application of an external field, magnetic moments tend to align with it to minimize the Zeeman energy

$$\mathcal{H}_Z = -\mu_0 \sum_{i=1}^{N_s} \boldsymbol{\mu}_i \cdot \boldsymbol{H}^i = -\mu_0 \sum_i \mu_i \boldsymbol{S_i} \cdot \boldsymbol{H}^i, \qquad (1.12)$$

where $\boldsymbol{H}^i$ is the external magnetic field at the position of the ith spin. For typical laboratory conditions, such as in magnetometer tools, the external field will be homogeneous and therefore, its superscript i may be dropped. For an external field of $\mu_0 H = 0.2$ T, which is a typical value for experiments here, the Zeeman energy per atom in Co is of the order of 10^{-23} J.

1.1.3.4 Other energy terms and total Hamiltonian

Further interactions can affect the magnetic state of a material. For instance, the magnetization of a sample can be affected by an electric field *via* the so-called magneto-electric effect. In a similar manner, the application of a stress can also tune the magnetization of a material by means of the magneto-elastic effect. Such terms are neglected for the purpose of this thesis and the total Hamiltonian considered here is a sum of the exchange interaction, and magnetostatic, MCA and Zeeman energies, such that

$$\mathcal{H} = \mathcal{H}_{ex} + \mathcal{H}_{dip} + \mathcal{H}_K + \mathcal{H}_z. \qquad (1.13)$$

The minimization of the energy of a ferromagnet is an extremely difficult task even at zero temperature, in particular because $\mathcal{H}_{ex}$ and $\mathcal{H}_{dip}$ depend on the state of the whole spin system. At finite temperatures entropic contributions need to be considered, which further complicates the task. In general, a competition between the four terms is established: ferromagnetic exchange tends to align the spins parallel to each other, dipolar interaction tries to minimize the

demagnetizing field inside the material, MCA energy is minimized if the spins lie along specific directions of the crystal and penalizes other directions, and the Zeeman energy favors an alignment of the spins along an external field. The resulting energy landscape is complex and exhibits many local minima. Therefore, the system frequently populates metastable states, as will become apparent in the next section, and as a consequence, the identification of the energy or free energy global minimum, even if it were an easy task, which is not, is insufficient to evaluate the behavior of the system.

1.2 Magnetization reversal

1.2.1 Hysteresis loop

Magnetization reversal is a process by means of which a FM system transitions from a state of being close to positive magnetic saturation to being close to negative magnetic saturation or vice versa, typically upon the application of an external magnetic field opposing the initial magnetization. The reversal process is in general a complex one and combines magnetic domain nucleation, growth, and rotation, as a consequence of the multiple local energy minima of the energy landscape of ferromagnets, until eventually, for sufficiently high fields, the magnetization of the sample is (almost) aligned with the external field [1].

The field-dependence of the magnetization of a ferromagnet is typically represented by plotting the projection of the magnetization along the field axis, denoted here as M_H, as a function of the applied field strength H, as shown in Fig. 1.3. For sufficiently high fields, possibly present domains in the sample align their magnetization parallel to the field and the sample (almost) reaches its saturation value M_S, shown by a green dashed line in Fig. 1.3. Upon decreasing the field to zero, M_H decreases and gets to its remanence value M_r, signaled by a blue circle. As the field strength crosses the $H = 0$ value, the ferromagnet undergoes a first order phase transition and the stable state of the magnetization changes sign. However, the state of antiparallel H and M_H can be metastable and the system may remain in such state during the timescale of the experiment. Such metastability gives rise to a hysteretic behavior of M_H vs. H, which is exemplarily shown in Fig. 1.3. The loop in Fig. 1.3 has two branches that are different in a range of H values around $H = 0$: the

decreasing field branch, signaled by orange arrows, and the increasing field branch, signaled by purple arrows. The area between the two branches is related to energy losses[7].
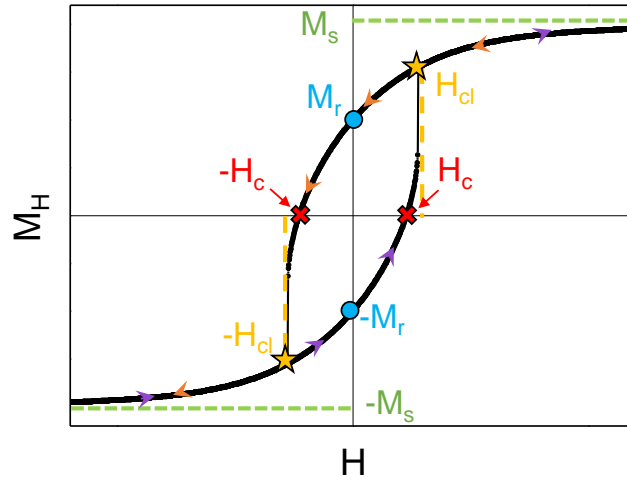

Figure 1.3 Exemplary hysteresis loop for a ferromagnet. Green lines indicate the saturation magnetization $\pm M_s$, the blue circles show the remanent magnetization $\pm M_r$, and the red crosses indicate the coercive field $\pm H_c$. Yellow stars point to the closure field $\pm H_{cl}$. Orange arrows indicate the decreasing field branch, and purple ones the increasing field branch.

By further decreasing the field to negative values one may eventually reach the demagnetized state at the coercive field $-H_c$, represented by a red cross, which can occur either because the sample contains domains with a total magnetization adding up to zero, or because the magnetization is perpendicular to the applied field axis and therefore M_H is zero, as will be the case in the macrospin model presented in Section 1.2.2. At the closure field $-H_{cl}$, shown as a yellow star in Fig. 1.3, both branches of the hysteresis loop combine and $M_H(H)$ is single-valued again. Eventually, for a sufficiently large negative H, magnetization reversal is completed and the system achieves a magnetization close to the negative saturation state $-M_s$.

In the increasing field branch the process is repeated in such way that

$$M_H^{inc}(H) = -M_H^{dec}(-H) \tag{1.14}$$

---

[7] In some applications large energy losses are desirable because of the higher stability of the magnetic states it brings with them; in some other applications, energy losses are to be minimized. Accordingly, materials are designed to exhibit larger or smaller hysteresis loops.

and at $H = 0$, $M_H = -M_r$. This leads to an interesting property of ferromagnets, which is that, depending on the previous magnetization state, there are two possible states at $H = 0$, making them suitable for storage of information.

1.2.2   Macrospin model

A useful model for the study of magnetization reversal, applicable to the thin film samples studied in Chapter 4, is the macrospin model, also called Stoner-Wohlfarth model [3, 34]. Here, simplifications are made for the total Hamiltonian of Eq. (1.13) and a free energy $\mathcal{F}$ expression is proposed based on the premise that the exchange interaction is much stronger than the rest of the terms. Assuming that the other energy terms do not modify the parallel alignment of the spins set by the exchange, the magnetization vector has a constant length, while the rest of the terms only affect its orientation. Exchange interaction is thus a constant that does not modify the magnetization orientation dependence of $\mathcal{F}$ and is ignored in this model. The whole material is assumed to have a single magnetic domain and to be described by a macrospin vector that rotates coherently. Therefore, it is only a valid model for samples with negligible magnetostatic energy, as is the case for the thin film samples fabricated and investigated in Chapter 4.

The effects of temperature are included in $\mathcal{F}$ by considering temperature-dependent anisotropy constants $K_i(T)$ and magnetization vector length $M_s(T)$, because thermal fluctuations prevent the perfect alignment of all the spins. In addition, if one considers a thin film with in-plane uniaxial anisotropy and with the external magnetic field applied in the plane of the sample, the magnetization will be contained in the xy plane shown in Fig. 1.4. With this restriction, the shape anisotropy given in Eq. (1.10) is just another constant energy term that can be ignored in the following. With these assumptions, and considering MCA up to second order, the free energy per volume unit for the macrospin model reads

$$\frac{\mathcal{F}}{V} = -\mu_0 M_s \hat{\boldsymbol{m}} \cdot \boldsymbol{H} + K_1(1 - (\hat{\boldsymbol{m}} \cdot \hat{\boldsymbol{e}})^2) + K_2(1 - (\hat{\boldsymbol{m}} \cdot \hat{\boldsymbol{e}})^2)^2. \tag{1.15}$$

$\mathcal{F}/V$, K_1, and K_2 have units of energy per volume. K_1 and K_2 are related to k_1 and k_2 in Eq. (1.11) by $K_1 = \frac{N_s}{V} k_1$ and $K_2 = \frac{N_s}{V} k_2$. $\hat{\boldsymbol{m}}$ is the unit vector of the magnetization, namely $\boldsymbol{M}/M_s$. Without loss of generality, $\boldsymbol{H}$ is assumed to be applied along the x axis. The angle between the EA and $\boldsymbol{H}$ is Φ_0, and the one between $\boldsymbol{M}$ and $\boldsymbol{H}$ is Φ_M, as shown in Fig. 1.4.

With those definitions, Eq. (1.15) can be rewritten as

$$\frac{\mathcal{F}}{V} = -\mu_0 M_s H \cos\Phi_M + K_1 \sin^2(\Phi_0 - \Phi_M) + K_2 \sin^4(\Phi_0 - \Phi_M). \tag{1.16}$$
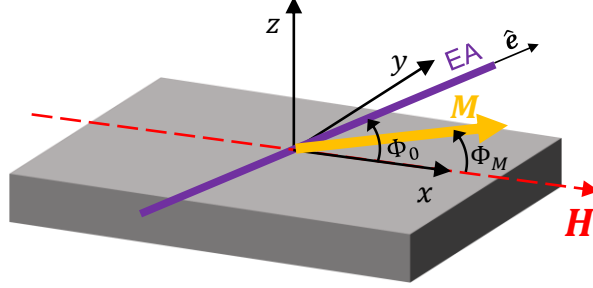
Figure 1.4 Schematics of the geometry of the macrospin model for thin films with the definition of the angles. The external magnetic field is applied along x, and the orientation of the EA is given by the unit vector $\hat{\boldsymbol{e}}$, contained in the xy plane, at an angle Φ_0 from the applied field axis. The magnetization $\boldsymbol{M}$ forms an angle Φ_M with the applied field axis.

By searching the local and absolute minima of $\mathcal{F}/V$ as a function of Φ_M for fixed Φ_0 and H [Appendix III], the stable and metastable values of $M_H = M_s \cos\Phi_M$ are obtained. In the $\mathcal{F}/V$ vs. Φ_M landscape absolute and local minima are separated by a barrier and thus, the observed magnetic state can be a metastable one with antiparallel field and magnetization depending on the previous state of the system, leading to hysteretic behavior. The model in Eq. (1.16) will be used in Section 4.2.3 to fit Φ_0- and H-dependent vibrating sample magnetometry data, in order to corroborate that the magnetization reversal in the fabricated epitaxial Co samples with in-plane EA is compatible with a macrospin type reversal.

1.3   Spin Hall effect

In addition to the study of magnetism in ferromagnetic materials, this thesis, in particular Chapter 3, also investigates the spin polarization of non-ferromagnetic metals induced by electrical means. This aspect is intimately related to the field of spintronics, which aims at exploiting not only the charge degree of freedom of electrons, but also their spin. In this regard, there is a great interest to study ways of generating, manipulating, and detecting spin currents [35-38], a magnitude that is defined in the following. Given the definition of a charge current density as

$$\boldsymbol{j}_c = \boldsymbol{j}_\uparrow + \boldsymbol{j}_\downarrow, \tag{1.17}$$

where $\boldsymbol{j}_\uparrow$ and $\boldsymbol{j}_\downarrow$ are current densities associated to electrons polarized with up and down spins, respectively, a spin current density is defined as:

$$\boldsymbol{j}_s = \boldsymbol{j}_\uparrow - \boldsymbol{j}_\downarrow \,. \tag{1.18}$$

Thus, if $\boldsymbol{j}_\uparrow$ and $\boldsymbol{j}_\downarrow$ are antiparallel, a pure spin current is achieved, where spin information is transported without charge flow.
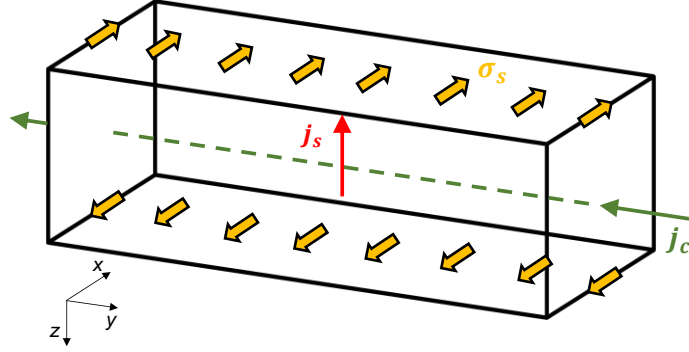

Figure 1.5   Schematics of the SHE geometry. The charge current $\boldsymbol{j}_c$ is represented by a green arrow and is parallel to y. Pure spin currents $\boldsymbol{j}_s$ arise due to SOC perpendicular to both $\boldsymbol{j}_c$ and to the spin polarization $\boldsymbol{\sigma}_s$ in all directions. One of the spin currents that is created is represented by a red arrow. The represented $\boldsymbol{j}_s$, along the z axis, is associated with spins polarized along $\pm x$. Due to the presence of surfaces, a spin accumulation arises parallel to them as represented by yellow arrows, with a polarization $\boldsymbol{\sigma}_s$ that is perpendicular to $\boldsymbol{j}_c$ and $\boldsymbol{j}_s$, and which has an opposite sign on opposite surfaces.

A phenomenon that is commonly exploited for the generation of pure spin currents is the spin Hall effect (SHE), while its counterpart, the inverse SHE, can be used for their detection. The SHE is a relativistic SOC-related phenomenon, in which spin currents are generated by electrical currents [39-42] in a process that is schematically depicted in Fig. 1.5. Upon the injection of a charge current $\boldsymbol{j}_c$ in a material with high SOC, electrons with opposite spin are preferentially deflected in opposite directions giving rise to a nonzero spin current $\boldsymbol{j}_s$ that is perpendicular both to $\boldsymbol{j}_c$ and to the polarization of the spins $\boldsymbol{\sigma}_s$. $\boldsymbol{j}_s$ will occur in all radial directions away from $\boldsymbol{j}_c$ and one of such is schematically shown in Fig. 1.5. While the charge current is being applied, $\boldsymbol{j}_s$ is maintained and, in a finite system, a spin accumulation[8] μ_s with inverse $\boldsymbol{\sigma}_s$ at opposite interfaces of the material will arise. While the detection of SHE in metals is typically done electrically [43-50], SHE has been measured in semiconductors by means of magneto-optical Kerr effect

---

[8] The spin accumulation μ_s is a difference in the chemical potential of the spin up and the spin down electrons, and as such is given in units of energy.

[51-55], a method that will be explained in Section 1.4. However, the detection of SHE in metals utilizing optical techniques is more challenging and is the focus of Chapter 3.

1.4 Light-matter interaction: principles of magneto-optics

1.4.1 Introduction

Magneto-optical (MO) effects are related to the interaction of polarized light with magnetized matter. The first observation of a MO effect was carried out by Faraday in 1845, when he subjected a piece of glass to a magnetic field and observed that the polarization of a light beam was modified when transmitted through it, with the change in polarization being proportional to the applied field [56]. Thereafter, Kerr observed a change in polarization of light reflected on the pole of a magnet [57, 58]. The Faraday effect in transmission and the MO Kerr effect (MOKE) in reflection are widely used nowadays for the investigation of magnetism. In this thesis, only the reflection geometry will be utilized. In addition, the focus here is the MOKE that depends linearly on the components of the magnetization or the spin polarization of materials, without considering bilinear or higher order effects in MOKE or effects that are quadratic in the magnetization such as the Voigt effect [59].

Early works utilized MO effects to probe bulk materials and an extensive bibliography of those may be found in a 1967 paper by Palik and Henvis [60]. In the subsequent decades, MO effects were regarded with interest [59] due to the development of commercial application of MO recording technologies [61-63]. In the 1980s, Bader and coworkers started to exploit MOKE to probe surface magnetism in ultrathin films. After the first use of MOKE as an experimental technique to probe magnetism in monolayers [64] many works followed this approach [65, 66] and MOKE became a well-established and widely used metrology tool in the field of nanomagnetism [67, 68].

Given its spectroscopic capabilities [69, 70], MOKE can be element specific [71, 72], because different elements give rise to MO transitions at different wavelengths, in particular in the ultraviolet part of the spectrum. Imaging with spatial resolution is also possible, including microscopy [31, 73]. MOKE is also a very adequate technique for the detection of ultrafast magnetic processes because it allows to perform pump-probe type experiments [74].

In addition, as light can only penetrate a certain thickness inside materials, MOKE only gets information up to a given depth, whose value depends on the material under study, the wavelength used to probe it and other parameters such as the angle of incidence. For transition metals and visible light, the information depth, which is the depth at which the MO signal decreases by 1/e, is in the order of 10 - 20 nm. Due to this fact, MOKE can get to a sensitivity level able to measure hysteresis loops of extremely thin ferromagnetic films [64]. It is also possible to perform depth-selective measurements by tuning the wavelength or the angle of incidence of light; this selectivity comes from the variation of the MOKE phase originating from FM layers located at different depths inside the multilayer structure [75, 76].

Due to all these advantages, as well as due to the fact that MOKE setups are relatively simple and cheap, MOKE is nowadays widely utilized for the characterization of the magnetic properties of thin films and nanostructures. In the following sections, details about the origin and the description of MOKE will be given.

1.4.2   Origin of MOKE and dielectric tensor

The most common mechanism for the interaction of light with matter is the absorption of one photon by one electron through an electric dipole transition[9]. In order to understand the microscopic origin of MOKE, one has to consider that exchange interaction in ferromagnets (or an external applied field in non-ferromagnetic materials) produces a splitting of electronic orbitals in the crystal and reduces the symmetry. Additionally, SOC generates a further splitting of the orbitals. The combination of both splittings leads to different optical absorptions for left and right circularly polarized light (CPL). As linearly polarized light can be described as a superposition of right and left CPL of the same amplitude, when linearly polarized light is sent to a system with exchange and SOC splitting, the difference in absorption for right and left CPLs leads to the fact that the reflected light will not be linear, but will acquire an ellipticity, which is exactly the principle of longitudinal and polar MOKE. Thus, both exchange and SOC splitting are necessary for MOKE to occur [78-80].

---

[9] The effect of the magnetic field of light onto the optical properties of a material is negligible at visible frequencies, so the magnetic permeability tensor $\overline{\overline{\mu}} = \mu_0 \mathbb{1}_{3\times3}$ [77]. $\overline{\overline{\mu}}$ relates the magnetic induction $\boldsymbol{B}$ and the magnetic field $\boldsymbol{H}$ by $\boldsymbol{B} = \overline{\overline{\mu}}\boldsymbol{H}$.

The microscopic origin of light-matter interaction is commonly translated to a macroscopic description in terms of a local optical property as the frequency-dependent dielectric tensor $\bar{\bar{\varepsilon}}(\omega)$ [77] (also called permittivity tensor)[10], which is represented by a 3×3 matrix:

$$\bar{\bar{\varepsilon}} = \begin{pmatrix} \varepsilon_{xx} & \varepsilon_{xy} & \varepsilon_{xz} \\ \varepsilon_{yx} & \varepsilon_{yy} & \varepsilon_{yz} \\ \varepsilon_{zx} & \varepsilon_{yx} & \varepsilon_{zz} \end{pmatrix}. \tag{1.19}$$

The materials considered here are optically isotropic, so $\varepsilon_{xx} = \varepsilon_{yy} = \varepsilon_{zz}$. In the absence of MOKE, the off-diagonal elements of $\bar{\bar{\varepsilon}}$ are zero. However, if the material is magneto-optically active, some off-diagonal components of $\bar{\bar{\varepsilon}}$ become nonzero, depending on the orientation of the magnetization with respect of the sample plane and the plane of incidence of light. Three configurations are hereby distinguished for MOKE, namely, longitudinal (L-MOKE), transverse (T-MOKE), and polar (P-MOKE). L-MOKE occurs when $\boldsymbol{M}$ is contained in the plane of the sample and in the plane of incidence, as shown in Fig. 1.6 (a), and gives rise to nonzero $\varepsilon_{yz} = -\varepsilon_{zy}$. T-MOKE configuration is realized when $\boldsymbol{M}$ is contained in the sample plane but is perpendicular to the plane of incidence as depicted in Fig. 1.6 (b), and gives rise to nonzero $\varepsilon_{xz} = -\varepsilon_{zx}$. In P-MOKE, $\boldsymbol{M}$ is perpendicular to the sample surface, as shown in Fig. 1.6 (c), giving rise to nonzero $\varepsilon_{xy} = -\varepsilon_{yx}$. For an arbitrary orientation of the magnetization with a unit vector given by $\hat{\boldsymbol{m}} = (m_x, m_y, m_z)$ (see definition of axes in Fig. 1.6), the dielectric tensor of a magneto-optically active and optically isotropic material has the form [68]:

$$\bar{\bar{\varepsilon}} = N^2 \begin{pmatrix} 1 & iQ_{MO}m_z & -iQ_{MO}m_y \\ -iQ_{MO}m_z & 1 & iQ_{MO}m_x \\ iQ_{MO}m_y & -iQ_{MO}m_x & 1 \end{pmatrix}, \tag{1.20}$$

where N is the refractive index of the medium and Q_{MO} is the so-called MO coupling constant, both of which are complex quantities and wavelength (or frequency) dependent. Because only optically and magneto-optically isotropic systems are considered here, a single N and Q_{MO} suffice to describe the dielectric tensor in all directions.

---

[10] The optical conductivity tensor $\bar{\bar{\sigma}}_{op}(\omega)$ is often used in literature instead of the dielectric tensor $\bar{\bar{\varepsilon}}(\omega)$. Both quantities are related by $\bar{\bar{\varepsilon}}(\omega) = \varepsilon_0 + \frac{i\bar{\bar{\sigma}}_{op}(\omega)}{\omega}$, where ε_0 is the vacuum permittivity and ω is the frequency.

$$\bar{\bar{\varepsilon}} = N^2 \begin{pmatrix} 1 & 0 & 0 \\ 0 & 1 & iQ_{MO} \\ 0 & -iQ_{MO} & 1 \end{pmatrix} \qquad \bar{\bar{\varepsilon}} = N^2 \begin{pmatrix} 1 & 0 & -iQ_{MO} \\ 0 & 1 & 0 \\ iQ_{MO} & 0 & 1 \end{pmatrix} \qquad \bar{\bar{\varepsilon}} = N^2 \begin{pmatrix} 1 & iQ_{MO} & 0 \\ -iQ_{MO} & 1 & 0 \\ 0 & 0 & 1 \end{pmatrix}$$
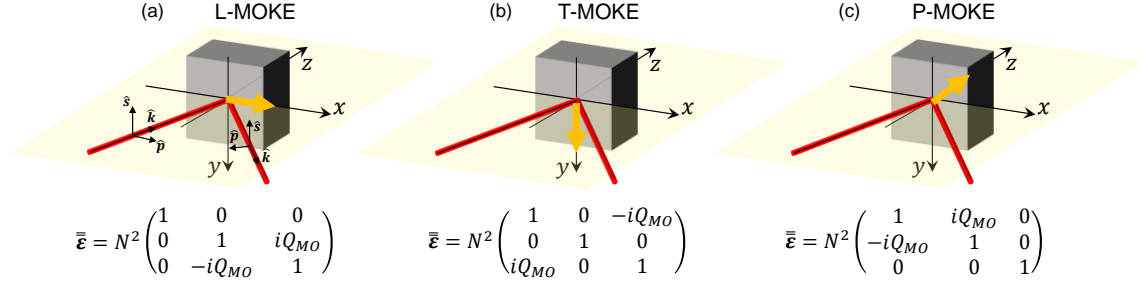
Figure 1.6 Schematics of L-, T-, and P-MOKE configurations, with the corresponding dielectric tensor in (a), (b), and (c), respectively. In (a) the unit vector of the wave vector ($\hat{k}$), as well as the orientations of s and p polarizations are given. $\boldsymbol{M}$ is represented by a yellow arrow. The path of the light beam is shown in red, and defines the plane of incidence, which is shown as a yellow shadow.

1.4.3   Reflection matrix in MOKE

Materials characterization in optics and magneto-optics typically aims at determining the dielectric tensor, which for optically and magneto-optically isotropic materials means determining two wavelength-dependent complex constants, N and Q_{MO}, as well as the orientation of the magnetization. However, $\bar{\bar{\varepsilon}}$ of a material cannot be directly accessed experimentally in a reflection experiment and, in addition, a sample consisting of multiple layers will have a different $\bar{\bar{\varepsilon}}$ for each material. The experimentally accessible quantity related to the multilayer structure and to $\bar{\bar{\varepsilon}}$ of each material[11] is the reflection matrix $\bar{\bar{R}}$ of the sample and will be presented in the following.

Given that light is a transverse electromagnetic wave whose electric and magnetic fields oscillate in a plane perpendicular to the propagation direction $\hat{k}$ of the wave in isotropic media, the polarization state of the incident and the reflected light[12] in a reflection configuration as shown for instance in Fig. 1.6 (a) can be described by a two-dimensional vector as [81]

$$\boldsymbol{E} = \begin{pmatrix} E_s \\ E_p \end{pmatrix}, \tag{1.21}$$

where E_s is the component perpendicular to the plane of incidence and E_p is the one contained in the plane of incidence (s and p directions are indicated in Fig. 1.6 (a)). Any planar optical element that does not affect the degree of polarization of light, including the sample, can therefore

---

[11] In practice, only $\bar{\bar{\varepsilon}}$ of the layers that are sufficiently close to the surface (a few times the penetration depth of light) determine $\bar{\bar{R}}$.

[12] When referring to the polarization of an electromagnetic wave, one typically refers to its electric field, the magnetic field being intimately related to it.

be represented by a 2×2 matrix in the Jones' matrix formalism [81]. Correspondingly, the reflection matrix for a sample can be written as

$$\bar{\bar{R}} = \begin{pmatrix} r_{ss} & r_{sp} \\ r_{ps} & r_{pp} \end{pmatrix}. \tag{1.22}$$

In the case of optically isotropic and magneto-optically active samples limited to linear MO effects, and under the assumption that those MO effects are much smaller than conventional optical effects, i.e., $Q_{MO} \ll N$, the reflection matrix reads [82]:

$$\bar{\bar{R}} = \begin{pmatrix} r_s & \alpha + \gamma \\ -\alpha + \gamma & r_p + \beta \end{pmatrix}. \tag{1.23}$$

Here r_s and r_p are purely optical Fresnel coefficients independent of $\boldsymbol{M}$. α, β, and γ are related to L-, T-, and P-MOKE respectively, i.e., they are proportional to a product of the magneto-optical coupling constant Q_{MO} and m_x, m_y, and m_z respectively. Therefore, α, β, and γ are inverted upon magnetization reversal. All the elements in Eq. (1.23) are complex parameters that depend on the wavelength of the light utilized in the experiment, as well as on the angle of incidence.

The relation between $\bar{\bar{R}}$ and $\bar{\bar{\varepsilon}}$ of the materials constituting the sample is given by the solution of Maxwell's equations inside the material taking into account adequate boundary conditions at each interface. For a semi-infinite medium formed of only one material, the elements of $\bar{\bar{R}}$ can be calculated analytically as a function of the elements of $\bar{\bar{\varepsilon}}$, the angle of incidence, and the wavelength of light [82]. For a multilayer system with planar interfaces where each material is characterized by its own $\bar{\bar{\varepsilon}}$, the relationship between $\bar{\bar{R}}$ and $\bar{\bar{\varepsilon}}$ of each material is more complex and is detailed in Section 2.5.

Considering the reflection matrix given by Eq. (1.23) one can readily identify the effects related to each magnetization component. If the sample is not magnetized ($\alpha = \beta = \gamma = 0$), incident light that is purely p- or s-polarized does not change its polarization state upon reflection[13]. However, if the sample is magnetized along the x axis, as in Fig. 1.7 (a), the off-diagonal component of the reflection matrix α causes a mixture of s and p components of the polarized

---

[13] Any other linearly polarized light that is a superposition of s- and p-polarized light with an electric field of the form $\boldsymbol{E}^{in} = \begin{pmatrix} E_s^{in} \\ E_p^{in} \end{pmatrix}$ will typically be elliptically polarized after reflection even in the absence of MOKE because in general $r_s \neq r_p$.

light causing a rotation by an angle θ_K, so-called Kerr rotation, and an ellipticity ϵ_K, called Kerr ellipticity, in the reflected light. θ_K and ϵ_K are small quantities that can be safely approximated as:

$$\theta_K = \mathrm{Re}\left(\alpha/r_p\right) \tag{1.24.a}$$

$$\epsilon_K = \mathrm{Im}\left(\alpha/r_p\right) \tag{1.24.b}$$

As α, θ_K and ϵ_K invert their sign upon magnetization reversal. If the sample is magnetized along z instead of x, an equivalent effect would occur, and α would need to be replaced by γ in Eqs. (1.24.a) and (1.24.b). Contrastingly, if the sample is magnetized along y, no mixture of s and p polarization is caused, because β, the element of the reflection matrix related to m_y, occurs in the diagonal of $\overline{\overline{R}}$. In particular, it is a modification of the r_{pp} component, and therefore T-MOKE causes a change in the p component of the incident light while leaving s-polarized light unchanged.
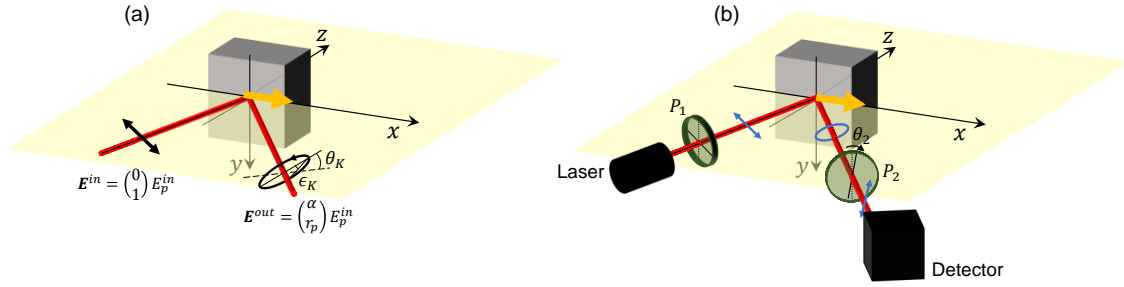

Figure 1.7 (a) Schematic representation of L-MOKE when p-polarized light is reflected on a sample magnetized along the x axis. The reflected light acquires a rotation θ_K and an ellipticity ϵ_K that are exaggerated to facilitate their identification. Jones vectors for the incident ($\boldsymbol{E^{in}}$) and the reflected light ($\boldsymbol{E^{out}}$) are also shown. (b) Crossed polarizers setup to measure θ_K. The first polarizer P_1 is aligned to provide p-polarized light. After the reflection, the second polarizer P_2 is aligned at an angle θ_2 with respect to the crossing with P_1.

Even though measuring all the elements of $\overline{\overline{R}}$ up to a proportionality factor is feasible (see Section 2.3) and is actually a core aspect of this thesis, MOKE is most commonly used as a tool to measure hysteresis loops and characterize ferromagnetic films rather than for the detection of MO effects *per se*. Generally, the L- or P-MOKE-induced polarization changes and the T-MOKE-induced intensity changes are measured to obtain information about specific components of the magnetization.

For L- and P-MOKE-induced polarization changes to be detected, they first need to be transformed into intensity changes, and different optical setups are utilized for this purpose. One

of the most widely used ones is the crossed polarizers setup [67, 68], as the one shown in Fig. 1.7 (b). A first polarizer P_1 is set to transmit p-polarized light[14]. After reflection on the magnetized sample, a second polarizer P_2 is set to be a small angle θ_2 away from extinction, as shown in Fig. 1.7 (b). This maximizes the sensitivity with respect to MOKE-induced rotation[15]. A detector is placed after P_2 and measures the light intensity I_D, which is proportional to θ_K (see Appendix I). Upon sweeping a magnetic field along the x (for L-MOKE) or the z (for P-MOKE) axis, the changes in I_D related to the changes in M_H are tracked as a function of H and hysteresis loops are measured. Under these experimental conditions, it can be shown (Appendix I) that

$$\theta_K = \frac{\theta_2}{4} \frac{\delta I}{I},$$

(1.25)

where $\delta I = I_D(+\boldsymbol{M}) - I_D(-\boldsymbol{M})$, and $I = \frac{1}{2}\big(I_D(+\boldsymbol{M}) + I_D(-\boldsymbol{M})\big)$.

Other types of polarization-sensitive setups are also widespread [83, 84]. It is also possible to tune the angle of incidence: even though both L- and P-MOKE give rise to θ_K and ϵ_K, the sensitivity to the m_x or to m_z component varies with the angle of incidence of light. For instance, at normal incidence, one is only sensitive to m_z, so this kind of configuration is commonplace for P-MOKE detection. L- and P-MOKE can also be separated by performing two measurements: one with incident p-polarized light and another with s-polarized light, given that α and γ are preceded by different signs in the r_{sp} and the r_{ps} components of the reflection matrix.

For T-MOKE detection, a straightforward measurement technique is to shine p-polarized light onto the sample magnetized along the y axis and detect the changes in light intensity upon magnetization reversal [85, 86]. Alternatively, one can use an incident light that is a mixture of s- and p-polarized light and detect effective polarization changes induced by the β element in the reflection matrix in a polarization sensitive setup, which substantially improves the sensitivity [87].

---

[14] Alternatively, it could be set to transmit s-polarized light, and P_2 to be near p-polarization.

[15] In order to detect Kerr ellipticity, a quarter wave-plate is added to the setup before the analyzer, which effectively transforms the Kerr ellipticity into a rotation signal.

References

[1] J. M. D. Coey, *Magnetism and Magnetic Materials* (Cambridge University Press, Cambridge, U. K., 2010).

[2] N. Goldenfeld, *Lectures on phase transitions and the renormalization group* (Addison-Wesley, 1992).

[3] S. Blundell, Magnetism in Condensed Matter (Oxford University Press, Oxford, U.K., 2006).

[4] N. W. Ashcroft, N. D. Mermin, Solid State Physics (Saunders College, Philadelphia, 1976).

[5] A. Aharoni, *Introduction to the Theory of Ferromagnetism,* (Oxford University Press, Oxford, U.K., 2007).

[6] W. Lenz, Z. Phys., **21**, 613-615 (1920).

[7] E. Ising, Z. Physik **31**,253 *(1925).*

[8] L. Udvardi, L. Szunyogh, K. Palotás, and P. Weinberger, Phys. Rev. B **68**, 104436 (2003).

[9] R. Skomski, A. Kashyap, J. Zhou, and D. J. Sellmyer, J. Appl. Phys. **97**, 10B302 (2005).

[10] I. Dzyaloshinskii, J. Phys. Chem. Solids **4** (4), 241 (1958).

[11] T. Moriya, Phys. Rev. **120**, 91 (1960).

[12] J. J. Prejean, M.J. Joliclerc, and P. Monod, J. Phys. **41**, 427-435 (1980).

[13] Y. Ishikawa, K. Tajima, D. Bloch, and M. Roth, Solid State Commun. **19**, 525 (1976).

[14] M. Plumer and M. Walker, Journal of Physics C: Solid State Physics **14**, 4689 (1981).

[15] A. Fert and Peter M. Levy, Phys. Rev. Lett. **44**, 1538 (1980).

[16] P. Lévy and A. Fert, Phys. Rev. B **23**, 4667 (1981).

[17] F. Keffer, Phys. Rev. **126**, 896 (1962).

[18] A. Crépieux and C. Lacroix, J. Magn. Magn. Mater. **182**, 341 (1998).

[19] A. N. Bogdanov and D. A. Yablonskii, Zh. Eksp. Teor. Fiz, **95**, 178 (1989).

[20] S. Mühlbauer, B. Binz, F. Jonietz, C. Pfleiderer, A. Rosch, A. Neubauer, R. Georgii, and P. Böni, Science **323**, 915–919 (2009).

[21] A. Neubauer, C. Pfleiderer, B. Binz, A. Rosch, R. Ritz, P. G. Niklowitz, and P. Böni, Phys. Rev. Lett. **102**, 186602 (2009).

[22] C. Pappas, E. Lelièvre-Berna, P. Falus, P. M. Bentley, E. Moskvin, S. Grigoriev, P. Fouquet, and B. Farago, Phys. Rev. Lett. **102**, 197202 (2009).

[23] A. Fert, V. Cros, and J. Sampaio, Nat. Nanotechnol. **8**, 152–156 (2013).

[24] S. Heinze, K. von Bergmann, M. Menzel, J. Brede, A. Kubetzka, R. Wiesendanger, G. Bihlmayer, and S. Blügel, Nat. Phys. **7**, 713–718 (2011).

[25] S. Woo *et al.*, Nat. Mater. **15**, 501–506 (2016).

[26] C. Moreau-Luchaire *et al.*, Nat. Nanotechnol. **11**, 444–448 (2016).

[27] O. Boulle *et al.*, Nat. Nanotech. **11**, 449–454 (2016).

[28] F. Hellman *et al.*, Rev. Mod. Phys. **89**, 025006 (2017).

[29] R. F. L. Evans, W. J. Fan, P. Chureemart, T. A Ostler, M. O. A. Ellis, and R. W. Chantrell, J. Phys.: Condens. Matter **26**, 103202 (2014).

[30] H. Kronmüller and S. Parkin (Ed.), *Handbook of Magnetism and Advanced Magnetic Materials Vol. 2: Micromagnetism* (JohnWiley & Sons, 2007).

[31] A. Hubert and R. Schäffer, Magnetic Domains, (Springer, Berlin,1998).

[32] H. Brooks, Phys. Rev. **58**, 909 (1940).

[33] J. Kübler, *Theory of Itinerant Electron Magnetism* (Oxford University Press, Oxford, U.K., 2017).

[34] E. C. Stoner and E. P. Wohlfarth, Philos. Trans. Royal Soc. A **240**, 599 (1948).

[35] S. Datta and B. Das, Appl. Phys. Lett. **56**, 665 (1990).

[36] D. Awschalom and N. Samarth, Physics **2**, 50 (2009).

[37] P. Chuang *et al.*, Nat. Nanotechnol. **10**, 35–39 (2015).

[38] M. Cahay, Nat. Nanotechnol. **10**, 21–22 (2015).

[39] M.I. Dyakonov and V.I. Perel, Sov. Phys. JETP Lett. **13**, 467 (1971).

[40] M. I. Dyakonov and V. I. Perel, Phys. Lett. **35**, 459 (1971).

[41] J. E. Hirsch, Phys. Rev. Lett. **83**, 1834 (1999).

[42] J. Sinova, S. O. Valenzuela, J. Wunderlich, C. H. Back, T. Jungwirth, Rev. Mod. Phys **87**, 1213 (2015).

[43] E. Saitoh, M. Ueda, H. Miyajima, and G. Tatara, Appl. Phys. Lett. **88**, 182509 (2006).

[44] K. Ando, S. Takahashi, K. Harii, K. Sasage, J. Ieda, S. Maekawa, and E. Saitoh, Phys. Rev. Lett. **101**, 036601 (2008).

[45] Y. Kajiwara, *et al.*, Nature **464**, 262 (2010).

[46] S. O. Valenzuela and M. Tinkham, Nature **442**, 176 (2006).

[47] T. Kimura, Y. Otani, T. Sato, S. Takahashi, and S. Maekawa, Phys. Rev. Lett **98**, 156601 (2007).

[48] P. Laczkowski *et al.*, Appl. Phys. Lett. **104**, 142403 (2014).

[49] E. Sagasta, Y. Omori, M. Isasa, M. Gradhand, L. E. Hueso, Y. Niimi, Y. Otani, and F. Casanova, Phys. Rev. B **94**, 060412(R) (2016).

[50] M. Isasa, E. Villamor, L. E. Hueso, M. Gradhand, and F. Casanova, Phys. Rev. B **91**, 024402 (2015); **92**, 019905(E) (2015).

[51] Y. K. Kato, R. C. Myers, A. C. Gossard, and D. D. Awschalom, Science **306**, 1910 (2004).

[52] V. Sih, R. C. Myers, Y. K. Kato, W. H. Lau, A. C. Gossard, and D. D. Awschalom, Nat. Phys. **1**, 31 (2005).

[53] J. Wunderlich, B. Kaestner, J. Sinova, and T. Jungwirth, Phys. Rev. Lett. **94**, 047204 (2005).

[54] S. A. Crooker, M. Furis, X. Lou, C. Adelmann, D. L. Smith, C. J. Palmstrøm, and P. A. Crowell, Science **309**, 2191 (2005).

[55] N. P. Stern, D. W. Steuerman, S. Mack, A. C. Gossard, and D. D.Awschalom, Appl. Phys. Lett. **91**, 062109 (2007).

[56] M. Faraday, Trans. Roy. Soc. (London) **5**, 592 (1846).

[57] J. Kerr, Philos. Mag. **3**, 339 (1877).

[58] J. Kerr, Philos. Mag. **5**, 161 (1878).

[59] M.J. Freiser, IEEE Trans. Mag. **4**, 152 (1968).

[60] E. D. Palik and B. W. Henvis, Appl. Opt. **6**, 603-630 (1967).

[61] R. E. MacDonald and J. W. Beck, J. Appl. Phys. **40**, 1429 (1969).

[62] G.A.N. Connell, J. Magn. Magn. Mater. **54-57** 1561 (1986).

[63] P. Hansen, P. J. Magn. Magn. Mater. **83**, 6-12 (1990).

[64] E. R. Moog and S. D. Bader, Superlattice Microst., **1**(6), 543–552 (1985).

[65] E.R. Moog, S.D. Bader, P.A. Montano, G. Zajac, and T.H.Fleisch, Superlatt. Microstruct. **3**, 435 (1987).

[66] J. Araya-Pochet, C. A. Ballentine, and J. L. Erskine, Phys. Rev. B **38**, 7846(R) (1988).

[67] S.D. Bader, J. Magn. Magn. Mater. **100**, 440 (1991).

[68] Z. Q. Qiu and S. D. Bader, J. Magn. Magn. Mater. **200**, 664 (1999).

[69] V. N. Antonov, L. Uba, S. Uba, A. N. Yaresko, A. Y. Perlov, and V. V. Nemoshkalenko, Low Temp. Phys., **27**(6), 425-462 (2001).

[70] G. R. Harp, D. Weller, T. A. Rabedeau, R. F. C. Farrow, and M. F. Toney, Phys. Rev. Lett. **71**, 2493 (1993).

[71] A. R. Khorsand, M. Savoini, A. Kirilyuk, A. V. Kimel, A. Tsukamoto, A. Itoh, and Th. Rasing, Phys. Rev. Lett. **110**, 107205 (2013).

[72] S. Gang, R. Adam, M. Plötzing, M. von Witzleben, C. Weier, U. Parlak, D. E. Bürgler, C. M. Schneider, J. Rusz, P Maldonado, and P. M. Oppeneer, Phys. Rev. B **97**, 064412 (2018).

[73] J. McCord, J. Phys. D: Appl. Phys. **48**, 333001 (2015).

[74] E. Beaurepaire, J.-C. Merle, A. Daunois, and J.-Y. Bigot, Phys. Rev. Lett. **76**, 4250 (1996).

[75] J. Hamrle, *Magneto-optical determination of the in-depth magnetization profile in magnetic multilayers* (Ph.D. thesis, 2003).

[76] M. R. Pufall, C. Platt, and A. Berger, J. Appl. Phys **85**, 4818 (1999).

[77] L. D. Landau and E. M. Lifshitz, *Electrodynamics of Continuous Media*, (Pergamon, New York, 1984).

[78] H.R. Hulme, Proc. Roy. Soc. A **135**, 237 (1932).

[79] S. Visnovsky, *Optics in magnetic multilayers and nanostructures* (Crc Press, 2006).

[80] P. N. Argyres, Phys. Rev. **97**, 343 (1955).

[81] G.R. Fowles, *Introduction to Modern Optics* (Dover publications, Inc.,New York, U.S.A., 1975).

[82] C.-Y. You and S.-C. Shin, Appl. Phys. Lett. **69**, 1315 (1996).

[83] K. Sato, Jpn. J. Appl. Phys. **20**, 2403 (1981).

[84] P. Vavassori, Appl. Phys. Lett. **77**, 1605 (2000).

[85] T. Kokogawa, T. Numata, and S. Inokuchi, IEEE Trans. Magn. **29**, 3808 (1993).

[86] M. Tejedor, A. Fernández, and M. A. Cerdeira, Rev. Sci. Instrum. **69**,4000 (2011).

[87] E. Oblak, P. Riego, L. Fallarino, A. Martinez-de-Guerenu, F. Arizti, and A. Berger, J. Phys. D: Appl. Phys. **50**, 23LT01 (2017).

Chapter 2

Methods

The experimental and modeling methods that have been utilized in this thesis are explained. The principles of magnetron sputter deposition for thin film fabrication are presented in Section 2.1. The utilized structural characterization techniques are explained in Section 2.2. Generalized magneto-optical ellipsometry, a key technique in this thesis, is explained Section 2.3. Additional experimental techniques are presented in Section 2.4 and finally, the transfer matrix method for optical and magneto-optical modeling is explained in Section 2.5 as a key modeling technique.

2.1   Thin film fabrication: magnetron sputter deposition

2.1.1   Sputter deposition

Thin films studied in this work have thicknesses in the range of 5 - 150 nm and are in most cases multilayer structures, in which layers of different materials are stacked for the purpose of achieving specific physical properties. Their fabrication has been carried out by means of sputter deposition, a physical vapor deposition technique that is widely used due its stability in terms of operation and deposition conditions. The basis of this method is the erosion of atoms from the surface of a target material by means of mechanical collisions with high energy ions, which are generated by the discharge plasma of a suitable gas subjected to a voltage [1]. The whole process is carried out in a pre-pumped ultra-high vacuum chamber in which the gas that generates the plasma is introduced at an appropriate pressure. In this thesis, all sputtering processes are performed in an Ar environment, because reactions between the gas and the target material wanted to be avoided[16].

---

[16] For the generation of or compounds as oxides or nitrides, reactive sputtering can be used, using a reactive gas, such as oxygen (O_2) or nitrogen (N_2), in conjunction with a non-reactive gas at specific proportions.

By applying a voltage between the inner wall of the chamber (anode) and the target (cathode) Ar atoms are ionized giving rise to a plasma of free electrons (e⁻) and positively charged Ar⁺ ions[17]. Ar⁺ ions are accelerated towards the target and mechanically erode it, ejecting atoms of the material that travel ballistically in all directions, and part of them get to the surface that is intended to be coated. The process is schematized in Fig. 2.1.
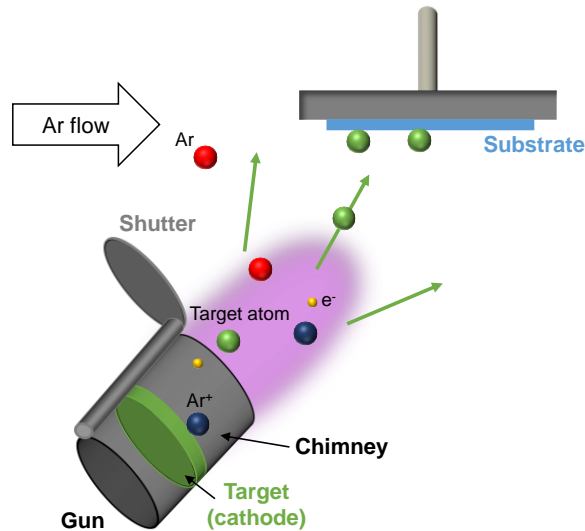

Figure 2.1 Schematics of the sputtering process. Ar atoms (red spheres) are ionized and the resulting Ar⁺ ions (dark blue spheres) collide with the negatively charged target (green disk), expelling atoms from it (green spheres) that travel ballistically, so that some of them are deposited on the substrate (shown in blue). The target is placed inside a gun with a chimney which has a shutter that can be opened and closed to impede or allow the eroded atoms to travel to the substrate. The decay of electronic excited states in Ar emits photons, which gives the plasma a characteristic glow, shown as a pink shadow around the gun.

For metallic targets the potential difference applied between the target and the chamber is DC. However, with insulating targets this leads to a positive charge accumulation at the surface that eventually impedes the plasma discharge. To avoid this, an AC radiofrequency (RF) voltage is applied to sputter insulators, so that during the negative half-cycle Ar⁺ ions charge the surface positively, and during the positive half-cycle free electrons neutralize it [2,3]. The erosion of the target occurs only during the negative half-cycle, and therefore, the deposition rate with RF sputtering is lower than for DC sputtering.

In order to sustain the plasma and increase the number of collisions of Ar⁺ ions with the target, magnetron sputtering is used in this thesis [1, 4]. In this scheme, permanent magnets are placed in specific configurations below the cathode to generate a static magnetic field that keeps the

---

[17] For suitable voltages and Ar pressures an equilibrium state is reached, where the formation of cations and free electrons is equilibrated with their recombination.

charged particles confined near the surface of the target due to the Lorentz force, thus increasing the erosion rate. This allows one to work at lower Ar pressures, minimizing collisions between Ar atoms and the atoms ejected from the target as the latter are on their way to the substrate, thus increasing the deposition rate. Unless otherwise stated, the Ar pressure utilized in the sputtering processes in this thesis was set to 0.4 Pa, with a continuous Ar gas flow of 20 $cm^3 \cdot min^{-1}$.
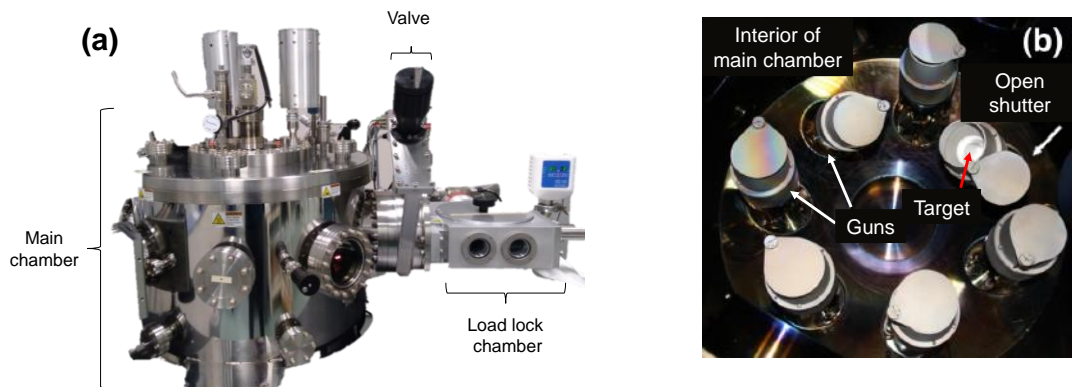

Figure 2.2 (a) Exterior of the AJA International Inc. ATC sputtering system. (b) Interior of the main chamber, showing the seven guns, two of which are tilted in the standard deposition conditions, and five of which are completely vertical.

The specific sputtering system used in this thesis is an AJA International Inc. ATC UHV magnetron sputter tool shown in Fig. 2.2. The chamber on the left of Fig. 2.2 (a) is the main chamber, where the sputtering processes that are described above occur. Its interior is shown in Fig. 2.2 (b), where seven guns can be seen, each of them equipped with a magnetron. Targets of different materials can be placed in them, electrically isolated from their respective chimneys, which are the metallic cylinders in which the targets are placed, as shown schematically in Fig 2.1. A set of permanent magnets are placed below the targets to confine the plasma close to their surface. A potential difference is applied to the targets by connecting them to one of the six power supplies that the system possesses, four of which are DC and two RF. Thus, up to six materials could be simultaneously co-sputtered, although this feature has not been utilized for this thesis. Instead, materials from different targets have been deposited in sequence forming multilayers.

The guns have a shutter whose opening and closing are controlled by compressed air, so that the target material can be eroded without its atoms being deposited on the substrate if the shutter is closed, which is useful for cleaning the surface of the targets and for establishing stable deposition conditions. In addition, the tilt of the guns can be controlled (see Fig. 2.2 (b), where five guns are completely vertical and two of them are tilted). In a typical operation where the desired layers

have homogeneous thickness, the guns are positioned facing the center of the sample holder. It is also possible to rotate the sample holder during the deposition to avoid lateral thickness variations. For the samples described in Chapter 4, one of the layers has a lateral variation of the thickness by design. In this process, the gun was not pointing to the center of the sample holder and the rotation of the sample holder was stopped.

If the main chamber in Fig. 2.2 (a) is vented, it takes about one day to pump it down to an adequately low pressure. Due to this fact it is only opened for the replacement of targets or for maintenance, while, for the purpose of introducing substrates to carry out a deposition process, one uses the load-lock, *i.e.* the chamber on the right of Fig. 2.2 (a). This chamber has a far lower volume and hence is pumped down much faster than the main chamber, in about two minutes. When the pressure in the load-lock is stabilized, the valve that separates it from the main chamber (shown in Fig. 2.2 (a)) can be opened and the sample holder can be transferred to the main chamber with a magnetic arm, which is retracted after the sample holder is properly held in the main chamber. The valve is then closed again and an Ar flow inside the main chamber is initiated. The whole process of loading a clean substrate and getting to a point where the main chamber is in the appropriate conditions to start the deposition process takes about five minutes, much less than if the loading of the sample were performed by opening the main chamber.

2.1.2   Thickness calibrations

The samples fabricated in this thesis require a high degree of control of the thickness of the layers involved and hence a careful calibration procedure needs to be followed. In such procedures, thin films of the material whose deposition rate is being calibrated are sputtered onto Si substrates under controlled and well-documented conditions of Ar pressure, sample position, gun tilt, power, and deposition time. The thickness of the calibration films is then measured by means of x-ray reflectivity (Section 2.2.2) or spectroscopic ellipsometry (Section 2.2.3). As an example, Fig. 2.3 (a) shows with black squares the thickness of Ag samples deposited at a power of 80 W for different deposition times. The thickness increases linearly with the deposition time and the deposition rate can be determined by a linear fit to the data (red line). Once deposition rates are known, the deposition time needed to get the desired thickness of a given material using the same deposition conditions is calculated in a straightforward manner.

It has also been observed that deposition rates depend linearly on the power applied to the target, which is the product of the current and the voltage difference between the target and the chamber. Therefore, power supplies typically run in stable-power mode, *i.e.*, keeping the power constant, rather than the voltage. Figure 2.3 (b) shows deposition rates of Ag as a function of power depicted as black squares, and the red line is a linear fit to the data.
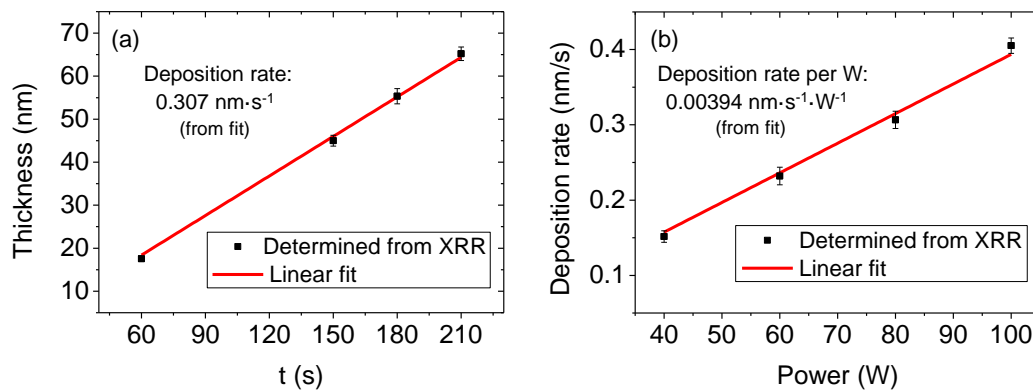

Figure 2.3 (a) Thickness determined by x-ray reflectivity (XRR) as a function of the deposition time for four different Ag films deposited at 80 W gun power setting. The deposition rate is determined by the slope of a linear fit to the data (red line). (b) Deposition rate as a function of gun power setting for Ag films. A linear fit to the data (red line) determines the deposition rate per W.

2.2 Structural characterization with x-rays

2.2.1 X-ray diffraction

In crystals atoms are arranged in regular lattices and diffraction effects can be observed when an electromagnetic wave with a wavelength of the order of the interatomic spacing impinges on them. Given that typical interatomic distances in crystals are of the order of 0.1 - 0.5 nm, the relevant part of the electromagnetic spectrum for the study of the crystalline structure of materials are x-rays, leading to the technique of x-ray diffraction (XRD) [5]. A periodicity exists between different crystal planes and, for instance, Fig. 2.4 shows schematically two different sets of planes, orange ones, with a separation of d_1 and green ones, with a separation of d_2. Figure 2.4 also shows an incident x-ray beam with an angle of incidence ω^X measured from the sample surface plane, as well as two diffracted waves at an angle $2\theta_i^X$ measured from the extension of the incident beam. For an incident x-ray beam with a wave vector $\boldsymbol{K_0}$ constructive interference between the waves scattered by a given set of planes will be achieved under the Laue condition [6, 7]:

$$K_i - K_0 = Q_i \, . \tag{2.1}$$

K_i is the wave vector of the light scattered by the set of planes $\{i\}$ and Q_i, which can be viewed as a momentum transfer, is a vector of the reciprocal lattice that is parallel to the normal of the set of planes $\{i\}$ and has a length that is an integer multiple of $2\pi/d_i$, where d_i is the distance between subsequent planes of the set. It is also important to note that only elastic x-ray scattering is considered here, so $|K_i| = |K_0|$. In Fig. 2.4 orange planes corresponding to the set $\{1\}$ are parallel to the sample surface, and thus Q_1 is normal to the sample surface and parallel to $\hat{n}_1$. Hence, the angle at which constructive interference is achieved occurs at some specific θ_1^X angles that fulfill $\theta_1^X = \omega^X$, *i.e.*, a symmetric x-ray source and the detector configuration. For green planes in set $\{2\}$, the momentum transfer Q_2 is parallel to $\hat{n}_2$, not normal to the surface, and an asymmetric source-detector configuration is needed to observe the constructive interference.
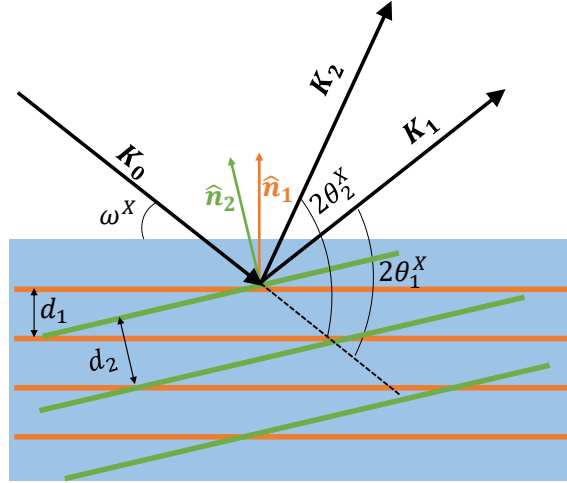

Figure 2.4 Sketch of two families of crystallographic planes ($\{1\}$, orange planes, $\{2\}$ green planes) and their normal vectors, an incident beam with wave vector K_0 at an angle of incidence ω, and two wave vectors for scattered rays, K_1 and K_2.

In this thesis, the most commonly used XRD configuration has been the so-called $\theta^X - 2\theta^X$ configuration, where the incidence angle of the x-rays $\omega^X = \theta^X$ is scanned while the position of the detector is simultaneously updated to be at $2\theta^X$. Therefore, this configuration is only sensitive to the distances between atomic planes that are parallel to the sample surface and intensity peaks corresponding to constructive interference occur when

$$2d_i \sin\theta_i^X = n\lambda \, , \tag{2.2}$$

which is the Bragg's condition, where n is an integer number and λ is the wavelength of the x-rays. By measuring the intensity as a function of $2\theta^X$ and knowing the materials that are present in the

thin film, one can identify the crystallographic planes that satisfy Bragg's law, which are typically classified using Miller indices (*hkl*). As will be shown in Chapter 4, XRD was used to determine the crystalline quality of multilayer thin films in which Co is epitaxially grown in a specific crystallographic orientation, namely hcp (10$\underline{1}$0).

2.2.2 X-ray reflectivity

X-rays can also be utilized for the measurement of thin-film thicknesses. The specific technique for this purpose is called x-ray reflectivity (XRR) and consists on measuring the intensity of a specularly reflected x-ray beam upon varying the angle of incidence with grazing incidence [8]. At the interfaces of a thin film there will be a change of electron density, *i.e.*, a change of refractive index from N_0 to N_1 at the top interface and from N_1 to N_2 at the bottom interface, and x-rays will be reflected and refracted at them. At the frequency of x-rays the refractive index of most materials is slightly smaller than 1, and thus, total external reflection can occur for sufficiently low incidence angles θ^X as defined in Fig. 2.5 (a). Total external reflection occurs up to a critical value of the angle of incidence, θ_c^X, which depends on the refractive index of the material under study and is independent of its thickness. For $\theta^X > \theta_c^X$ the paths of the x-ray beams are those shown in Fig. 2.5 (a). Upon an incident beam labeled as "1" in the figure, the detected light intensity will be given by the interference between rays "2" and "6", whose optical path difference is $2d \sin \theta^X$, where d is the thickness of the film. In the measurement process, the x-ray source and the detector are tilted synchronously and the reflected x-ray intensity is recorded as a function of $2\theta^X$, giving rise to a pattern like the one shown in Fig. 2.5 (b) for Ag films of different thicknesses deposited on a Si substrate. As observed in Fig. 2.5 (b), for $\theta^X < \theta_c^X$ the reflected intensity is almost constant, as x-rays cannot penetrate the thin film and the total external reflection condition is fulfilled. θ_c^X is independent of the thickness of the film, as it can be seen in Fig. 2.5 (b). For $\theta^X > \theta_c^X$ the incident x-rays can penetrate inside the thin film and an interference pattern between rays "2" and "6" is measured as a function of θ^X, showing fringes that are called Kiessig fringes [9]. The interference is constructive when the optical path difference is an integer multiple of the wavelength λ of the x-rays, and destructive interference occurs when the optical path difference is an odd multiple of $\lambda/2$. From the period of the Kiessig fringes the thickness d of the thin film can be determined. A quick estimate may be obtained because the difference in θ^X between two consecutive maxima or minima of the intensity is inversely proportional to d. This can be seen in Fig. 2.5 (b), where, the

thicker the Ag film is, the smaller the period of the Kiessig fringes is. It is also observed that the detected x-ray intensity decreases with increasing θ^X and that Kiessig fringes are damped because the thin film is absorptive.
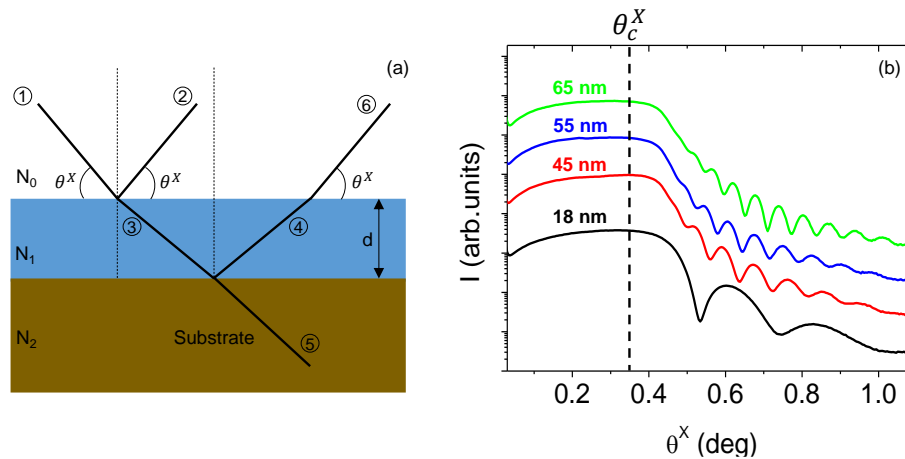

Figure 2.5 (a) Sketch of the path followed by the x-ray beams (reflected, refracted and transmitted) upon an incident beam (1) with an angle of incidence θ^X in the presence of a thin film (blue) of refractive index N_1 between a substrate and an incidence medium. (b) Intensity measured in specular reflection in a grazing incidence XRR experiment for four Ag samples with different thicknesses. The curves are vertically shifted with respect to each other to improve the visibility.

An X'Pert PRO PANalytical x-ray diffractometer has been used for the XRR and XRD measurements shown in this thesis. This system is equipped with a precise and reproducible ω^X - $2\theta^X$ goniometer with an angular precision of 10 μdeg. X-rays are generated by a Cu anode, whose K_α radiation ($\lambda = 0.154$ nm) has been utilized for the measurements, the K_β radiation being removed by a hybrid monochromator.

2.3   Generalized magneto-optical ellipsometry

After having explained the basics of MOKE in Section 1.4, this section focuses on generalized magneto-optical ellipsometry (GME), the magneto-optical characterization technique that has been used for the most part of the thesis, in particular in Chapters 3 and 4. Based upon the very simple hardware of a crossed polarizers setup presented in Section 1.4, this technique can access the full reflection matrix of a sample up to a complex constant, and is thus able to separate purely optical from magneto-optical effects, as well as to measure and disentangle longitudinal (L-), transverse (T-), and polar (P-) MOKE without the need of modifying or extending the simple setup [10-12].

2.3.1   GME optical setup

A generic GME optical setup is shown in Fig. 2.6 and consists of a light source, two rotatable linear polarizers and a photodetector. The light from the source is linearly polarized by the first polarizer P_1. The angle formed between the s polarization direction (shown in Fig. 2.6) and the polarization of the incident light is called $\tilde{\theta}_1$. In a general case, the light intensity on the sample and thus the noise level will depend on $\tilde{\theta}_1$. However, if one is able to make the light entering P_1 be circularly polarized, the light intensity at the sample will be constant for all $\tilde{\theta}_1$. After P_1, the light is specularly reflected from the sample and this will provoke a change in the light polarization. In a general case, the reflected light will be elliptically polarized. The reflected light passes through a second linear polarizer P_2, also called analyzer. P_2 projects the electric field of the reflected light onto its polarizing axis, which is positioned at an angle $\tilde{\theta}_2$, referenced to s polarization direction, as shown in Fig. 2.6. Finally, the light intensity I_D is measured by a photodiode detector.
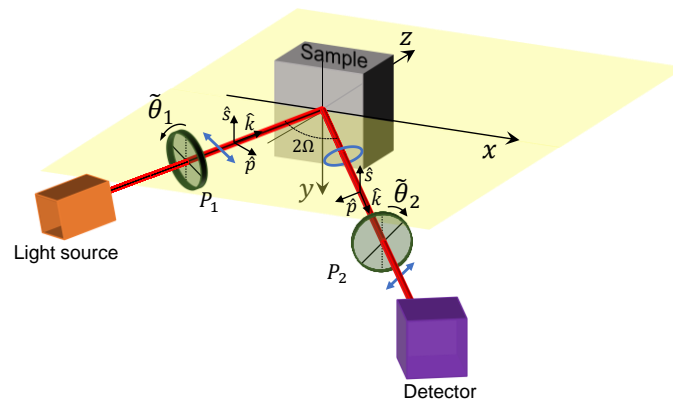

Figure 2.6 Schematics of the basic GME optical setup. The electric field of light after each optical element is represented in blue. The light path is represented by a red ray that goes through the optical elements and gets reflected at the sample surface. The angle of incidence is Ω, measured with respect to the normal of the sample. The polarizer angles $\tilde{\theta}_1$ and $\tilde{\theta}_2$ are measured from s polarization, with the positive sense being counterclockwise as seen by the light entering the polarizer.

The angles of the polarizers $\tilde{\theta}_1$ and $\tilde{\theta}_2$ are measured in the frame of reference of the plane of incidence, which is determined by the alignment of the optical elements and the sample. However, this alignment is not perfect, and such frame of reference will often differ slightly from the laboratory frame of reference, which is defined by the optical table. In this regard, the angles of the polarizer and the analyzer are measured in reference to the normal of the optical table and are called θ_1 and θ_2. *A priori* unknown offsets $\Delta\theta_1$ and $\Delta\theta_2$ relate $\tilde{\theta}_1$ with θ_1 and $\tilde{\theta}_2$ with θ_2.

2.3.2 Mathematical description of the experiment

In the implementation of GME used in this thesis it is assumed that the degree of polarization is conserved, so that the mathematical description of all optical elements can be done by Jones matrices, while Mueller matrices would be required to tackle the case of partially unpolarized light [13]. The maximum information one can get from a reflection experiment with polarization degree conservation is the reflection matrix of the sample given by Eq. (1.23) and reproduced here:

$$\overline{\overline{R}} = \begin{pmatrix} r_s & \alpha + \gamma \\ -\alpha + \gamma & r_p + \beta \end{pmatrix} = r_p \begin{pmatrix} \widetilde{r_s} & \tilde{\alpha} + \tilde{\gamma} \\ -\tilde{\alpha} + \tilde{\gamma} & 1 + \tilde{\beta} \end{pmatrix} = r_p\, \widetilde{R}. \tag{2.3}$$

The goal of GME is to determine the normalized reflection matrix $\widetilde{R}$ in order to extract from it information about the optical and MO constants of the materials in the sample, as well as the orientation of the sample magnetization, and eventually to obtain the dielectric tensor of a relevant material in the sample. As already mentioned in Section 1.4, r_p and r_s are the standard Fresnel coefficients [13], purely optical variables that do not depend on the magnetic state of the sample. In turn, α, β, and γ are related to the L-, T-, and P-MOKE respectively. Importantly, the amplitudes of α, β, and γ are much smaller than the amplitudes of r_s and r_p and therefore, the sensitivity of the detection technique needs to be optimized for the observation of the MOKE they provoke onto the reflected light. This is achieved in GME, on the one hand, by carrying out the measurements relatively close to the crossing point of the polarizers to minimize the total light intensity, thus maximizing sensitivity to the small $\tilde{\alpha}$, $\tilde{\beta}$, and $\tilde{\gamma}$ values. Furthermore, while $\widetilde{r_s}$ and r_p remain unchanged upon magnetization reversal, $\tilde{\alpha}$, $\tilde{\beta}$, and $\tilde{\gamma}$, which are proportional to m_x, m_y, and m_z respectively, all change sign as M is reversed

$$\tilde{\alpha}(-M) = -\tilde{\alpha}(+M) \tag{2.4.a}$$

$$\tilde{\beta}(-M) = -\tilde{\beta}(+M) \tag{2.4.b}$$

$$\tilde{\gamma}(-M) = -\tilde{\gamma}(+M) \tag{2.4.c}$$

This fact enables the differential detection of the MOKE and is exploited by GME to determine $\widetilde{R}$. Actually, the quantity that is measured in GME to maximize the sensitivity to the MO parameters is the normalized change of intensity upon magnetization reversal $\delta I/I$, where

$$\delta I = I_D(M) - I_D(-M) \tag{2.5}$$

and

54

$$I = \frac{1}{2}\big(I_D(\boldsymbol{M}) + I_D(-\boldsymbol{M})\big). \tag{2.6}$$

In GME one performs measurements of $\delta I/I$ for different combinations of the angles of the polarizers, θ_1 and θ_2, in order to exploit the symmetries of $\frac{\delta I}{I}(\theta_1, \theta_2)$ with respect to the different elements in the reflection matrix to determine $\widetilde{\boldsymbol{R}}$. The functional form of $\frac{\delta I}{I}(\theta_1, \theta_2)$ can be obtained by using Jones calculus to compute the electric field of the light at the detector

$$E_F = \overline{\overline{\boldsymbol{P}}}_2\, \overline{\overline{\boldsymbol{R}}}\, \overline{\overline{\boldsymbol{P}}}_1\, E_I\,, \tag{2.7}$$

where $\overline{\overline{\boldsymbol{R}}}$ is the reflection matrix given by Eq. (2.3), E_I and E_F are the Jones vector of the incident and detected light, with the form given in Eq. (1.21), and $\overline{\overline{\boldsymbol{P}}}_1$ and $\overline{\overline{\boldsymbol{P}}}_2$ are the Jones matrices of the polarizers given by

$$\overline{\overline{\boldsymbol{P}}}_i(\tilde{\theta}_i) = \begin{pmatrix} \cos^2 \tilde{\theta}_i & \sin \tilde{\theta}_i \cos \tilde{\theta}_i \\ \sin \tilde{\theta}_i \cos \tilde{\theta}_i & \sin^2 \tilde{\theta}_i \end{pmatrix}, \tag{2.8}$$

with $i = 1, 2$. $\tilde{\theta}_i$ are the angles of the polarizer and the analyzer referenced to the s polarization direction as shown in Fig. 2.6, and are related to the angles measured in the laboratory reference frame θ_i by $\theta_i = \tilde{\theta}_i + \Delta\theta_i$.

After the calculation of E_F, the detected intensity I_D can be calculated as a function of the polarizer and analyzer angles in the frame of reference θ_1 and θ_2, and from I_D one can derive $\frac{\delta I}{I}(\theta_1, \theta_2)$. The whole calculation is shown in Appendix II, and only the result for the functional form of $\frac{\delta I}{I}(\theta_1, \theta_2)$ is presented here [10]:

$$\frac{\delta I}{I}(\theta_1, \theta_2) = 4\frac{B_1 f_1 + B_2 f_2 + B_3 f_3 + B_4 f_4 + B_5 f_5 + B_6 f_6}{f_3 + B_7 f_7 + 2B_8 f_4 + I_0}\,, \tag{2.9}$$

with

$$B_1 = \mathrm{Re}(\tilde{\alpha}) \tag{2.10.a}$$
$$B_2 = \mathrm{Re}(\tilde{r}_s \tilde{\alpha}^*) \tag{2.10.b}$$
$$B_3 = \mathrm{Re}(\tilde{\beta}) \tag{2.10.c}$$
$$B_4 = \mathrm{Re}(\tilde{r}_s \tilde{\beta}^*) \tag{2.10.d}$$
$$B_5 = \mathrm{Re}(\tilde{\gamma}) \tag{2.10.e}$$
$$B_6 = \mathrm{Re}(\tilde{r}_s \tilde{\gamma}^*) \tag{2.10.f}$$
$$B_7 = |\tilde{r}_s|^2 \tag{2.10.g}$$
$$B_8 = \mathrm{Re}(\tilde{r}_s)\,, \tag{2.10.h}$$

where "*" stands for the complex conjugate, and

$$f_{1,5}(\theta_1, \theta_2) = \sin^2(\tilde{\theta}_1)\sin(\tilde{\theta}_2)\cos(\tilde{\theta}_2) \mp \sin^2(\tilde{\theta}_2)\sin(\tilde{\theta}_1)\cos(\tilde{\theta}_1) \tag{2.11.a}$$
$$f_{2,6}(\theta_1, \theta_2) = \cos^2(\tilde{\theta}_2)\sin(\tilde{\theta}_1)\cos(\tilde{\theta}_1) \mp \cos^2(\tilde{\theta}_1)\sin(\tilde{\theta}_2)\cos(\tilde{\theta}_2) \tag{2.11.b}$$

$$f_3\left(\theta_1,\theta_2\right) = \sin^2\left(\tilde{\theta}_1\right)\sin^2\left(\tilde{\theta}_2\right) \tag{2.11.c}$$

$$f_4\left(\theta_1,\theta_2\right) = \sin\left(\tilde{\theta}_1\right)\cos\left(\tilde{\theta}_1\right)\sin\left(\tilde{\theta}_2\right)\cos\left(\tilde{\theta}_2\right) \tag{2.11.d}$$

$$f_7\left(\theta_1,\theta_2\right) = \cos^2\left(\tilde{\theta}_1\right)\cos^2\left(\tilde{\theta}_2\right) \tag{2.11.e}$$

where $\tilde{\theta}_i = \theta_i - \Delta\theta_i$. $\Delta\theta_1$ and $\Delta\theta_2$ are experimental corrections to the nominal positions of the polarizers in the laboratory reference frame. I_0 in Eq. (2.9) is a constant term representing a residual intensity that may arise due to a measured background light intensity that is not well filtered or due to an electrical offset signal in the detector circuit.

The purpose of GME is to experimentally access $\delta I/I$ for several combinations of (θ_1,θ_2) and then fit the data with Eq. (2.9), where the fitting parameters are B_i ($i = 1,\dots,8$), $\Delta\theta_1$, $\Delta\theta_2$, I_0 to reconstruct the normalized reflection matrix with Eqs. (2.10 a-h).

2.3.3 Exploiting the symmetries of $\frac{\delta I}{I}(\boldsymbol{\theta_1, \theta_2})$

Noting that B_1 and B_2 are related to $\tilde{\alpha}$, *i.e.*, to L-MOKE, B_3 and B_4 are related to $\tilde{\beta}$, *i.e.*, to T-MOKE, and B_5 and B_6 are related to $\tilde{\gamma}$, *i.e.*, to P-MOKE, one can readily separate the contributions of the different MOKE components in Eq. (2.9) as

$$\frac{\delta I}{I}(\theta_1,\theta_2) = (B_1 g_1 + B_2 g_2) + (B_3 g_3 + B_4 g_4) + (B_5 g_5 + B_6 g_6)$$

$$= \left[\frac{\delta I}{I}\right]^L + \left[\frac{\delta I}{I}\right]^T + \left[\frac{\delta I}{I}\right]^P, \tag{2.12}$$

where

$$g_i = \frac{4 f_i}{f_3 + B_7 f_7 + 2 B_8 f_4 + I_0}, \tag{2.13}$$

with $i = 1, \dots, 6$. The formal separation in Eq. (2.12) is very relevant for practical purposes because each of the MOKE components have different symmetries with respect to θ_1 and θ_2 in their contribution to $\frac{\delta I}{I}$, related to the different g_i functions. Thanks to their different symmetries, all MOKE components can be experimentally separated from each other in a very robust manner, even in the presence of significant noise. Fig 2.7 shows in color-coded maps the six g_i as a function of θ_1 and θ_2 considering ideal conditions with $\Delta\theta_1 = \Delta\theta_2 = I_0 = 0$. Red color corresponds to a positive value and blue to a negative value. B_7 and B_8, which appear in the denominator of all g_is

are taken to be those of semi-infinite Fe at 635 nm and an incidence angle of 45 deg[18]. The relevant symmetry elements are shown in Figs. 2.7 (a), (c), and (e). Two exemplary inversion centers "i" at two non-equivalent crossing points of the polarizers are shown, as well as two exemplary mirror planes σ_1 and σ_2. The specific shape of the maps will depend on the actual values of the optical parameters B_7 and B_8, but the symmetries with respect to i, σ_1, and σ_2 will be preserved. The components related to L-MOKE, g_1 and g_2, have the same symmetry pattern: they are antisymmetric with respect to i and σ_1, and symmetric with respect to σ_2; g_3 and g_4, related to T-MOKE, are symmetric with respect to all the symmetry elements; g_5 and g_6, related to P-MOKE, are antisymmetric with respect to i and σ_2, and symmetric with respect to σ_1.
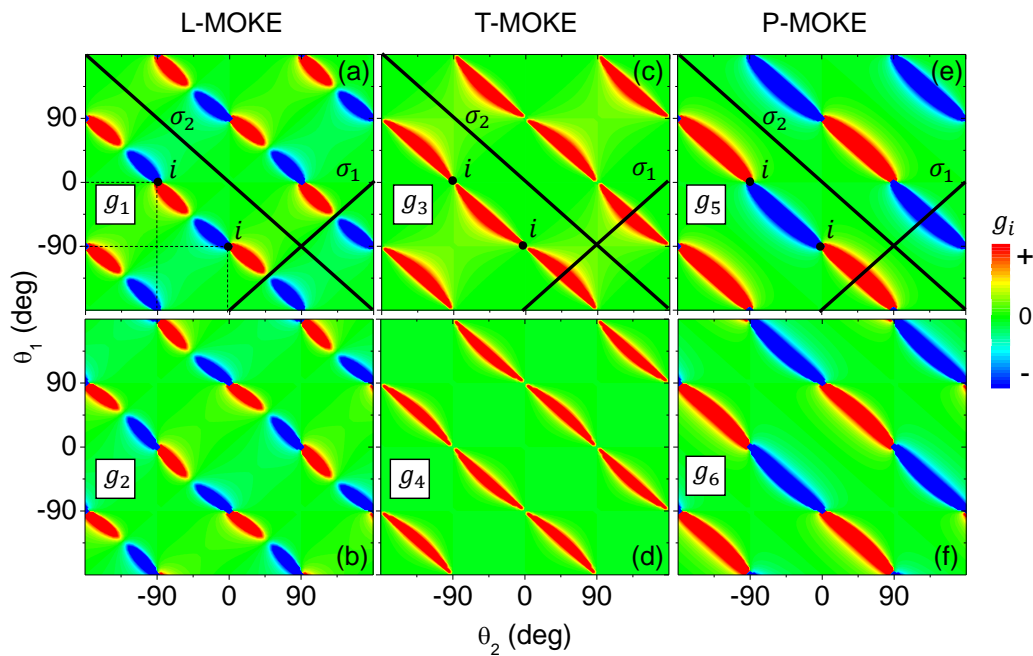

Figure 2.7 Color-coded maps of g_i as a function of θ_2 and θ_1 for $i = 1, \dots, 6$, visualizing the symmetries of $\frac{\delta I}{I}(\theta_1, \theta_2)$ for each of the MOKE components. The exact value of g_i is not relevant here: it is only important to note that the color scale is symmetric around zero. Green color corresponds to zero, red to positive and blue to negative. In (a), (c), and (e) the three relevant symmetry elements are shown.

These symmetries are summarized in Table 2.1, where "+" stands for symmetric and "-" for antisymmetric with respect to each of the symmetry elements. Altogether, none of the three MOKE components have the same symmetry with respect of the three relevant symmetry

---

[18] The refractive index of Fe at 635 nm has been used taken from [14] $N = 2.3995 + 3.3265\,i$, and $\widetilde{r}_s$, which enters the formula of B_7 and B_8, has been calculated applying the Fresnel equations for a semi-infinite material [25]: $r_s = \frac{\cos\Omega_i - N\cos\Omega_t}{\cos\Omega_i + N\cos\Omega_t}$ and $r_p = \frac{N\cos\Omega_i - \cos\Omega_t}{N\cos\Omega_i + \cos\Omega_t}$, where Ω_i is the incidence angle and Ω_t is the angle of refraction, which can be calculated by Snell's law.

elements and therefore, L-, T-, and P-MOKE can be robustly separated from each other by fitting experimental data to Eq. (2.9). Thus, GME enables 3-dimensional vector magnetometry that furthermore works in a self-calibrated way because the longitudinal, transverse, and polar components of the magnetization are defined with respect to the plane of incidence, which is determined by the reflection geometry of the experiment itself[19].

Symmetry element	L-MOKE (g_1, g_2)	T-MOKE (g_3, g_4)	P-MOKE (g_5, g_6)
i	-	+	-
σ_1	-	+	+
σ_2	+	+	-

Table 2.1. Summary of the symmetries (symmetric "+" or antisymmetric "-") of the different MOKE components with respect to the symmetry elements of the measurement geometry as shown in Fig. 2.11.

Given that g_i is actually $\frac{\partial(\delta I/I)}{\partial B_i}$, Fig. 2.7 also gives information about the (θ_1, θ_2) configurations for which the sensitivity to the MO parameters $B_1, \dots, B_6$ is maximal. The maximum sensitivity points happen to be around the diagonals of slope -1 connecting the crossing points of the polarizers, namely, the points for which the difference between θ_1 and θ_2 is 90 deg. This provides a guideline for the choice of the polarizer orientations that should be utilized during experimental measurements.

2.3.4   Data acquisition scheme

In order to experimentally access the $\delta I/I$ quantity as defined by the ratio of Eq. (2.5) and Eq. (2.6), the light intensity has to be measured for two states with inverted $\tilde{\alpha}$, $\tilde{\beta}$ and $\tilde{\gamma}$, i.e., with inverted $\boldsymbol{M}$. This could be achieved, for instance, by an ultrafast laser pulse in a process of all-optical switching [15], or via spin transfer torques [16]. Nevertheless, the procedure used in this

---

[19] If a sample with in-plane magnetization is measured in another type of magnetometry technique, a misalignment of the sample in the setup could lead to a signal that one can erroneously interpret as an out-of-plane component of the magnetization. Magneto-optical methods, in contrast, ensure that if a polar signal is measured, it really comes from a component of the magnetization that is perpendicular to the sample surface, because it is the sample surface that determines the reflection geometry, and thus the definition of L-, T-, and P-MOKE components.

thesis to trigger the reversal of the magnetization of a ferromagnet is a more conventional one, namely, the application of an external magnetic field with an electromagnet[20].

One has to take into account that in ferromagnets $\boldsymbol{M}$ *vs.* $\boldsymbol{H}$ is hysteretic and $\boldsymbol{M}(-\boldsymbol{H}) = -\boldsymbol{M}(\boldsymbol{H})$ in opposite branches of the hysteresis. Therefore, to ensure that the magnetization is reversed, the evaluation of states with opposite magnetization needs to be done for inverted field values of opposite branches:

$$\frac{\delta I}{I} = 2 \frac{I_D(\boldsymbol{M}) - I_D(-\boldsymbol{M})}{I_D(\boldsymbol{M}) + I_D(-\boldsymbol{M})} = 2 \frac{I_D^{dec}(+H) - I_D^{inc}(-H)}{I_D^{dec}(+H) + I_D^{inc}(-H)} \tag{2.14}$$

where $I_D^{dec}(+H)$ is the light intensity measured for the decreasing field branch for a field strength $+H$[21], and $I_D^{inc}(-H)$ is the light intensity measured for the increasing field branch for a field strength $-H$. $\delta I/I$ can be calculated for any value of H. Figure 2.8 (a) shows an example of the measured photovoltage (related to the light intensity) as a function of the external magnetic field for a uniaxial FM sample for a specific orientation of the polarizer and the analyzer given in the inset. As the field decreased from its maximum value of $\mu_0 H = 0.13$ T, the black data were measured; when the field increased from its minimum value $\mu_0 H = -0.13$ T, the blue data were observed. Data points for two selected values of the field are represented in Fig. 2.12 (a) with stars ($\mu_0 H_1 = 0.1$ T) and circles ($\mu_0 H_2 = 0.025$ T), the ones filled in black corresponding to $+H$ in the decreasing field branch, and the ones filled in blue to $-H$ in the increasing field branch, as shown in the legend of the figure. In Fig. 2.8 (b) the corresponding hysteresis loop, but for a different configuration of the polarizer and the analyzer is shown. As observed, the shape of the curve changes, because the optical conditions are different.

---

[20] In Chapter 3 the magnitude whose inversion is presumed is the spin polarization $\boldsymbol{\sigma_s}$ arising from the spin Hall effect, so in that case $\delta I/I$ is measured upon the inversion of $\boldsymbol{\sigma_s}$, which is achieved experimentally by reversing the sign of an applied electric current with current density $\boldsymbol{j_c}$.
[21] $+H$ does not necessarily mean a positive field value, it can be a negative value as well.
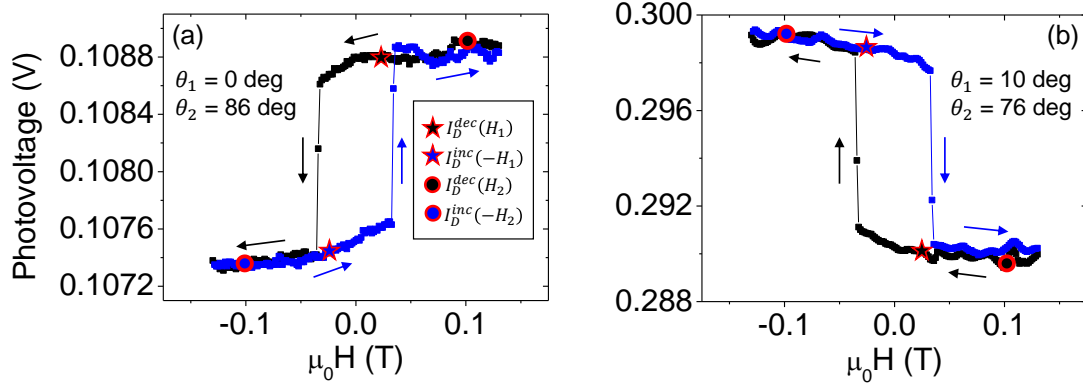
Figure 2.8 Photovoltage (linearly related to the light intensity in the operation regime utilized here) as a function of H for two different polarizer-analyzer configurations. In (a) $\theta_1 = 0$ deg, $\theta_2 = 86$ deg; in (b) $\theta_1 = 10$ deg, $\theta_2 = 76$ deg. The sample is a uniaxial Co sample with the magnetic easy axis being 75 deg away from the applied magnetic field axis. The behavior of the photovoltage is hysteretic and black (blue) symbols correspond to the decreasing (increasing) field branch. Symbols with red outline indicate specific data points. The data points signaled in (a) and (b) with circles filled in black and blue correspond to inverted field values ($\mu_0 H_1 = 0.1$ T) and opposite branches of the hysteresis loop, so they have inverted magnetization states. The same goes for the stars filled in black and blue, where $\mu_0 H_1 = 0.025$ T.

An important aspect about GME is that, given that the analyzed quantity is a difference between states with inverted $\boldsymbol{M}$, contributions to the detected light intensity from terms that are quadratic, bilinear, or of a higher even order in $\boldsymbol{M}$ are eliminated in this methodology. This is very relevant because, even though quadratic or bilinear effects are generally smaller than linear ones, they are not negligible in some cases and are sometimes used in measurements [17]. Thus, if GME did not intrinsically cancel out their contribution, the precision of the measurements would be impacted, as the measured $\delta I/I$ is compared to an equation that assumes only linear MOKE terms. One could have a contribution of higher order odd powers of $\boldsymbol{M}$, but those are typically much smaller than the contribution linear in $\boldsymbol{M}$ and thus, such terms are not included in the analysis.

In order to extract the parameters in Eq. (2.9) for a given magnetization state (determined by the external field) one has to measure $\delta I/I$ for several (θ_1, θ_2) combinations, at least as many as the number of fit parameters in Eq. (2.9). The procedure followed here is to measure $\delta I/I$ on a (θ_1, θ_2) grid with a number of points that significantly exceeds the number of fitting parameters. This enables a robust determination of the fitting parameters and allows one to check the validity of Eq. (2.9). The polarizer grid is selected to maximize the sensitivity to MO parameters following the guidelines provided by Fig. 2.7. Therefore, instead of taking a rectangular polarizer grid, a diagonal one is taken, and typically of the form shown in Fig. 2.9 [12]. θ_1 is scanned in a range r around the center, so that $\theta_1^c - r/2 \leq \theta_1 \leq \theta_1^c + r/2$. For a given θ_1, the scanning range of θ_2

is $(\theta_1^c + \theta_2^c - \theta_1 - r/2) \leq \theta_2 \leq (\theta_1^c + \theta_2^c - \theta_1 + r/2)$. The sensitivity to MO parameters is maximized if the center of the scan range $(\theta_2^c,\ \theta_1^c)$ is taken to be a crossing point of the polarizers, either *p-s* or *s-p*, i.e, (*e.g.*) $\theta_1^c = 90$ deg and $\theta_2^c = 0$ deg, or (*e.g.*) $\theta_1^c = 180$ deg and $\theta_2^c = -90$ deg. The scanning range r and the step size are variable depending on the specific needs of an experiment.

For an in-plane magnetized sample where P-MOKE is absent, data acquisition around one of the crossing points is sufficient to separate L-MOKE and T-MOKE, given that their contributions to $\delta I/I$ have different symmetries with respect to the crossing points of the polarizers, one of which is represented as "*i*" in Fig. 2.7 (a). However, for a sample with all three components of the magnetization being nonzero, measurements around two non-equivalent crossing points, for instance $(\theta_1^c,\theta_2^c) = (90$ deg, 0 deg) and $(\theta_1^c,\theta_2^c) = (180$ deg, -90 deg), *i.e.*, *p-s* and *s-p* crossing points, are required to separate P-MOKE from L-MOKE, as the symmetry of L- and P-MOKE with respect to the *i* points is the same and their different symmetry with respect to σ_1 and σ_2 needs to be exploited. This aspect will become relevant in Chapter 4.
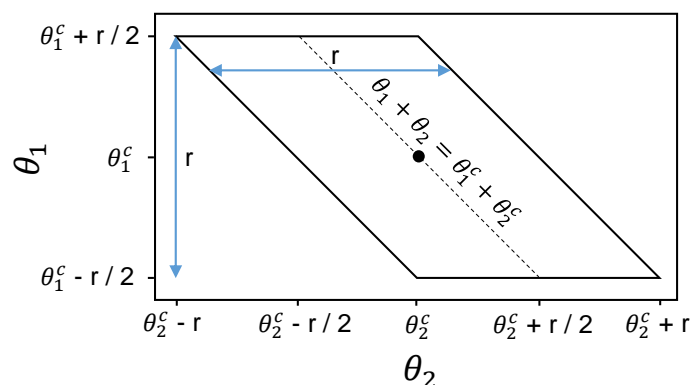

Figure 2.9 Grid for GME measurements.

The procedure to measure $\frac{\delta I}{I}(\theta_1, \theta_2)$ for various values of H is the following. θ_1 and θ_2 are fixed and the detected photovoltage is recorded as a H is swept, from the maximum positive value, to the minimum negative value, and back to the maximum value in predefined steps. Once the hysteresis loop for a given (θ_1, θ_2) configuration is measured, the polarizers are moved to a new configuration and the process is repeated. After the complete set of hysteresis loop data are acquired for the desired (θ_1, θ_2) configurations, the $\frac{\delta I}{I}(\theta_1, \theta_2)$ maps are constructed for each selected field value following Eq. (2.14) and are fitted with Eq. (2.9), thus obtaining a set of fitting parameters $\{B_i, \Delta\theta_1, \Delta\theta_2, I_0, i = 1,\ldots,8\}$ for each value of H.

2.3.5   Specific implementations of the GME setup

The GME setup used in the thesis is shown in Fig. 2.10. A polarization and intensity stabilized diode laser providing light of a wavelength $\lambda = 635$ nm was used as a light source[22]. In order for the light intensity impinging on the sample to be constant regardless of the angle of the first polarizer, the laser is aligned in such way that it provides p-polarized light and, right after the laser, a quarter waveplate (QWP) is placed with the fast axis fixed 45° away from the polarization axis of the light emitted by the laser, such that light that enters P_1 is circularly polarized. P_1 and P_2 are broadband Glan-Taylor polarizers mounted on an automated rotatable stage. The orientation of the QWP is fixed and that of P_1 and P_2 is controlled by a computer.
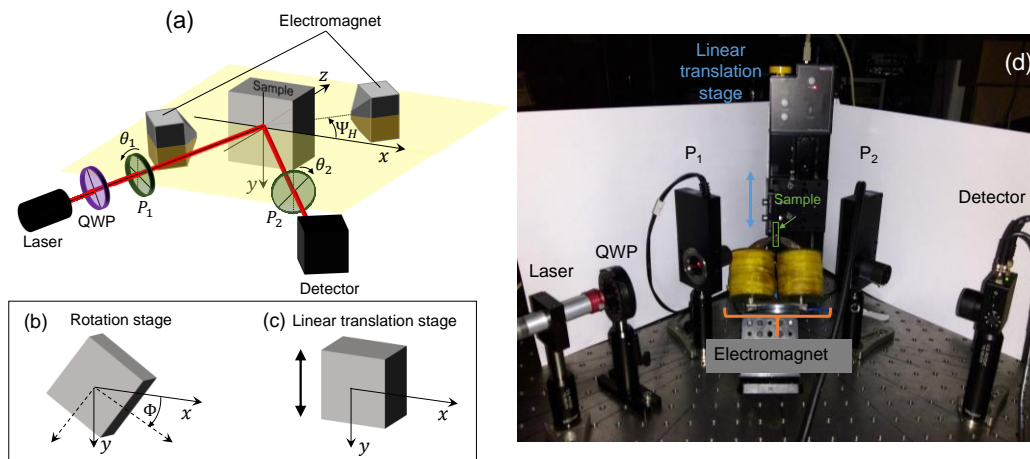

Figure 2.10 (a) Sketch of the implementation of the GME setup utilized in this thesis to measure ferromagnetic materials, which is explained in the main text. (b) and (c) show two possible configurations for the sample holder. (b) Rotation stage, useful for the study of anisotropic samples; (c) Linear translation stage, used for inhomogeneous samples with position-dependent properties. (d) Image of the GME setup with the linear translation stage implementation.

For the type of experiments where the magnetization of a ferromagnet is inverted applying an external magnetic field[23], the sample is mounted between the poles of an electromagnet, as shown in Figs. 2.10 (a) and (d). The current for the electromagnet is provided by a power supply that is controlled by an input voltage generated in a computer-controlled input/output card. The electromagnet could in principle have any orientation, but in the specific implementation here,

---

[22] An alternative to incorporate spectroscopic capabilities to GME is to replace the diode laser by a tunable laser with an acousto-optic tunable filter that can provide light in a wide range of wavelengths [18].

[23] For experiments where the spin polarization due to the spin Hall effect is inverted using a current, the setup is modified in a way that is described in Chapter 3.

the generated field is contained in the xz plane, forming an angle Ψ_H with the x axis, with the most common configuration being $\Psi_H = 0$ deg, *i.e.*, a magnetic field applied parallel to the x axis.

For sample orientation-dependent studies, samples are mounted on a stage whose rotation is automated. Alternatively, for position-dependent measurements, the sample is mounted on a linear translation stage that can move vertically between the poles of the electromagnet, and whose movement can also be computer-controlled to automate measurements at different positions of the sample. These two options for the sample holder are shown in Fig. 2.10 (b) and (c) respectively. Figure 2.10 (d) shows the setup with the linear translation stage, where the sample is placed and scanned vertically. Typically, a Hall probe is placed close to the sample to sense the magnetic field during the experiment. However, the Hall probe is not exactly positioned at the spot where the laser hits the sample, so that proper field calibration measurements had to be performed without a sample by placing the Hall probe at the exact position where the measured sample spot is during an actual measurement.

The control of the setup and the data acquisition is performed with a NI LabView program. The program controls the rotation of the polarizers, the rotation of the sample holder (or the displacement of the linear translation stage), and the voltage applied to the power supply that drives a current through the coils of the electromagnet, and reads out the signal from the Hall probe and the photodetector. The software creates independent data files for each sample orientation (or vertical position). In these data files, the orientation of the polarizer and the analyzer are stored, as well as the magnetic field and the light intensity for each magnetic field value. Each of the data files is then analyzed using a MATLAB [19] code that computes and fits $\frac{\delta I}{I}(\theta_1, \theta_2)$ maps for selected magnetic field values. In this thesis, the LabView program as well as the MATLAB codes for the analysis of the data have been optimized for the specific needs of the experiments performed here.

2.3.6 Example of GME application to study a uniaxial ferromagnet

Using the methodology and the setup explained above, measurements on a uniaxial Co film with in-plane easy axis (EA) applying a magnetic field along the x axis are shown as an example of the methodological capabilities of GME (see Fig. 2.10 (a) for the definition of the axes). Given the anisotropy of the sample and the orientation of the applied field, the magnetization reversal

process occurs in the plane of the sample and can be described with a macrospin model for the largest part of the applied field range[24], facilitating the description of the process. Figure 2.11 shows selected $\frac{\delta I}{I}(\theta_2, \theta_1)$ maps for four magnetic field values. In all the measurements shown the EA of the sample was set -75 deg away from the x axis, which is the axis along which the magnetic field was applied.

The first row shows the experimentally measured $\frac{\delta I}{I}(\theta_2, \theta_1)$ maps. In the insets, the EA of the film is represented as a purple straight line, and the magnetization of the sample is depicted with a brown arrow. At $\mu_0 H$ = 0.13 T, shown in Fig. 2.11 (a), the magnetization is tilted towards the x axis. However, it is not completely parallel to the field axis, as the strength of the field is not sufficiently high to saturate the sample. Therefore, the pattern observed in $\delta I/I$ is not the one described for L-MOKE in conjunction with Figs. 2.7 (a) and (b), but instead a superposition of L-MOKE and T-MOKE from which the magnetization angle Φ_M can be extracted[25]. The remanence state is shown in Fig. 2.11 (d). In this case, the magnetization lies along the EA, as it is the energetically favored state in the absence of field. The map shows that the dominant effect is T-MOKE, but there is also some L-MOKE left, because the EA is not aligned with the y axis. A field of $\mu_0 H$ = -0.027 T is needed to obtain a magnetization that is almost exclusively in the transverse direction, which gives rise to almost symmetric lobes around the crossing point of the polarizers, as shown in Fig. 2.11 (g). For $\mu_0 H$ = - 0.13 T, shown in (j), the magnetization, and thus the $\delta I/I$ signal, are reversed with respect to the case in Fig. 2.11 (a).

The second row shows the fitting of the experimental maps with Eq. (2.9), from where the fit parameters B_i, $i = 1, ... ,8$, the corrections of the polarizers $\Delta\theta_1$ and $\Delta\theta_2$, as well as I_0 were obtained. Actually, in the fitting procedure B_5 and B_6 were set to zero, as the sample is in-plane magnetized. Upon comparing Figs. 2.11 (b), (e), (h) and (k) with the raw data in Figs. 2.11 (a), (d), (g), and (j), hardly any difference can be noticed, proving that Eq. (2.9) describes experimental data with great accuracy.

---

[24] Except near the coercive field, where non-uniform switching occurs.

[25] Φ_M can be obtained from the fitted B_i parameters as $\Phi_M = \text{atan}\left[\left(\frac{B_3(H)}{B_3(H=0)}\right)\Big/\left(\frac{B_1(H)}{B_1(H=0)}\right) \times \tan\Phi_0\right]$, where Φ_0 is the angle of the EA with respect to the applied field axis. In the case shown in Fig 2.11 Φ_0 = - 75 deg.
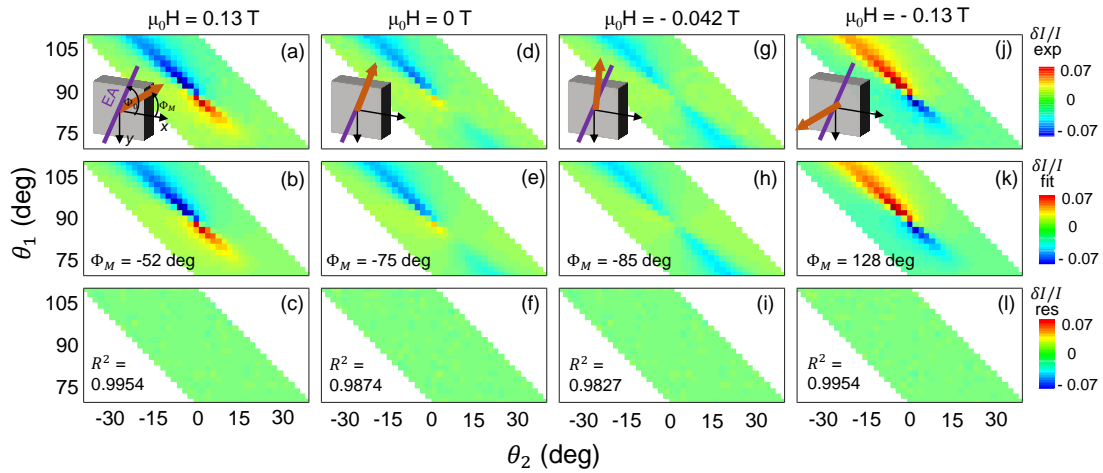
Figure 2.11 First row: color-coded maps of the measured $\frac{\delta I}{I}(\theta_2, \theta_1)$ for different field values indicated on top. The insets represent the orientation of the EA (purple line) with respect to the applied field axis (x), and the orientation of $\boldsymbol{M}$ at each value of the field with a brown arrow. Second row: fitted $\frac{\delta I}{I}(\theta_2, \theta_1)$ for each of the selected field values using Eq. (2.9). Inset shows the magnetization angle Φ_M for each field value. Third row: Color-coded map of the residuals. The goodness of the fit is shown as an inset for each of the maps. The color scale for each of the rows is on the right-hand side.

The bottom row shows the maps of the residuals, *i.e.*, the difference between the experimental data and the fits. They display randomly scattered values that correspond to uncorrelated noise, showing no specific pattern. On the bottom left corner of each of the residual maps the R^2 goodness of the fit for each selected field value is shown. As observed, it is larger than 0.98 in all cases, which corroborates the excellent agreement of experiment and fit and demonstrates that the light reflection process is understood, at least for this particular sample and measurement geometry.
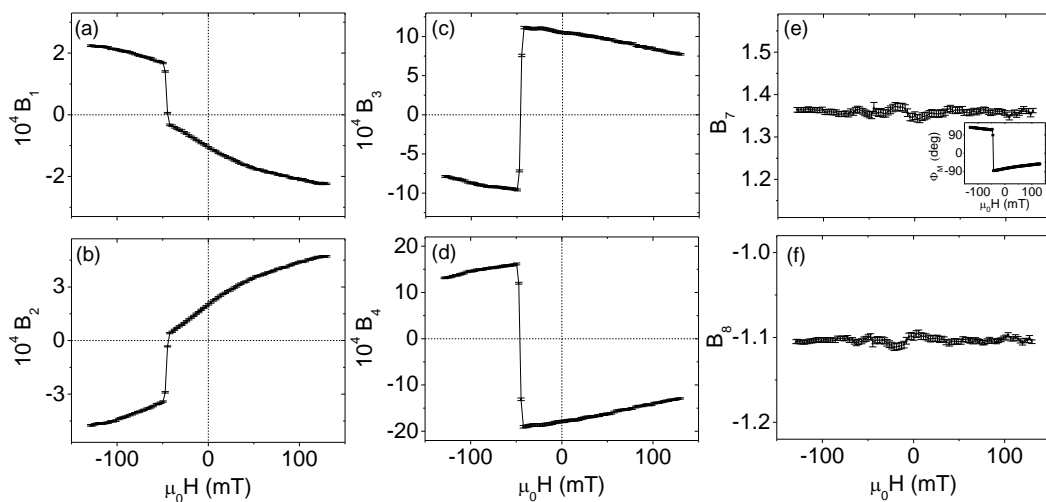

Figure 2.12 Fitted B_i parameters as a function of the applied magnetic field. Optical parameters B_7 and B_8 do not depend on the field. Inset in (e) shows the magnetization angle Φ_M as a function of H.

From the fits of $\frac{\delta I}{I}(\theta_1, \theta_2)$ for the various field values, $B_i(H)$ values were obtained. Figure 2.12 shows L-MOKE B_1 and B_2 fit parameters, T-MOKE-related B_3 and B_4, and optical B_7 and B_8 parameters. Only the decreasing field branch parameters are shown, as due to the GME procedure the increasing field branch of B_i, $i = 1, ..., 6$ is just antisymmetric with respect to the $(H = 0, B_i = 0)$ point. B_1 and B_2 have opposite signs and decrease their amplitude upon decreasing the fields, until they reach the minimum absolute value at $\mu_0 H = -0.042$ T, in accordance to the almost pure T-MOKE symmetry observed in Figs. 2.11 (g) and (h). Correspondingly, the amplitude of B_3 and B_4 is maximal at this field value. Upon further decreasing the field the magnetization eventually switches. The optical parameters shown in Figs. 2.12 (e) and (f) are field-independent, as they should be. Importantly, all these B_i parameters are fitted with high precision, as can be seen from the small error bars in Fig. 2.12. The inset in Fig. 2.12 (e) shows the angle of the magnetization Φ_M with respect to the x axis as determined from the ratio between B_3 and B_1 (see footnote 25).

The fitting parameters related to corrections of the polarizers and noise, *i.e.*, $\Delta\theta_1$, $\Delta\theta_2$, and I_0 in Eq. (2.9) are also field-independent and small, as shown in Figs. 2.13 (a), (b), and (c). In addition, the goodness of the fit, shown in Fig. 2.13 (d) is well above 0.98 for most of the field range and only becomes lower at the coercive field. Around that field value, the noise is also higher in B_7 and B_8 as shown in Figs. 2.12 (e) and (f), as well as in $\Delta\theta_1$, $\Delta\theta_2$, and I_0 shown in Figs. 2.13 (a), (b), and (c). In the vicinity of the coercive field the sample has non-homogeneous magnetic domains and therefore, it could be that the description of the optical properties of the sample based on the reflection matrix in Eq. (2.3), on top of which the GME mathematical formalism is derived, is not valid. However, with the exception of those field values, the quality of the fit is excellent.
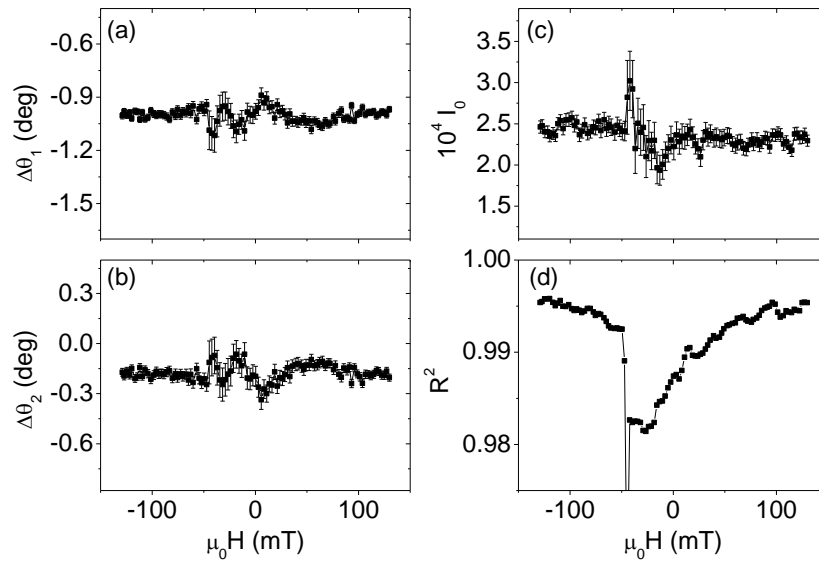
Figure 2.13 Fitted corrections of the polarizer and the analyzer, in (a) and (b), respectively. (c) Fitted intensity background. (d) Goodness of the fit. All data are shown as a function of H.

2.4   Other experimental techniques
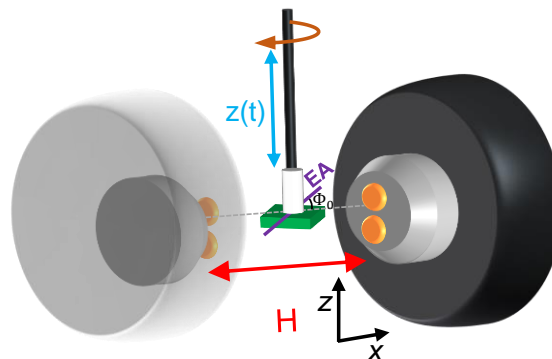
2.4.1 Vibrating sample magnetometry

Figure 2.14 Schematics of the magnetometer used for VSM. A sample (green) is attached to the end of a rod that vibrates vertically while an external magnetic field is applied in the x direction by an electromagnet (black and gray cylinders). The time-dependent magnetic flux generated by the vibrating sample induces a current in the pick-up coils (orange disks). The EA of the sample is in-plane, marked by a purple line. The angle between the EA and the applied field is Φ_0.

Vibrating sample magnetometry (VSM) has been utilized to measure the macroscopic magnetic moment and determine the magnetization of the samples [20-22]. The magnetometer utilized here is schematically depicted in Fig. 2.14. A sample is located between a set of pick-up coils (orange disks in Fig. 2.14) and, after setting its magnetic state by applying an external magnetic field with an electromagnet that generates a uniform magnetic field along the x axis, a vibration

is induced to the magnetized sample along the z axis. This movement creates a time-dependent magnetic flux[26] through the pick-up coils, which due to the Faraday-Lenz law of induction, creates in them a potential difference that generates a current proportional to the magnetic moment of the sample. By measuring the current generated at the coils, and thanks to a calibration procedure, the projection of the magnetic moment along the applied field axis, which is collinear with the axis of the pick-up coils, can be detected. After determining the total magnetic volume of the sample[27], its field-projected magnetization can be determined for each applied field value. By varying the strength of the external field, hysteresis loops can be measured. In addition, the magnetometer used in this thesis allows to rotate the sample around the z axis, and thus explore the in-plane anisotropy of the sample by changing the angle between the EA and the applied field axis.

2.4.2 Spectroscopic ellipsometry

Spectroscopic ellipsometry (SE) has been utilized to determine the spectroscopic optical properties of samples but, especially, as a tool to determine the thickness of thin layers of a given material. SE analyzes the changes of polarization of light of different wavelengths upon reflection from a sample [23, 24] and exploits the sensitivity to the phase of light to achieve a resolution that is much smaller than the wavelength of light utilized in the experiment. This technique measures the ratio of the Fresnel coefficients r_{pp} and r_{ss} of the sample (see reflection matrix in Eq. (1.22)) in a spectroscopic way, for wavelengths ranging from 210 to 955 nm in the case of the setup used here. In order to determine the thickness of a given layer from the measured r_{pp}/r_{ss}, an optical model with appropriate assumptions is needed (*e.g.*, fixed refractive index and variable layer thickness). Using procedures similar to the ones that will be described in Section 2.5, the expected r_{pp}/r_{ss} ratio for the model can be calculated as a function of the wavelength. The thickness of the

---

[26] The time-dependence of the magnetic flux is only affected by the field generated by the vibrating sample. The magnetic field generated by the electromagnet does not contribute to this signal because it does not change with time, or at least it does so in a far slower time scale, so it does not interfere with the detection frequency.

[27] In the case of thin films, the procedure to determine the magnetic volume of a sample is the following. First, the sample is weighted, and all the weight is ascribed to the substrate, which is around 10^4 times thicker than the deposited films. The thickness and the density of the substrate are known, so that its area can be determined. Finally, the thickness of the magnetic layer is known thanks to XRR calibrations, so that the magnetic volume is found by multiplying the sample area times the layer thickness.

layer of interest is determined to be the one yielding the optical response r_{pp}/r_{ss} that is most similar to the experimental data.

2.5   Transfer matrix method for optical and magneto-optical modeling

Section 2.3 has shown how GME can access the normalized reflection matrix $\widetilde{R}$. What one is typically interested in, though, are the dielectric tensors $\overline{\overline{\varepsilon}}$ of the materials forming the sample. In a semi-infinite material the relation between its $\overline{\overline{\varepsilon}}$ and $\widetilde{R}$ is straightforward and is given analytically [25]. In multilayer structures, where the effects in the reflected light are determined by several layers of different materials characterized by distinct $\overline{\overline{\varepsilon}}$ and by the interfaces between them, a more evolved method is required to obtain $\widetilde{R}$. In particular, a transfer matrix method [26] will be presented in the following paragraphs to calculate $\widetilde{R}$ of a multilayer system with planar layers of materials having specific thicknesses and dielectric tensors given by Eq. (1.19). Conversely, knowing $\widetilde{R}$, the method presented here can be used to determine relevant elements of the dielectric tensors of the layers of a multilayer sample *via* a fitting procedure.

Figure 2.15 shows the multilayer stack with N_L layers of different thicknesses d_j, each of which has a corresponding $\overline{\overline{\varepsilon}}^{(j)}$. The incident (exit) medium is on the left (right) hand side. The reflected light beam, which is the one of interest, is on the left hand side. The angle of incidence is Ω_a, the wave vector of the incident light is k_a, and that of the reflected light is k_a'. The p and s components of the electric field of the incident light are A_p and A_s respectively, and those of the reflected light are B_p and B_s. The transmitted light has an exit angle Ω_f, a wave vector k_f, and p and s components of the electric field represented by C_p and C_s. In the exit medium no back-traveling waves are considered. A transfer matrix $\overline{\overline{T}}$ that relates C_p and C_s to A_p, A_s, B_p, and B_s can be defined as [23]

$$(A_s \quad B_s \quad A_p \quad B_p)^T = \overline{\overline{T}} \, (C_s \quad 0 \quad C_p \quad 0)^T \tag{2.15}$$
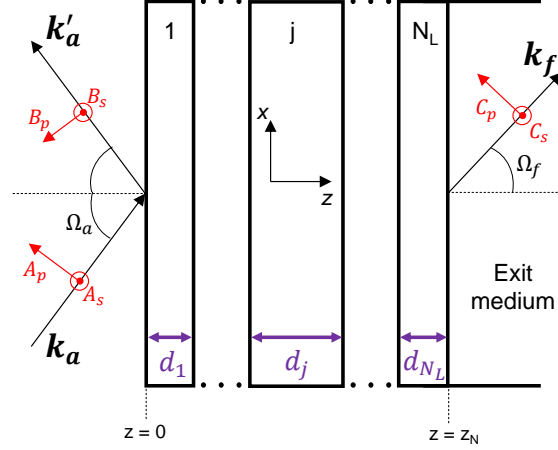
Figure 2.15 Sketch of a multilayer system with N_L layers, an incident medium *a* and an exit medium *f*. The thickness of the jth layer is given by d_j. The wave vectors of the incident, reflected and transmitted waves are $\mathbf{k}_a$, $\mathbf{k}'_a$, and $\mathbf{k}_f$, respectively. The amplitudes of the *p* and *s* component of the electric field of the incident (A_s and A_p), reflected (B_s and B_p), and transmitted (C_s and C_p) waves are shown in red.

For a multilayer structure as the one shown in Fig. 2.15, a partial transfer matrix $\overline{\overline{T}}_p^{(j)}$ can be defined in each homogeneous layer *j* of thickness d_j, which connects the in-plane (tangential) components of the electric field of the wave at the interface at $z = z_j$ and $z = z_j + d_j$. Another matrix, $\overline{\overline{L}}_a$, projects the incident and the reflected wave amplitudes through the surface, and $\overline{\overline{L}}_f$ projects the transmitted amplitudes through to the exit medium. $\overline{\overline{T}}$, $\overline{\overline{T}}_p^{(j)}$, $\overline{\overline{L}}_a$, and $\overline{\overline{L}}_f$ are 4×4 matrices. Accordingly,

$$\overline{\overline{T}} = \overline{\overline{L}}_a^{-1} \left(\prod_{j=1}^{N} \left[\overline{\overline{T}}_p^{(j)}(d_j) \right]^{-1} \right) \overline{\overline{L}}_f \, , \tag{2.16}$$

where, for symmetry reasons $\left[\overline{\overline{T}}_p^{(j)}(d_j) \right]^{-1} = \overline{\overline{T}}_p^{(j)}(-d_j)$, so no matrix inversion calculation is required in this computation. $\overline{\overline{T}}_p^{(j)}$ matrices are defined as the solution to Berreman's [27] equations for the in-plane components of the electric (E_x, E_y) and magnetic (H_x, H_y) fields.

By defining

$$\boldsymbol{\psi}^{(j)}(z) = \begin{pmatrix} E_x^{(j)}(z) & E_y^{(j)}(z) & H_x^{(j)}(z) & H_y^{(j)}(z) \end{pmatrix}^T \tag{2.17}$$

as a 4×1 vector encompassing the electric and magnetic fields in a given layer *j*, $\overline{\overline{T}}_p^{(j)}$ of that layer fulfills:

$$\boldsymbol{\psi}^{(j)}(z + d_j) = \overline{\overline{T}}_p^{(j)} \boldsymbol{\psi}^{(j)}(z) \, , \tag{2.18}$$

where

$$\overline{\overline{T}}_p^{(j)} = \exp\left(i\frac{\omega}{c}\overline{\overline{\Delta}}^{(j)}d_j\right).$$ (2.19)

$\overline{\overline{\Delta}}^{(j)}$ is a 4×4 matrix that can be calculated from Maxwell's equations [27] and takes the form

$$\overline{\overline{\Delta}}^{(j)} = \begin{pmatrix} -k_x\dfrac{\varepsilon_{zx}^{(j)}}{\varepsilon_{zz}^{(j)}} & -k\dfrac{\varepsilon_{zy}^{(j)}}{\varepsilon_{zz}^{(j)}} & 0 & 1-\dfrac{k_x{}^2}{\varepsilon_{zz}^{(j)}} \\ 0 & 0 & -1 & 0 \\ \dfrac{\varepsilon_{yz}^{(j)}\varepsilon_{zx}^{(j)}}{\varepsilon_{zz}^{(j)}} - \varepsilon_{yx}^{(j)} & k_x^2 - \varepsilon_{yy}^{(j)} + \dfrac{\varepsilon_{yz}^{(j)}\varepsilon_{zy}^{(j)}}{\varepsilon_{zz}^{(j)}} & 0 & k_x\dfrac{\varepsilon_{yz}^{(j)}}{\varepsilon_{zz}^{(j)}} \\ \varepsilon_{xx}^{(j)} - \dfrac{\varepsilon_{xz}^{(j)}\varepsilon_{zx}^{(j)}}{\varepsilon_{zz}^{(j)}} & \varepsilon_{xy}^{(j)} - \dfrac{\varepsilon_{xz}^{(j)}\varepsilon_{zy}^{(j)}}{\varepsilon_{zz}^{(j)}} & 0 & -k_x\dfrac{\varepsilon_{xz}^{(j)}}{\varepsilon_{zz}^{(j)}} \end{pmatrix},$$ (2.20)

where $k_x = k_0 \sin\Omega_a$, k_0 is the wavelength of the light in vacuum and Ω_a is the angle of incidence. $\varepsilon_{\mu\nu}^{(j)}$ are the elements of the dielectric tensor of layer j given in Eq. (1.20), where for a layer that is not magneto-optically active $Q_{MO} = 0$. Following Eq. (2.20), $\overline{\overline{\Delta}}^{(j)}$ can be calculated for each layer j in the system from the dielectric tensor $\overline{\overline{\varepsilon}}^{(j)}$ of each of the materials. In addition, $\overline{\overline{\Delta}}^{(j)}$ depends on k_x, which is related to both the vacuum wavelength of the light used to probe the system and the angle of incidence. A calculation of the eigenvalues of $\overline{\overline{\Delta}}^{(j)}$ allows for a calculation of $\overline{\overline{T}}_p^{(j)}$ [28] as defined by Eq. (2.19), which will depend also on the thickness of the layer d_j.

While the partial transfer matrices $\overline{\overline{T}}_p^{(j)}$ connect electric and magnetic field components tangential to the surface, the s and p components of the incident, reflected, and transmitted waves in Eq. (2.15) are not equal to the tangential components, because the angle of incidence can be oblique. In that regard, the transition matrix $\overline{\overline{L}}_a$ used in Eq. (2.16) projects the tangential electric and magnetic fields of the waves in the incident medium through to the first interface, whereas $\overline{\overline{L}}_f$ projects them from the last interface into the exit medium, such that:

$$\overline{\overline{L}}_a(A_s \quad B_s \quad A_p \quad B_p)^T = (E_x(z=0) \quad E_y(z=0) \quad H_x(z=0) \quad H_y(z=0))^T$$ (2.21)

and

$$(E_x(z=z_N) \quad E_y(z=z_N) \quad H_x(z=z_N) \quad H_y(z=z_N))^T = \overline{\overline{L}}_f(C_s \quad 0 \quad C_p \quad 0)^T.$$ (2.22)

Explicit solutions for $\overline{\overline{L}}_a^{-1}$ and $\overline{\overline{L}}_f$ for homogeneous, nonmagnetic, and isotropic incident and exit media are given in [28]. With the knowledge $\overline{\overline{L}}_a^{-1}$, $\overline{\overline{L}}_f$, and $\overline{\overline{T}}_p^{(j)}$, the general transfer matrix $\overline{\overline{T}}$ can be calculated using Eq. (2.16).

Finally, a relationship between the elements of $\overline{\overline{T}}$ and those of the Jones reflection matrix in Eq. (2.5) can be established, as shown in [29]:

$$r_{ss} = \left(\frac{B_s}{A_s}\right)_{A_p=0} = \frac{T_{21}T_{33} - T_{23}T_{31}}{T_{11}T_{33} - T_{13}T_{31}} \tag{2.23.a}$$

$$r_{sp} = \left(\frac{B_p}{A_s}\right)_{A_p=0} = \frac{T_{41}T_{33} - T_{43}T_{31}}{T_{11}T_{33} - T_{13}T_{31}} \tag{2.23.b}$$

$$r_{ps} = \left(\frac{B_s}{A_p}\right)_{A_s=0} = \frac{T_{11}T_{23} - T_{21}T_{13}}{T_{11}T_{33} - T_{13}T_{31}} \tag{2.23.c}$$

$$r_{pp} = \left(\frac{B_s}{A_p}\right)_{A_s=0} = \frac{T_{11}T_{43} - T_{41}T_{13}}{T_{11}T_{33} - T_{13}T_{31}} \tag{2.23.d}$$

All in all, with the knowledge of the dielectric tensor and the thickness of each layer in the sample, the wavelength of the probing light and the angle of incidence, the reflection matrix of the sample can be calculated following this method. It is also noteworthy that it is not necessary to know the dielectric tensor of all the layers in the sample, but only of those significantly affecting the reflection process, which in practice means layers down to a few times the skin depth of the sample.

In this thesis, a MATLAB code where this transfer matrix method is implemented has been modified for two purposes. On the one hand, the code was used to calculate the reflection matrix elements of a multilayer structures with known $\overline{\overline{\varepsilon}}^{(j)}$ of the involved layers and specific experimental conditions as wavelength and angle of incidence. On the other hand, for a sample whose $\widetilde{R}$ is known thanks to a GME experiment, a least-squares fitting procedure was developed to determine materials parameters, such as refractive indices, MO coupling constants or magnetization components m_i entering $\overline{\overline{\varepsilon}}$. In multilayer samples not all the parameters defining the dielectric tensor of each of the constituent materials can be fitted at the same time, given the limited number of variables to be fitted, namely, four complex parameters, $\widetilde{r_s}$, $\widetilde{\alpha}$, $\widetilde{\beta}$, and $\widetilde{\gamma}$ or, alternatively, eight real GME parameters $B_1, \dots, B_8$, related to the previous four *via* Eqs. (2.10 a-h). For this reason, appropriate models of multilayers have been constructed, where some of the materials properties are fixed, *e.g.*, as obtained from other experiments or from literature[28], and some others, in particular those related to the aspects one wants to extract from the experiment,

---

[28] For instance, the thickness of the layers can be extracted from XRR calibrations and the refractive index of a given material from spectroscopic ellipsometry measurements.

are fitted. This fitting procedure allows to retrieve relevant materials parameters even in samples with a complex optical structure, *e.g.*, composed of multiple thin layers. A code that allows to adapt the geometry of the multilayer structure and make different parameters variables of the least-square fit has been optimized, allowing for a MO characterization that goes far beyond the standard MOKE measurements.

References

[1] K. Wasa and S. Haykawa, *Handbook of Sputter Deposition Technology: Principles, Technology and Applications* (Noyes Publication, New Jersey, 1992).
[2] K. Wasa, *Handbook of Sputtering Technology*, (William Andrew, Oxford, 2012).
[3] P. D. Davidse, Vacuum **17**, 139-145 (1967).
[4] P.J. Kelly and R. D. Arnell, Vacuum **56**, 159 (2000).
[5] B. D. Cullity and S. R. Stock, *Elements of X-ray Diffraction* (Prentice Hall, New Jersey, 2001).
[6] E. Zolotoyabko, *Basic Concepts of X-ray Diffraction* (Wiley-VCH, Weinheim,
[7] N. W. Ashcroft, N. D. Mermin, *Solid State Physics* (Saunders College, Philadelphia, 1976).
[8] M. Birkholz, *Thin Film by X-ray Scattering* (Wiley-VCH Veralg GmbH & Co., Weinheim, Germany, 2006).
[9] M. Yasaka, J. Rigaku **26**, 1 (2010).
[10] A. Berger and M. R. Pufall, Appl. Phys. Lett. **71**, 965 (1997).
[11] A. Berger and M. R. Pufall, J. Appl. Phys. **85**, 4583 (1999).
[12] J. A. Arregi, J. B. González-Díaz, E. Bergaretxe, O. Idigoras, T. Unsal, and A. Berger, J. Appl. Phys. **111**, 103912 (2012).
[13] G.R. Fowles, *Introduction to Modern Optics* (Dover publications, New York, U.S.A., 1975).
[14] M. R. Querry. Optical constants, Contractor Report CRDC-CR-85034 (1985).
[15] C-H. Lambert *et al.*, Science **345**, 1337 (2015).
[16] I. M. Miron *et al.*, Nature **476**, 189–193 (2011).
[17] X. Fan, A. R. Mellnik, W. Wang, N. Reynolds, T. Wang, H. Celik, V. O. Lorenz, D. C. Ralph, and J. Q. Xiao, Appl. Phys. Lett. **109**, 122406 (2016).
[18] P. Riego, S. Tomita, K. Murakami, T. Kodama, N. Hosoito, H. Yanagi, and A. Berger, J. Phys. D: Appl. Phys. **50**, 19LT01 (2017).
[19] MATLAB and Statistics Toolbox Release 2012b, The MathWorks, Inc., Natick, Massachusetts, United States.
[20] S. Foner, Rev. Sci. Instrum., **30**, 548 (1959).
[21] S. Foner, IEEE Trans. Magn. MAG-**17**, 3358 (1981).
[22] F. Fiorillo, Metrologia **47**, S114 (2010).
[23] H. Fujiwara, *Spectroscopic ellipsometry, principles and applications* (Wiley, Hoboken, 2007).
[24] H. G. Tompkins, *Handbook of ellipsometry* (William Andrew, Norwich, 2005).
[25] C-Y. You and S-C. Shin, J. Appl. Phys. **84**, 541 (1998).
[26] M. Schubert, T. E. Tiwald, and J. A. Woollam, Appl. Opt. **38**, 177-187 (1999).
[27] D. W. Berreman, J. Opt. Soc. Am. **62**, 502-510, 1972.
[28] M. Schubert, Phys. Rev. B **53**, 4265 (1996).
[29] P. Yeh, Surf. Sci. **96**, 41-53 (1980).

Chapter 3

Detection of the spin Hall effect in metals by means of generalized magneto-optical ellipsometry

The capabilities of generalized magneto-optical ellipsometry (GME) to separate magneto-optical signals from signals generated by purely optical effects or secondary signal sources are exploited to study the detectability of the spin Hall effect (SHE) in metals by means of the magneto-optical Kerr effect (MOKE). Measurements are performed on three materials, namely, Pt, W, and Ta. While a current-induced effect in the detected light intensity is observed, the GME analysis reveals that it is not related to the SHE-induced spin accumulation. This leads to the conclusion that, if SHE-related MOKE is present in metals, it is an extremely small effect and far smaller than what had been reported in literature. An improvement of the sensitivity of the setup is thus required to achieve the SHE detection with MOKE. The motivation for the study is given in Section 3.1, followed by details on the design of the experiment and the samples in Section 3.2 and experimental results and their discussion in Section 3.3. Conclusions, related works and a general outlook are given in Section 3.4.

3.1   Introduction and motivation

As introduced in Section 1.3, the spin Hall effect (SHE) is a phenomenon that gives rise to pure spin currents in materials with high spin-orbit coupling (SOC) upon passing through them spin-unpolarized charge currents $\boldsymbol{j_c}$. Due to SOC, electrons are preferentially deflected in a given direction depending on the polarization of their spin $\boldsymbol{\sigma_s}$, giving rise to a spin current perpendicular both to $\boldsymbol{j_c}$ and $\boldsymbol{\sigma_s}$. At the interfaces of the material, spins of a given $\boldsymbol{\sigma_S}$ are accumulated, creating a difference in chemical potential between spins of opposite polarization, which is denoted as the spin accumulation μ_s. $\boldsymbol{\sigma_s}$ has inverse sign at opposite interfaces of the material.

The first experimental observation of the SHE was performed by detecting such spin accumulation *via* magneto-optical Kerr effect (MOKE) microscopy measurements for a

semiconductor [1]. A polar Kerr rotation was observed at the edges of a lithographically defined semiconducting channel upon applying a current along it. The Kerr rotation had opposite sign at opposite edges, in agreement with the expected reversed polarization of the spin accumulation for SHE. The origin of the Kerr signal was verified by applying an external magnetic field along the channel, which produced a spin precession that was detected as a reduction of the polar Kerr rotation. Following research also utilized MOKE to detect the SHE but, until recently, this approach was limited to semiconductors [2-5].

In metals, SHE and its counterpart, the inverse SHE, which creates charge currents from spin currents, are typically detected electrically, using different approaches such as spin pumping [6-8], lateral spin valves [9-12] or spin-torque ferromagnetic resonance [14-16]. Some of these electrical techniques often require evolved nanofabrication processes or the coupling of the material to be studied to an adjacent ferromagnet. Magneto-optical (MO) detection of the SHE would allow for a much simpler sample fabrication (in principle, just a thin film of the material with electrical contacts is needed). In addition, magneto-optics is non-invasive, enables fast characterization, can incorporate spatial resolution, and can be performed in an ultrafast way with the aim of studying dynamical processes. Despite the advantages of MOKE, it is challenging to apply this technique for the detection of SHE in metals because, as opposed to the case of semiconductors, the number of free carriers in metals is so large that the number of optically probed electrons greatly exceeds the difference between spin up and spin down electrons, related to μ_S.

From 2014 on, a number of works reported the possibility to detect the SHE-generated spin accumulation in nonmagnetic metals by optical means. For instance, Pattabi et $al.$ could detect current-induced spin accumulation in Pt by means of second harmonic generation experiments [17], also demonstrating the feasibility of time-resolved studies. However, the interpretation of such signals is not as straightforward as for conventional MOKE. In contrast, van 't Erve et $al.$ [18] performed longitudinal (L-) MOKE measurements on Pt and β-W and reported for the latter material a SHE-induced Kerr rotation θ_K only five times smaller than that of a magnetically saturated Fe reference film.

Sparked by the findings in [18], a detailed study on the possibility and limitations to detect SHE-induced μ_S with MOKE in metals as Pt, Ta and W has been carried out. Generalized magneto-optical ellipsometry (GME) is utilized for that purpose, given that it can separate purely

optical reflectivity effects or other secondary effects from MO signals by exploiting the symmetries of the detected signal with respect to the polarization direction of the incident and the detected light as shown in Section 2.3.

3.2   Design of the experiment and samples

Pt, β-W, and Ta samples were fabricated by the Nanodevices group at nanoGUNE, motivated by the large spin Hall angles[29] reported for these materials [12, 14-16, 19], which should make them good candidates to exhibit a measurable MOKE signal. In addition, direct comparison with results in [18] would be possible for Pt and β-W. The thickness of the samples was selected based on a trade-off of the depth-dependence of both the MOKE sensitivity and the spin accumulation[30]. The convolution of both facts determines the MO signal that will be observed [20]. In order to ensure that the depth-dependence of μ_s and the MO sensitivity do not combine in such way that the resulting expected θ_K practically vanishes, two Pt samples of different thicknesses were fabricated, a 15-nm-thick one and a 100-nm-thick one. The latter one is clearly thicker than the penetration depth of visible light in Pt and of the spin diffusion length of the material, so any SHE-related signal detected would only come from the spins of the top interface. For W and Ta only samples with a thickness of 15 nm were fabricated, which is larger than the spin diffusion length of those materials [21, 22] and sufficiently thick for the MO sensitivity to be distinctly different on opposite interfaces of the film. All the samples were sputter deposited onto low-doping Si substrates with 150 nm-thick thermal SiO_2 utilizing a Hall-bar-shaped shadow mask with a length of 6 mm and a width of 1 mm.

The MO setup utilized for the measurements is schematically shown in Fig. 3.1. The optical setup corresponds to the GME setup described in Section 2.3, where a laser beam (λ = 635 nm) at 45° angle of incidence passes through a quarter waveplate that polarizes circularly the light, and then through a rotatable polarizer P_1. The beam is then reflected by the central part of the Hall bar

---

[29] The spin Hall angle is the ratio between the spin current density generated *via* the SHE and the applied current density.

[30] The depth-dependence of the MOKE sensitivity is affected by the refractive index of the material, the wavelength of the probing light and the angle of incidence. If the film is too thin, the MOKE sensitivity at the top and bottom interfaces could be similar and the effects of opposite σ_s would cancel out. The depth-dependence of the spin accumulation μ_s and its magnitude depend on the spin diffusion length of the material.

structure, and passes through a second rotatable polarizer (analyzer) P_2. The light intensity I_D after P_2 is detected by a photodiode. In contrast to the setup presented in Section 2.3, no external magnetic field is applied to the sample. Instead, the setup and the software controlling it were modified to apply to the sample a current $\Im$ with a Keithley 6221 power supply giving rise to a corresponding current density $\boldsymbol{j_c}$. The applied $\boldsymbol{j_c}$ gives rise to a spin accumulation at the surface of the sample due to the SHE. The reflection geometry is devised such that $\boldsymbol{j_c}$ is parallel to the long channel of the Hall bar (y axis), such that the spin accumulation at the interface is polarized with $\boldsymbol{\sigma_s}$ along the x axis, leading to an L-MOKE configuration. The inversion of $\Im$ leads to an inversion of $\boldsymbol{\sigma_s}$ [23] and thus, the $\delta I/I$ magnitude relevant for GME is given by

$$\frac{\delta I}{I} = 2\frac{I_D(\boldsymbol{\sigma_s}) - I_D(-\boldsymbol{\sigma_s})}{I_D(\boldsymbol{\sigma_s}) + I_D(-\boldsymbol{\sigma_s})} = 2\frac{I_D(\Im) - I_D(-\Im)}{I_D(\Im) + I_D(-\Im)}. \tag{3.1}$$

The voltage drop in the sample was measured simultaneously by a multimeter in order to monitor the sample resistance from four-point measurements.
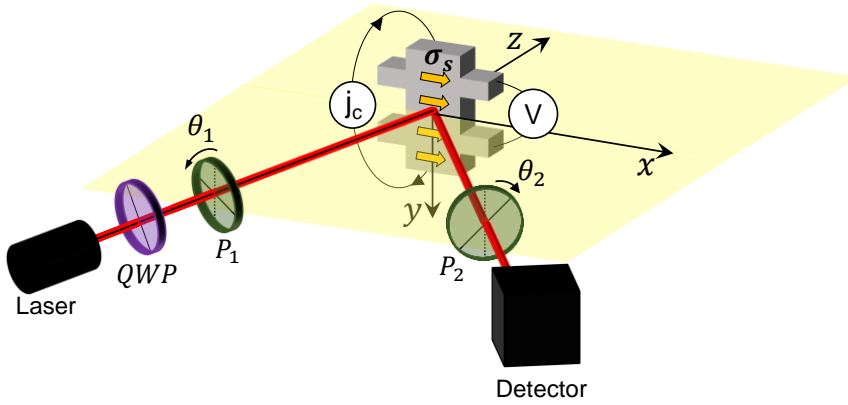

Figure 3.1 Adapted GME setup for the detection of SHE in metals. The laser, the quarter waveplate (QWP), the two rotatable polarizers (P_1 and P_2), and the detector have the same role as in the description of GME in Section 2.3. The plane of incidence is colored in yellow. A current driven by a Keithley 6221 power supply gives rise to a current density $\boldsymbol{j_c}$ parallel to the y axis that generates a spin accumulation at the interfaces of the material. The spin polarization $\boldsymbol{\sigma_s}$ at the top surface is shown by yellow arrows parallel to the x axis. $\boldsymbol{\sigma_s}$ is reversed upon reversing $\boldsymbol{j_c}$. The voltage drop across the Hall bar is monitored by a multimeter.

By measuring $\delta I/I$ for different angles of the polarizer and the analyzer, GME extracts the reflection matrix elements *via* a fit to Eq (2.9), reproduced here for convenience:

$$\frac{\delta I}{I}(\theta_1, \theta_2) = 4\frac{B_1 f_1 + B_2 f_2 + B_3 f_3 + B_4 f_4 + B_5 f_5 + B_6 f_6}{f_3 + B_7 f_7 + 2B_8 f_4 + I_0}. \tag{3.2}$$

B_i and f_i are given by Eqs. (2.10 a-h) and Eqs. (2.11 a-e). Even though a current applied along the y axis is expected to lead just to L-MOKE, $\frac{\delta I}{I}(\theta_2, \theta_1)$ maps have been fitted with all the terms in Eq. (3.2), to account for possible misalignments of the axis of the current application that would give rise to transverse (T-) or even polar (P-) MOKE. Importantly, the longitudinal Kerr rotation θ_K, which is the quantity measured in other studies and to which the results here will be compared, is accessible in a straightforward manner, since $B_1 = \theta_K$. The expected signal is not as large as for ferromagnets shown in Section 2.3 and, accordingly, the sensitivity to MOKE, and in particular to L-MOKE, $i.e.$, to B_1 and B_2, has to be maximized. In order to do so, the scan range for P_1 and P_2 around the crossing point of the polarizers is taken to be smaller than the range typically utilized for ferromagnets (see Section 2.3).

Based on the expected orientation of $\boldsymbol{\sigma_s}$, the symmetry pattern for the $\frac{\delta I}{I}(\theta_2, \theta_1)$ maps should be the one described for L-MOKE in Section 2.3. Assuming the θ_K= 350 μrad reported for β-W in Ref. [18] and vanishing T- and P- MOKE, the expected $\frac{\delta I}{I}(\theta_2, \theta_1)$ maps were computed and are shown in Fig. 3.2, with different hypotheses for the Kerr ellipticity ϵ_K indicated as an inset in the different subfigures, as this quantity was not measured in Ref. [18]. The refractive index of W at 635 nm is obtained from Ref. [24] and an incidence angle of 45 deg is assumed to calculate the optical parameters B_7 and B_8. Depending on the hypothesis for ϵ_K the specific shape of the maps is different, but in all cases two lobes with opposite signs represented in blue (negative) and red (positive) arise around the ($\theta_2 = 0$ deg, $\theta_1 = 90$ deg) point, in agreement with the L-MOKE symmetry. In reference to the $\delta I/I$ reported in Section 2.3.6 for a ferromagnet, the expected $\delta I/I$ for the SHE experiment are quite large, and should therefore be very easy to detect with the GME setup. The values of $\delta I/I$ and correspondingly θ_K will of course depend on the amplitude of the applied current density j_c, as θ_K depends linearly on the spin accumulation, which in turn scales linearly with j_c [23]. It therefore makes sense to report θ_K values normalized to j_c. In Ref. [18] j_c = 6.25×10⁴ A·cm⁻² for β-W, which leads to $\frac{\theta_K}{j_c} \approx$ 5.6 nrad·A⁻¹·cm². Maps in Fig. 3.2 were constructed for the θ_K reported for this specific j_c value; varying j_c would only scale the absolute value of $\delta I/I$, keeping the symmetries unaltered. In the experiments shown here, j_c was chosen to be as high as possible while avoiding overheating that would alter or even destroy the sample.
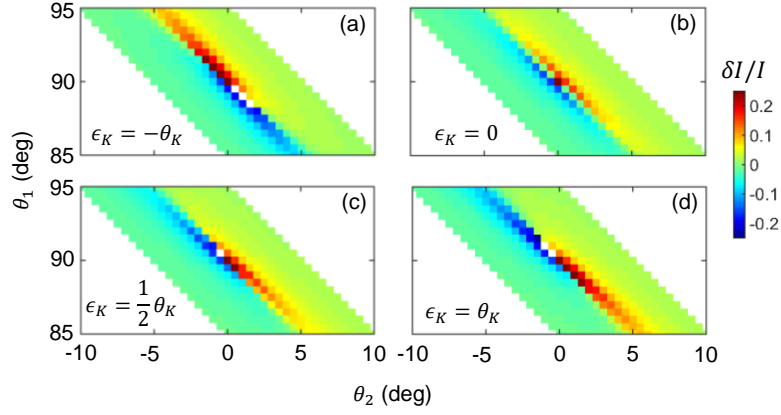
Figure 3.2 Color-coded $\frac{\delta I}{I}(\theta_2, \theta_1)$ maps computed for β-W, assuming the θ_K reported by van 't Erve *et al.* [18] and different hypotheses for ϵ_K, displayed in the bottom left corner of each of the subfigures. The refractive index $N = 0.92685 + 6.6160\,i$ at 635 nm is taken from [24], leading to $B_7 = 1.0588$ and $B_8 = -1.0068$.

3.3 Results

3.3.1 Generalized magneto-optical ellipsometry analysis

GME measurements were performed for all samples applying a quasi-DC alternating current $\mathfrak{I}$ with square form, whose value and corresponding j_c are shown in the third and fourth columns of Table 3.1. The resulting $\delta I/I(\theta_2, \theta_1)$ maps are shown in the first row of Fig. 3.3 and importantly, the detected $\delta I/I$ values are much smaller than the expected ones from Section 3.2. It becomes apparent that none of them displays the MOKE signal symmetries discussed in Section 2.3, let alone the specific L-MOKE symmetry of Fig. 3.2 expected for the experiment. Instead, the only feature is a distribution of non-vanishing $\delta I/I$ values with random magnitude and sign near the diagonal of the maps, *i.e.*, at points where the difference between θ_1 and θ_2 is close to 90 deg. The fact that P_1 and P_2 are almost perpendicular to each other makes I to be very low and, as a consequence $\frac{\delta I}{I}(\theta_2, \theta_1)$ becomes rather noisy and thus creates this "noise diagonal". It is important to stress that the noise level observed in the experiment is not unexpectedly large; in fact, it corresponds to the typical level of noise of the residuals, once the MOKE fitted signal is subtracted from the measured maps.
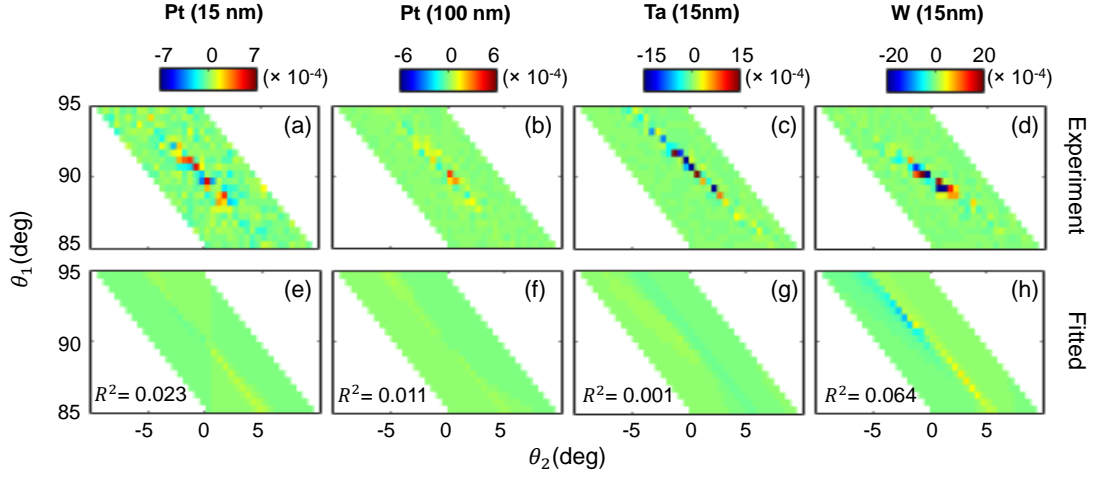
Figure 3.3 (a)-(d) Color-coded $\frac{\delta I}{I}(\theta_2, \theta_1)$ maps measured for each of the four samples. The identifier of the sample to which each map corresponds is on top of the maps, as well as the color scale for $\delta I/I$. (e)-(h) Corresponding fitted maps, using Eq. (3.2) as a fitting function. The R^2 goodness of each fit is shown on the bottom left corner of each fitted map.

Sample	ρ (μΩ cm)	$\mathfrak{I}$ (mA)	j_c (A cm^{-2})	θ_K (μrad)	Upper limit θ_K/j_c (nrad A^{-1} cm^2)
Pt (15 nm)	31	45	3.0×10^5	(-0.02 ± 0.05)	1.67×10^{-4}
Pt (100 nm)	25	33	3.3×10^4	(0.04 ± 0.02)	1.21×10^{-3}
Ta (15 nm)	180	9	6.0×10^4	(0.3 ± 0.7)	1.16×10^{-2}
β-W (15 nm)	225	15	1.0×10^5	(-0.2 ± 0.2)	2.00×10^{-3}

Table 3.1 List of samples and their thickness (column 1) and corresponding resistivities (column 2). Column 3 shows the current applied to each sample during the experiment to construct the $\delta I/I$ maps and column 4 the corresponding current density. The measured Kerr rotation is shown in column 5, where the error bars determine the sensitivity of the experiment utilized here. Based on them, column 6 shows the determined upper limit of θ_K normalized to the applied current density.

The signals were quantified by fitting the measured $\delta I/I$ maps of each sample to Eq. (3.2). The optical parameters B_7 and B_8 were calculated from literature optical constants for each of the materials [24-26] in order to reduce the number of fitting parameters[31]. The fittings are shown in Figs. 3.3 (e)-(h) in the same color scale as the experimental data. As it can be observed, hardly any actual signal pattern can be extracted and correspondingly, the R^2 goodness values of the fits, which are shown in the bottom left corner of Fig. 3.3 (e)-(h) are very low, because the symmetries of the fit function in Eq. (3.2) are not present in the data. This means that the measured data

---

[31] The data were also fitted leaving B_7 and B_8 as fitting parameters. However, this is problematic, given that there is no actual MOKE signal. Thus, fitting B_7 and B_8 did not improve the quality of the fit.

cannot be explained as a MOKE-induced light polarization effect. It is important to note that neither of the Pt samples with different thickness exhibit an observable MOKE, so one can rule out the fact that the lack of MO signal is due to an unfortunate combination of MO sensitivity and spatial distribution of SHE-generated spin accumulation. In contrast to the measurements performed here, GME $\frac{\delta I}{I}(\theta_2, \theta_1)$ maps for samples that exhibit a sufficiently large MOKE signal show clear symmetry patterns, and least-squares fits to Eq. (3.2) yield R^2 values that are typically above 0.98, as shown in Section 2.3.

This exhaustive data analysis allows one to determine upper bounds for the MOKE signal. In particular, θ_K values were determined from the fits and are listed in the fifth column of Table 3.1 with error bars corresponding to a 95% confidence interval. For all samples, the size of the error bar is comparable to the determined value of θ_K, indicating that the contribution of L-MOKE to the experimental data is negligible, despite achieving a detection limit of the order 0.5 μrad in all cases, and even of 0.05 μrad in the case of Pt. This means that, if the L-MOKE signal were larger than such a value, it should have been detectable by GME. The last column in Table 3.1 shows the detectability limit of θ_K/j_c determined by the ratio between the error bar of θ_K and j_c, or, in the cases where the fitted θ_K is larger than the error bar, the ratio between the fitted θ_K and j_c. The data are in obvious disagreement with the findings of Ref. [18], where the reported θ_K/j_c values are at least two orders of magnitude larger than the detection limit that was achieved here using GME, so that if said signals were indeed present, they should have been easily observed.

3.3.2 Possible sources of the misinterpretation of the results in non-ellipsometric setups

The inconsistency between the results obtained in Section 3.3.1 and those shown in prior reports can be explained by the limitations of conventional MOKE metrology. As opposed to the case of GME, where θ_1 and θ_2 are scanned, the orientations of P_1 and P_2 are fixed close to their crossing point in conventional MOKE experiments, as the ones performed in Ref. [18]. With such scheme the determination of θ_K relies on a net intensity change in a polarization sensitive experiment [27] (see Appendix I) and various MO and purely optical contributions are mixed [27-30]. As one operates at low light intensity levels, if the experiment generates a light intensity change that is unrelated to an actual polarization effect, such experimental conditions can be susceptible to

misinterpretation, which is exactly what occurs at the individual data points along the "noise diagonals" shown in Fig. 3.3 (a)-(d). The strength of GME is that by combining $\delta I/I$ measurements for several (θ_1, θ_2) configurations, it allows for the separation of actual MOKE effects from such spurious signals, because the MOKE signal pattern has to fulfill the symmetries described by Eq. (3.2).

In order to investigate the origin of the features along the diagonal of the $\delta I/I$ maps, which conventional MOKE measurement could misinterpret as MO signals, additional non-ellipsometric measurements with fixed P_1 and P_2 near the crossing point were performed, for which the photodetector signal was recorded as $\Im$ was continuously swept. For such configuration of the polarizers, the true MOKE-related intensity I_D scales linearly with θ_K (see Appendix I), which is in turn linearly dependent on $\Im$. Hence, if the signal is SHE-related, I_D should be proportional to $\Im$. However, the resulting signal shown in Fig. 3.4 (a) for the Pt (15 nm) sample, where the polarizers were fixed at orientations $\theta_1 = 90$ deg and $\theta_2 = 5$ deg, does not show the expected linear trend, but rather a quadratic, slightly hysteretic dependence on $\Im$. The four-point resistance shown in Fig. 3.4 (b) also exhibits a slightly hysteretic quadratic dependence on $\Im$ consistent with Joule heating, and mimics the light intensity data. Thus, the signal in Fig. 3.4 (a) can be explained by a change of the sample reflectivity due to such heating effects proportional to $\Im^2$ because, even if the setup is devised to be polarization-sensitive, it also senses non-polarization-induced absolute changes in sample reflectivity. The same kind of experiment was performed without polarizer P_2, thus removing the polarization sensitivity from our setup, and results equivalent to those in Fig. 3.4 (a) were obtained. Ta and W samples also show a quadratic $I_D(\Im)$ dependence.
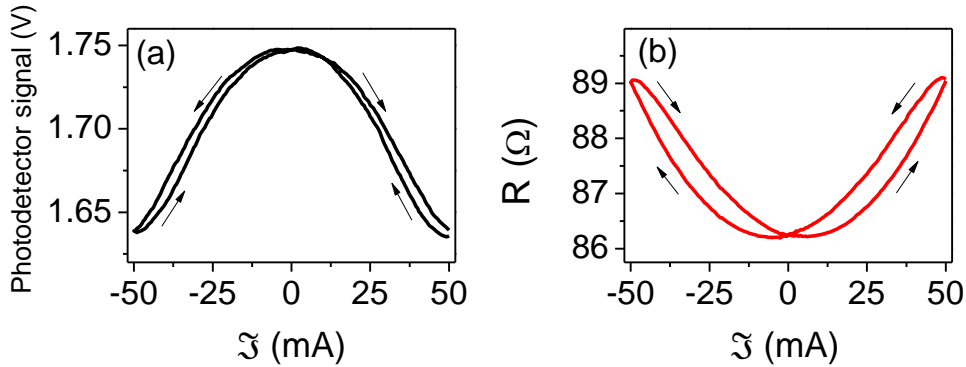

Figure 3.4 (a) Signal at the photodetector upon continuous quasi-DC sweeping the current applied to the Pt (15 nm) sample, with the polarizer and analyzer angles set to $\theta_1 = 90$ deg and $\theta_2 = 5$ deg, respectively. (b) Monitored sample resistance, obtained by dividing the measured voltage drop by the applied current. The arrows indicate the sense of sweeping of the current.

Under ideal measurement conditions, this quadratic dependence would give rise to a null $\delta I = I_D(+\Im) - I_D(-\Im)$ signal. However, due to the hysteretic behavior, noise sources and other experimental imperfections, the light intensity upon current inversion might not be completely identical, thus causing a nonzero δI value. Combined with the fact that near the diagonal of the maps I is extremely low, $\delta I/I$ becomes very sensitive to noise- or imperfection-induced δI, which explains the "noise diagonals" in the experimental maps.

Actually, if due to some experimental imprecision the applied current has a small bias $\delta_\Im$ and thus the absolute values of the positive and the negative current are not exactly identical, the resulting difference in the reflectivity of the sample for the two different values of Joule heating corresponding to $(\Im + \delta_\Im)^2$ and $(\Im - \delta_\Im)^2$ will lead to a difference in the detected light intensity that can be misinterpreted as a MOKE signal. This is shown in Fig. 3.5, where an intentional bias was introduced to the current applied to the Pt (15 nm) sample, such that the positive current was 40 mA, while the negative was -50 mA. For the acquisition of these specific data, P_1 was set to $\theta_1 = 0$ deg and P_2 to $\theta_2 = 93$ deg, *i.e.*, close to a crossed polarizers setting. Figures 3.5 (a) and (b) show in blue the applied current as a function of time in the right vertical axis. In Fig. 3.5 (a) the signal at the detector is plotted in black symbols (left vertical axis). Despite the obvious delay, and the lack of sufficient time to reach the stable value, the detected photovoltage clearly follows the time sequence of the applied current, with larger absolute values of the current (occurring during the negative half-cycle) leading to lower light intensity at the detector, in agreement with Fig. 3.4 (a). The change in the signal at the detector is related to the change in resistance, shown in Fig. 3.5 (b) in red (left vertical axis). In this case, the larger absolute values of the current lead to higher resistance, which is consistent with Fig. 3.4 (b). The $\delta I/I$ observed in Fig. 3.5 (a) could be erroneously interpreted as a MOKE signal, and given that the polarizer and the analyzer are almost crossed, and that L-MOKE is expected, one would calculate θ_K as $\theta_K = \frac{\Delta}{4}\frac{\delta I}{I}$, where Δ is the deviation of θ_2 from the crossing point, *i.e.* in this case $\Delta = +3$ deg, yielding a perceived Kerr rotation of 63 μrad. Upon reversing Δ to -3 deg, the measured $\delta I/I$ kept the same sign (not shown here), contrary to what should occur if the observed signal were related to a polarization rotation created by MOKE. While the asymmetry in the current is deliberately introduced here, this is an effect that could be unintentional and hard to identify, still leading to a signal at the detector, which could be misinterpreted as a MOKE signal.
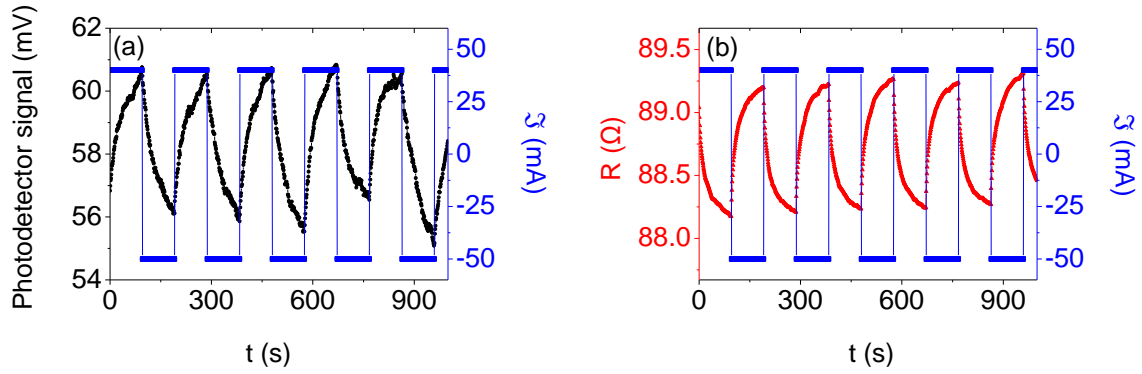
Figure 3.5 Response of the Pt (15nm) sample to an applied current that is intentionally asymmetric. The applied current is shown in blue in both panels (right vertical axis). In (a), the measured photodetector signal is shown in black (left vertical axis), and in (b), the four-point resistance in shown in red (left vertical axis).

3.4   Conclusions and related works

MOKE signals arising from SHE-induced spin accumulations in Pt, Ta and W proved to be extremely small in contrast to some reports in literature [18, 31], and too small to be detected by the methodology utilized here. Given that GME allows for a disentanglement of purely optical effects from polarization changes related to MOKE, it was possible to determine that the observed signals are not of magneto-optical origin, and to robustly determine upper limits for the signals to be detected [32].

A simplistic argument can be made to justify the inability to detect SHE-induced MOKE with the methodology presented here, which constitutes a state-of-the-art linear MOKE experiment. For the j_c values used here, the number of electrons participating in the transport and thus, the number of electrons that can potentially be polarized *via* the SHE, is negligible compared to the number of electrons that participate in the optical reflection for metals and typical photon energies of about 2 eV. Accordingly, the ratio between the spin-polarized electrons and the probed ones is many orders of magnitude smaller than in MOKE experiments on ferromagnets. This also justifies why the detection of SHE with MOKE is possible in semiconductors: in this case, the ratio of the spin-polarized electrons to the optically excited ones is larger than in the case of metals. Or, to put it in other words, semiconductors are less reflective than metals, so that the proportion of reflected light carrying MOKE-related polarization information with respect to the total reflected light is larger than in the case of metals.

These results, which were published in 2016 [32], show that a significantly better sensitivity in MOKE metrology and/or higher current densities are necessary to achieve the detection of SHE in metals. Since then, subsequent works have continued to study the issue. A relevant publication confirming the need of better sensitivity in MOKE to detect SHE was published in 2017 [33], where the authors calculated that in order to obtain a Kerr rotation of 1.75 μrad in β-W a current density of about 10^8 A·cm^{-2} is needed, *i.e.*, they predicted a Kerr rotation per applied current density of -1.75 × 10^{-5} nrad·A^{-1}·cm^2, two orders of magnitude lower than the upper limit that was observed here, and therefore in agreement with it. Later in 2017, Stamm *et al.* [20] achieved the excellent sensitivity of 5 nrad in their MOKE setup using AC current modulation. They also applied current densities that are at least an order of magnitude larger than the ones used in this thesis and they observed a signal that scaled linearly with the applied current density, as expected for MOKE. The combination of a better sensitivity and a larger current density made them able to detect a Kerr rotation per current density of 1.95 × 10^{-6} nrad·A^{-1}·cm^2 for 15-nm-thick Pt and of -5.97 × 10^{-6} nrad·A^{-1}·cm^2 for 10-nm-thick W. Combining measurements for samples with different Pt thicknesses, ab initio calculations and MO modeling, Stamm *et al.* were able to determine the spin diffusion length of Pt [20].

Utilizing MOKE for the detection of the SHE in metals now seems an achievable goal with state of the art technology; however it must be kept in mind that, given the smallness of the expected signals, high precision is required. In addition, cross-checking that the signals are actually arising from MOKE and not from other undesired effects appears necessary. In this regard, GME is a very powerful to unambiguously distinguish in between true MOKE signals and other occurring optical effects, such as pure reflectivity changes.

References

[1] Y. K. Kato, R. C. Myers, A. C. Gossard, and D. D. Awschalom, Science **306**, 1910 (2004).
[2] V. Sih, R. C. Myers, Y. K. Kato, W. H. Lau, A. C. Gossard, and D. D. Awschalom, Nat. Phys. **1**, 31 (2005).
[3] J. Wunderlich, B. Kaestner, J. Sinova, and T. Jungwirth, Phys. Rev. Lett. **94**, 047204 (2005).
[4] S. A. Crooker, M. Furis, X. Lou, C. Adelmann, D. L. Smith, C. J. Palmstrøm, and P. A. Crowell, Science **309**, 2191 (2005).
[5] N. P. Stern, D. W. Steuerman, S. Mack, A. C. Gossard, and D. D.Awschalom, Appl. Phys. Lett. **91**, 062109 (2007).
[6] E. Saitoh, M. Ueda, H. Miyajima, and G. Tatara, Appl. Phys. Lett. **88**, 182509 (2006).
[7] K. Ando, S. Takahashi, K. Harii, K. Sasage, J. Ieda, S. Maekawa, and E. Saitoh, Phys. Rev. Lett. **101**, 036601 (2008).

[8] Y. Kajiwara, *et al.*, Nature **464**, 262 (2010).

[9] S. O. Valenzuela and M. Tinkham, Nature **442**, 176 (2006).

[10] T. Kimura, Y. Otani, T. Sato, S. Takahashi, and S. Maekawa, Phys. Rev. Lett **98**, 156601 (2007).

[11] P. Laczkowski *et al.*, Appl. Phys. Lett. **104**, 142403 (2014).

[12] E. Sagasta, Y. Omori, M. Isasa, M. Gradhand, L. E. Hueso, Y. Niimi, Y. Otani, and F. Casanova, Phys. Rev. B **94**, 060412(R) (2016).

[13] M. Isasa, E. Villamor, L. E. Hueso, M. Gradhand, and F. Casanova, Phys. Rev. B **91**, 024402 (2015); **92**, 019905(E) (2015).

[14] L. Liu, T. Moriyama, D. C. Ralph, and R. A. Buhrman, Phys. Rev. Lett. **106**, 036601 (2011).

[15] L. Liu, C. F. Pai, Y. Li, H. W. Tseng, D. C. Ralph, and R. A. Buhrman, Science **336**, 555 (2012).

[16] C.-F. Pai, L. Liu, Y. Li, H. W. Tseng, D. C. Ralph, and R. A. Buhrman, Appl. Phys. Lett. **101**, 122404 (2012).

[17] A. Pattabi, Z. Gu, J. Gorchon, Y. Yang, J. Finley, O. J. Lee, H. A. Raziq, S. Salahuddin, and J. Bokor, Appl. Phys. Lett. **107**, 152404 (2015).

[18] O. M. J. van't Erve, A. T. Hanbicki, K. M. McCreary, C. H. Li, and B. T. Jonker, Appl. Phys. Lett. **104**, 172402 (2014).

[19] S. Vélez, V. N. Golovach, A. Bedoya-Pinto, M. Isasa, E. Sagasta, M. Abadia, C. Rogero, L. E. Hueso, F. S. Bergeret, and F. Casanova, Phys.Rev. Lett. **116**, 016603 (2016).

[20] C. Stamm, C. Murer, M. Berritta, J. Feng, M. Gabureac, P. M. Oppeneer, and P. Gambardella, Phys. Rev. Lett. **119**, 087203 (2017).

[21] Q. Hao and G. Xiao, Phys. Rev. Applied **3**, 034009 (2015).

[22] R. Yu, B. F. Miao, L. Sun, Q. Liu, J. Du, P. Omelchenko, B. Heinrich, Mingzhong Wu, and H. F. Ding, Phys. Rev. Materials **2**, 074406 (2018)

[23] J. E. Hirsch Phys. Rev. Lett. **83**, 1834 (1999).

[24] W. S. M. Werner, K. Glantschnig, and C. Ambrosch-Draxl, J. Phys Chem Ref. Data **38**, 1013-1092 (2009).

[25] A. D. Rakić, A. B. Djurišic, J. M. Elazar, and M. L. Majewski., Appl. Opt. **37**, 5271-5283 (1998).

[26] M. A. Ordal, R. J. Bell, R. W. Alexander, L. A. Newquist, and M. R. Querry, Appl. Opt. **27**, 1203-1209 (1988).

[27] Z. Q. Qiu and S. D. Bader, Rev. Sci. Instrum. **71**, 1243 (2000).

[28] E. R. Moog and S. D. Bader, Superlattices Microstruct. **1**, 543 (1985).

[29] Z. Q. Qiu, J. Pearson, A. Berger, and S. D. Bader, Phys. Rev. Lett. **68**, 1398 (1992).

[30] J. McCord, J. Phys. D: Appl. Phys. **48**, 333001 (2015).

[31] R. Bansal, N. Behera, A. Kumar,and P. K. Muduli, Appl. Phys. Lett. 110, 202402 (2017).

[32] P. Riego, S. Vélez, J. M. Gomez-Perez, J. A. Arregi, L. E. Hueso, F. Casanova, A. Berger, Appl. Phys. Lett. **109**, 172402 (2016).

[33] Y. Su, H. Wang, J. Li, C. Tian, R. Wu, X. Jin, and Y. R. Shen, Appl. Phys. Lett. **110**, 042401 (2017).

Chapter 4

Magneto-optical investigation of the effect of a Co/Ru interface in the magnetization reversal of crystalline Co

This chapter explores how a thin Ru overcoat affects the magnetic and magneto-optical properties of a single crystal Co film with uniaxial in-plane magneto-crystalline anisotropy. After an introduction on the relevance of interfaces in nanomagnetism in Section 4.1, details about the fabrication of single crystal Co films and their structural and magnetic characterization are given in Section 4.2. Subsequently, Section 4.3 focuses on the fabrication of such kind of Co films with Ru overcoats. In particular, the Ru overcoat was designed to have a thickness gradient along the length of the sample, which is achieved by obliquely depositing the Ru layer. The so-obtained samples were characterized by means of generalized magneto-optical ellipsometry and the corresponding results are discussed in Section 4.4. Unexpectedly, a polar magneto-optical Kerr effect signal is observed in remanence in samples with obliquely deposited Ru overcoats, even though the crystallographic easy axis of Co is in-plane. This effect is studied and is found to be related to the Co/Ru interface. A model to explain the data is given in Section 4.5 and includes an antisymmetric exchange energy term, the so-called Dzyaloshinskii-Moriya interaction. The main conclusions of this overall work, as well as an outlook, are presented in Section 4.6.

4.1   Introduction and motivation

It is well known in the field of nanomagnetism and spintronics that interfacial and proximity effects lead to very significant changes of the physical properties of magnetic materials [1]. The aim of this chapter is to perform a detailed study of the interface between an ultrathin non-ferromagnetic (NM) metallic overcoat and a thin ferromagnetic (FM) film. In particular, the goal is to investigate the effect of the NM overcoat onto the optical, but especially onto the magneto-optical (MO) and magnetic properties of the FM. As a material system, Co has been utilized as the FM material, and Ru as the NM one.

Among the interfacial effects that may arise between FM and NM materials, a well-known phenomenon is the fact that, in the proximity of a ferromagnet, a magnetic moment may be induced in atoms of NM materials, notably in those close to exhibiting ferromagnetism, such as Pt or Pd [2, 3]. Plus, due to the symmetry breaking at interfaces, the surface normal becomes a unique crystal axis and this can lead to surface anisotropy, given that the electronic structure of the material differs from that of the bulk [4, 5]. For instance, magnetic bilayers and multilayers including ultrathin layers of FM and NM metals [6, 7], as well as combinations of ferromagnets with some oxides [8, 9] are known to display interface-induced perpendicular magnetic anisotropy. Regarding the materials relevant in this chapter, Co and Ru, perpendicular magnetic anisotropy was found in Co/Ru multilayers [10]. MO properties are also affected by the presence of interfaces [11-13] and, in particular, thickness-dependent oscillatory MO signals that were observed in a Co/Ru interface [14].

Interlayer exchange coupling, a phenomenon that occurs in FM films separated by a NM spacer layer, is yet another manifestation of interfacial magnetism. The electronic state in the spacer can generate a coupling between the magnetizations of both FM layers by mediating an exchange interaction[15] whose strength was found to oscillate as a function of the non-magnetic spacer thickness [16], a fact that can be explained [17] in terms of Ruderman-Kittel-Kasuya-Yoshida coupling [5]. Interlayer exchange coupling can be FM or antiferromagnetic, which has led to the use of this kind of interaction for the fabrication of synthetic antiferromagnets [18-21], for which Ru is a commonly used spacer layer [22-24].

The mentioned interfacial phenomena in magnetism started to be explored and exploited decades ago, with an enormous impact in technological applications. A paradigmatic example is the discovery of giant magneto-resistance (GMR) in FM/NM/FM exchange-coupled structures [25, 26], where it was observed that the electrical resistance of a FM/NM/FM stack differed very significantly if the two FM layers are magnetized in a parallel or antiparallel fashion. This was a key finding for the development of GMR magnetic field sensors in hard disk drives, even though in technological application GMR is not based on exchange-coupled systems. Nowadays, newer and promising spintronics technologies as magnetic random access memories [27] also rely on interfacial magnetic effects, and the constant evolution of electronic devices makes the study of FM/NM interfaces a very relevant field.

Yet another consequence of the symmetry breaking at interfaces, namely interfacial Dzyaloshinskii-Moriya interaction (DMI), has recently sparked increasing interest because of its link to skyrmions, which are topologically non-trivial spin textures that have been proposed for energy-efficient information storage in racetrack memories [28]. In addition, it has been recently reported that DMI is not just relevant within a given layer of a FM material, as it can lead to a type of interlayer exchange coupling between FM layers separated by a NM spacer that is chiral in nature [29, 30]. DMI, as already mentioned in Chapter 1, is an exchange interaction that favors the perpendicular alignment between two spins and changes sign upon swapping them, therefore favoring a specific chirality of domain walls and promoting the formation of non-collinear spin textures. For DMI to occur, spin-orbit coupling (SOC) is required in addition to inversion symmetry breaking, and this can be provided by placing heavy NM atoms near a FM surface, as demonstrated in multilayers of FM and NM heavy metals [31-34]. Thus, a NM overcoat with relatively high SOC on a FM material can give rise to DMI. Although Ru, with an atomic number $Z = 44$, is not a particularly heavy metal, its SOC could be sufficiently high to give rise to substantial DMI [35, 36], so DMI could be a relevant energy contribution in the Co/Ru samples investigated here.

For an accurate and systematic study of the effect of the Ru overcoat on the magnetic properties of Co and its magnetization reversal process one ideally needs a Co film whose magnetization reversal path is simple, robust, well-understood, reproducible, and easily described, in such way that the modifications induced by the overcoat are easy to identify. A macrospin type of reversal as described in Section 1.2.2 would be ideal due to its simplicity. This requires single-crystal samples with a high degree of uniaxial anisotropy to avoid multi-domain states[32]. In that regard, Co in its hexagonal closed packed (hcp) phase is a good candidate, as this material has an easy axis (EA) of magnetization along the crystallographic [0001] direction. In addition, if thin films are grown with the EA in the plane of the film, demagnetization effects can be minimized. As has already been demonstrated [37, 38], the growth of hcp Co films with in-plane [0001] crystallographic direction can be achieved by a robust and well-optimized heteroepitaxial growth sequence, leading to a macrospin type magnetization reversal upon the application of an in-plane magnetic field.

---

[32] Only in the proximity of the switching field, the single-domain state may break into domains.

As for the characterization technique, magneto-optics is a well-suited tool for the study of a single Co/Ru interface due to its significant surface sensitivity (See Section 1.4). Plus, the capabilities of generalized magneto-optical ellipsometry (GME) are exploited here to perform three-dimensional vector magnetometry and determine the orientation of the magnetization.

In the rest of the chapter, the fabrication and characterization of single-crystal Co samples with in-plane EA covered by Ru overcoats will be presented. In Section 4.2, samples without Ru overcoat will be discussed. The heteroepitaxial growth of the Co films utilizing sputtering deposition will be described, as well as their crystallographic and magnetic characterization. Section 4.3 focuses on the design and fabrication of the Ru overcoat and provides a list of all the different samples fabricated for this study. In Section 4.4, GME three-dimensional vector magnetometry results are presented and discussed for the different types of samples. Finally, a simple model is proposed in Section 4.5 to explain the results in a qualitative manner. Conclusions and an outlook are discussed in Section 4.6.

4.2 Growth and characterization of Co samples with in-plane easy axis

4.2.1 Growth sequence

As described in Section 4.1, the experiments here were performed on hcp Co samples with in-plane crystallographic EA. The crystallographic EA of hcp Co lies along the [0001] direction of the crystal and, for such direction to lie in the plane, the surface crystallographic orientation of the Co layers grown here is (10$\underline{1}$0). It has been shown experimentally that Co can be grown with such orientation on Si (110) substrates following the epitaxial growth sequence with Ag and Cr template layers presented in [39], which was later on optimized for the specific sputtering deposition system presented in Section 2.1 [38]. The same type of procedure has been used in this thesis to obtain crystalline Co samples with very good epitaxy. The epitaxial relations between the different materials utilized are described below.

Prior to the deposition of any layer, single-crystal Si (110) substrates were cleaned first with acetone, subsequently with isopropanol and were then rinsed with deionized water to remove residues on their surfaces. Afterwards, the substrates were etched with hydrofluoric (HF) acid to remove the native SiO_2 that naturally grows on them, thus leaving the Si surface exposed. The

substrates were immediately transferred to the sputter main chamber to start the deposition process and hence minimize the formation of SiO₂ on the substrates.

Given the diamond cubic crystal structure of Si, its (110) crystallographic plane results in a rectangle as the one shown on the top left corner of Fig. 4.1 (a). Heteroepitaxial growth of Ag, with a surface unit cell as the one shown on the top right corner of Fig. 4.1 (a), is possible because the dimensions of a 3×3 supercell of Si (110) match very well with a 4×4 supercell of Ag (110), with only a mismatch of 0.4 % along the Si (110) [001] / Ag (110) [001] direction, and 0.35 % in the Si (110) [1$\underline{1}$0] / Ag (110) [1$\underline{1}$0] direction. bcc Cr can subsequently grown on top of the Ag (110) surface acquiring the (211) orientation shown on the bottom left corner of Fig. 4.1 (a), whose [0$\underline{1}$0] direction only has a -0.25% mismatch with the Ag (110) [001] orientation. The perpendicular in-plane direction of Cr (211) [$\underline{1}$11] has a -13.5 % mismatch with the Ag (110) [1$\underline{1}$0] orientation, but still an adequate epitaxy that enables the growth of crystalline Co on Cr is possible. Finally, hcp Co is grown on top of the Cr layer acquiring a (10$\underline{1}$0) surface orientation as shown on the bottom right corner of Fig. 4.1 (a), with a -0.5 % mismatch along the Cr (211) [110] / Co (10$\underline{1}$0) [0001] direction, and a 0.4 % mismatch in the Cr (211) [111] / Co (10$\underline{1}$0) [1010] direction. The stacking of the Si, Ag, Cr, and Co surface unit cells are shown in Fig. 4.1 (c). It is important to note that according to this sequence the EA of Co, which is the [0001] direction, lies along the Si (110) [001] direction of the substrate. This will become important in Section 4.2 for the design of the samples.

All the mentioned layers (Ag, Cr, and Co) were deposited with the sputter gun facing the center of the sample holder and with the sample holder rotating during the deposition, with the aim of obtaining films that are as homogeneous as possible. The deposition of the Ag, Cr, and Co layers was performed with an Ar pressure of 0.4 Pa. The power utilized for the Ag deposition was 40 W, obtaining a deposition rate of 0.156 nm·s⁻¹; for Cr, 100 W, yielding a deposition rate of 0.077 nm·s⁻¹; and for Co, 100 W, with a deposition rate of 0.060 nm·s⁻¹.

Based on the optimization process carried out in [38], the thickness of Ag was selected to be 75 nm and the thickness of Cr to be 40 nm. The Co thickness t_{Co} (given in nm) is a variable of the experiments. Good epitaxy, high magnetocrystalline anisotropy, and in-plane magnetization rotation that is describable by a macrospin model upon applying in-plane magnetic fields were achieved in the entire Co film thickness range of 5 – 100 nm.

4.2.2 Structural characterization

To verify the epitaxial growth of the samples x-ray diffraction measurements were performed on the $Co(t_{Co})$/Cr(40nm)/Ag(75nm)/Si(substrate) samples. Figure 4.1 (b) shows the θ^X - $2\theta^X$ scan of a prototypical sample with a 20-nm-thick Co layer. As explained in Section 2.2, in this kind of scans, only diffraction peaks caused by planes parallel to the sample surface arise. Therefore, only peaks related to Si (110), Ag (110), Cr (211), and Co (10$\underline{1}$0) planes should be visible if the growth sequence described in Section 4.2.1 is fulfilled, and this is indeed the case. The absence of any other peaks confirms that other crystallographic orientations are severely suppressed.
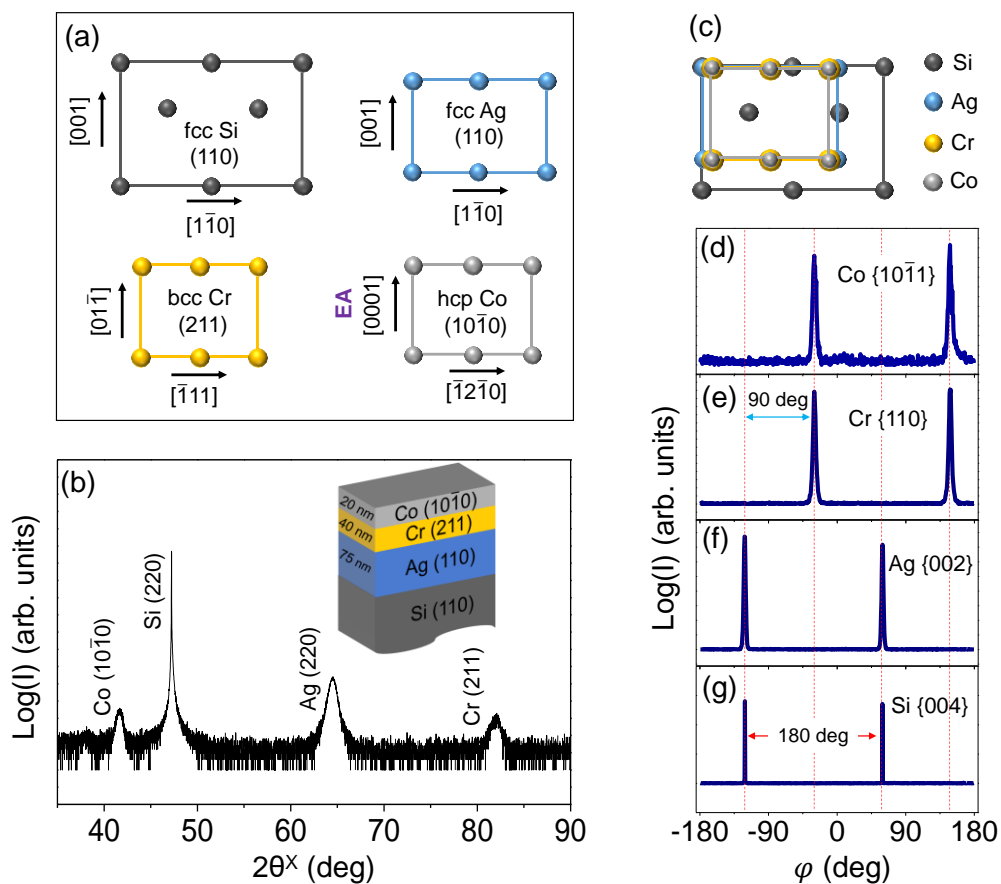
Figure 4.1 (a) Schematics of the top view of Si, Ag, Cr, and Co lattices with the desired surface orientation. (b) θ^X - $2\theta^X$ XRD scans for an exemplary sample with a 20-nm-thick Co layer showing the diffracted intensity as a function of $2\theta^X$. Inset: schematics of the sample structure indicating the thickness of the layers (not in scale). (c) Expected stacking of Si/Ag/Cr/Co for heteroepitaxial growth, with the legend for the color of the atoms given on the right-hand-side. (d)-(g) φ-scans of different poles of Co, Cr, Ag, and Si for the exemplary sample. (d) Co {10$\underline{1}$1} pole, with Ψ = 28 deg and $2\theta^X$ = 47.4 deg. (e) Cr {110} pole, with Ψ = 30 deg and $2\theta^X$ = 44.0 deg. (f) Ag {002} pole, with Ψ = 45 deg and $2\theta^X$ = 44.3 deg. (g) Si {004} pole, with Ψ = 45 deg and $2\theta^X$ = 69.1 deg.

The presence of just the predicted orientation in the θ^X - $2\theta^X$ scan does not give any information about the in-plane orientation of the crystallites, which could in principle have random azimuthal orientations. Hence, in order to confirm that the stacking of the different materials occurs in the correct epitaxial orientations described in Section 4.2.1, φ-scans were performed. In this type of scans one detects the diffraction of a crystal plane with Miller indices (*hkl*) that is not parallel to the sample surface. In order to do so, the sample is tilted by an angle Ψ determined by the angle between the plane parallel to the sample surface and the crystalline plane that one wants to detect. Furthermore, the source and the detector are placed in a θ^X - $2\theta^X$ configuration required to get a diffraction peak from the investigated (*hkl*) plane, and the intensity is recorded as a function of φ, the azimuthal rotation angle with respect to the surface normal. If the crystallites of the layer are not randomly oriented but instead have a predefined azimuthal orientation, the intensity will vary in a specific manner determined by the symmetry of the crystal. Figures 4.1 (d) – (g) show φ-scans for specific Co, Cr, Ag, and Si poles of the sample with a 20-nm-thick Co layer for which the θ^X - $2\theta^X$ scan is shown in Fig. 4.1 (b). The Ψ and $2\theta^X$ configurations used for each material are given in the figure caption, and were selected to be sensitive to the {004} pole of Si, the {002} pole of Ag, the {110} pole of Cr, and the {10$\underline{1}$1} pole of Co. For Si, Fig. 4.1 (g) shows two narrow peaks related to the {004} pole, separated by 180 deg, corroborating the single-crystal nature of the substrate. The fact that Ag shows two peaks at the same values of φ as Si (see Fig. 4.1 (f)), and no further peaks, means that the Ag [001] direction has grown parallel to the Si [001] direction. Figure 4.1 (e) shows the φ-scan of the Cr {110} pole. The scan shows only two peaks that are 180 deg apart and that are displaced with respect to the Ag ones by 90 deg, which is indicative of the Cr [01$\underline{1}$] direction growing parallel to the Ag [001] direction. Finally, the two peaks in Fig. 4.1 (d) for the Co {10$\underline{1}$1} pole, which occur at the same φ values of the ones in Fig. 4.1 (e), indicate that the Co [0001] direction, namely the EA of Co, grows parallel to the Cr [01$\underline{1}$] direction, *i.e.*, parallel to the [001] direction of the Si substrate. The peaks of the φ-scans of the Ag, Cr, and Co layers are narrow, comparable to typical values for high quality epitaxial metal films, which is indicative of the near perfect alignment of neighboring crystallites in the desired orientation.

4.2.3 Magnetic characterization

In order to investigate the in-plane magnetization reversal of the fabricated samples in-plane vibrating sample magnetometry (VSM) measurements were performed. An important thing to

keep in mind is that VSM measures the magnetization along the applied field axis, which will be denoted in the following as M_H. For the experiment presented here, M_H vs. applied magnetic field strength H hysteresis curves were measured for different orientations of the applied field with respect to the EA of Co, with the magnetic field being always in the plane of the sample. The geometry of the experiment in shown in Fig. 4.2 (a). The EA of the sample forms an angle Φ_0 with the applied field axis (the x axis). Given that the experiments are performed with an in-plane applied field, demagnetization energy is neglected. The competition between the applied field and the magneto-crystalline anisotropy (MCA) will determine the angle of the magnetization vector Φ_M with respect to the x axis.
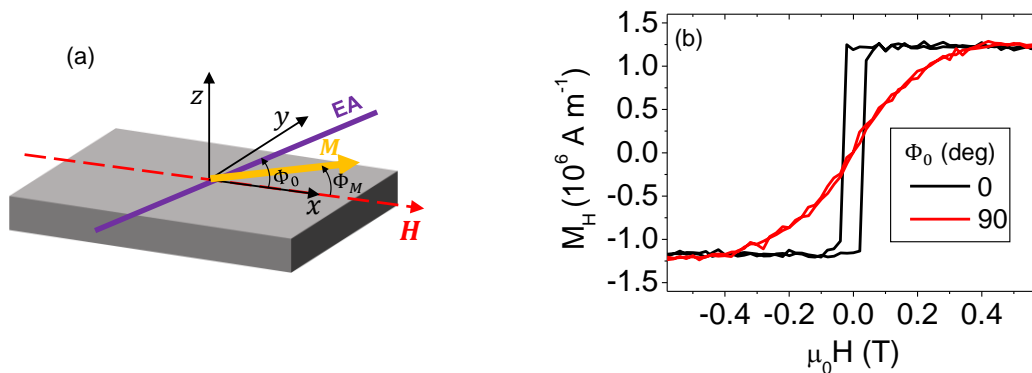
Figure 4.2 (a) Schematics of the VSM measurement geometry. The magnetic field is applied along the x axis, the angle between the applied field and the EA of the sample (purple straight line) is Φ_0, and Φ_M is the angle between the magnetization (yellow arrow) and the EA. (b) Hysteresis loops showing M_H vs. H with the field applied along the EA ($\Phi_0 = 0$ deg, black line) and perpendicular to it ($\Phi_0 = 90$ deg, red line) after the correction of a linear background related to the diamagnetic contribution of the substrate and the sample holder.

Exemplary hysteresis loops measured on a sample with a 20-nm-thick Co layer are shown in Fig. 4.2 (b), one with the field applied along the EA (black line), and another with the field applied perpendicular to the EA (red line). As expected for a macrospin-type reversal, for the EA loop the field-projected magnetization value remains constant until the magnetization switches abruptly, while for the $\Phi_0 = 90$ deg loop the magnetization vector gradually rotates exhibiting no hysteresis, so that for $H = 0$, the field-projected magnetization is zero.

For a thorough study of the orientation dependence of the M_H vs. H behavior, in-plane hysteresis loops were measured for different Φ_0 angles between the EA and the applied field axis by rotating the sample in steps of 2 deg. The measured M_H was analyzed for the decreasing field branch from the maximum applied field value down to remanence, $H = 0$. Figure 4.3 (a) shows in a color-coded

map the M_H field-projected magnetization[33] as a function of the field orientation angle Φ_0 and the field strength H.
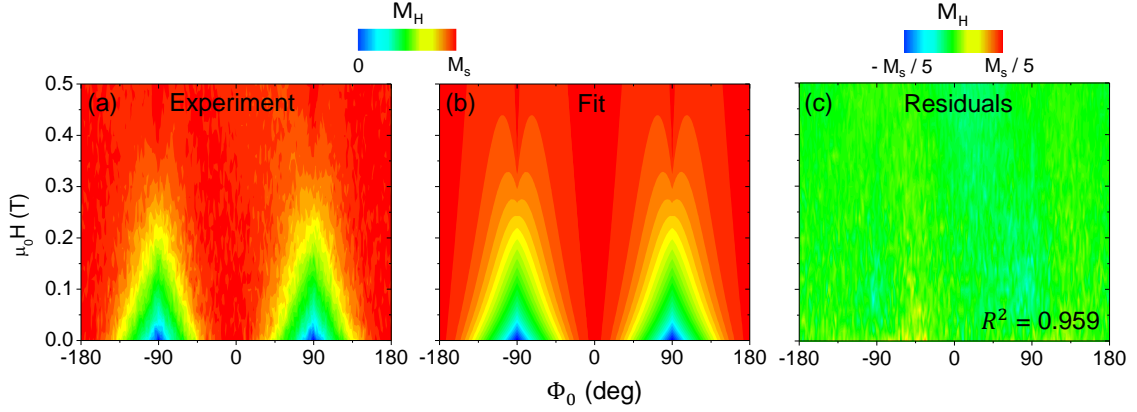

Figure 4.3 (a) Color-coded map of experimental field-projected magnetization M_H as a function of applied field orientation Φ_0 and strength H, upon decreasing the field from saturation to remanence. (b) Fit to the data in (a) minimizing Eq. (4.2). (c) Difference between the experimental and the fitted data. The color scale for (a) and (b) is displayed in between the two plots on the top. The color scale for (c) is on top of panel (c). The fitted values for M_s, K_1, and K_2 are: M_s = (1.21 ± 0.09) A·m^{-1}; K_1 = (8.0 ± 0.2) ×10^4 J·m^{-3}; K_2 = (7.0 ± 0.5) ×10^4 J·m^{-3}.

The whole H and Φ_0 dependence of M_H can be explained by a macrospin model described by the free energy that was already discussed in conjunction with Eq. (1.16):

$$\frac{\mathcal{F}}{V} = -\mu_0 H M_s \cos(\Phi_M) + K_1 \sin^2(\Phi_0 - \Phi_M) + K_2 \sin^4(\Phi_0 - \Phi_M), \qquad (4.1)$$

where Φ_M is the angle between the magnetization and the applied field axis, M_s is the saturation magnetization and K_1 and K_2 are the first and second order uniaxial anisotropy constants, with units of energy per volume unit. The equilibrium magnetization angle Φ_M is representative of the local minimum in the free energy according to Eq. (4.1) following the specific field history, *i.e.*, in the case presented here, from saturation to remanence. Equation (4.1) can be rewritten as

$$\frac{\mathcal{F}}{V} = -\mu_0 H M_s \cos(\Phi_M) - \widetilde{K}_1 \cos^2(\Phi_0 - \Phi_M) - \widetilde{K}_2 \cos^4(\Phi_0 - \Phi_M), \qquad (4.2)$$

---

[33] For the display in Fig. 4.3 and the fits, the data have been corrected. First, a vertical shift has been applied to the magnetization *vs.* field data to correct for an offset in the measured magnetic moment. In a second step, a linear fit has been performed to the data above the saturating field, and the slope has been subtracted in order to remove the diamagnetic background coming from the non-ferromagnetic materials (substrate, non-FM layers, sample holder…). Third, a sinusoidal fit was performed to the data in saturation as a function of the sample orientation to correct for an orientation-dependence of the sensitivity of the detection coils and make the signal in saturation independent of the orientation, as it should. Also, while the VSM measures the magnetic moment of the sample, the magnetization has been calculated by normalizing the magnetic moment to the magnetic volume of the sample.

where $\widetilde{K}_1 = K_1 + 2K_2$ and $\widetilde{K}_2 = -K_2$ and constant terms have been neglected. The minimization of Eq. (4.2) is achieved following the procedure given in Appendix III. Each experimental $M_H(\Phi_0, H)$ dataset is fitted with only three parameters $\widetilde{K}_1$, $\widetilde{K}_2$ and M_s, and M_s, K_1, and K_2 parameters in Eq. (4.1) are extracted from them.

Figure 4.3 (b) shows a color-coded map of the fitting of the dataset in Fig. 4.3 (a). The features present in the experimental data are reproduced very well by the fits and, despite having only three fit parameters, the agreement between experimental data and fit is excellent, as corroborated by the R^2 value shown in the bottom right hand side of Fig. 4.3 (c). The extracted K_1, K_2 and M_s are listed in the caption of Fig. 4. The difference between the measured data and the fit is shown in Fig. 4.3 (c) utilizing a different color scale. Despite using a zoom-in-scale, the differences between the experiment and the fit are very small, and therefore one can corroborate that the in-plane field strength and field orientation dependence of the stable magnetic state of the fabricated epitaxial Co samples is well described by a macrospin model.

4.3 Design and fabrication of samples with locally varying overcoat thickness

4.3.1 Design of elongated samples with position-dependent overcoat

Samples with varying Ru overcoat thickness were designed and fabricated in order to study the effect of a NM metallic overcoat onto the magnetic and MO properties of Co. For a robust and efficient fabrication process, samples with a locally varying Ru thickness were conceived, to avoid fabricating multiple samples with different Ru overcoat thicknesses where the Co base layers are not identical in their properties, and thus less comparable. To that end, 80 mm × 5 mm strips were cut from Si (110) wafers with the aim of growing samples with a Ru thickness gradient along the 80-mm-long axis of the strips, with the Co layer, and also the Ag and Cr underlayers needed to obtain single-crystal Co films, having a homogeneous thickness, as well as homogeneous structural and magnetic properties.

This design offers two technical advantages. On the one hand, a large amount of sub-samples with differing Ru thicknesses can be fabricated at the same time, with nominally the exact same base structure of Ag, Cr, and Co. On the other hand, generalized magneto-optical ellipsometry (GME)

measurements of different points on the strip can be automated thanks to the linear translation stage (LTS) implementation presented in Section 2.3, thus allowing for the investigation of a very large number of Ru thicknesses under virtually identical conditions and base layer structures.

Given the geometry of the GME LTS setup, the elongated sample is fixed in such way that the field is applied along the short axis of the strip, and therefore, the orientation of the EA of Co with respect to the applied field is fixed by the orientation of the cut of the Si wafer. The samples were designed to have the EA $\Phi_0 = -75$ deg away from the applied field axis, so that the magnetization reversal process leads to a large range of magnetization angles[34]. Thus, Si (110) wafers were cut in strips with the long axis being 15 deg away from the [001] direction, which is the direction along which the EA of Co will lie. With this procedure, the EA of Co is 75 deg away from the short axis of the strip.

4.3.2 Fabrication of samples with Ru overcoats with a thickness gradient along the long axis of the strip

In order to achieve a local variation of the Ru thickness along the strips, the sputter deposition process was performed without rotating the sample holder, as opposed to the cases where laterally homogeneous samples are fabricated. The center of the 80 mm × 5 mm Si substrate strip was aligned with the central point of the sample holder, and during the Ru deposition its long axis was aligned along the line that connects the center of the Ru target and the center of the sample holder, as illustrated in Fig. 4.4 (a). In addition, the tilt of the Ru sputter gun was altered by setting it to a more vertical position instead of making the gun face the central part of the sample holder, so that there is a difference between the Ru atom flux from one end to the other, as represented in Fig. 4.4 (b). The tilting was tuned to achieve a specific Ru thickness ratio of about 5-to-1 between one end and the other, because the intended Ru thickness range was from ~0.3 nm to ~1.5 nm of nominal thickness. In order to find the appropriate tilting for the sputter gun, thickness calibrations were performed for different tilting angles at various locations along the line of the

---

[34] See definition of Φ_0 in Fig. 4.2 (a). The specific choice of -75 deg is a bit arbitrary and represents a compromise. If the EA would be too close to the applied field direction, *i.e.*, nearly aligned with the short axis of the strip, the magnetization would undergo almost no rotation and the accessible magnetization orientation range would be very limited. On the other hand, having the EA along the long axis of the strip, so that the field would be applied along the hard axis, one could not ensure a reproducible magnetization reversal path, because both magnetization rotation senses would be equivalent.

strip. The desired gradient was obtained for a tilting angle of θ_{tilt} = 14 deg, as defined in Fig. 4.4 (b), and the rotation of the sample holder was not activated. In contrast, for the deposition of homogeneous layers θ_{tilt} = 30 deg and the sample holder was kept rotating. The power of the Ru gun was set to 75 W during deposition.
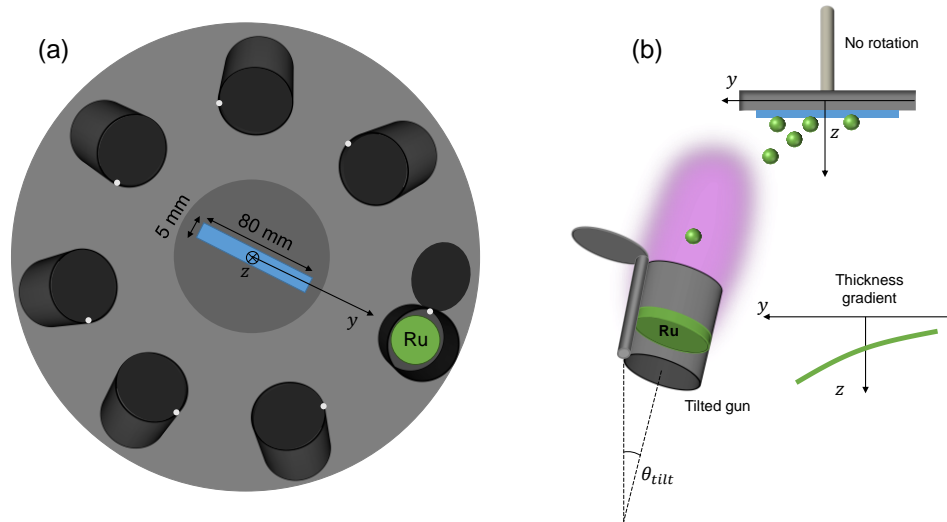

Figure 4.4 (a) Top view schematics of the main chamber of the sputtering system in the configuration for the deposition of a Ru wedge. The 80 mm × 5 mm Si strip is aligned along the y axis, which is parallel to the substrate surface and goes from the center of the strip to the vertical projection of the center of the Ru target. Guns are drawn in perspective; the closed ones are facing the center of the substrate, while the one containing the Ru target is open and is tilted towards the vertical direction. (b) Lateral view of the Ru gun and the sample holder with the Si strip. The gun is tilted towards the vertical direction, forming an angle θ_{tilt} with the z axis. More Ru atoms (green spheres) get to the $y>0$ side and a thickness gradient is achieved.

A calibration strip was fabricated using the selected θ_{tilt} and a defined alignment of the strip, which was marked for reproducibility. The resulting samples were cut in 5 mm × 5 mm pieces to perform x-ray reflectivity (XRR) measurements with the aim of determining the deposition rate at each position on the strip. Figure 4.5 shows the deposition rate (left vertical axis) measured on a calibration sample[35] with a deposition time of 1600 s. Black symbols correspond to XRR measurements and the red line is a quadratic fit to the data. The position label axis was assigned as the distance from the center of the strip to the center of each 5 mm × 5 mm piece for which the thickness was measured by means of XRR. The right vertical axis shows the position-dependent nominal thickness of a Ru wedge deposited for 18 s, based upon the calibration for the thicker wedge sample. The deposition time used for Ru in the actual samples described in Section 4.3.3

---

[35] With the XRR configuration used in this work, the precision of the thickness determination is best when the thicknesses are of the order of tens of nm. Therefore, the calibration sample for the Ru wedge was fabricated targeting thicknesses in that range; this is the reason for the long deposition time of 1600 s.

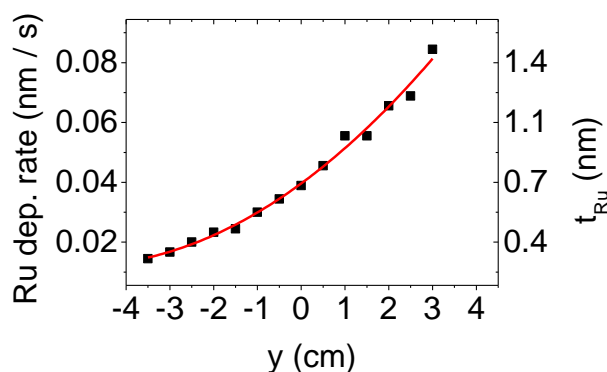was 18 s, unless otherwise stated. The wedge is fairly shallow, as the thickness gradient is about 0.1 nm·cm^{-1}.

Figure 4.5 Left vertical axis: deposition rate measured for different positions of a calibration strip with θ_{tilt} = 14 deg. Right vertical axis: expected position-dependent Ru nominal thickness for 18 s of deposition, which is the time used for the deposition of wedge-type Ru overcoats in the actual samples described in Section 4.3.3. Black squares are data points extracted from XRR measurements in the calibration sample, the red line is a quadratic fit to the data.

4.3.3 Set of samples
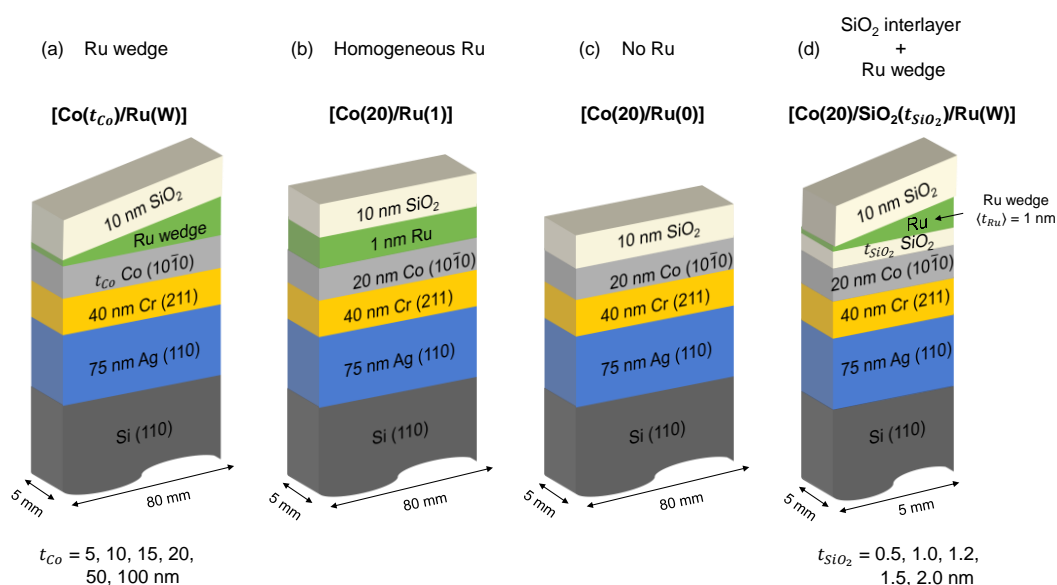
Figure 4.6 Schematic representation of the different types of samples fabricated. All have hcp Co (10$\underline{1}$0) layers grown on Si (110) substrates with templates of Ag and Cr, and all are covered with a 10-nm-thick SiO₂ layer. The name given to the different samples is indicated on top of the structures in bold. Two identical sister samples were grown in each fabrication process. Samples of type (a), (b), and (c) were deposited onto elongated strips; samples of type (d) onto smaller chips. Samples of type (a) have an obliquely deposited Ru overcoat with the thickness profile shown in Fig. 4.5 (right axis). Samples with different t_{Co} indicated on the bottom of (a) were fabricated. In the samples in (b) the Ru layer was homogeneously deposited using the same θ_{tilt} = 30 deg and sample rotation procedure used to grow the homogeneous Ag, Cr, Co and SiO₂ layers, and the Co thickness was fixed to 20 nm. In (c), no Ru overcoat was deposited and the thickness of Co was 20 nm. Samples of type (d) have a 20-nm-thick Co layer, a SiO₂ interlayer on top of it, and an obliquely deposited Ru layer with a thickness of 1 nm at the center of the chip. Different samples with varying SiO₂ interlayer thickness given at the bottom of (d) were fabricated.

The procedure explained in Section 4.2.1 was used to grow Co films with ($10\underline{1}0$) surface orientation, *i.e.*, with in-plane EA along the Si (110) [001] direction. 75-nm-thick Ag and 40-nm-thick Cr layers were grown while the sample holder was rotating and the respective guns were facing the center of the sample, with a θ_{tilt} = 30 deg. The same growth conditions were used for the Co layers of varying thickness t_{Co}. In a first set of samples, shown in Fig. 4.6 (a), Co was covered with a Ru wedge, deposited as explained in Section 4.3.2, with the position dependent thickness given by the right-hand-side axis of Fig. 4.5. Six of such samples were fabricated, namely, with t_{Co} = 5, 10, 15, 20, 50, and 100 nm. These samples are referred to as Co(t_{Co})/Ru(W), where t_{Co} is given in nm. Another sample with a homogeneous Ru overcoat deposited following the same procedure as the Ag, Cr, and Co layers was fabricated to compare the effect of homogeneous and tilted deposition. Such sample is shown in Fig. 4.6 (b). In this case, t_{Co} = 20 nm and t_{Ru} = 1 nm, and the sample is referred to as Co(20)/Ru(1). In addition, a sample without Ru overcoat and t_{Co} = 20 nm, referred to as Co(20)Ru(0) and shown in Fig. 4.6 (c), was fabricated to test the homogeneity along the 80 mm of the length of the strip. Finally, samples as the ones shown in Fig. 4.6 (d) were fabricated. In this case, 5 mm × 5 mm Si chips were used to grow 20-nm-thick Co layers, with the appropriate Ag and Cr underlayers, on top of which SiO₂ interlayers of varying thickness were grown (t_{SiO_2} = 0.5, 1.0, 1.2, 1.5, and 2.0 nm) between Co and Ru. Ru was deposited using a tilted gun, as for the samples in Fig. 4.6 (a). The substrate was placed at a position in the sample holder where the deposition led to a Ru thickness of t_{Ru} = 1 nm at the center of the chip. These samples are referred to as Co(20)/SiO₂(t_{SiO_2})/Ru(W).

All samples were covered with a 10-nm-thick SiO₂ layer to protect them from degradation and oxidation. This SiO₂ layer was deposited using RF sputtering at 100 W and 0.4 Pa of Ar pressure in a homogeneous fashion, *i.e.*, with a θ_{tilt} = 30 deg and with sample rotation.

In each sputter deposition process, two nominally identical sister samples were fabricated. Position-dependent measurements were performed using the LTS in the GME setup and GME rotational scans as a function of the angle between the EA and the applied field axis were performed on 5 mm × 5 mm cut pieces from one of the two sister strip samples Co(20)/Ru(0), Co(t_{Co})/Ru(W), and Co(20)/Ru(1).

4.4   Generalized magneto-optical ellipsometry results

4.4.1 t_{Co} = 20 nm sample without Ru overcoat

4.4.1.1 Rotational scans

In a first step GME measurements were performed on a Co sample without Ru overcoat. One of the two strips Co(20)/Ru(0) was cut into pieces, and for one of them $\frac{\delta I}{I}(\theta_2, \theta_1)$ maps were measured in the GME setup with the automated sample rotation stage for multiple values of the applied field strength H and of Φ_0, the angle of the EA with respect to the applied field axis. In the experiments here, the field is applied along the x axis, *i.e.*, the intersection between the plane of incidence and the sample plane.
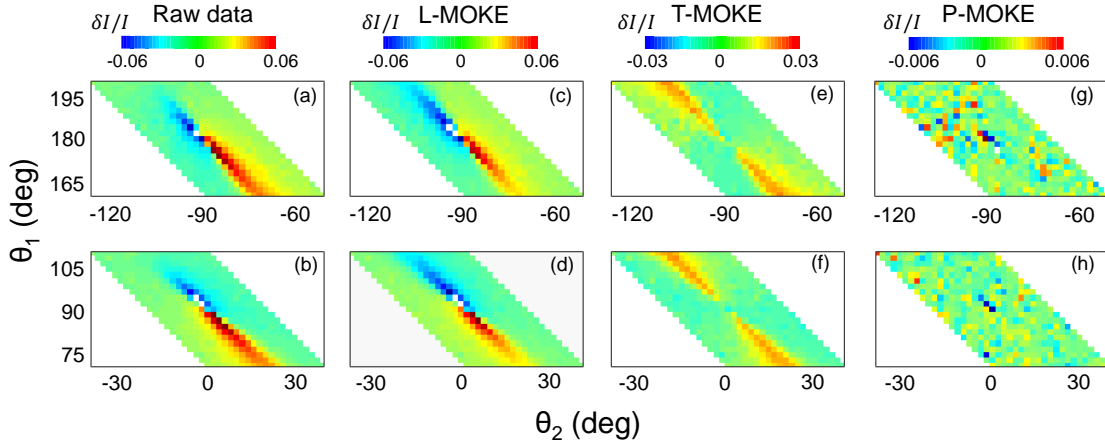
Figure 4.7 Exemplary $\frac{\delta I}{I}(\theta_2, \theta_1)$ color-coded maps with Φ_0 =35 deg and H = 0 for a piece of a Cu(20)/Ru(0) sample. (a) and (b) Measured raw $\delta I/I$ data. (c) and (d) Extracted L-MOKE signal. (e) and (f) Extracted T-MOKE signal. (g) and (h) Extracted P-MOKE signal. (a), (c), (e), and (g) show data around the *s-p* crossing point of the polarizer and the analyzer; (b), (d), (f), and (h) show data around the *p-s* crossing point. The color scale for each column is placed on top.

As an example of the measured $\frac{\delta I}{I}(\theta_2, \theta_1)$, Figs. 4.7 (a) and (b) show the maps measured for H = 0 for Φ_0 = 35 deg, around the *p-s* and the *s-p* crossing points of the polarizers respectively. By fitting these datasets with the GME fitting function in Eq. (2.9) the B_i parameters related to the reflection matrix are extracted. Using those parameters, the measured $\frac{\delta I}{I}(\theta_2, \theta_1)$ can be decomposed into three terms corresponding to each of the MOKE geometries, as shown in Eq. (2.12). This decomposition of the dataset in Figs. 4.7 (a) and (b) is shown in Figs. 4.7 (c)-(h). In particular, Figs. 4.7 (c) and (d) show the L-MOKE contribution to $\delta I/I$ with two lobes of

opposite sign meeting at the crossing point; Figs. 4.7 (e) and (f) show the T-MOKE contribution with two lobes of equal sign; and Figs. 7.7 (g) and (h) show the P-MOKE contribution, which does not show the symmetries presented in Section 2.3.3 and is only displaying random noise, indicating that the P-MOKE signal is absent.

The type of measurements shown in Figs. 4.7 (a) and (b) were performed for different field values and various Φ_0 orientations of the sample, from which the field and Φ_0 dependence of the B_i GME fit parameters was extracted. Figures 4.8 (b)-(d) show the fitted B_1, B_3, and B_5 in remanence for the decreasing field branch as a function of Φ_0. As a reminder, B_1 is related to the magnetization component along x, B_3 along y, and B_5 along z. The measured values are represented by orange squares.
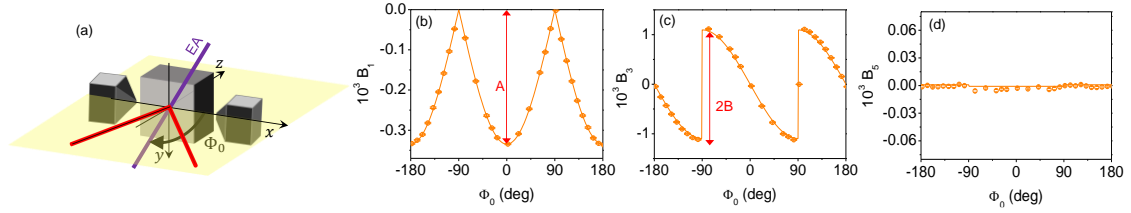

Figure 4.8 (a) Schematics of the geometry of the sample and applied field. The field is applied along the x axis with an electromagnet. The sample can rotate and thus the angle between the EA (purple line) and the x axis (angle Φ_0) can be varied. The red lines indicate the laser beam, the yellow plane is the plane of incidence. (b), (c), and (d) Φ_0-dependence of the measured GME B_1, B_3, and B_5 parameters in remanence for the decreasing field branch for a piece of a Co(20)/Ru(0) sample. The measured data points are shown as orange symbols, and orange solid lines are fits to Eq. (4.3) in (b), to Eq. (4.4) in (c), and to Eq. (4.5) in (d). The vertical double-arrowed line in (b) indicates the amplitude A of Eq. (4.3) and that in (c) twice the amplitude B of Eq. (4.4).

B_1 and B_3 correspond well to the expected rotation of a macrospin rotating in the plane of the sample, which is the behavior that is expected for this kind of samples, as already shown in Section 4.2. In remanence the magnetization lies along the EA, because in the absence of an applied field this is the configuration that minimizes the energy of the system. Given that the measurements in Fig. 4.8 were taken in the decreasing field branch, the projection of the magnetization along the x axis is positive in remanence, as the magnetization will rotate towards the side of the EA that is closest to the x axis. Hence, the B_1 data in Fig. 4.8 (b), which are related to L-MOKE and are proportional to the projection of the magnetization on the x axis, can be fitted with

$$B_1(H = 0) = A|\cos \Phi_0| . \tag{4.3}$$

The fit to the B_1 data with Eq. (4.3) is shown as a solid orange curve in Fig. 4.8 (b) and the very good agreement between the experimental values is evident. The T-MOKE component, proportional to the projection of the magnetization along the y axis, on the other hand, changes as a function of Φ_0 as follows:

$$B_3(H = 0) = \begin{cases} B\sin\Phi_0\,, |\Phi_0| \leq 90 \text{ deg} \\ -B\sin\Phi_0\,, 90 \text{ deg} < |\Phi_0| < 180 \text{ deg} \end{cases}. \tag{4.4}$$

The fit to the data in Fig. 4.8 (c) is shown as a solid orange line and the agreement with the measurements is again excellent. B_2 and B_4 (not shown here) are also described very precisely by Eqs. (4.3) and (4.4), respectively, with their corresponding amplitudes being A' and B'.

Finally, Fig. 4.8 (d) shows that the measured P-MOKE component is negligible in remanence and that, therefore, the magnetization is in the plane of the sample for all Φ_0 values, in agreement with what is expected for this sample having in-plane uniaxial and shape anisotropy, and with the observed P-MOKE contribution to the $\delta I/I$ signal shown in Figs. 4.7 (g) and (h) for the specific value of Φ_0 = 35 deg.

4.4.1.2 Homogeneity along the strip: linear translation stage measurements
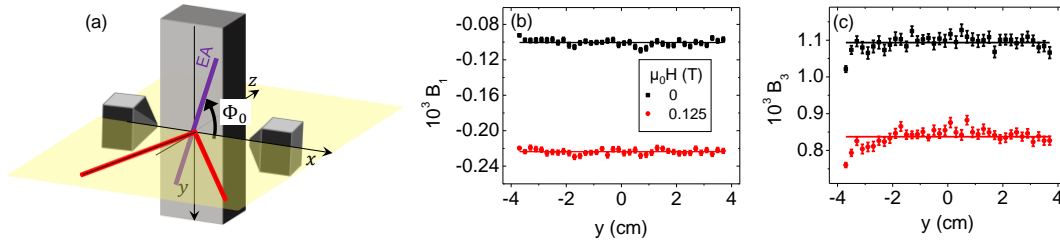

Figure 4.9 (a) Schematics of the geometry of the applied field, along the x axis, and the alignment of the sample, with the EA at Φ_0 = - 75 deg. The sample can be moved vertically with an automated stage so that the laser beam (red lines) hits different y points of the sample, at which GME measurements are performed. (b) and (c) B_1 and B_3, respectively, for applied field strengths of H = 0 (remanence) as black squares, and $\mu_0 H$ = 0.125 T, as red circles, as a function of y, where y = 0 is the center of the sample. The horizontal lines represent the average of the data, demonstrating that no significant variation is observed along the length of the sample.

In order to test the homogeneity of the Co layer, the uncut Co(20)/Ru(0) sample was characterized by means of GME with the LTS setup, as shown in Fig. 4.9 (a). The B_i GME fitting parameters were retrieved at different positions along the y axis. Figures 4.9 (b) and (c) show the values of B_1 and B_3 respectively as a function of the position of the measurement, in remanence (in black

squares) and at $\mu_0 H = 0.125$ T (in red circles). Horizontal black and red lines display the average value of each of the datasets and stress that the B_1 and B_3 values for the two different field values are stable over the whole length of the strip, thus indicating that the MO properties of Co are homogeneous along the whole sample. In thesemeasurements the EA is always at an angle $\Phi_0 = -75$ deg from the applied field axis. In that regard, the measured remanence values in Figs. 4.9 (b) and (c) fully agree with the values measured in the rotational scans for the same orientation of the EA shown in Figs. 4.8 (c) and (d). B_5, corresponding to P-MOKE, is not shown, because its contribution is negligible, just as demonstrated already in Fig. 4.8 (d). The rest of the GME parameters are also virtually constant along the y axis, with a variance in the range of the third significant digit, as shown in Table 4.1. Magnetic properties are also uniform along the sample, as corroborated by field-dependent measurements (not shown here).

These measurements prove the high degree of homogeneity of the magnetic and MO properties of the Co layer along the 80 mm of the strip. Given that the Co layer in all the strip samples shown in Figs. 4.6 (a), (b), and (c) was fabricated following the same procedure, changes observed in strips with a Ru overcoat are to be ascribed to the presence of Ru and not to position-dependencies of the properties of Co.

Parameter	Mean value in remanence	Variance in remanence
B_1	-1.00×10^{-4}	0.03×10^{-4}
B_2	1.95×10^{-4}	0.07×10^{-4}
B_3	1.09×10^{-3}	0.02×10^{-3}
B_4	-1.88×10^{-4}	0.04×10^{-3}
B_7	1.37	0.01
B_8	-1.107	0.004

Table 4.1 Mean value and variance of B_i GME fit parameters along the Co(20)/Ru(0) strip.

4.4.2 Effect of obliquely deposited 1-nm-thick Ru overcoat

4.4.2.1 Experimental observations in remanence

To study the effect of the Ru overcoat, one of the two Co(20)/Ru(W) samples was cut into pieces. In this subsection, the piece that has a nominal Ru thickness of 1 nm at is center is studied in detail. Other pieces with different Ru thickness are studied in Section 4.4.3. Following the same procedure as in Section 4.4.1, GME $\frac{\delta I}{I}(\theta_2, \theta_1)$ maps were measured. In analogy to Fig 4.7,

Fig. 4.10 shows exemplary $\frac{\delta I}{I}(\theta_2, \theta_1)$ maps in (a) and (b), measured in remanence for $\Phi_0 = 40$ deg, and the corresponding L-, T-, and P-MOKE contributions in the subsequent columns. As opposed to the case in Fig. 4.7 for the Co(20)/Ru(0) sample, a non-vanishing P-MOKE signal is present, as observed in Figs. 4.10 (g) and (h). At this juncture the importance of performing $\delta I/I$ measurements at two non-equivalent crossing points of the polarizers becomes apparent: while $\delta I/I$ has lobes of opposite signs meeting at the crossing point of the polarizers in Figs. 4.10 (c), (d), (g), and (h), the symmetries of L- and P-MOKE are different. For instance, L-MOKE has the negative (blue) lobe below the diagonal of the map for the *s-p* crossing point (in Fig. 4.10 (c)), and above the diagonal for the *p-s* crossing point (in Fig. 4.10 (d)), whereas P-MOKE has the negative (blue) lobe below the diagonal in both cases in Figs. 4.10 (g) and (h). Such symmetries, related to the symmetry elements σ_1 and σ_2 discussed in Section 2.3.3, allow for an unambiguous separation of L- and P-MOKE.
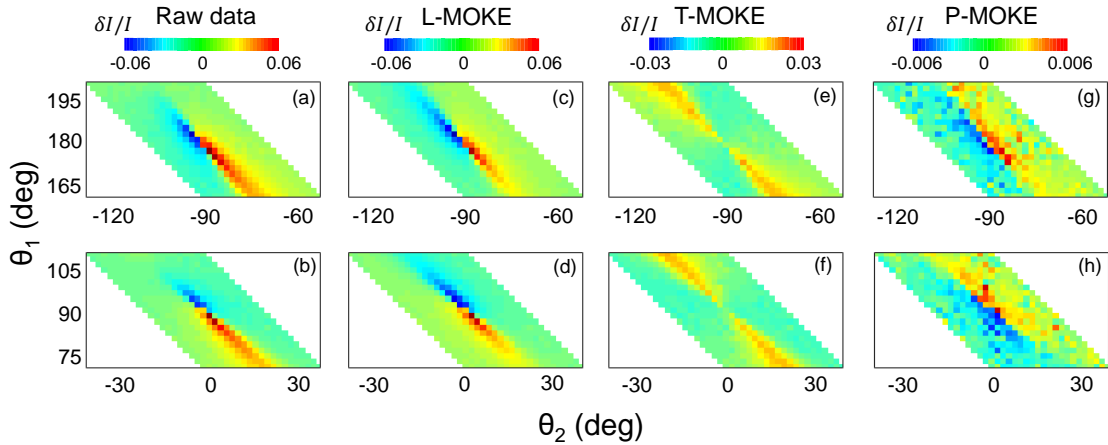

Figure 4.10 Exemplary $\frac{\delta I}{I}(\theta_2, \theta_1)$ color-coded maps for $\Phi_0 = 40$ deg and $H = 0$ of a piece of a Cu(20)/Ru(W) sample with a Ru thickness of 1 nm at the center of the piece. (a) and (b) Measured raw $\delta I/I$ data. (c) and (d) Extracted L-MOKE signal. (e) and (f) Extracted T-MOKE signal. (g) and (h) Extracted P-MOKE signal. (a), (c), (e), and (g) show data around the *s-p* crossing point of the polarizer and the analyzer; (b), (d), (f), and (h) show data around the *p-s* crossing point. The color scale for each column is placed on top.

$\frac{\delta I}{I}(\theta_2, \theta_1)$ were measured and B_i parameters were obtained for different field values H and sample orientations Φ_0. Figure 4.11 shows the extracted B_1, B_3, and B_5 in remanence as a function of Φ_0 with black symbols. The results for B_1 in Fig. 4.11 (b) and for B_3 in Fig. 4.11 (c) are compatible with those measured for the sample without the Ru overcoat and were fitted with Eqs. (4.3) and (4.4), respectively. However, one observes in Fig. 4.11 (d) a P-MOKE component B_5 that is clearly detectable and larger than the error bar despite being about one order of magnitude smaller than

B_1, in agreement with the observed P-MOKE signal in Figs. 4.10 (g) and (h). In addition, B_5 has a specific step-like behavior as a function of Φ_0 that can be described as

$$B_5(H = 0) = \begin{cases} C\,, |\Phi_0| \leq 90 \text{ deg} \\ -C, 90 \text{ deg} < |\Phi_0| < 180 \text{ deg} \end{cases}.$$ (4.5)

The fit of the B_5 data to Eq. (4.5) is displayed as a solid black line in Fig. 4.11 (d), showing excellent agreement with the experimental data. B_6, which is not shown here, also behaves according to Eq. (4.5) while exhibiting a different amplitude factor C'.
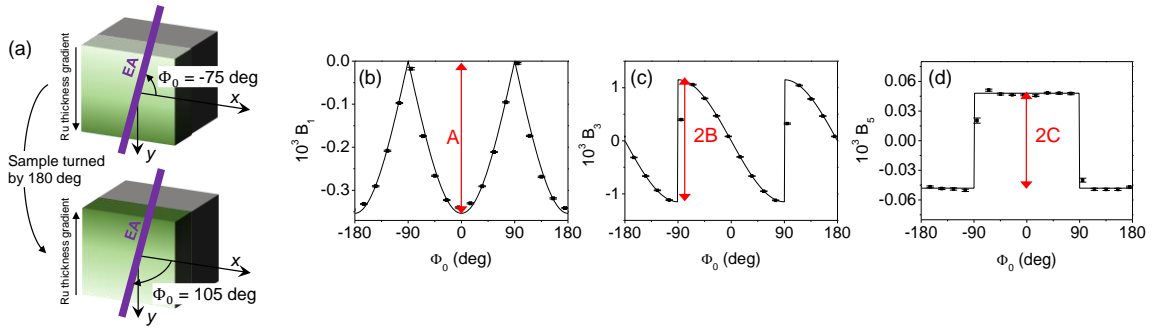
Figure 4.11 (a) Definition of the reference point for Φ_0 with respect to the direction of the Ru thickness gradient, as the 180 deg symmetry is broken by the graded deposition of Ru. (b), (c), and (d) Φ_0-dependence of the measured GME parameters B_1, B_3, and B_5 in remanence for a piece of a Co(20)/Ru(W) sample with a Ru thickness of 1 nm at the center of the piece. The measured data points are shown as black symbols, and black solid lines are fits to Eq. (4.3) in (b), to Eq. (4.4) in (c), and to Eq. (4.5) in (d). The vertical double-arrowed line in (b) indicates the amplitude A of Eq. (4.3), that in (c) twice the amplitude B of Eq. (4.4), and that in (d) twice the amplitude C of Eq. (4.5).

While B_1 and B_3 have a 180 deg periodicity in Φ_0, B_5 has a 360 deg periodicity, which is compatible with the geometry of the sample because the graded Ru overcoat causes the breaking of the symmetry of the sample by a 180 deg rotation, as shown in Fig. 4.11 (a). On the contrary, the piece belonging to the Co(20)/Ru(0) sample analyzed in Fig. 4.8 has such symmetry and therefore, it cannot show a P-MOKE signal as the one in Fig. 4. 11 (d). With the loss of the 180 deg rotation symmetry it becomes relevant to define precisely the Φ_0 angle and the corresponding references for this are given in Fig. 4.11 (a). When the sample is oriented with the Ru thickness gradient in such way that the thinner Ru part is on top, as in the top figure in Fig. 4.11 (a), the angle of the EA with the x axis is defined to be Φ_0 = -75 deg. When the sample is turned by 180 deg, as in the bottom figure in Fig. 4.11 (a), Φ_0 = 105 deg.

4.4.2.2 Tilted easy axis model

The observation of a polar component of MOKE is incompatible with the expected in-plane character of the remanent magnetization. The specific Φ_0-dependence observed for B_5 points to a small out-of-plane tilt of the EA, as sketched in Fig. 4.12. Such a model breaks the 180 deg symmetry of the in-plane uniaxial anisotropy axis as follows. In the situation represented in Fig. 4.12 (a), when coming from a positive H applied along the x axis, the remanent magnetization (yellow arrow) will have an $m_z > 0$ component. Upon a 180 deg rotation of the sample, the remanent magnetic state coming from a $H > 0$ state will lead to a $m_z < 0$ component, as shown in Fig. 4.12 (b), while the in-plane components m_x and m_y are unaltered. This is consistent with the 180 deg periodicity in the L- and T-MOKE signals in Figs. 4.11 (a) and (b), and with the 360 deg periodicity in the P-MOKE signal in Fig. 4.11 (c).
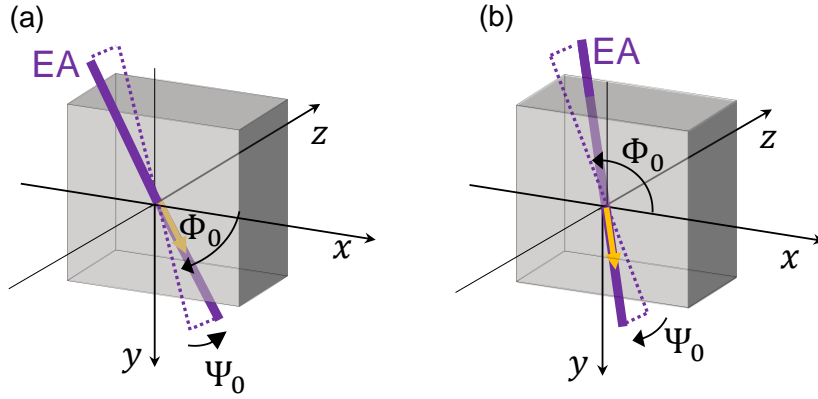

Figure 4.12 Schematics of the tilted EA model showing the Cartesian axes in black, the EA in purple, and the angles describing the orientation of the EA Φ_0 and Ψ_0. The yellow arrows show the magnetization vector in remanence after the application and subsequent removal of an external magnetic field along the positive x axis. Upon a 180 deg rotation of the sample the out-of-plane tilt Ψ_0 changes sign, and so does the z component of the remanent magnetization.

In order to verify that an out-of-plane tilted EA would lead to the rotational dependence of L-, T-, and P-MOKE observed in Fig. 4.11, a model was derived, based on the minimization of the free energy of a macrospin with an EA that is not in the plane of the sample and a term for the demagnetizing energy, described by the free energy expression

$$\frac{\mathcal{F}}{V} = -\hat{\boldsymbol{m}} \cdot \tilde{\boldsymbol{h}} + K_1(1 - (\hat{\boldsymbol{m}} \cdot \hat{\boldsymbol{e}})^2) + K_d(1 - (\hat{\boldsymbol{m}} \cdot \hat{\boldsymbol{z}})^2) \,. \tag{4.6}$$

The first term in Eq. (4.6) is the Zeeman energy, where $\tilde{h}$ is related to the external magnetic field. The second is the first order uniaxial magneto-crystalline anisotropy (MCA) energy which, with $K_1 > 0$, promotes the alignment of the magnetization along the EA, whose unit vector is

$$\hat{e} = (\cos \Phi_0 \cos \Psi_0, \sin \Phi_0 \cos \Psi_0, \sin \Psi_0). \qquad (4.7)$$

The shape anisotropy is represented as an easy-plane anisotropy with $K_d < 0$; z is thus a hard axis and the magnetization is energetically favored to lie in the xy plane. In the model here, $\tilde{h}$ ranges from 0.3 to -0.3, $K_1 = 0.2$, and $K_d = -0.6$. As for the macrospin model described in Section 4.2.3, the minimization of the energy should be performed self-consistently. With such a model, the components of the magnetization along the three Cartesian axes m_x, m_y, and m_z were calculated for two different tilts of the EA given by Ψ_0. Fig. 4.13 shows their values in remanence, as a function of the in-plane angle of the EA Φ_0, for two values of Ψ_0, namely -1 deg and -3 deg.

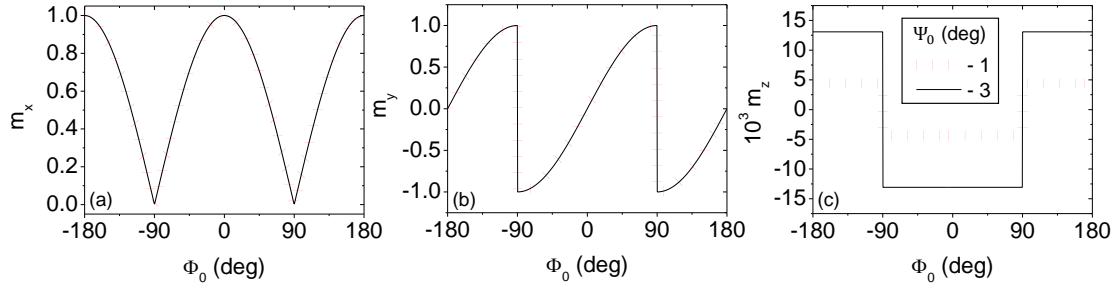Figure 4.13 Φ_0-dependence of the remanent components of the magnetization along the x, y, and z axes, in (a), (b), and (c), respectively, calculated for the tilted EA model with $K_1 = 0.2$ and $K_d = -0.6$. The Φ_0 orientation of the EA is scanned in the plots, while Ψ_0 is fixed; data for $\Psi_0 = -1$ deg are shown dotted red lines and for $\Psi_0 = -3$ deg as black solid lines. In each case, the remanent state is achieved after the application of a positive external magnetic field along the positive x axis and its subsequent removal.

In order to calculate the MO response in remanence of a sample that has a Co layer whose magnetization is given by a minimization of Eq. (4.6), two optical models were designed and the corresponding reflection matrix was calculated by means of the transfer matrix method described in Section 2.5. In the first place, a multilayer model with all the layers present in the sample was considered. As shown in Fig. 4.14 (a), the thickness of each layer in the model was taken to be equal to its nominal thickness. The optical constants considered for each of the layers were taken from literature: for SiO₂, $N = 1.457$ [40]; for Ru, $N = 2.78 + 3.86\,i$ [41]; for Co, $N = 2.474 + 4.075\,i$ [42]; for Cr, $N = 3.1357 + 3.3171\,i$ [43]; for Ag, $N = 0.055738 + 4.2931\,i$ [44]; for Si, $N = 3.8787 + 0.019221\,i$ [45]. An incidence angle of 45 deg and a wavelength of 635 nm were assumed in the calculation. The MO coupling constant of Co was used as a free fit parameter to match the

observed B_1 and B_3 (see Figs. 4.8 (b) and (c)), yielding Q_{MO} = 0.02423 − 0.00650 i. The only magneto-optically active layer was considered to be Co, whose magnetization in remanence was calculated by minimizing the free energy expression in Eq. (4.6) with $\tilde{h}$ = 0. Agreement between the experimental B_5 data and the computed one was achieved with an out-of-plane tilt of the EA Ψ_0 = -3 deg (see Fig. 4.14 (e)).
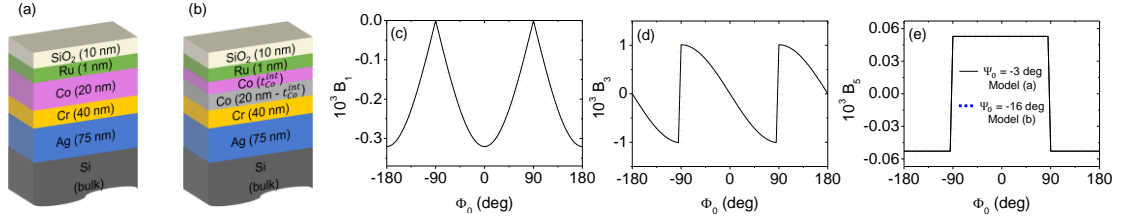

Figure 4.14 (a) and (b) Multilayer models for which the reflection matrix was calculated using the transfer matrix method described in Section 2.5 with the optical and MO constants given in the main text. (a) has a single Co layer (pink), with an EA tilted out-of-plane by an angle Ψ_0. (b) has a 2-nm-thick interfacial Co layer with out-of-plane tilted EA (pink), and a 18-nm-thick Co layer with in-plane EA (gray). (c), (d), and (d) show the calculated B_1, B_3, and B_5 in remanence as a function of Φ_0. The results that are shown correspond to the case where model (a) has Ψ_0 = -3 deg (black curves) and model (b) has Ψ_0 = -16 deg (blue dotted curves) and yield compatible B_1, B_3, and B_5 values.

However, this model is not very realistic because, if it is the 1-nm-thick Ru overcoat that is creating the anomalous polar component in the magnetization, its effect cannot extend to the whole 20-nm-thick Co layer. It is more sensible to assume that the affected Co is limited to the interface region. Based upon this assumption, a second model was designed, which separates the Co layer in two subsection: an interfacial Co layer of thickness t_{Co}^{int} with an out-of-plane tilted EA with $\Psi_0 \neq 0$ and a Co layer of thickness (20 nm - t_{Co}^{int}) with in-plane EA, *i.e.*, Ψ_0 = 0. The magnetization in each Co layer was calculated minimizing Eq. (4.6). The choice of t_{Co}^{int} is somewhat arbitrary in the model and the possibility that the interfacial Co layer has N and Q_{MO} different from the in-plane magnetized Co layer is not considered in this simplistic model[36]. With t_{Co}^{int} = 2 nm, an out-of-plane tilt of the EA by Ψ_0 = -16 deg is necessary in the interfacial Co to reproduce the experimentally observed B_5 values, as shown in Fig. 4.14 (e) as dotted blue lines, but it should not be forgotten that some of the physical properties assumed, such as the MO coupling in the

---

[36] Also, a more sophisticated model would include a depth dependent tilt of the EA, but would only provide a quantitative improvement and the physics would remain the same.

interfacial region, may not be in agreement with real values, so that the actual Ψ_0 values of the hypothetical EA tilt are not necessarily given by the values obtained in the calculation here.

4.4.2.3 Field-dependent observations

The orientation-dependence of the L-, T-, and P-MOKE components in Fig. 4.11 appears to be in agreement with a Ru overcoat-induced out-of-plane tilt of the EA of Co. However, for a verification of the model it is necessary that it also explains the field dependence of the various MOKE components. The free energy expression in Eq. (4.6) has been minimized for different values of h and different orientations of the applied field.

The first column in Fig. 4.15 shows field-dependent experimental measurements of B_1, B_3, and B_5 for different in-plane orientations of the sample. The second column shows the field-dependent B_1, B_3, and B_5 calculated for the optical model shown in Fig. 4.14 (b) using the magnetization components calculated by minimizing Eq. (4.6). By looking at Figs. 4.15 (a) and (b), one can see that B_1 is the same for Φ_0= -30 deg, 30 deg, -150 deg, and 150 deg, while the data are also very similar for Φ_0= -60 deg and 60 deg with respect to each other. By fitting the slope of the $B_1(H)$ curves around remanence for all measured Φ_0 orientations, the experiments yield the $dB_1/d(\mu_0 H)$ data shown in Fig. 4.15 (c), which are in qualitative agreement with the Φ_0-dependence of the B_1 slope obtained from the model calculations that are shown in Fig. 4.15 (d).

In a similar fashion, experimental field-dependent B_3 values are shown in Fig. 4.15 (e). In this case, the data for $\Phi_0 = -30$ deg and -150 deg are identical, but different from the $\Phi_0 = 30$ deg and 150 deg cases, because B_3 is related to T-MOKE, *i.e.*, to the m_y magnetization component, which changes sign upon changing the sign of Φ_0. Field-dependent B_3 data computed for the tilted EA model and shown in Fig. 4.15 (f) are also in very good agreement with the experimental observations. In both the experiment and the model, the absolute value of B_3 decreases upon increasing H, because the field is applied along the x axis and the magnetization rotates towards it, giving rise to a decrease in m_y. A linear fit of the $B_3(H)$ curves close to remanence verifies that the orientation dependence of the B_3 slope for the modelling data, shown in Fig. 4.15 (h), shows the same behavior and symmetries as the experimentally measured slope, shown in Fig. 4.15 (g).
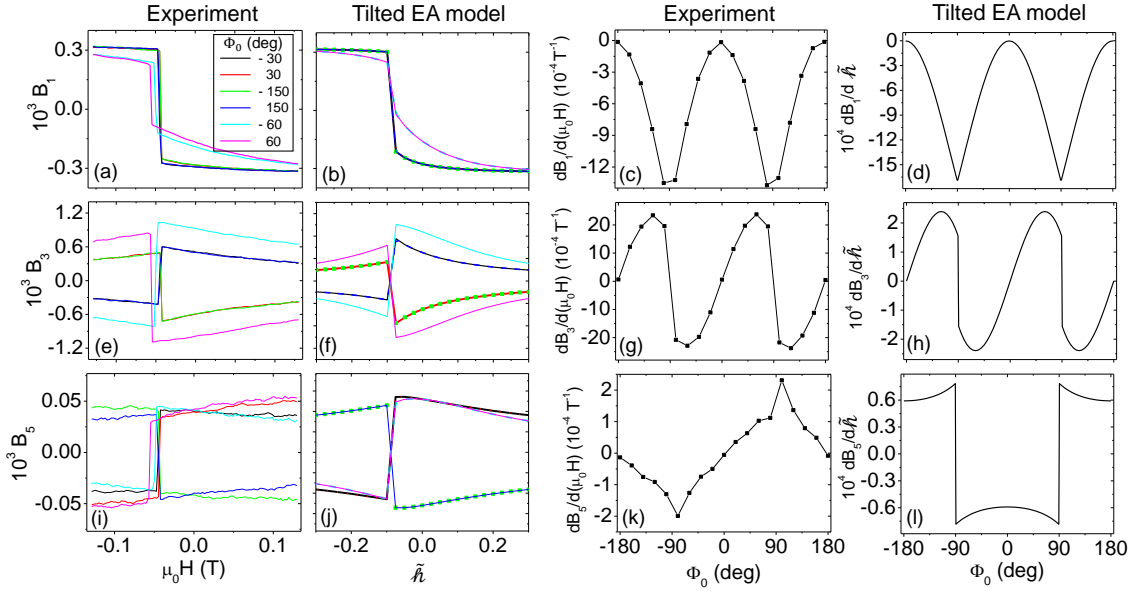
Figure 4.15 First column ((a), (e), and (i)): Experimental results of B_i parameters as a function of the applied field strength for different orientations of the EA with respect to the x axis. Legend in (a). Second column ((b), (f), and (j)): Field-dependence of B_i parameters calculated for the optical model in Fig. 4.14 (b) with $\Psi_0 = -16$ deg in the interfacial Co layer. Legend in (a). Third column ((c), (g), and (k)): Slope of the experimental $B_i(H)$ parameters around the $H = 0$ point as a function of the orientation of the EA with respect to the x axis. Data points are shown as black symbols, the solid line is a guide to the eye. Fourth column ((d), (h), and (l)): Same type of data as in the third column extracted from the computation results using the optical model. The first row is related to B_1, the second to B_3, and the third to B_5. Experimental data are for a piece of a Co(20)/Ru(W) sample with a Ru thickness of 1 nm at the center of the piece.

In the case of the field dependence of B_5, the tilted EA model, as shown in Fig. 4. 15 (j), gives rise to identical curves for opposite orientations $\pm\Phi_0$. However, the experimental data, shown in Fig. 4.15 (i), reveal a fundamental difference between the field-dependence of B_5 for $\Phi_0 = -30$ deg and 30 deg, $\Phi_0 = -150$ deg and 150 deg, and $\Phi_0 = -60$ deg and 60 deg. For the tilted EA model data, the absolute value of B_5 decreases from its remanence value as H increases in all Φ_0 cases, related to a decrease in the polar component of the magnetization once an in-plane oriented field is applied. In contrast, in the experimental data, the absolute value of B_5 near H=0 increases for some values of Φ_0 and decreases for others. The experimental slope of B_5 is actually antisymmetric with respect to $\Phi_0 = 0$ deg, as shown in Fig. 4.15 (k), while the data computed for the tilted EA model are symmetric. Therefore, despite the excellent agreement between the experiment and the tilted EA model for the remanence data, the field-dependent measurements reveal that a Ru-overcoat induced out-of-plane tilt of the EA cannot explain the overall observed anomalous P-MOKE behavior.
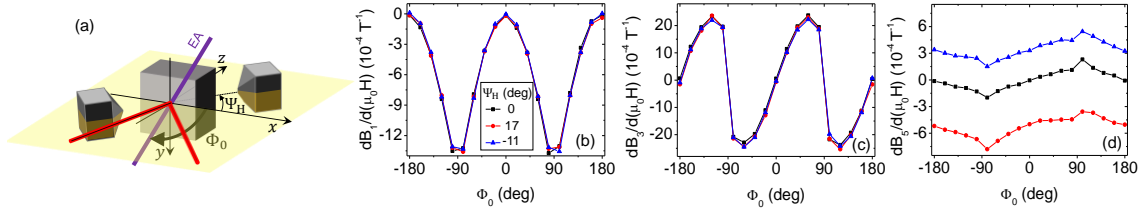
4.4.2.4 Out-of-plane tilted field

Figure 4.16 (a) Schematics of the geometry of the sample and applied field. The field is applied in the xz plane, forming an angle Ψ_H with the x axis. (b), (c), and (d) Φ_0-dependence of the field-dependent slope near remanence of experimentally measured $B_1(H)$, $B_3(H)$, and $B_5(H)$. Data points are shown as symbols, the solid lines are guides to the eye. Black points correspond to measurements performed with $\Psi_H = 0$, red points with $\Psi_H = 17$ deg, and blue points with $\Psi_H = -11$ deg. Measured sample: a piece of a Co(20)/Ru(0) sample with a Ru thickness of 1 nm at the center of the piece.

For the purpose of gaining a better understanding of the unexpected P-MOKE signals, experiments with an out-of-plane tilted applied field were carried out. Figure 4.16 (a) shows schematically the geometry of the experiment, with the applied field forming an angle Ψ_H with the x axis. In remanence, the GME parameters are the same as in Fig. 4.11. Their field dependence, however, depends on the alignment of the applied field. Figures 4.16 (b)-(d) show the slope of the $B_i(H)$, with $i = 1$, 3, and 5 in (b), (c), and (d), respectively. While the slopes of B_1 and B_3 are basically independent of Ψ_H for the small Ψ_H values utilized in the experiment, B_5, related to the out-of-plane component of the magnetization, has a strong dependence with Ψ_H. Still, the shape observed for $\Psi_H = 0$ in Fig. 4.15 (k) is preserved and only a vertical shift of the curves occurs, with an opposite sign for Ψ_H values of opposite sign. The tilted EA model also shows the experimentally observed shift of the slope for $m_z(H)$ but again, the Φ_0-dependence of the slope does not respect the experimentally observed symmetries.

4.4.3   Varying Ru thickness

4.4.3.1 Rotational scans

More of the 5 mm × 5 mm pieces obtained from the cut Co(20)/Ru(W) strip were analyzed in addition to the one with a central Ru thickness of 1 nm already analyzed in Section 4.4.2, to study the Ru thickness dependence of the anomalous P-MOKE.

With the same procedure as in Section 4.4.2, $B_i(H)$ parameters were obtained for various pieces as a function of Φ_0. Figures 4.17 (a)-(c) show, respectively, the values of B_1, B_3, and B_5 in

remanence for samples having different Ru thicknesses. Also added to the datasets, one can find in orange the data corresponding to the piece of Co(20)/Ru(0) measured in Section 4.4.1, and the data corresponding to the Co(20)/Ru(W) piece with 1-nm-thick central Ru thickness. As shown in Fig. 4.17 (a), B_1 increases slightly with increasing Ru thickness[37]. B_3, in turn, is independent of t_{Ru}, and the strongest Ru thickness-dependence is observed in the polar component B_5, as observed in Fig. 4.17 (c). The amplitude of B_5 clearly increases with t_{Ru}, although for the highest t_{Ru} values the effect seems to saturate. The curves in Fig. 4.17 (a)–(c) were fitted utilizing Eqs. (4.3)-(4.5) to extract the amplitudes of B_1, B_3, and B_5, A, B, and C respectively.
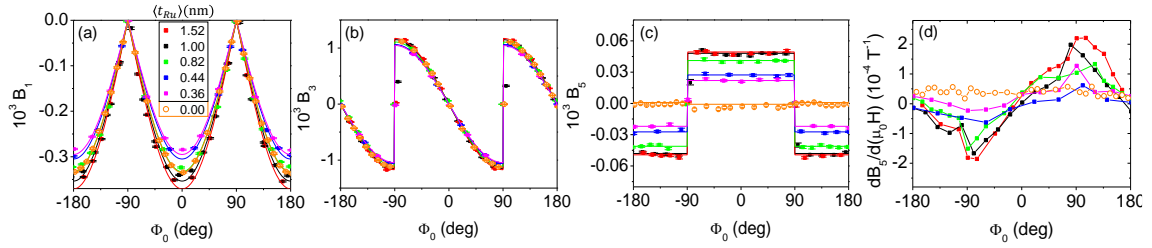

Figure 4.17 Φ_0-dependence of the measured remanent B_1, B_3, and B_5, in (a), (b), and (c), respectively, for different pieces of a Co(20)/Ru(W) sample with different Ru thicknesses. The thickness of Ru is indicated *via* the legend in (a) with the values corresponding to the nominal Ru thickness at the central position of the piece. Data for zero Ru thickness are taken from a piece of a Co(20)/Ru(0) sample and has already been shown in Fig. 4.8. The measured data points are shown as symbols, and solid lines are fits to Eq. (4.3) in (a), to Eq. (4.4) in (b), and to Eq. (4.5) in (c). (d) Orientation dependence of the field-dependent slope of $B_5(H)$ for the different Co thicknesses given by the legend in (a). Lines in (d) are a guide to the eye.

Figure 4.17 (d) shows the field-dependent slope of B_5 as a function of Φ_0. While the slopes of B_1 and B_3 (not shown) are virtually independent of the Ru thickness and thus nearly identical to Figs. 4.15 (c) and (g), respectively, Fig. 4.17 (d) shows that the shape of $dB_5/d(\mu_0 H)$ *vs.* Φ_0 observed in Fig. 4.15 (k) for Co(20)/Ru(W) with $t_{Ru} = 1$ nm is preserved for all t_{Ru} values, and only the amplitude varies, with smaller amplitude for lower t_{Ru} values and a saturation effect at higher t_{Ru} of the order of 1 nm. Thus, this asymmetric P-MOKE slope that cannot be reproduced by the tilted EA model is a reproducible effect for all Ru thicknesses.

---

[37] The data corresponding to Co(20)/Ru(0) falls out of the trend, which could be simply related to a sample-to-sample variation of the Co properties, as this piece belongs to a different sample, while all the others were obtained from the same Co(20)/Ru(W) strip.

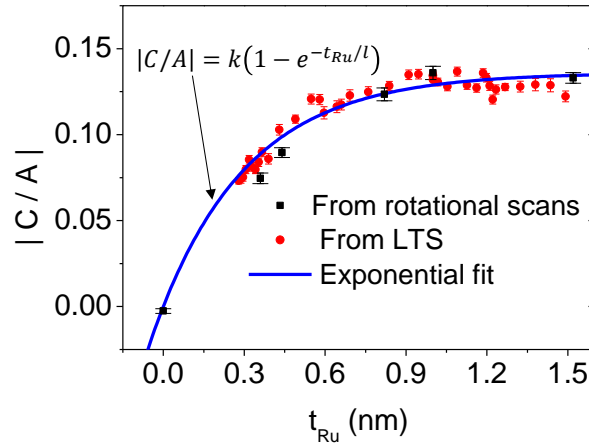## 4.4.3.2 Position-dependent measurements with fixed orientation of the easy axis

Figure 4.18 Absolute value of the ratio between C, the amplitude of B_5 given by Eq. (4.5) and A, the amplitude of B_1 given by Eq. (4.3), as a function of the Ru overcoat thickness of the Co(20)/Ru(W) sample. The t_{Ru} = 0 nm reference data point was measured for a Co(20)/Ru(0) sample (data shown in Fig. 4.8 and Fig. 4.17). Black symbols correspond to the orientation-dependent measurements shown in Fig. 4.17. Red symbols corresponds to data of position-dependent scans with the LTS with fixed EA orientation for an uncut Co(20)/Ru(W) sample. The blue line is a fit to the function shown in the figure, yielding k = 0.136 ± 0.004 and l = (0.34 ± 0.03) nm.

The Co(20)/Ru(W) sister sample that was left uncut was measured with GME utilizing the LTS implementation of the sample holder. GME maps were measured at different positions of the strip, corresponding to different values of t_{Ru} as determined *via* the calibration curve in Fig. 4.5. B_i parameters for each Ru thickness were extracted as a function of the applied field strength. The field was applied along the x axis. The orientation of the EA with respect to the applied field axis is Φ_0 = -75 deg in all cases, with the part of the Ru wedge with less Ru at the top (y < 0), and the thicker part at the bottom (y > 0) (see Fig. 4.11 (a)). To compare the position-dependent measurements with the rotational scans, the polar-to-longitudinal MOKE ratio $|C/A|$ was calculated, which is indicative of the size of the out-of-plane magnetization. In order to do so, A, the amplitude of B_1 as defined by Eq. (4.3) was calculated by dividing by $\cos \Phi_0$ the B_1 value measured in remanence for each position of the strip. C was taken to be the measured B_5 value in remanence at each position. The resulting $|C/A|$ data are plotted as red dots in Fig. 4.18. The $|C/A|$ data corresponding to the rotational scans is obtained from the fitting of the data in Figs. 4.17 (a) and (c) and are displayed as black symbols in Fig. 4.18. The data from both types of measurements are in excellent agreement with each other and both show a Ru thickness-dependence of the polar-to-longitudinal-MOKE ratio, with a clear saturation effect. The Ru

thickness dependence was fitted with a function of the form $|C/A| = k\left(1 - e^{-t_{Ru}/l}\right)$, yielding a value of $l = (0.34 \pm 0.03)$ nm. Thus, the lengthscale in which the out-of-plane component of the magnetization develops is of the order of one monolayer of Ru.

4.4.4 Homogeneous Ru thickness

As shown in Fig. 4.6 (b), two sister samples with a 1-nm-thick Ru overcoat homogeneously deposited onto 20-nm-thick Co were also fabricated, labeled as Co(20)/Ru(1). One of them was cut in pieces and GME rotational scans were performed. Figure 4.19 compares the orientation-dependent remanent B_1, B_3, and B_5 measured in Section 4.4.2 for the sample with 1-nm-thick Ru overcoat deposited in an oblique fashion (black data points) with the ones measured for the sample with homogeneous Ru overcoat (pink data points). While there is an excellent match in the longitudinal and transverse signals in Figs. 4.19 (a) and (b) respectively, the B_5 component of the sample with the homogeneous Ru layer indicates that there is basically no polar magnetization component, while a most significant presence of a P-MOKE component is evident in the case of the sample with obliquely deposited Ru overcoat. This fact was verified by the fabrication and characterization of further samples with both kinds of Ru layers, to corroborate that the observations are not due to anomalies in the fabrication of just one specific sample, and it was established that hcp Co (10$\underline{1}$0) samples with homogeneously deposited Ru overcoats show no significant P-MOKE, while a Ru-thickness dependence P-MOKE signal arises when the Ru overcoat is deposited as a wedge, even if the wedge is extremely flat.
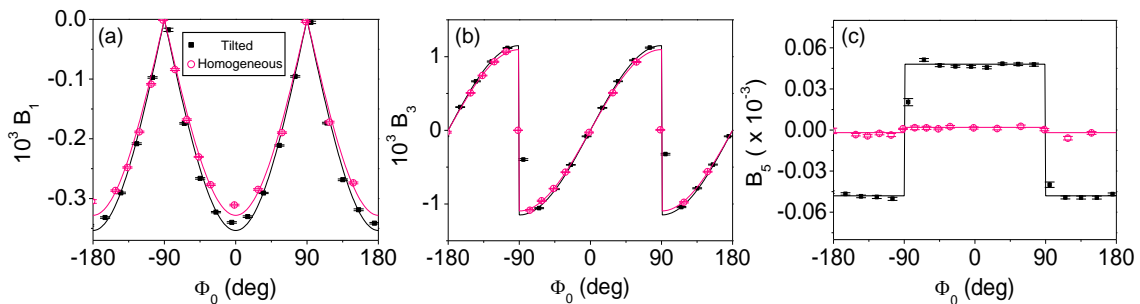

Figure 4.19 Φ_0-dependence of the measured remanent B_1, B_3, and B_5, in (a), (b), and (c), respectively. The data in black are the ones already shown in Fig. 4.11 for the piece of Co(20)/Ru(W) with a Ru thickness of 1 nm at its center. The data in pink correspond to a piece of a Co(20)/Ru(1) sample, *i.e.*, a sample with a homogeneously deposited 1-nm-thick Ru layer. The measured data points are shown as symbols, and solid lines are fits to Eq. (4.3) in (a), to Eq. (4.4) in (b), and to Eq. (4.5) in (c).

4.4.5 t_{Co} dependence

So far, only samples with 20-nm-thick Co layers have been described. However, a study of the Co thickness-dependence of the observed effects is required to corroborate the interfacial nature of the effect. Co(t_{Co})/Ru(W) samples were cut in pieces and the pieces with a nominal central Ru thickness of 0.82 nm were characterized by means of GME. $B_i(H)$ parameters were measured for various Φ_0 orientations for t_{Co} = 5 nm, 10 nm, 15 nm, 20 nm, 50 nm, and 100 nm.
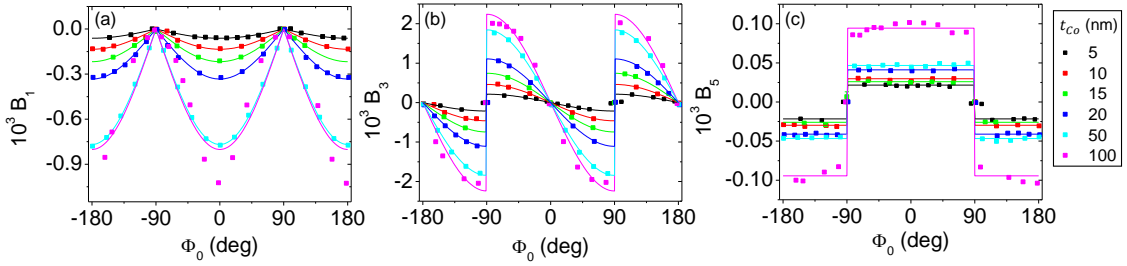

Figure 4.20 Φ_0-dependence of the measured remanent B_1, B_3, and B_5 values in (a), (b), and (c), respectively, for pieces of samples Co(t_{Co})/Ru(W) with a central Ru thickness of 0.82 nm. The different Co thicknesses are coded by the legend on the right hand side. The measured data points are shown as symbols, and solid lines are fits to Eq. (4.3) in (a), to Eq. (4.4) in (b), and to Eq. (4.5) in (c).

Figure 4.20 shows the orientation-dependent remanent values of B_1, B_3, and B_5 for the different samples. As expected, all three MO parameters are lower for the samples with thinner Co layers, but this is particularly so for B_1 and B_3, while B_5 is not reduced in the same proportion for the thinnest of the Co samples. The plots include the fits to Eqs. (4.3) – (4.5) as solid lines and one can see the excellent match between the experimental values and the fit[38], except for the case of t_{Co} = 100 nm.

The data as well as the fits demonstrate that the ratio between the B_5 and the B_1 amplitudes decreases as the Co thickness increases, as shown in Fig. 4.21. Actually, as shown in the inset of Fig. 4.21, $|C/A|$ values follow a linear behavior with the inverse of t_{Co}, which is indicative of an interfacial effect. Indeed, as argued in conjunction with the design of the optical model in Fig. 4.14 (b), if the Ru overcoat is inducing changes in Co that give rise to the presence of P-MOKE, it will only do so at the interface. Hence, the thinner the Co layer is, the greater an

---

[38] Spectroscopic ellipsometry and GME experiments show that the sample with t_{Co} = 100 nm displays a significant optical anisotropy that distorts the orientation dependence of the MO parameters and makes its behavior more complicated yet. Specifically, it is observed that the overall MO quantities are not simply proportional to the orientation dependence of the magnetization components, because the proportionality factors in between B_1, B_3, and B_5 and m_x, m_y, and m_z, respectively, are themselves orientation-dependent.

impact this modification will have relative to the total MO signal of the sample produced by the total Co film thickness.
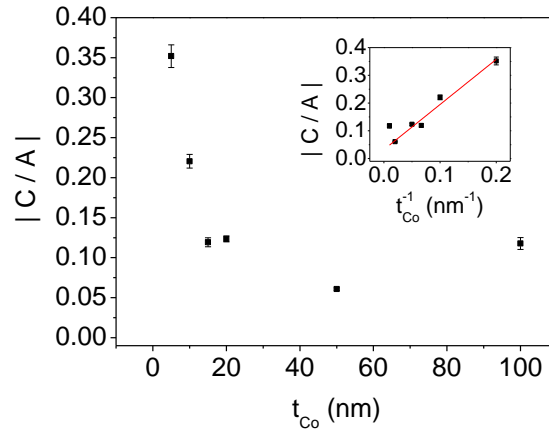

Figure 4.21 Absolute value of the ratio between the C amplitude of B_5, given by Eq. (4.5), and the amplitude A of B_1, given by Eq. (4.3), determined for the data shown in Fig. 4.20, plotted as a function of the Co thickness. Inset: $|C/A|$ as a function of the inverse of the Co thickness. Black symbols are the actual data points, the red line is a linear fit to the data.

4.4.6 Insertion of a SiO₂ layer between Co and obliquely deposited Ru

Yet another confirmation that the rise of P-MOKE is related to the Ru overcoat and that it constitutes an interfacial effect is obtained by studying the samples with a SiO₂ layer in between Co and Ru, namely Co(20)/SiO₂(t_{SiO_2})/Ru(W) samples in Fig. 4.6 (d). GME measurements were performed for these samples and the $|C/A|$ ratio between the amplitudes of B_5 and B_1 is shown as a function of the SiO₂ layer thickness in Fig. 4.22. For a 1.2-nm-thick SiO₂ layer $|C/A|$ is severely decreased already, and the P-MOKE signal has completely vanished for 2 nm of SiO₂, thus confirming that the P-MOKE signal indeed appears due to the Co/Ru interface.
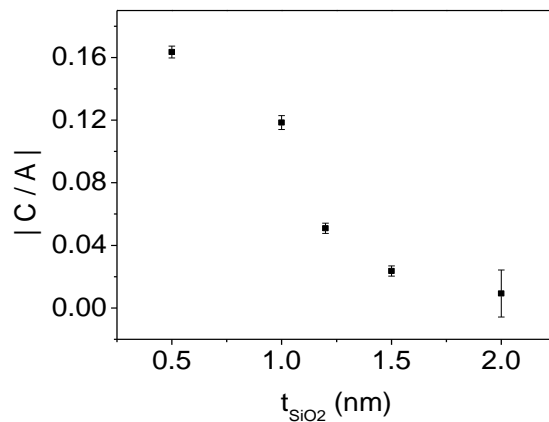

Figure 4.22 Absolute value of the ratio between the amplitude of B_5 (C) and the amplitude of B_1 (A) determined for the samples Co(20)/SiO₂(t_{SiO_2})/Ru(W) as a function of the SiO₂ thickness.

4.5 Model including Dzyaloshinskii-Moriya interaction

4.5.1 Inclusion of Dzyaloshinskii-Moriya interaction

While the macrospin model is able to explain the in-plane reversal of the Co/Ru samples, the observed P-MOKE effect with its asymmetric orientation dependence of $dB_5/d(\mu_0 H)$ requires a model refinement, which includes an energy term that can cause a breaking of the right-left symmetry, such as Dzyaloshinskii-Moriya interaction (DMI). As discussed in Section 1.1.2.3, DMI favors the perpendicular alignment of neighboring spins with a certain chirality. Inversion symmetry breaking is necessary for the presence of DMI, and this is granted by the Co/Ru interface in the samples investigated here. Additionally, spin-orbit coupling (SOC) is needed for a system to display DMI and, as presented in Section 1.1.2.3, this can occur in heterostructures combining thin films of FM and NM metals providing SOC. Typically heavy metals are used as the SOC-providing elements, such as Pt, Ir, or Pt. Here, Ru (Z = 44) has a lower atomic number, and thus has lower SOC, but could still mediate a DMI [35, 36].

Despite the feasibility of having non-vanishing DMI at the interface between Co and Ru, some questions arise. First, the mechanism by which DMI would give rise to a net rotation of the magnetization creating a non-vanishing out-of-plane magnetization seen as a P-MOKE signal needs to be elucidated. Secondly, any explanation proposed here needs to account for the asymmetry observed in the orientation dependence of the P-MOKE *vs. H* slope. Last, but not least, it needs to be explained why a homogeneous overcoat of Ru does not produce the same effect as a Ru overcoat deposited obliquely. The aim of this section is to shed light on these questions, for which atomistic Hamiltonians including DMI are proposed here.

4.5.2 Atomistic Hamiltonian with Dzyaloshinskii-Moriya interaction

For the inclusion of DMI in the modelling, the macrospin approximation must be abandoned, as DMI itself will produce a non-collinear alignment of the spins. Therefore, an atomistic model based on the complete Hamiltonian presented in Eq. (1.13) was utilized. Symmetric exchange and DMI were only considered to couple nearest neighbor spins. Furthermore, the symmetric exchange J is assumed to be constant. Regarding MCA, only its first order was considered, and the crystallographic EA was set to be in the plane of the sample. While DMI will create non-

uniformities in the magnetization, those deviations are assumed to be small and thus, the demagnetizing energy can be considered to a very good approximation to have the form given in Eq. (1.10) for a uniformly magnetized thin film. With those considerations, the atomistic Hamiltonian used for the modelling reads:

$$\mathcal{H} = -\frac{1}{2} \sum_{i \in \mathcal{N}_1(j)} \sum_{j=1}^{N_s} J\, \boldsymbol{S}_i \cdot \boldsymbol{S}_j - \frac{1}{2} \sum_{i \in \mathcal{N}_1(j)} \sum_{j=1}^{N_s} \boldsymbol{D}_{ij} \cdot \left(\boldsymbol{S}_i \times \boldsymbol{S}_j \right) - \sum_{j=1}^{N_s} k_1 \left(\hat{e} \cdot \boldsymbol{S}_j \right)^2$$
$$-\sum_{j=1}^{N_s} k_d \left(\hat{z} \cdot \boldsymbol{S}_j \right)^2 - \sum_{j=1}^{N_s} \boldsymbol{\hbar} \cdot \boldsymbol{S}_j \,, \tag{4.8}$$

where a spin $\boldsymbol{S}_j$ is ascribed to each Co atom. The first and second terms, the symmetric exchange and the DMI respectively, only consider the interaction between nearest neighbors, which is represented by the sum over the ensemble $\mathcal{N}_1(j)$, the nearest neighbors of spin j. The third term is the MCA, with $k_1 > 0$ creating an EA along $\hat{e}$, the fourth term is the magnetostatic energy, with $k_d < 0$ favoring an in-plane magnetization, and the last term is the Zeeman energy, where $\boldsymbol{\hbar}$ is proportional to the applied magnetic field. Using the properties of the vector product, the second term can be rewritten as

$$-\frac{1}{2} \sum_{i \in \mathcal{N}_1(j)} \sum_{j=1}^{N_s} \boldsymbol{D}_{ij} \cdot \left(\boldsymbol{S}_i \times \boldsymbol{S}_j \right) = -\frac{1}{2} \sum_{i \in \mathcal{N}_1(j)} \sum_{j=1}^{N_s} \left(\boldsymbol{D}_{ij} \times \boldsymbol{S}_i \right) \cdot \boldsymbol{S}_j \tag{4.9}$$

and the whole Hamiltonian can be written as

$$\mathcal{H} = -\sum_{j=1}^{N_s} \boldsymbol{H}_j^{eff} \cdot \boldsymbol{S}_j \tag{4.10}$$

with

$$\boldsymbol{H}_j^{eff} = \frac{1}{2} J \sum_{i \in \mathcal{N}_1(j)} \boldsymbol{S}_i + \frac{1}{2} \sum_{i \in \mathcal{N}_1(j)} \left(\boldsymbol{D}_{ij} \times \boldsymbol{S}_i \right) + k_1 \left(\boldsymbol{S}_j \cdot \hat{e} \right) \hat{e} + k_d \left(\boldsymbol{S}_j \cdot \hat{z} \right) \hat{z} + \boldsymbol{\hbar} \,. \tag{4.11}$$

For specific implementations of the model, the energy of the whole system is minimized by aligning each spin with the effective field $\boldsymbol{H}_j^{eff}$ acting upon it. It is important to note that this is a zero temperature model.

4.5.3 Isolated dimer

As a first and simple model to explore the effect of DMI, an isolated dimer is considered, without an externally applied field and neglecting dipole-dipole interactions that lead to magnetostatic energy. As shown in Fig. 4.23, the spin locations are separated along the x axis, although the actual position of the spins is not relevant, as it does not affect the energy of the system in the simple model utilized here. The spins are considered to be classical magnetic moment vectors of unit length described by:

$$\boldsymbol{S}_i = (\cos \Phi_i \cos \Psi_i, \sin \Phi_i \cos \Psi_i, \sin \Psi_i), \qquad i = 1,2 \ . \tag{4.12}$$

The Hamiltonian of the system is

$$\mathcal{H} = -J\boldsymbol{S}_1 \cdot \boldsymbol{S}_2 - \boldsymbol{D}_{12} \cdot (\boldsymbol{S}_1 \times \boldsymbol{S}_2) - k_1((\hat{e} \cdot \boldsymbol{S}_1)^2 + (\hat{e} \cdot \boldsymbol{S}_2)^2) \ . \tag{4.13}$$

The EA has been considered to be along the x axis. The Hamiltonian in Eq. (4.13) has been minimized for different orientations of $\boldsymbol{D}_{12}$ keeping the amplitude $|\boldsymbol{D}_{12}| = \Lambda = 1/5$, and setting $J=1$ and $k_1 = 0.3$. Table 4.2 shows the three components of the equilibrium state of each spins for different $\boldsymbol{D}_{12}$ vectors shown in the second column.
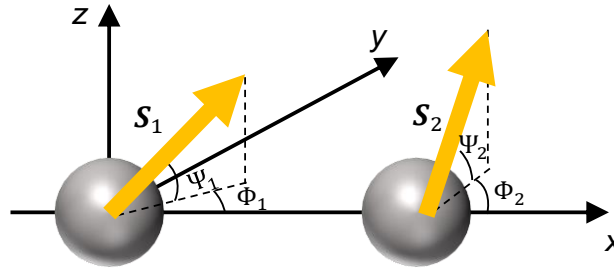

Figure 4.23 Schematics of the two spin system, with definitions of the angles defining the orientation of each spin.

As can be seen from case 1 in Table 4.2, if $\boldsymbol{D}_{12}$ is oriented along the EA, DMI does not have any effect. Cases 2, 3, and 4 have $\boldsymbol{D}_{12}$ perpendicular to the EA. In this case, DMI creates a deviation of the spins from the EA, but of the same magnitude and opposite sign, so that their vector product is parallel to $\boldsymbol{D}_{12}$ to minimize the DMI. This results in no rotation of the net magnetization, just a reduction of its component along the EA. However, if $\boldsymbol{D}_{12}$ has components along the EA and perpendicular to it, *e.g.*, along z, as in case 5 of Table 4.2, a net tilt occurs in the z axis. In particular, each of the individual spins have a tilt of equal magnitude and opposite sign in y, creating a

nonzero cross product of the spins, together with a tilt of equal magnitude and sign in z, which tries to orient the cross product of the spins parallel to $\boldsymbol{D}_{12}$. The larger $|\boldsymbol{D}_{12}|$ and the lower k_1, the larger the tilt. This tilt in both spins yields a net rotation of the magnetization in the z direction. A similar situation occurs in the cases shown in cases 6 and 7 in Table 4.1, with net tilts of the total magnetization in z and y respectively. Finally, in the last row, when $\boldsymbol{D}_{12}$ has components along all the Cartesian axes, there is a net rotation of the magnetization in both z and y.

Case	$\boldsymbol{D}_{12}$	S_1^x	S_1^y	S_1^z	S_2^x	S_2^y	S_2^z
1	$^1/_5\,(1,0,0)$	1	0	0	1	0	0
2	$^1/_5\,(0,0,1)$	0.9971	- 0.0763	0	0.9971	0.0763	0
3	$^1/_5\,(0,1,0)$	0.9971	0	0.0763	0.9971	0	- 0.0763
4	$^1/_{5\sqrt{2}}(0,1,1)$	0.9971	- 0.0539	0.0539	0.9971	0.0539	- 0.0539
5	$^1/_{5\sqrt{2}}(1,0,1)$	0.9984	- 0.0548	- 0.0128	0.9984	0.0548	- 0.0128
6	$^1/_{5\sqrt{2}}(1,0,-1)$	0.9984	0.0548	0.0128	0.9984	- 0.0548	0.0128
7	$^1/_{5\sqrt{2}}(1,1,0)$	0.9984	- 0.0128	0.0548	0.9984	- 0.0128	- 0.0548
8	$^1/_{5\sqrt{3}}(1,1,1)$	0.9979	- 0.0529	0.0361	0.9979	0.0361	- 0.0529

Table 4.2 Equilibrium configuration of a spin dimer with the Hamiltonian given in Eq. (4.15) for different DMI vectors given in column 2. Columns 3, 4, and 5 show the x, y, and z components of the first spin; columns 6, 7, and 8 show the corresponding components for the second spin.

The simplistic model of a spin dimer already shows that a combination of uniaxial MCA and properly oriented DMI can give rise to a deviation of the net remanent magnetization with respect to the crystallographic EA orientation.

Zeeman and magnetostatic energies can be included, leading to a Hamiltonian that reads

$$\mathcal{H} = -J\boldsymbol{S}_1 \cdot \boldsymbol{S}_2 - \boldsymbol{D}_{12} \cdot (\boldsymbol{S}_1 \times \boldsymbol{S}_2) - k_1((\hat{e} \cdot \boldsymbol{S}_1)^2 + (\hat{e} \cdot \boldsymbol{S}_2)^2)$$
$$- k_d((\hat{z} \cdot \boldsymbol{S}_1)^2 + (\hat{z} \cdot \boldsymbol{S}_2)^2) - \hbar(\boldsymbol{S}_1 + \boldsymbol{S}_2). \tag{4.14}$$

The energy has been minimized for different orientations of the applied field with respect to the EA, given by the angle Φ_0, within the xy plane. Some parameters in Eq. (4.14) are fixed: $J = 1$, $k_1 = 0.2$, $k_d = -0.4$. $\hbar$ is a parameter related to the applied field. The strength of the DMI is given by the modulus of the DMI vector $\boldsymbol{D}_{12}$, where $|\boldsymbol{D}_{12}| = \Lambda$ and calculations have been carried out for two different orientations of $\boldsymbol{D}_{12}$. The unit vector of the total magnetization of the system has been calculated as $\hat{\boldsymbol{m}} = \frac{1}{2}(\boldsymbol{S}_1 + \boldsymbol{S}_2)$. With $\hat{\boldsymbol{m}}$ being known, the MO response has been calculated

using the optical model in Fig. 4.14 (b), where a 2-nm-thick Co layer has the calculated $\hat{\boldsymbol{m}}$, which includes an out-of-plane component, and the rest of the Co layer is magnetized in-plane. Figure 4.24 illustrates the orientation dependence of B_5 in remanence and of the $dB_5/d\hbar$ slope near remanence, for two different orientations of the DMI vector. The remanence values and slopes of B_1 and B_3 have the same shape as those shown in Fig. 4.15 for the macrospin model with tilted EA and the experiments.
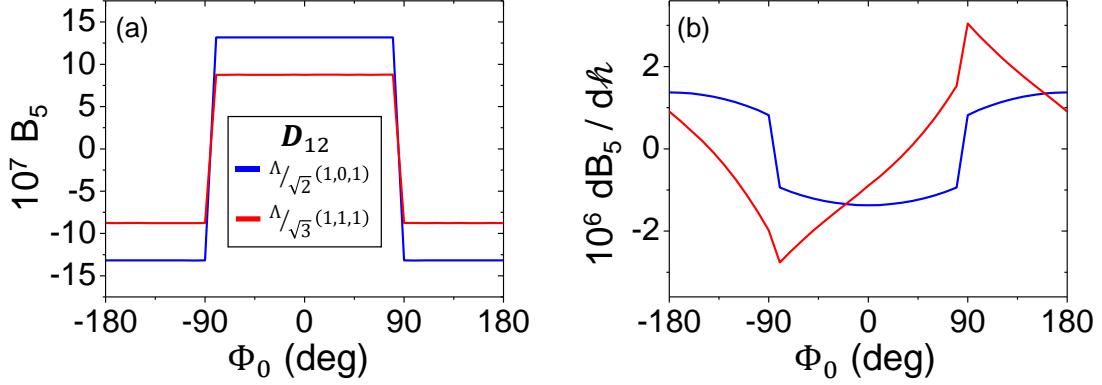

Figure 4.24 (a) Computed B_5 as a function of Φ_0 for a spin dimer described by the Hamiltonian in Eq. (4.13) with DMI interaction given by the legend ($\Lambda = 0.1$). (b) Corresponding field-dependent derivative of B_5.

For both of the exemplary orientations of the DMI vector shown in Fig. 4.24, the orientation-dependence of B_5 in remanence is in agreement with the one observed experimentally, as shown for instance in Fig. 4.11 (d). $dB_5/d\hbar$, however, is symmetric with respect to $\Phi_0 = 0$ when $\boldsymbol{D}_{12}$ is parallel to (1,0,1), as shown in Fig. 4.24 (b) as a blue curve. When $\boldsymbol{D}_{12}$ is parallel to (1,1,1), though, the slope is asymmetric (red curve in Fig. 4.24 (b)) and resembles the experimental observation in Fig. 4.15 (k) and Fig. 4.17 (d). While the magnitude of the plotted variables does not match the experimental values, one needs to keep in mind that only a spin dimer is considered here and that the experimental observations stem from the collective behavior of the entire Co/Ru interface. However, the aim of the calculation here is to demonstrate that in contrast to a tilted anisotropy axis (utilized in the macrospin model in Section 4.4.2.2), a DMI energy term with a specific orientation of the DMI vector can indeed produce the very asymmetry that is observed experimentally for the orientation dependence of the P-MOKE *vs.* applied field behavior.
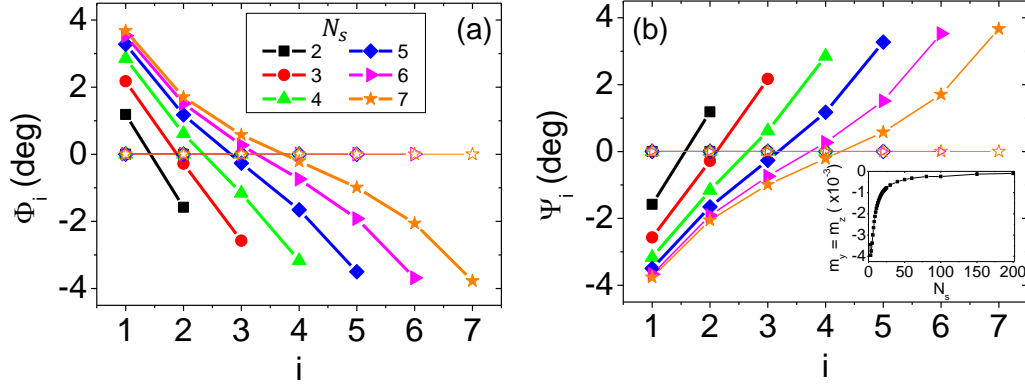
4.5.4   Spin chain

Figure 4.25 In-plane (Φ_i, in (a)) and out-of-plane (Ψ_i, in (b)) tilt of each of the spins composing a chain as a function of the spin location i. Energy minimization has been performed for chains of different length N_s and the legend in (a) is used to identify the different curves. Curves with filled (empty) symbols correspond to calculations with open (periodic) boundary conditions. Inset in (b): chain-averaged net magnetization along the y and z axes as a function of the length of the chain for the calculation with open boundary conditions. All lines are guides to the eye.

In order to extend the calculation of the previous section to larger one-dimensional systems, *i.e.*, spin chains, the following Hamiltonian is considered

$$\mathcal{H} = -J \sum_{i=1}^{N_s-1} \boldsymbol{S}_i \cdot \boldsymbol{S}_{i+1} - \sum_{i=1}^{N_s-1} \boldsymbol{D}_{i,i+1} \cdot (\boldsymbol{S}_i \times \boldsymbol{S}_{i+1}) - k_1 \sum_{i=1}^{N_s} (\hat{\mathbf{e}} \cdot \boldsymbol{S}_i)^2 \qquad (4.15)$$

and minimized with respect to the orientations Φ_i and Ψ_i of each of the spins, with $\hat{\mathbf{e}} = \hat{\mathbf{x}}$. Two cases are considered: systems with open boundary conditions, *i.e.*, finite systems with N_s spins, and systems with periodic boundary conditions (PBC), where the spin N_s is coupled *via* symmetric exchange and DMI to the first spin. The parameters in Eq. (4.15) are fixed to: $J = 1$, $k_1 = 0.2$, and $\boldsymbol{D}_{i,i+1} = \frac{0.1}{\sqrt{3}}(1,1,1)$. Figure 4.25 shows the equilibrium values of Φ_i and Ψ_i for each spin in the chain, for chains of length ranging from $N_s = 2$ to 7, in systems with open boundary conditions and PBC, with filled and empty symbols respectively.

For systems with open boundary conditions, the specific symmetry selected for this DMI vector creates both an in-plane and an out-of-plane tilt. Specifically, given that $\boldsymbol{D}$ is proportional to $(1,1,1)$, the system satisfies the condition $\Phi_i = \Psi_{N_s-1+i}$. As also seen in the curves in Figs. 4.25 (a) and (b), the deviation of the spins from the x axis is larger for the spins at the end points of the chain, while those in the center show only a smaller tilt. As the chain gets longer, the tilt of the majority of the spins is almost zero and only those at the edges are significantly tilted.

The possible occurrence of a DMI-induced tilt at the edges of a nanoscale structure has been known for some time [46]. However, in extended systems, the contribution of the edges becomes negligible and the total magnetization in y and z vanishes. This is shown in the inset in Fig. 4.25 (b), where the y and z components of the net magnetization are displayed as a function of N_s. With PBC, where the last spin in the chain is coupled *via* symmetric and antisymmetric (DMI) exchange to the first one, no tilting occurs in any of the spins, as shown by the empty symbols in Figs. 4.25 (a) and (b).

These calculations indicate that, while in systems with a reduced number of spins DMI can induce a net rotation of the magnetization from the crystallographic EA in the absence of an applied external field, such a tilt of the magnetization does not occur in extended systems. This is the case because a spin that is not right at the edge of the chain has to satisfy exchange energy interactions with spins to the right and to the left. If the DMI vector is the same for both interactions ($\boldsymbol{D}_{i,i+1} = -\boldsymbol{D}_{i,i-1}$), a helicoidal state with gradual rotation of the spins would be favored in the absence of MCA. But with uniaxial MCA this state is not favorable, and small misalignments of the spins with respect to the crystallographic EA are preferred by the system. This leads to the fact that as one goes from spin *i* to spin *i+1*, the same rotation of the spin with the same chirality is not always possible. A rotation of spin *i* that reduces its DMI with *i-1* can create an increase in DMI with spin *i+1*. For sufficiently large MCA in extended systems this results in a negligible rotation of the individual spins and a subsequent vanishing DMI-induced rotation of the net magnetization.

The situation changes most significantly if the DMI is not the same between all pairs of spins. For this to occur, a locally varying DMI has to be present in the system. To illustrate this, an exemplary model of a spin chain with nonhomogeneous DMI is depicted in Fig. 4.26 (a). In this case spins in odd positions interact *via* DMI with a vector $\boldsymbol{D}$ with those on their right, but not with those in the left. The opposite goes for spins in even positions: they interact with $-\boldsymbol{D}$ with the spins on their left and do not interact *via* DMI with those on their right. Symmetric exchange is the same between all nearest neighbors and is not spatially modulated, and MCA is also assumed to be the same for all spins. The Hamiltonian of such chain is the following:

$$\mathcal{H} = -J \sum_{i=1}^{N_s-1} \boldsymbol{S}_i \cdot \boldsymbol{S}_{i+1} - \sum_{i=1}^{N_s/2} \boldsymbol{D}_{2i-1,2i} \cdot (\boldsymbol{S}_{2i-1} \times \boldsymbol{S}_{2i}) - k_1 \sum_i^{N_s} (\hat{e} \cdot \boldsymbol{S}_i)^2. \qquad (4.16)$$
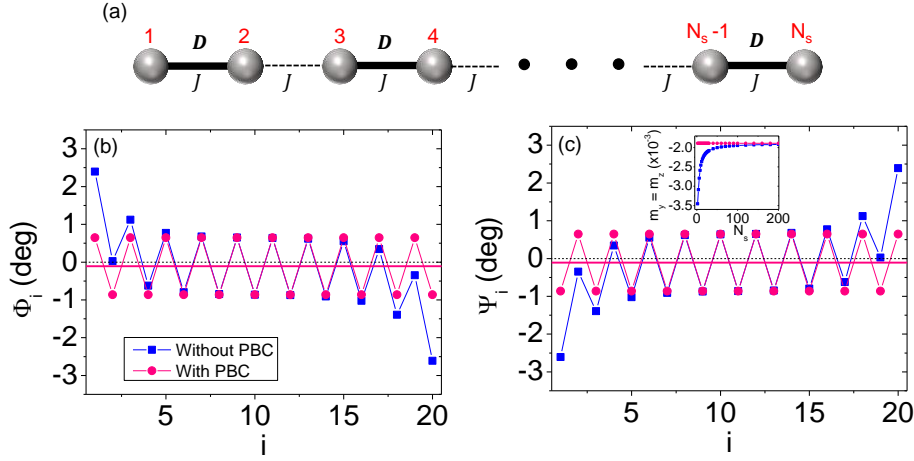
Figure 4.26 (a) Schematics of a spin chain with periodic spatially varying DMI. The spheres correspond to the positions of the spins. All spins are coupled *via* symmetric exchange J but DMI is only present for every second bond, represented by solid thick lines. The links where DMI is absent are represented by dashed thin lines. (b) and (c) Equilibrium Φ_i and Ψ_i respectively, as a function of spin position i for a system of $N_s = 20$ with DMI and symmetric exchange interaction given by the model in (a). Blue squares show the solution for systems with open boundary conditions, and pink circles for systems with PBC. Lines between the points are guides to the eye. A horizontal dashed black line marks zero as a reference to visualize that Φ_i and Ψ_i do not oscillate around it, but have a net nonzero bias. The horizontal pink solid line in (b) and (c) shows the mean value of Φ_i and Ψ_i respectively for the calculation with PBC. Inset in (c): net magnetization along the y and z axes as a function of the length of the chain, without PBC in blue and with PBC in pink.

Figures 4.26 (b) and (c) show the in-plane tilt (Φ_i) and the out-of-plane tilt (Ψ_i) that minimize the energy given by Eq. (4.16) for each spin in a chain of length $N_s = 20$, for a calculation without PBC in blue and with PBC in pink. The values of the parameters in the Hamiltonian are: $J = 1$, $\boldsymbol{D}_{2i-1,2i} = \frac{0.1}{\sqrt{3}}(1,1,1)$ and $k_1 = 0.2$. Without PBC, spins at the edges have larger tilts, with opposite signs on the left and right edges. For the central spins, both calculations give rise to virtually identical solutions, as should be the case for sufficiently large systems. Focusing on the tilt of the central spins, one can observe that the sign of Φ_i and Ψ_i alternates with the spin number. However, the positive and negative values are not equal in magnitude, so that the net tilt does not average to zero. Thus, a net rotation of the total magnetization arises due to the periodically modulated DMI, even in extended systems. In the inset in Fig. 4.24 (c) the net y and z components of the magnetization are shown as a function of the length of the chain. In extended systems and systems with PBC, with the parameters used for this simulation the chain averaged magnetization values $m_y = m_z = -1.9 \times 10^{-3}$, which corresponds to net in-plane and out-of-plane tilts of the magnetization of -0.1 deg.
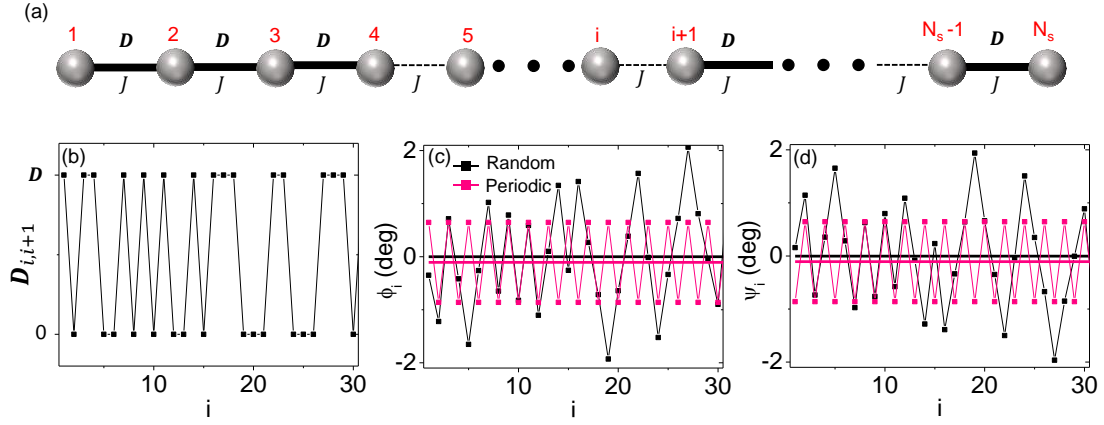
Figure 4.27 (a) Schematics of a chain with random distribution of DMI with nonzero DMI in half of the bonds, $N_s/2$. (b) One possible realization of the random distribution of DMI vectors between spin i and spin $i+1$, where a DMI-active bond has a DMI vector $\boldsymbol{D}_{i,i+1} = \boldsymbol{D} = \frac{0.1}{\sqrt{3}}(1,1,1)$ and an inactive one has $\boldsymbol{D}_{i,i+1} = 0$. A chain with $N_s = 100$ is considered, but only the first 30 spins are shown. (c) and (d) Equilibrium Φ_i and Ψ_i respectively for the first 30 spins, in black for the random distribution of DMI vectors given by (b), and in pink for a periodic distribution as given by Fig. 4.26 (a). Horizontal solid lines in (c) and (d) give the mean value of Φ_i and Ψ_i respectively, in black for the random distribution and in pink for the periodic one.

In the model with periodically modulated DMI given by Eq. (4.16) a tilt of the net magnetization occurs for the specific DMI vectors utilized here. On the other hand, it is interesting to study systems where the DMI between adjacent spin is randomly distributed, being only present in the same amount of bonds as in Fig. 4.26, *i.e.*, in $N_s/2$ bonds, but where the determination of whether a given spin i and its neighbor $i+1$ are coupled *via* DMI is done at random, as shown in Fig. 4.27 (a). For a given realization of the generation of the random distribution of bonds displaying DMI, Fig. 4.27 (b) shows the spatial distribution of the DMI by representing whether spina i and $i+1$ are DMI coupled with a vector $\boldsymbol{D}_{i,i+1} = \boldsymbol{D} = \frac{0.1}{\sqrt{3}}(1,1,1)$ or not, as a function of i. The calculations were done for a chain of length $N_s = 100$, but only the first 30 sites are shown in Fig. 4.27 (b). The energy of such chain has been minimized, yielding the Φ_i and Ψ_i *vs. i* values shown in Figs. 4.27 (c) and (d) as black symbols, which have a mean value given by the horizontal black lines. The mean value of Φ_i is -6.5×10^{-4}, and the one for Ψ_i is -4.3×10^{-3}. In contrast, the calculation for a $N_s = 100$ chain with a periodically modulated DMI as described by Eq. (4.16) is shown in pink, where both Φ_i in Fig. 4.27 (c) and Ψ_i in Fig. 4.27 (d) have a mean value of -0.1083. Above 150 realizations of the calculations with different random distributions of the DMI vectors have been carried out, and in all cases the out-of-plane rotation of the net magnetization, m_z, is below the one obtained with the periodic modulation of the DMI.

In conclusion, no tilt of the total magnetization is observed in extended systems if the DMI is spatially homogeneous, either with DMI being active in all bonds or having a random spatial distribution. However, systems that have a lateral periodic variation of the DMI strength can exhibit a rotation of the magnetization away from the crystallographic EA in remanence. This spatial modulation of DMI could be at the core of the difference between the effects observed for samples with homogeneous Ru overcoats and obliquely deposited Ru overcoats, as will be explained in the next section.

4.5.5 Spatially modulated DMI in two dimensions

As presented in Section 4.4, the GME data taken for Co samples with obliquely deposited Ru overcoats reveal a P-MOKE component even in the absence of an external field, pointing to a net rotation of the magnetization away from the crystallographic EA even in remanence. However, for the samples whose Ru overcoat was deposited in a homogeneous way, no such P-MOKE signal in remanence was observed. In principle no difference would be expected between the two types of samples, especially because the wedge is extremely shallow, with a thickness gradient of approximately 0.1 nm·cm^{-1}. Therefore, on the scale of the laser spot area utilized for the GME experiments, the Ru layer is presumed to be homogeneous, as the thickness variation is in the range of 0.01 nm. The observed difference in behavior for both sample types is thus puzzling, even though oblique deposition is known to lead to deposited layers with specific geometries due to shadowing effects [47].

However, based upon the knowledge developed in the previous sections that (i) DMI can in principle cause a magnetization state that exhibits a net tilt away from the crystallographic EA as well as an asymmetric field dependence, and that (ii) a spatially inhomogeneous DMI is required to give rise to such effects in laterally extended systems, a microscopic model can be sketched for the purpose of explaining the difference between samples with homogeneously and obliquely deposited Ru overcoats as illustrated in Fig. 4.28. In Figs. 4.28 (a) and (b) the gray spheres represent the topmost atoms of the Co layer and their nearest neighbors at a different z plane, assuming the layer to have a perfect termination. This representation is of course a simplistic one, but will serve to schematically present the fundamental difference between the two types of Ru deposition. As can be seen more clearly in Fig. 4.28 (c), Co atoms form a zigzag pattern as viewed in the xz plane. When the Ru layer is deposited with the sputter gun facing the center of the sample

and the sample holder rotates during the deposition, Ru atoms can take their equilibrium positions without any preference for the "u" or "v" facets depicted in Fig. 4.28 (c), giving rise to the equal probability type coverage shown in Fig. 4.28 (a). If, on the contrary, the Ru layer is deposited in an oblique way, *e.g.*, with the flow of Ru atoms coming from the right-hand-side of Fig. 4.28 (b), the Ru atoms should preferentially populate the facets labeled as "u" in Fig. 4.28 (c). The situation depicted in 4.28 (b) is an extreme situation where the facets "v" are unpopulated, and it is furthermore limited to one particular Ru layer thickness only. Nonetheless, in the oblique deposition case, a preferential initial growth can occur in specific directions, including a preferential intermixing pattern, which will maintain a specific lateral modulation pattern in the interface as the Ru film continues to grow. While this microscopic representation does not intend to be an all-encompassing microscopic model for arbitrary Ru thickness, it can nevertheless justify the fundamental difference in the experimental observations for both kinds of samples.
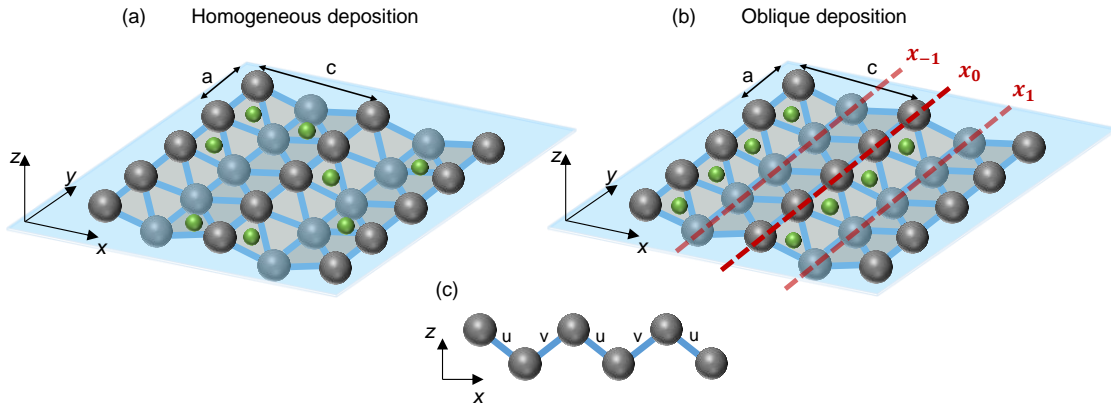

Figure 4.28 Schematics of the Co surface and the Ru overcoat. Co atoms are represented as gray spheres, Ru atoms as green spheres. (a) Scenario with homogeneous Ru deposition, where the Ru atoms are deposited with no preference on either facet of the Co surface. (b) Scenario with oblique Ru deposition. (c) Side view of the Co surface, with faces "u" and "v" having different slopes.

In order to justify that an inhomogeneous distribution of Ru atoms as in Fig. 4.28 (b) can lead to a spatial modulation of the DMI strength, the three-atom model proposed by Levy and Fert [48] for DMI between two ferromagnetic spins mediated by a non-magnetic atom is considered. This model gives the following DMI vector for the DMI between a spin i located at $\boldsymbol{r}_i$ and a spin j located at $\boldsymbol{r}_j$ mediated by a non-magnetic atom l located at $\boldsymbol{r}_l$:

$$\boldsymbol{D}_{ij}^l(\boldsymbol{r}_{li}, \boldsymbol{r}_{lj}, r_{ij}) = -V_1 \frac{\sin\left(k_F(r_{li} + r_{lj} + r_{ij}) + (\pi/10)Z_d\right)(\boldsymbol{r}_{li} \cdot \boldsymbol{r}_{lj})(\boldsymbol{r}_{li} \times \boldsymbol{r}_{lj})}{|r_{li}|^3 |r_{lj}|^3 r_{ij}}, \quad (4.17)$$

where V_1 and k_F are material-specific quantities, and $\boldsymbol{r}_{li} = \boldsymbol{r}_i - \boldsymbol{r}_l$, $\boldsymbol{r}_{lj} = \boldsymbol{r}_j - \boldsymbol{r}_l$, and $\boldsymbol{r}_{ij} = \boldsymbol{r}_j - \boldsymbol{r}_i$. In general terms, the DMI strength between two spins decreases with the distance of the spins to the mediating atom. Hence, in the case depicted in Fig. 4.28 (b), which tries to mimic the case of oblique Ru deposition, Co spins in the chain along x_0, indicated as a dashed red line, will couple with a higher DMI strength to the nearest neighbor Co spins positioned at x_1 than to those at x_{-1}, giving rise to a spatial modulation of DMI. However, when the Ru deposition is homogeneous, for a full monolayer coverage DMI will not be spatially modulated and will not lead to a net rotation of the magnetization away from the crystallographic EA in extended systems, as already seen for the spin chain case in Fig. 4.25. For less than full coverage, the homogeneous deposition of Ru will make the Ru atoms to be randomly placed at the "u" and "v" facets as in Fig. 4.28 (a), leading to a random distribution of the DMI that results in a small net magnetization rotation as compared to the periodically modulated DMI case, as explained in conjunction with Fig. 4.27 for spin chains.
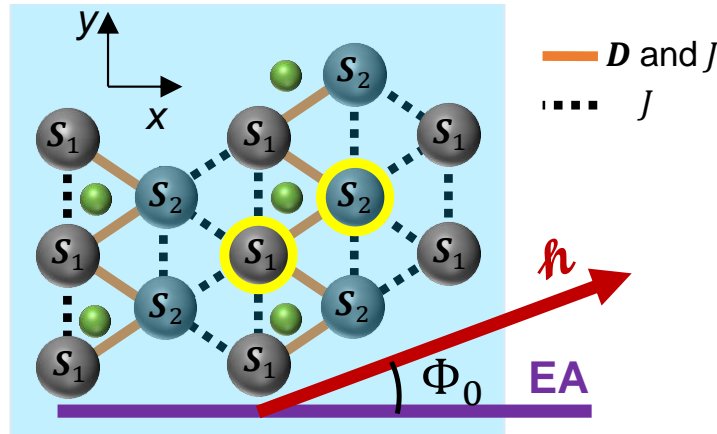

Figure 4.29 Schematics of the two-dimensional model with spatially modulated DMI based on a top view of Fig. 4.28 (b). Gray spheres represent the Co spins, of which $\boldsymbol{S}_1$ and $\boldsymbol{S}_2$ are at different z heights and are non-equivalent. Green spheres represent Ru atoms that mediate the DMI between spins. Thick solid orange lines represent links with symmetric exchange with strength J and DMI with a vector $\boldsymbol{D}_{12} = \boldsymbol{D}$. Dotted lines show the links with J and without DMI. The red arrow is the applied field, the horizontal purple line is the EA. The yellow circles signal two spins of different types on which one can focus to write the effective field in Eqs. (4.19.a) and (4.19.b).

With the aim of extending the spin chain model discussed in the previous section to the description of the Co/Ru interface with an obliquely deposited Ru layer, a two-dimensional model based on an ideal Co surface has been constructed. A top view of the Co surface is sketched in Fig. 4.29, where Co spins $\boldsymbol{S}_1$ are equivalent to each other but are non-equivalent to $\boldsymbol{S}_2$, which are placed at a different z height and are also equivalent among each other. Each spin has six nearest

neighbors: each S_1 has two S_1 and four S_2 nearest neighbors; each S_2 has two S_2 and four S_1 nearest neighbors. The links between the spins in Fig. 4.29 indicate the type of exchange interaction between the pair of spins: dotted black lines indicate a link with only symmetric exchange J, while solid orange lines indicate the presence of J and DMI. The DMI distribution in Fig. 4.29 is representative of the situation depicted in Fig. 4.28 (b), where the Ru atoms are preferentially deposited in one of the facets. In this case, Ru atoms mediate a stronger DMI only between certain spins; in particular, S_1 will be (relevantly) DMI-coupled to only two of the S_2, namely, the ones on their right. The DMI coupling along the y axis, *i.e.*, between spins of the same type (S_1 with S_1 and S_2 with S_2) will also be strong but it will not result in a net tilting of the magnetization because it is not spatially modulated, and it is therefore ignored in the model presented here. The DMI vectors between S_1 and the two S_2 on its right are considered to be equal[39]. The crystallographic EA lies along the x axis forming an angle Φ_0 with the applied field axis. The Hamiltonian of the system represented in Fig. 4.29 can be written as

$$\mathcal{H} = -\frac{N_s}{2}\sum_{i=1}^{2} \boldsymbol{H}_i^{eff} \cdot \boldsymbol{S}_i \ , \tag{4.18}$$

where

$$\boldsymbol{H}_1^{eff} = 4J\boldsymbol{S}_2 + 2J\boldsymbol{S_1} + 2\boldsymbol{D} \times \boldsymbol{S}_2 + k_1(\boldsymbol{S}_1 \cdot \hat{x})\hat{x} + k_d(\boldsymbol{S}_1 \cdot \hat{z})\hat{z} + \boldsymbol{\hbar} \tag{4.19.a}$$

$$\boldsymbol{H}_2^{eff} = 4J\boldsymbol{S}_1 + 2J\boldsymbol{S_2} - 2\boldsymbol{D} \times \boldsymbol{S}_1 + k_1(\boldsymbol{S}_2 \cdot \hat{x})\hat{x} + k_d(\boldsymbol{S}_2 \cdot \hat{z})\hat{z} + \boldsymbol{\hbar} \ . \tag{4.19.b}$$

The values considered in the calculations here are $J = 1$, $k_1 = 0.1$, and $k_d = -0.3$. A DMI of tunable strength $|\boldsymbol{D}| = \Lambda$ of the form $\boldsymbol{D} = \frac{\Lambda J}{\sqrt{3}}(1,1,1)$ has been considered.

For this simplified spin system, the energy has been minimized for different strengths and orientations of the applied magnetic field $\boldsymbol{\hbar}$. After obtaining the Cartesian components of the magnetization m_ν for this two-dimensional model, the optical model of Fig. 4.14 (b) has been utilized to calculate the MO response of such a system for the conditions used in the experiment, *i.e.*, a wavelength of 635 nm and an angle of incidence of 45 deg. In the optical model the Co layer

---

[39] This is an approximation of the model used here. In a more refined model where the symmetries of the lattice are considered and the DMI vectors are calculated based on the Lévy-Fert three-site model in Eq. (4.17) those two DMI vectors would be different. Such microscopic analysis is beyond the scope of this thesis. Instead, the focus here is to try to explain the experimental data with a simple atomistic model that is not necessarily constrained by the symmetry of the lattice.

is divided in two sublayers: first, a 2-nm-thick Co layer with the magnetization components obtained from an energy minimization of Eqs. (4.18) and (4.19) using $\boldsymbol{D} \neq 0$; second, a 18-nm-thick in-plane magnetized Co, whose magnetization components have been calculated minimizing the energy expression in Eqs. (4.18) and (4.19) but with $\boldsymbol{D} = 0$.

In particular, Fig. 4.30 (a) shows the calculated GME parameter B_5 in remanence, related to P-MOKE, as a function of Φ_0, *i.e.*, the orientation of the crystallographic EA with respect to the applied field axis, for two values of the DMI strength Λ. As observed, the larger Λ is, the larger the P-MOKE signal will be. In the experimental data it was observed that the P-MOKE signal increases upon increasing the Ru overcoat thickness, and that it does so up to a certain saturation point with a fall-off length of about 0.3 nm. The comparison of the experimental data with the model in Fig. 4.30 (a) points to the fact that an increasing Ru thickness gives rise to an increase of DMI strength in the thickness range of 1-2 monolayers, and that the effect saturates at very low Ru thicknesses, which is in agreement with studies of the heavy metal overcoat thickness dependence of DMI [49]. On the other hand, Fig. 4.30 (b) shows the derivative of B_5 with respect to the field strength for two values of Λ, qualitatively reproducing the symmetry of the experimental results in Fig. 4.15 (k) and Fig. 4.17 (d). Even though an exact quantitative agreement with the experimental data has not been achieved given the simplicity of this model, it does reproduce the symmetry of the field-dependent slope of the P-MOKE, which could not be explained by means of a tilted anisotropy axis. Again, the comparison of Fig. 4.30 (b) and Fig. 4.17 (d) points to a proportionality between t_{Ru} and Λ in the very initial growth of the Ru film up to about $1 - 2$ monolayers.
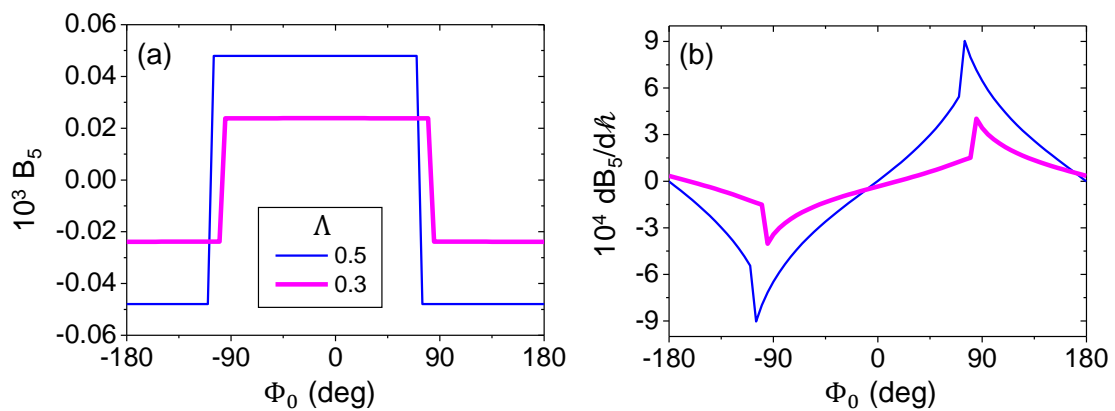

Figure 4.30 (a) Computed B_5 as a function of Φ_0 for two different values of Λ of the DMI strength. (b) Field-dependent slope of B_5 near remanence as a function of Φ_0 for the two values of Λ.

Another aspect worth noting is the fact that, as a function of Φ_0, *i.e.*, the angle between the applied field and the crystallographic EA, B_5 does not change sign exactly at $\Phi_0 = \pm 90$ deg, but rather at a Φ_0 value that depends on the DMI strength, as is clearly seen by comparing the two curves in Fig. 4.30 (a). B_5 actually changes sign at the Φ_0 where the longitudinal component, *e.g.*, B_1, goes to zero, *i.e.*, at the *effective* or *perceived* hard axis. This occurs because, for the model to reproduce the observed P-MOKE slope, the DMI vector $\boldsymbol{D}$, which is parallel to $(1,1,1)$, also creates an in-plane tilt of the magnetization, so that the crystallographic and the perceived effective EA are not the same. For the measurements performed with rotational scans, this in-plane rotation, which is expected to be a small effect measured on top of a large rotation range, is difficult to detect, because each sample is aligned manually and the crystallographic EA can only be aligned with a precision of about 2 deg. The determination of Φ_0 was actually calibrated by finding the point where the longitudinal magnetization vanishes in remanence, and ascribing to this position $\Phi_0 = \pm 90$ deg. Therefore, Φ_0 in Figs. 4.8, 4.11, 4.15-17, and 4.19-20 is not necessarily the angle between the applied field and the crystallographic EA, but rather the angle between the applied field and the *effective* EA, which, according to the models including DMI, is not necessarily the same as the crystallographic EA. Contrastingly, in GME measurements that utilize the linear translation stage, the elongated sample is aligned once, and for each measurement along the strip, the orientation between the field and the crystallographic EA is the same, nominally $\Phi_0 = -75$ deg. What varies from measurement point to measurement point is the Ru thickness of the sample, which is assumed to affect the DMI strength Λ. GME measurements with the LTS thus provide a good test to corroborate the validity of the model.
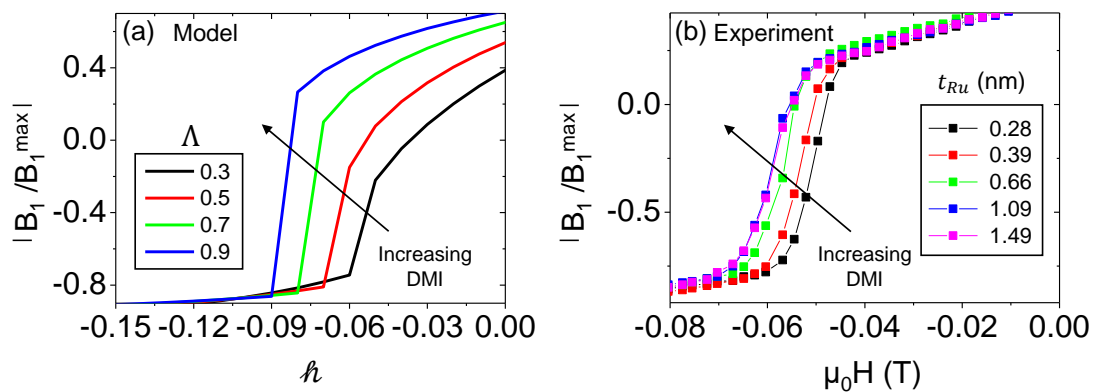

Figure 4.31 (a) Absolute value of calculated B_1 normalized to its maximum value as a function of the applied field, calculated for different strengths of the DMI Λ in the model in Eqs. (4.18) and (4.19) for $\Phi_0 = -75$ deg. (b) Absolute value of experimental B_1 normalized to its maximum value as a function of the applied field, with a nominal $\Phi_0 = -75$ deg, measured for the Co(20)/Ru(W) sample using the LTS at different points, corresponding to the different Ru thicknesses given in the legend.

A key consequence of the in-plane tilt of the magnetization predicted by the model with DMI described by Eq. (4.18) is the increase in switching field upon increasing the DMI strength Λ. Figure 4.31 (a) shows specifically the calculated B_1 as a function of the applied field strength for different values of Λ and for $\Phi_0 = -75$ deg. As can be seen, for larger Λ the switching field increases. This trend is also observed in the GME experiments performed on the Co(20)/Ru(W) strip-type sample utilizing the LTS, for which nominally $\Phi_0 = -75$ deg. Figure 4.31 (b) shows B_1 as a function of the field measured at different points of the sample, corresponding to different Ru thicknesses. For thicker Ru thicknesses, the switching field increases, which by comparison with the model is indicative of a small in-plane tilt of the magnetization due to a Ru overcoat-induced and thickness-dependent DMI. It is also observed that the increase of the switching field actually saturates at sufficiently large t_{Ru}, just as the P-MOKE signal saturates as a function of t_{Ru}.

4.6   Conclusions and outlook

The careful design and fabrication of samples with single-crystal Co films with in-plane uniaxial MCA and decorated with ultrathin Ru overcoats, together with an extensive characterization by means of GME to perform three-dimensional vector magnetometry, has led to the discovery of a Ru-overcoat-induced out-of-plane tilt of the magnetization of Co. The observations are incompatible with a mere modification of MCA, either in strength or in orientation, while the consideration of a surface DMI energy can explain the entirety of the results.

Furthermore, the magnetization tilt is only observed in samples for which the Ru overcoat is deposited obliquely, while in samples with homogeneously deposited Ru overcoat the sample has a macrospin type magnetization reversal. Based on atomistic models, this difference between the samples with obliquely and homogeneously deposited Ru overcoats is ascribed to a spatial modulation of the surface DMI. It is hereby discussed that in samples with uniform Ru layers, Ru atoms mediate a laterally homogeneous DMI between the Co spins, which is found to be ineffective. In contrast, for the case with obliquely deposited Ru layers, in which Ru atoms can take preferential positions, a spatially inhomogeneous DMI is generated that give rise to a net out-of-plane magnetization tilt.

The simple models presented here show that only spatially modulated DMI can produce a net rotation of the total magnetization. The dependence of the magnetization tilt with the applied field strength and the orientation of the field with respect to the crystallographic EA of the sample are qualitatively reproduced by the models with inhomogeneous DMI, assuming that the DMI vector exhibits certain orientations. The overcoat thickness dependence of the magnetization tilt is explained as an increased DMI strength with increasing Ru thickness, up to a point of saturation that occurs in a very short length sale with a characteristic length of about 0.3 nm given by the exponential fit in Fig. 4.18.

It would also be interesting to perform a microscopic characterization of the Co/Ru interface and ideally get to know the positions of the Co and Ru atoms and the differences between the homogeneous and the tilted Ru overcoats. Given that large differences in the observed P-MOKE signal occur at the monolayer level, surface science measurement techniques such as scanning tunneling microscopy would be required for this task. A detailed investigation of the position of the Co and Ru atoms would allow to construct an atomistic model that represents the exact symmetries of the system with DMI interactions.

On the other hand, to truly confirm the presence of DMI and quantify its strength, spin wave dispersion measurements would be useful, as DMI is known to create an asymmetry in the spin wave spectra [50, 51]. To that end, Brillouin light scattering experiments could help determine the magnitude of interfacial DMI in samples similar to the ones used here [52, 53]. Recently, the effect of periodically modulated DMI (with much larger periods than the ones presented here, though) onto spin waves has been studied [54], and those findings could open a pathway to characterize the effects observed for the samples here.

In order to corroborate the hypothesis that with the tilted deposition there is a preferential position for the Ru atoms on top of the Co surface, further experiments could be performed for different relative orientations between the Co [0001] axis and the direction of the flow of Ru atoms, which occurs along the long axis of the 80 mm × 5 mm strips. In the samples described here, only the case where the angle between the long axis of the strips and the EA of Co is 15 deg is examined, while the DMI and its assumed spatial modulation could change with this angle in between atom flow and surface orientation.

Finally, it would be interesting to test other overcoat materials. Preliminary results utilizing Pt, which is known to produce strong DMI, show essentially the same effect. Overcoats of lighter metals that should not produce any DMI could also be tested to verify that the observed magnetization tilts are indeed related to DMI.

References

[1] F. Hellman *et al.*, Rev. Mod. Phys. **89**, 025006 (2017).

[2] F. Wilhelm *et al.*, Phys. Rev. Lett. **85**, 413 (2000).

[3] L. Cheng, Z. Altounian, D. H. Ryan, J. O. Ström-Olsen, M. Sutton, and Z. Tun, Phys. Rev. B **69**, 144403 (2004).

[4] A. Fert, Mater. Sci. Forum **59–60**, 439 (1990).

[5] J. M. D. Coey, *Magnetism and Magnetic Materials* (Cambridge University Press, Cambridge, U. K., 2010).

[6] P. F. Carcia, A. D. Meinhaldt, and A. Suna, Appl. Phys. Lett. **47**, 178 (1985).

[7] N. Nakajima, T. Koide, T. Shidara, H. Miyauchi, H. Fukutani, A. Fujimori, K. Iio, T. Katayama, M. Nývlt, and Y. Suzuki, Phys. Rev. Lett. **81**, 5229 (1998).

[8] S. Ikeda, K. Miura, H. Yamamoto, K. Mizunuma, H. D. Gan, M. Endo, S. Kanai, J. Hayakawa, F. Matsukura, and H. Ohno, Nat. Mater. **9**, 721–724 (2010).

[9] H. X. Yang, M. Chshiev, B. Dieny, J. H. Lee, A. Manchon, and K. H. Shin, Phys. Rev. B **84**, 054401 (2011).

[10] M. Sakurai, T. Takahata, and I. Moritani, IEEE Trans. J. Magn. Japan **7**, 176–82 (1992).

[11] G. Y. Guo and H. Ebert, J. Magn. Magn. Mater., **156**, 173-174 (1996).

[12] S. Uba, L. Uba, A. N. Yaresko, A. Ya Perlov, V. N. Antonov, and R. Gontarz., J. Phys.: Condens. Matter **10**, 3769 (1998).

[13] E. Th. Papaioannou, M. Angelakeris, N. K. Flevaris, P. Fumagalli, and Ch. Mueller, J. Appl. Phys **101**, 023913 (2007).

[14] A. Carl and D. Weller, Phys. Rev. Lett. 74, 190 (1995).

[15] P. Grünberg, R. Schreiber, Y. Pang, M. B. Brodsky, and H. Sowers, Phys. Rev. Lett. **57**, 2442 (1986).

[16] S. S. P. Parkin, N. More, and K. P. Roche, Phys. Rev. Lett. **64**, 2304 (1990).

[17] P. Bruno and C. Chappert, Phys. Rev. B **46**, 261 (1992).

[18] O. Hellwig, T. L. Kirk, J. B. Kortright, A. Berger, and E. E. Fullerton, Nat. Mater **2**, 112-116 (2003).

[19] O. Hellwig, A. Berger, and E. E. Fullerton, Phys. Rev. Lett. **91**, 197203 (2003).

[20] O. Hellwig, A. Berger, J.B. Kortright, and E. E. Fullerton, J. Magn. Magn. Mater. **319**, 13-55 (2007).

[21] R. A. Duine, K.-J. Lee, S. S. P. Parkin, and M. D. Stiles, Nat. Phys. **14**, 217–219 (2018).

[22] J. L. Leal and M. H. Kryder, J. Appl. Phys. **83**, 3720 (1998).

[23] Y. Huai, J. Zhang, G. W. Anderson, P. Rana, S. Funada, C.-Y. Hung, M. Zhao, and S. Tran, J. Appl. Phys. **85**, 5528 (1999).

[24] K. Inomata, T. Nozaki, N. Tezuka, and S. Sugimoto Appl. Phys. Lett. **81**, 310, (2002).

[25] M.N. Baibich, J.M. Broto, A. Fert, F. Nguyen van Dau, F. Petroff, P. Eitenne, G. Creuzet, A. Friederich, and J. Chazelas, Phys. Rev. Lett. **61**, 2472 (1988).

[26] G. Binasch, P. Grünberg, F. Saurenbach, and W. Zinn, Phys. Rev. B **39**, 4828 (1989).

[27] J. Åkerman, Science, **308**(5721), 508-510 (2005).

[28] A. Fert, V. Cros, and J. Sampaio, Nat. Nanotechnol. **8**, 152–156 (2013).

[29] D.-S. Han *et al.*, Nat. Mater. (2019).

[30] A. Fernández-Pacheco *et al.*, Nat. Mater. (2019).

[31] S. Heinze, K. von Bergmann, M. Menzel, J. Brede, A. Kubetzka, R. Wiesendanger, G. Bihlmayer, and S. Blügel, Nat. Phys. **7**, 713–718 (2011).

[32] S. Woo *et al.*, Nat. Mater. **15**, 501–506 (2016).

[33] C. Moreau-Luchaire *et al.*, Nat. Nanotechnol. **11**, 444–448 (2016).

[34] O. Boulle *et al.,* Nat. Nanotech. **11**, 449–454 (2016).

[35] D. Khadka,S. Karayev, and S. X.Huang, J. Appl. Phys. **123**, 123905 (2018).

[36] H. Yang *et al.*, Nat. Mater **17**, 605–609 (2018).

[37] O. Idigoras, U. Palomares, A. K. Suszka, L. Fallarino, and A. Berger, Appl. Phys. Lett. **103**, 102410 (2013).

[38] O. Idigoras, A. K. Suszka, P. Vavassori, B. Obry, B. Hillebrands, P. Landeros and A. Berger, J. Appl. Phys. **115**, 083912 (2014).

[39] W. Yang, D. N. Lambeth, and D. E. Laughlin, J. Appl. Phys. **85**, 4723 (1999).

[40] I. H. Malitson. J. Opt. Soc. Am. **55**, 1205-1208 (1965).

[41] K. A. Kress and G. J. Lapeyre, J. Opt. Soc. Am. **60**, 1681-1684 (1970).

[42] J. A. Arregi, J. B. González-Díaz, O. Idigoras, and A. Berger, Phys. Rev. B **92**, 184405 (2015).

[43] P. B. Johnson and R. W. Christy, Phys. Rev. B **9**, 5056-5070 (1974).

[44] P. B. Johnson and R. W. Christy, Phys. Rev. B **6**, 4370-4379 (1972).

[45] D. E. Aspnes and A. A. Studna, Phys. Rev. B **27**, 985-1009 (1983).

[46] S. Rohart and A. Thiaville, Phys. Rev. B **88**, 184422 (2013).

[47] A. Barranco, A. Borras, A. R. González-Elipe, A. Palmero, Prog. Mater. Sci. **76**, 59-153 (2016).

[48] P. Lévy and A. Fert, Phys. Rev. B **23**, 4667 (1981).

[49] S. Tacchi, R. E. Troncoso, M. Ahlberg, G. Gubbiotti, M. Madami, J. Åkerman, and P. Landeros, Phys. Rev. Lett. **118**, 147201 (2017).

[50] Kh. Zakeri, Y. Zhang, J. Prokop, T.-H. Chuang, N. Sakr, W. X. Tang, and J. Kirschner, Phys. Rev. Lett. **104**, 137203 (2010).

[51] D. Cortés-Ortuño and P. Landeros, J. Phys. Condens. Matter **25**, 156001 (2013).

[52] K. Di, V. L. Zhang, H. S. Lim, S. C. Ng, M. H. Kuok, J. Yu, J. Yoon, X. Qiu, and H. Yang, Phys. Rev. Lett. **114**, 047201 (2015).

[53] M. Belmeguenai, J. P. Adam, Y. Roussigné, S. Eimer, T. Devolder, J. V. Kim, and A. Thiaville, A. Phys. Rev. B **91**, 180405 (2015).

[54] R. A. Gallardo, D. Cortés-Ortuño, T. Schneider, A. Roldán-Molina, F. Ma, R. E. Troncoso, K. Lenz, H. Fangohr, J. Lindner, and P. Landeros, Phys. Rev. Lett. **122**, 067204 (2019).

Chapter 5

Dynamic phase transitions

The response of a ferromagnet to an oscillating magnetic field with a period comparable to the relaxation time of the system is studied by means of magneto-optical Kerr effect measurements and calculations based on a kinetic Ising model within a mean field approximation. By changing the field period, a dynamic phase transition (DPT) occurs between two dynamic phases: an ordered phase at low periods, and a disordered one, at high periods. Sections 5.1 and 5.2 describe the phenomenon and discuss the implementation of the kinetic Ising model. Section 5.3 describes the similarities between DPTs and conventional equilibrium thermodynamic phase transitions (TPTs) based on previous experimental and modeling evidence. Section 5.4 analyzes the differences between DPTs and TPTs that have been identified in this work, which confront the long-established idea that both phase transitions are equivalent. Finally, Section 5.5 summarizes the main results.

5.1   Introduction

While in the previous chapter the applied magnetic field was much slower than τ, the intrinsic relaxation time of the ferromagnet associated with the transitions between the two stable states of the system in a static field, the spotlight of this chapter are the dynamic effects that arise when the period of the magnetic field is comparable to τ. The uniaxial ferromagnetic system considered here is described by an Ising Hamiltonian with nearest-neighbor symmetric exchange interaction subjected to a time-dependent external field, which reads:

$$\mathcal{H} = -\frac{1}{2}\sum_{i=1}^{N_s} \sum_{j\in\mathcal{N}_1(i)} J_{ij}S_iS_j - \sum_{i=1}^{N_s} \hbar_i(t)S_i. \tag{5.1}$$

The first term is the exchange energy: J_{ij} is the pairwise exchange constant and, if positive, favors a ferromagnetic ground state. S_i and S_j are one-dimensional local spins that can take the values +1 and -1. $\mathcal{N}_1(i)$ represents the ensemble of nearest neighbors of spin i; thus the sum over j is performed over all the spin sites that are nearest neighbors of i. The sum in i runs from 1 to N_s,

where N_s is the total number of spins in the system. The second term is the Zeeman energy, where $\hbar_i(t)$ is a time-dependent magnetic field that is applied at each spin site i and is taken to be parallel to the quantization axis of the Ising spins. J and $\hbar_i$ have units of energy, and S_i are dimensionless. The form of the Hamiltonian in Eq. (5.1) is generic and can be used to describe a great number of systems with different lattices in two and three spatial dimensions. The form of the external field can also vary, but only a site-independent sinusoidal field applied homogeneously along the whole sample is considered here, with the form:

$$\hbar(t) = \hbar_0 \cos\left(\frac{2\pi}{P}t\right) + \hbar_b, \qquad (5.2)$$

where $\hbar_0$ is the amplitude of the oscillating part, P is the period, and $\hbar_b$ is a constant offset called bias field.

An experimental study of the properties of the kinetic Ising model (KIM) requires an appropriate sample and settings that make Eq. (5.1) applicable. Ferromagnets with negligible demagnetization effects and uniaxial anisotropy, subjected to a time-dependent magnetic field applied along the anisotropy axis, constitute a good choice, given that in such circumstances the magnetization can only be aligned in the two directions along the easy axis (EA) in equilibrium. From the modeling perspective, the goal is to determine the time dependence of the steady-state thermal expectation value of S_i, called m_i, which corresponds to the magnetization normalized to its saturation value[40]. $m_i(t)$ is calculated for a given set of parameters such as temperature T, P, $\hbar_0$ or $\hbar_b$. To this end, Monte Carlo simulations and mean-field approximation (MFA) computations are the most used methods, of which the latter is used here because, despite its simplicity, it can still capture the physics of the model at a much lower computational cost.

As first reported by Tomé and de Oliveira within the MFA [1], a key aspect of the KIM is that systems described by Eq. (5.1) undergo qualitative changes of behavior as the external driving force varies[41]. For instance, in a bulk (translationally invariant) system at a fixed temperature T

---

[40] The saturation value taken for normalization is different in experiments and simulations. In simulations, the saturation magnetization at zero temperature is taken as a reference; in experiments, such value is unknown, so the magnetization is normalized to the saturation magnetization at the temperature at which the experiment is performed, *i.e.*, room temperature. Actually, the experiments here are based on magneto-optics and the key quantity for the normalization is the maximum magneto-optical signal.

[41] Early works on the response of a magnetic system to an oscillating field study the behavior as a function of temperature and considering an oscillating field of fixed period. The description for a fixed temperature

below the Curie temperature T_C, at a fixed amplitude of the oscillating field $\hbar_0$, and for $\hbar_b = 0$, the shape of $m(t)$ *vs.* $\hbar(t)$ hysteresis loops qualitatively varies as the period P of the field changes. For large enough periods, the applied field is sufficiently slow and the magnetization can follow it, even if there is a lag that gives rise to hysteresis in the $m(t)$ *vs.* $\hbar(t)$ curve, as it can be observed in Fig. 5.1 (a). Equivalently, Fig. 5.1 (b) shows the time-dependence of $m(t)$ (in blue) and $\hbar(t)$ (in red). For lower values of P, the lag between $\hbar(t)$ and $m(t)$ increases and the hysteresis loop acquires an elliptic shape. Despite the field oscillating rather fast, in the situation represented in Fig. 5.1 (c) and Fig. 5.1 (d) m is still able to reverse within a single field cycle and thus, $m(t)$ oscillates around zero. However, by further decreasing P, the oscillation of the field eventually becomes so fast that the magnetization of the system cannot be fully reversed within a cycle and instead oscillates around a nonzero value that will be either positive or negative depending on the initial configuration of the system. The m *vs.* $\hbar$ hysteresis loop will be shifted vertically, as it is observed in Fig. 5.1 (e), and the same will be observed in the m *vs.* t curve, as in Fig. 5.1 (f). Interestingly, this symmetry breaking occurs even though on average (over a period), there is no symmetry-breaking field, *i.e.*, $\int_0^P \hbar(t)dt = 0$. Subsequent studies within the MFA or utilizing Monte Carlo simulations [2-5] focused on the P and $\hbar_0$ dependence of the shape and area of hysteresis loops and it was found that, for large periods, the area of the hysteresis loop follows a scaling behavior, while the center of the hysteresis loop deviates from zero for sufficiently small P, a behavior that was confirmed experimentally in ultrathin films [6, 7].

After further theoretical investigations of the KIM [8-12] it became established that the fundamental change of behavior at high and low P is best reflected in the change from a zero to a nonzero value of the period-averaged magnetization, which is defined as

$$Q = \frac{1}{P}\int_0^P m(t)dt. \qquad (5.3)$$

Q plays the role of the dynamic order parameter and defines two phases: a dynamically disordered (dynamically paramagnetic, DPM) phase with $Q = 0$ at large P and a dynamically ordered (dynamically ferromagnetic, DFM) phase with $Q \neq 0$ at small P. The value of Q for each case is shown in Fig. 5.1 as horizontal green lines in all panels. The transition between the DPM and the

---

and varying period of the external field is equivalent and more appropriate for the following sections, so the seminal works on the topic will also be discussed in that framework.

DFM phases occurs at a single specific period called the critical period P_c, at which a so-called dynamic phase transition (DPT) occurs. The value of P_c depends not only on the relaxation time of the system τ, but also on the external parameters T and $\hbar_0$. Before giving further details on the properties of the DPT, the next section presents the methodology to perform MFA calculations.
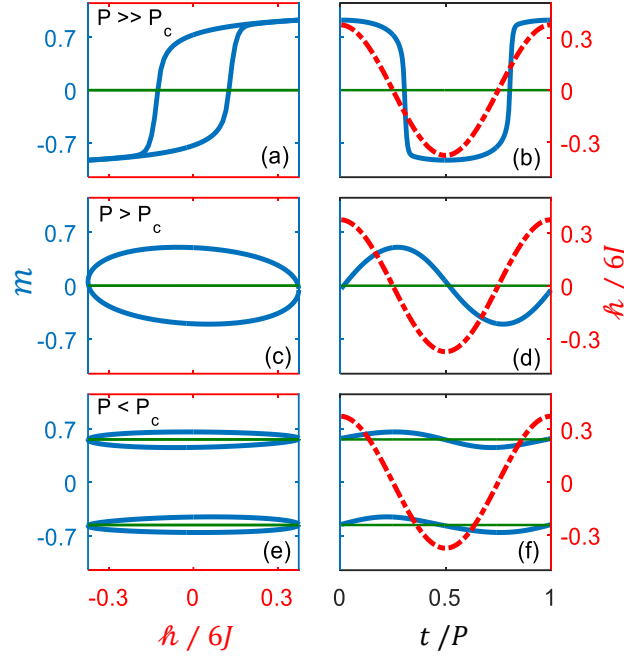

Figure 5.1 Schematic of the changes observed in the magnetization as the period of the oscillating field decreases. Left column: m *vs.* $\hbar$ hysteresis loops (blue line). Right column: m *vs.* t (blue line, left vertical axis) and $\hbar$ *vs.* t curves (red dash-dotted line, right vertical axis). (a) and (b) represent the slow field case $P \gg P_c$; (c) and (d) show the $P > P_c$ case; (e) and (f) show the $P < P_c$ case. Q is shown as horizontal green lines. In the $P < P_c$ case, the two possible stable states with opposite values of Q are shown. Modified from Ref. [13].

5.2 Equation of motion for the magnetization within the mean-field approximation and its numerical implementation

The modeling approach followed here is the MFA. Taking Eq. (5.1) as a starting point, Tomé and de Oliveira [1] calculated the evolution of the system using Glauber stochastic dynamics [14] and derived the following equation for the magnetization:

$$\tau \frac{dm(t)}{dt} = -m(t) + \tanh\left[\frac{T_C}{T}\frac{1}{\xi J}\left(\hbar^{MF}(t) + \hbar(t)\right)\right]. \tag{5.4}$$

Here, τ is the relaxation time of the ferromagnet, ξ is the number of nearest neighbors for each spin, and J is the exchange constant. $\hbar(t)$ is the external field given by Eq. (5.2), and $\hbar^{MF}$ stands

for the mean field to which a spin is subjected, which is given by the exchange field produced by the nearest neighbor spins such that

$$\hbar^{MF}(t) = \xi J m(t). \tag{5.5}$$

In order to solve Eq. (5.4), the work of Idigoras *et al.* [15] has been followed. Time is discretized into K elements, with a counter k running from 1 to K. $\frac{t}{P}$ is set to be equal to $\frac{k}{K}$, and thus $dt \sim \Delta t = \frac{P}{K}\Delta k = \frac{P}{K}$. The time derivative is evaluated by means of finite differences. This leads to the following self-consistent equation for $m(k)$:

$$m(k) = F\big(m(k)\big) =$$
$$\frac{1}{1+\frac{K}{P}\tau}\left\{\frac{K}{P}\tau\,m(k-1) + \tanh\left[\frac{T_C}{T}\frac{1}{\xi J}\left(\hbar^{MF}(k) + \hbar_0\cos\left(2\pi\frac{k}{K}\right) + \hbar_b\right)\right]\right\} \tag{5.6}$$

with periodic boundary conditions for the time axis, *i.e.*, for $k = 1$, $k - 1$ is identical to $k = K$.

Equation (5.6) is solved self-consistently [15]. Before the first iteration, the initial conditions are set to

$$m^{i=0}(k) = 0.15 + 0.4\cos\left(2\pi\frac{k}{K}\right) \tag{5.7}$$

and the magnetization of subsequent i^{th} iterations is given by

$$m^i(k) = m^{i-1}(k) + s\left[F\left(m^{i-1}(k)\right) - m^{i-1}(k)\right] \tag{5.8}$$

where s is a mixing parameter that determines the fraction of the difference between $F\left(m^{i-1}(k)\right)$ and $m^{i-1}(k)$ that is added to $m^{i-1}(k)$ in order to generate the next iterative solution. The value of s can be changed to ensure the stability of the iteration procedure, and the value chosen here is $s = 0.5$. The iterative process is continued until

$$\left|F\left(m^{i-1}(k)\right) - m^{i-1}(k)\right| < \zeta \tag{5.9}$$

for all k. Convergence in terms of ζ and the number of k points was tested and, based on that, ζ is chosen to be 10^{-11} and $K = 200$, as in Ref. [15].

Once self-consistency is achieved, the order parameter is calculated as

$$Q = \langle m \rangle = \frac{1}{K}\sum_{k=1}^{K} m(k) \tag{5.10}$$

143

for each selected T, P, h_0 or h_b value. Any other period-averaged quantity is calculated as

$$\langle f \rangle = \frac{1}{K} \sum_{k=1}^{K} f(k). \tag{5.11}$$

In the following, values of the field amplitude $\hbar_0$ and the bias field $\hbar_b$ are given in terms of normalized quantities $h_0 = \frac{\hbar_0}{\xi J}$ and $h_b = \frac{\hbar_b}{\xi J}$. The temperature has been fixed to $T/T_c = 0.8$, thus restricting the calculations to the parameter range in which only second-order DPTs occur and avoiding first-order DPTs that were observed in literature but may be an artifact of MFA [15, 16].

For the purpose of comparison, MFA calculations of corresponding equilibrium Ising models are also performed. Taking Eq. (5.4) as a starting point, the equilibrium MFA equation for the time-independent equilibrium m can be recovered by setting $\frac{dm(t)}{dt} = 0$ and removing the time-dependence of the applied magnetic field, leading to

$$m = \tanh\left[\frac{T_c}{T}\frac{1}{\xi J}(\hbar^{MF} + \hbar)\right]. \tag{5.12}$$

$\hbar^{MF}$ is given by Eq. (5.5), after the time dependence is removed, and $\hbar$ is related to a constant external magnetic field and has units of energy. Equation (5.12) has been solved numerically by the iterative process described above. The model reproduces the "conventional" thermodynamic phase transition (TPT) that the system undergoes at T_c transiting from a ferromagnetic to a paramagnetic phase upon increasing T (see Section 1.1.1).

5.3 Similarities between dynamic and thermodynamic phase transitions

Since the first report of the DPT [1], numerous works have explored its properties with Monte Carlo simulations, MFA-based calculations, and analytical derivations [8-11, 15, 17-19]. In addition, the phenomenon was addressed in a rather small number of experimental works [6, 7, 20-22]. Overall, a consensus emerged on the similarity between TPTs and DPTs based on the evidence that will be described in this section.

After the initial studies mentioned in Section 5.1, it was established that the symmetry breaking from the DPM ($Q = 0$) to the DFM ($Q \neq 0$) state occurs at a single point [1, 23] at $P = P_c$ and that this DPT is a second-order one, at least for the temperature and field amplitude values

144

relevant here [15]. The order parameter Q changes from nonzero to zero continuously upon increasing P towards P_c, following a power law behavior of the form

$$Q(P \to P_c^-) \propto (P_c - P)^{\beta_D} , \qquad (5.13)$$

where β_D is a critical exponent [11]. This power law can be compared to the one that holds for TPTs, where m is the order parameter that transitions from being nonzero to being zero at $T = T_c$ following

$$m(T \to T_c^-) \propto (T_c - T)^{\beta_T} \qquad (5.14)$$

with a critical exponent β_T [24], and therefore, DPTs and TPTs were found to belong to the same universality class [11, 25-28] supporting the symmetry argument given in [29]. Quantitative agreement between β_D and β_T was theoretically found for different kinetic spin models and their equilibrium counterparts, *e.g.*, for the Monte Carlo simulated 2-dimensional [11] and 3-dimensional KIM [28], as well as for the MFA. In the latter case, $\beta_D = \beta_T = 1/2$ [15, 19]. Accordingly, Q *vs.* P has the same shape as m *vs.* T close to the phase transition, as shown by the MFA calculations for the DPT and the TPT displayed in Fig. 5.2 (a) and (b) respectively with black solid lines.
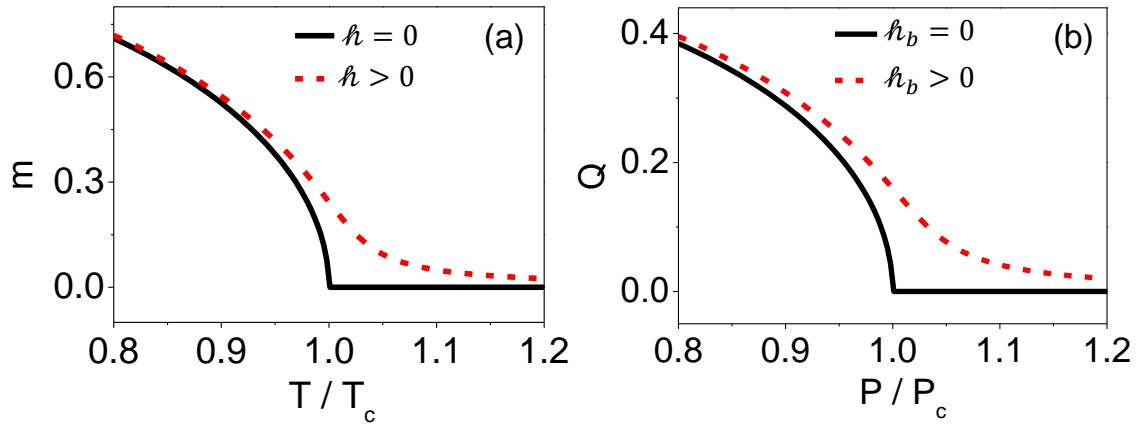

Figure 5.2 (a) Magnetization normalized to saturation magnetization *vs.* temperature for the equilibrium Ising model with zero and positive applied external fields H, in black solid and dashed red lines, respectively. (b) Equivalent plot for the order parameter of the DPT, Q, as a function of the period of the oscillating field, for zero and positive bias fields $\hbar_b$, in black solid and dashed red lines, respectively. $h_0 = 0.375$ and $T/T_c = 0.8$ for the data in (b).

Further similarities between TPTs and DPTs arise when a bias field $\hbar_b \neq 0$ is included in the field driving the DPT, as in Eq. (5.2). Several works found that $\hbar_b$ is the conjugate field of Q [15, 19, 30], or at least a large part of it [31], and that it plays the same role that an external magnetic field $\hbar$ plays in a TPT for m, namely, modifying the order parameter in both the ordered

and the disordered phase, especially near the phase transition. The effect of $\hbar_b$ onto $Q(P)$ and that of $\hbar$ onto $m(T)$ are shown in Fig. 5.2 (a) and (b) respectively, with red dashed lines. For $\hbar_b \neq 0$ the DPT is suppressed, because $\hbar_b$ is always able to induce some order $Q \neq 0$ in the system.

$\hbar_b$ was first introduced in experiments in Ref. [21] and its role was systematically explored experimentally in [22]. In this latter work, as well as in the results presented in Section 5.4, the magnetization of a uniaxial ferromagnetic Co sample similar to the ones described in Chapter 4 was measured as a function of time by means of the magneto-optical Kerr effect (MOKE), while an external field with a bias H_b and an oscillatory part of amplitude H_0 was applied along the EA of the sample[42]. In this case, MOKE measurements have been performed in a non-ellipsometric way (see Section 1.4.3), as opposed to the previous chapters where generalized magneto-optical ellipsometry (GME) has been used[43].

For each field cycle the field-projected MOKE signal *vs.* time was obtained and the period-averaged value Q was calculated, normalizing it to the maximum MOKE signal. In order to reduce the noise level, Q was averaged over several field cycles ν as

$$\bar{Q} = \frac{1}{C} \sum_{\nu=1}^{C} Q_{\nu},$$ (5.15)

where C is the number of field cycles considered for the averaging. In the following, a quantity averaged over C cycles measured under the same conditions of T, P, H_b, and H_0 is defined as

---

[42] In the description of the experimental work, H_0 and H_b have units of magnetic field and are related to $\hbar_0$ and $\hbar_b$ by a factor of $\mu_0 M_s$, where μ_0 is the vacuum permeability and M_s is the saturation magnetization of the sample.

[43] This is the case for a number of reasons. First, the magnitude to track is the magnetization along the applied field axis (which coincides with the EA), because it is the component of the magnetization that serves to construct the order parameter Q, and thus, there is no need to perform vector magnetometry. Second, GME assumes a reproducible magnetization reversal upon field reversal so that measurements taken at different polarizer and analyzer configurations can be analyzed jointly. However, near the DPT fluctuations arise and the behavior of the magnetization is not repeatable. In addition, the measurements are performed in real time, so GME is not suitable because it needs to perform a large number of data acquisitions. Finally, the magneto-optical behavior of the utilized samples is well-established and there is no need to utilize GME to separate optical and magneto-optical effects.

$$\bar{f} = \frac{1}{C} \sum_{\nu=1}^{C} f_{\nu}. \tag{5.16}$$

Measurements of $\bar{Q}$ were performed as a function of P and H_b, for different values of H_0 and at room temperature.

An exemplary $\bar{Q}(P, H_b)$ diagram obtained from Ref. [22] is shown in Fig. 5.3 (a). The critical point at $P = P_c$ and $H_b = 0$ is signaled with a black dot. For $P > P_c$ the system is in the DPM state and, upon applying $H_b \neq 0$, order is gradually induced in the system. However, for $P < P_c$, in the DFM phase, as H_b changes sign, the stable state of $\bar{Q}$ changes abruptly in a first order phase transition, while the state of $\bar{Q}$ with the opposite sign of H_b remains metastable leading to a hysteretic $\bar{Q}(H_b)$ behavior shown in Fig. 5.3 (b). The same behavior was observed in MFA calculations for a bulk system [22], as shown in Fig. 5.3 (c). For $P > P_c$, h_b modifies Q gradually, while for $P < P_c$ there is an abrupt change in Q at the $h_b = 0$ line. Accordingly, MFA calculations also reproduce the Q vs. h_b hysteresis in the DFM phase[44].

The features presented in Fig. 5.3 are reminiscent of those of the equilibrium IM, where m has a hysteretic behavior around $H = 0$ in the ferromagnetic phase at $T < T_C$ and in the paramagnetic phase at $T > T_C$, H gradually modifies m, which is zero for $H = 0$. At $(T = T_c, H = 0)$, a second order phase transition, the TPT, occurs.

It was also shown within MFA that, as $\hbar_b$ approaches zero at $P = P_c$, Q satisfies [15, 19]

$$Q(\tilde{H}_b \rightarrow 0) \propto \hbar_b^{\delta_D}, \tag{5.17}$$

a power-law with the same critical exponent as the equilibrium counterpart [24]

$$m(H \rightarrow 0) \propto \hbar^{\delta_T}. \tag{5.18}$$

$\delta_D = \delta_T$ as also shown for the two-dimensional KIM as compared to its equilibrium counterpart by means of Monte Carlo simulations [30]. Furthermore, an equation of state was derived within

---

[44] If Fig. 5.3 (b) and (d) are compared, one can see that in (d) Q keeps on increasing upon increasing h_b, while in (b) $\bar{Q}$ is stable. This is the case because, in the MFA simulations based on the Ising model, $\hbar_b$ is of the order the exchange interaction J in order to be able to reverse the spins. Therefore, the energy related to $\hbar_b$ is comparable to the thermal energy and its increase produces a significant change in the magnetization of the system. On the contrary, in experiments, the energy related to H_b is much smaller than the exchange interaction and the thermal energy and therefore does not significantly affect the maximum value of the magnetization.

MFA for the DPT, which was shown to be equivalent of that of the TPT [19], but a more general derivation beyond MFA remains an open issue. The existence of a conjugate field enables the definition of the dynamic susceptibility as[45]

$$\chi^D = \frac{dQ}{dh_b}.$$ (5.19)

χ^D is used in the following sections as an identification of the DPT, given that this susceptibility diverges (or, numerically, shows a peak with high values) at the phase transition point.
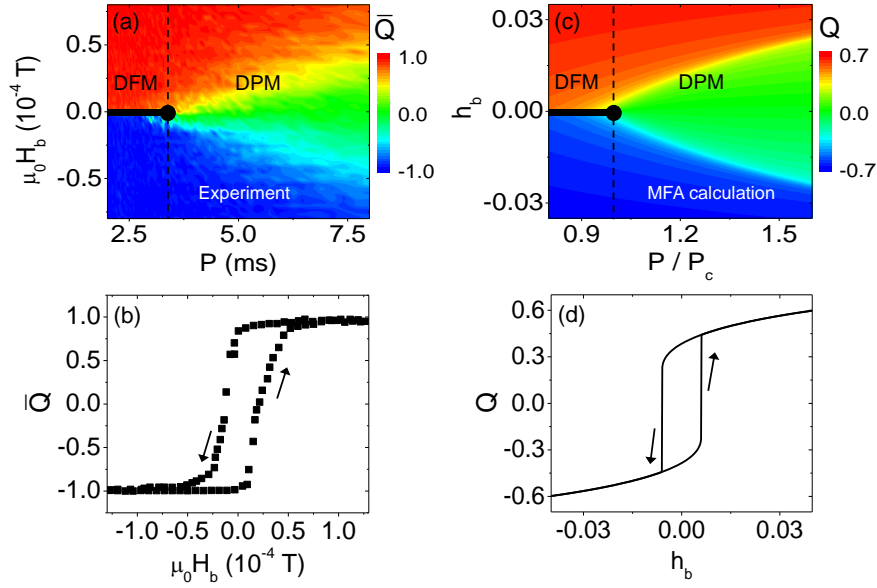

Figure 5.3 (a): Experimental and (c) MFA calculated color-coded maps of the DPT order parameter as a function of the period of the oscillating field and of the bias field. Color scales are on the right hand side of each subplot. For (a) $\mu_0 H_0 = 29.8 \times 10^{-4}\,T$; for (c) $h_0 = 0.1$. Dynamic paramagnetic (DPM) and dynamic ferromagnetic (DFM) phases are separated by a vertical dashed line. The black dot represents the DPT point, and the horizontal solid line at $H_b = 0$ and $h_b = 0$ respectively indicates the first order phase transition line. (b) and (d): Hysteretic behavior for $P < P_c$ of the order parameter as a function of the bias field, in experiments and MFA calculations respectively. The arrows indicate the direction in which the field was swept.

All in all, the phase diagram of the DPT has been shown to be consistent with that of the TPT over the last years, with a critical point of a second-order phase transition at $(P = P_c, H_b = 0)$ and $(T = T_c, H = 0)$ respectively and a first-order phase transition line at $H_b = 0$ for $P < P_c$ and at $H = 0$ for $T < T_c$ respectively. In addition, the KIM and equilibrium Ising model correspond to the same universality class and the agreement of scaling laws and critical exponents for both models has been shown numerically within the MFA and for Monte Carlo simulations.

---

[45] For experiments, χ^D is calculated as $d\bar{Q}/dH_b$ by means of finite differences.

Nevertheless, critical exponents of the DPT have not been measured experimentally, and thus no comparison with the experimentally obtained critical exponents of the TPT has been possible to date.

Even though all prior evidence seemed to indicate a full correspondence between DPTs and TPTs, the following sections present very significant discrepancies between both transitions that were found as part of this thesis work.

5.4 Metamagnetic anomalies near dynamic phase transitions

All findings presented so far indicate that DPTs and TPTs are equivalent, as all features found for the dynamic order parameter Q have a counterpart in the equilibrium order parameter m. However, a close look at the experimental data in Ref. [22] already points to some discrepancies between equilibrium and dynamic phase diagrams in the vicinity of the critical point. As it can already be seen in the data of Figs. 5.3 (a) and (b), the effect of H_b in the DPM phase is a gradual increase the absolute value of Q. However, rather steep changes of $|Q|$ at specific $\pm|H_b|$ points, whose value depends on P, occur. For a better identification, the susceptibility and the fluctuations of the order parameter are evaluated. Fluctuations are determined for experimental data from the measurements acquired for several field cycles as

$$\sigma^D = \sqrt{\overline{(Q^2)} - (\bar{Q})^2} \,, \qquad (5.20)$$

where the definition in Eq. (5.16) has been used, and χ^D is calculated by finite differences from $\bar{Q}$ measurements taken at adjacent H_b values.

Figure 5.4 shows side by side $\bar{Q}$, χ^D and σ^D as a function of P and H_b obtained for two different values of H_0 specified on the right-hand-side of the figure. There is a clear qualitative correspondence between χ^D and σ^D that stems from a generalization of the fluctuation-dissipation theorem for dynamic systems [29], although σ^D has a better signal-to-noise ratio. The highest values of the fluctuations and the susceptibility (red and orange color in the color maps) occur in the close vicinity of the critical point: χ^D and σ^D are maximal at the DPT. In addition, in the DPM phase two sidebands of high values of χ^D and σ^D are present (green color). Such sidebands are symmetric with respect to $H_b = 0$ and occur at the same $\pm H_b(P)$ positions where $\bar{Q}$ changes most abruptly. In the following, these specific H_b values are denoted

as H_b^m. At such H_b^m values, the system shows a sudden increase of the order parameter that occurs due to a small increase of the conjugate field, *i.e.*, the DPT analogue of metamagnetism. Most importantly, these metamagnetic fluctuations are absent in conventional TPTs of the equilibrium IM [24] and constitute a deviation in the equivalency picture between TPTs and DPTs presented in the previous section.
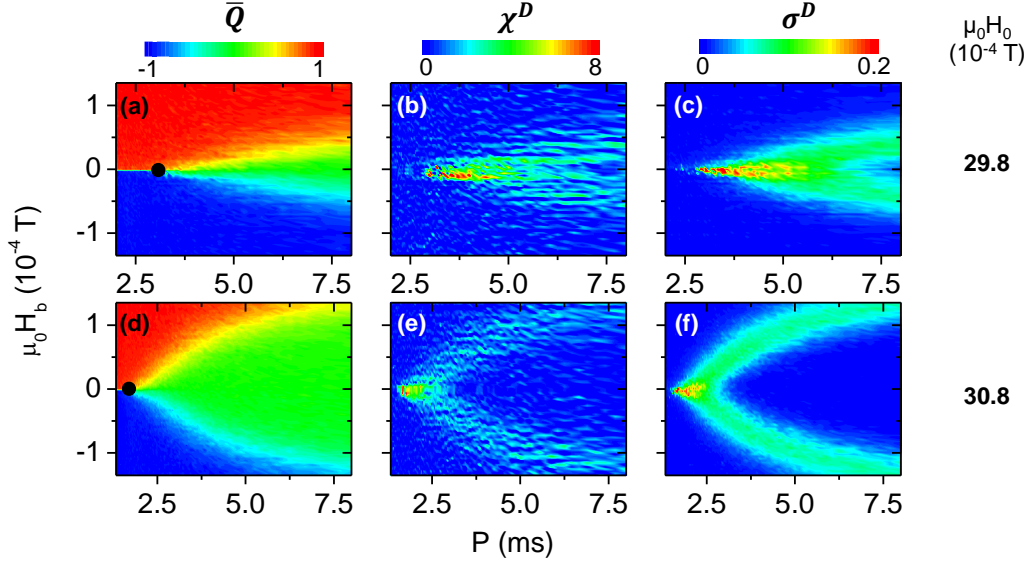

Figure 5.4 Color-coded maps of experimental data of the order parameter $\bar{Q}$ in (a) and (d), of the susceptibility χ^D in (b) and (e), and of the fluctuations σ^D in (c) and (f), all of them as a function of the period and bias field, for two different amplitudes H_0 of the oscillating field indicated on the right. The critical point in each H_0 case is signaled as a black dot in (a) and (d). The color bar for each of the magnitudes is placed on top of each column.

In Fig. 5.4 one can also note the effect of H_0. A higher H_0 corresponds to a lower P_c, *i.e.*, faster critical dynamics. The sidebands in χ^D and σ^D also have a strong H_0-dependence: on the one hand, their opening angle increases as H_0 increases, *i.e.*, for larger H_0, at a specific P, $|H_b^m|$ gets larger; on the other hand, the values of χ^D and σ^D of the sidebands decrease with increasing H_0, as one can see from the less intense green color of the sidebands in Fig. 5.4 (e) and 5.4 (f) as compared to those in Fig. 5.4 (b) and 5.4 (c) respectively.

In order to better understand the properties of these metamagnetic fluctuations and to test whether their occurrence is something intrinsic to the KIM, MFA calculations for a bulk system were performed for different amplitudes of the oscillating field h_0. Fig. 5.5 shows the h_0 dependence of P_c: as for the experimental data, high h_0 leads to small P_c, *i.e.*, fast critical dynamics, and low h_0 to large P_c, *i.e.*, slow critical dynamics. In the following, the period axis for MFA calculations is normalized to the P_c value corresponding to the specific h_0 in each case.
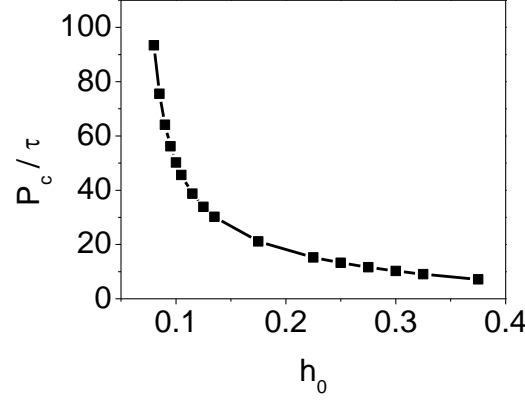
Figure 5.5 Dependence of P_c with h_0 from MFA calculations.

Figure 5.6 shows MFA-calculated $Q(P, h_b)$ diagrams for different h_0 values and, below them, the calculated susceptibilities $\chi^D(P, h_b)$. Fluctuations are suppressed within the MFA and therefore, σ^D cannot be calculated. The corresponding TPT (equilibrium) plots for the order parameter $m = M/M_s$ and the susceptibility χ calculated within the MFA by solving Eq. (5.12) for several T and $\hbar$ have been plotted in Figs. 5.6 (e) and (j) for comparison. As seen in Fig. 5.6 (j), the equilibrium susceptibility χ is maximal at the critical point, but displays no metamagnetic tendencies in the form of sidebands. In the DPT case, as observed in the experimental data, the susceptibility sidebands shown in Figs. 5.6 (f)-(i) are large for low h_0 and it gradually decrease in value as h_0 increases. At high enough h_0, as exemplified by the data in Fig. 5.6 (i), the sidebands are almost undetectable and a qualitative equivalence with the TPT is recovered. The MFA calculations also reproduce the opening of the sidebands observed in the experiments. Crucially, these metamagnetic tendencies do not constitute a divergence of the susceptibility, so they are not related to a second-order phase transition.
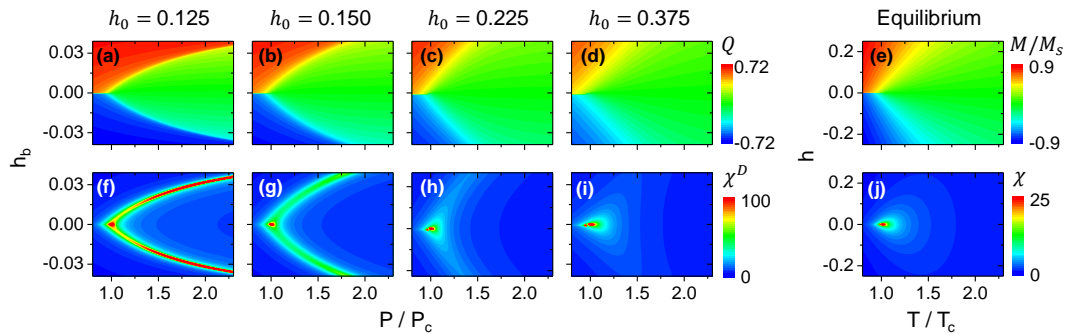

Figure 5.6 Color-coded maps of MFA calculated $Q(P, h_b)$ in (a)-(d) and corresponding $\chi^D(P, h_b)$ in (f)-(i) for different values of $h_0 = \hbar_0/6J$ given on the top. (e) and (j) $m(T, h)$ and corresponding $\chi(T, h)$ color-coded maps for the thermodynamic equilibrium IM case calculated within MFA, where $h = \hbar/6J$. The color scale for (a)-(d) is next to (d); that for (f)-(i) is next to (i). The color scale for (e) and (j) is next to them respectively.

151

χ^D curves at constant h_b or P values are plotted in Fig. 5.7 as a function of P and h_b respectively. The equivalent curves for the TPT are also shown. First, Fig. 5.7 (a) shows χ^D for a fixed h_b as a function of P for two given h_0, shown as black and red curves. In both cases the data show a single χ^D peak at a given P value. As a comparison, the TPT susceptibility χ is shown for a fixed h as a function of T (see top horizontal axis) as a blue line, and it also shows a single peak at a given T. On the other hand, Figs. 5.7 (b) and (c) show χ^D as a function of h_b for fixed values of P, $P/P_c = 1.1$ in Fig. 5.7 (b) and $P/P_c = 1.7$ in Fig. 5.7 (c), again for two values of h_0. In the case shown in Fig. 5.7 (c), both χ^D curves have a local minimum at $h_b = 0$, while the TPT related χ curve for fixed $T/T_c = 1.7$ as a function of h, shown as a blue line, has a maximum at $h = 0$, as shown in the inset. Thus, the behaviors of the TPT and DPT are qualitatively different at this distance from the critical point, $T/T_c = 1.7$ for the TPT and $P/P_c = 1.7$ for the DPT. In addition, the black curve corresponding to χ^D for $h_0 = 0.125$ shows in the h_b range of Fig. 5.7 (c) two peaks at symmetric h_b^m values. In the case displayed in Fig. 5.7 (b), which is closer to the critical point because $T/T_c = P/P_c = 1.1$, the red curve of χ^D for $h_0 = 0.375$ has a maximum for $h_b = 0$ and thus behaves qualitatively as the TPT χ vs. h curve, shown as a blue line. Therefore, it seems that the equivalence between DPT and TPT is recovered close enough to the critical point. However, χ^D vs. h_b for $h_0 = 0.125$, shown in black in Fig. 5.7 (b), still shows a minimum at $h_b = 0$ and two peaks at h_b^m values that are smaller than the h_b values at which χ^D has a peak in the corresponding curve in Fig. 5.7 (c). For the $h_0 = 0.125$ χ^D to behave qualitatively as the TPT curve, with a maximum at $h_b = 0$, one needs to go even closer to the critical point. The conclusion of Fig. 5.7 is that, as P/P_c decreases, the behavior of the DPT converges towards the behavior of the TPT; however, the P/P_c value at which the χ^D minimum at $h_b = 0$ turns into a maximum depends on h_0, and for lower h_0 one needs to get closer to the critical point to achieve the equivalence between DPT and TPT.
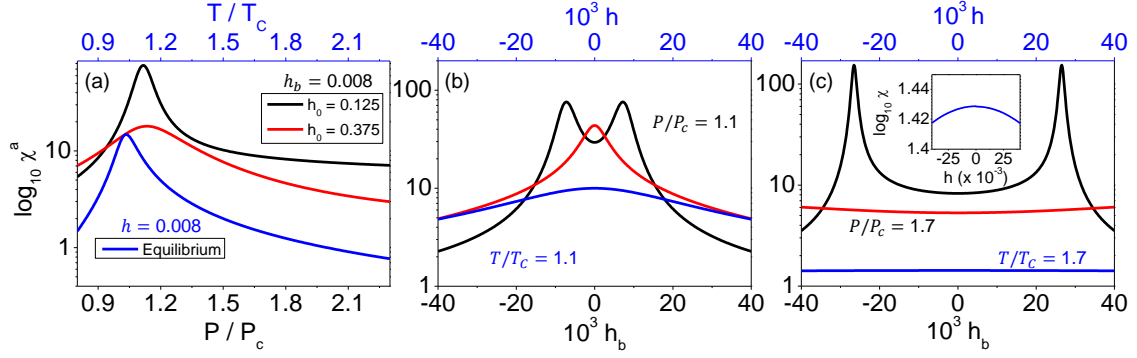
Figure 5.7 Susceptibility curves for two DPT cases ($h_0 = 0.125$ in black and $h_0 = 0.375$ in red) and for the TPT case (in blue). χ^a in the legend of the vertical axis in (a) stands for χ in the TPT case and for χ^D in the DPT cases. (a) Susceptibility χ^D *vs.* P for the DPT curves (bottom axis); χ *vs.* T for the TPT curve (top axis). (b) and (c) Susceptibility *vs.* conjugate field, *i.e.*, h_b for the DPT curves (bottom axis) and h for the TPT curve (top axis) for fixed $P/P_c = 1.1$ in (b) and $P/P_c = 1.7$ in (c), ($T/T_C = 1.1$ and 1.7 respectively for the TPT curves). All DPT curves were calculated for a temperature of $T = 0.8\,T_C$. Inset in (c): Zoom of the χ *vs.* h curve around $h = 0$.

The presence of anomalous metamagnetic tendencies in the DPM phase and their dependence with h_0 can be understood in terms of an interplay between the energetics and the dynamics of the system. Figures 5.8 (a) and (d) show schematically the MFA equilibrium energy $\mathcal{E}$ of the magnetic system under an applied field $+h_0$ (solid curve) and $-h_0$ (dashed curve), *i.e.*, the two extreme values of the oscillating field $h(t)$, for high h_0 in (a) and low h_0 in (d). As $h(t)$ oscillates, the stable state of the magnetization shifts and, as long as $h(t)$ is slow enough ($P > P_c$), $m(t)$ shifts symmetrically from the right-hand-side well ($m > 0$) to left-hand-side well ($m < 0$) and back in a steady-state dynamic behavior that leads to $Q = 0$[46]. In the high h_0 case shown in Fig. 5.8 (a), the metastable wells are relatively shallow, and thus $m(t)$ can follow $h(t)$ rather easily, making the shape of $m(t)$ fairly sinusoidal as may be seen in the red curve of Fig. 5.8 (c). Conversely, in the low h_0 case in Fig. 5.8 (d) the metastable states of antiparallel m *vs.* h alignment have a significant depth, and the magnetic system exhibits a certain lifetime in them, leading to a deviation from a purely sinusoidal $m(t)$, as shown by the red curve in Fig. 5.8 (f).

---

[46] If $h(t)$ is too fast, for $P < P_c$, the systems has less time to react to the change of energy produced by the change of the external field and will remain in the same parameter half-space ($m > 0$ or $m < 0$, depending on how the system was initialized), leading to a nonvanishing order parameter Q. This is what occurs in the DFM phase.
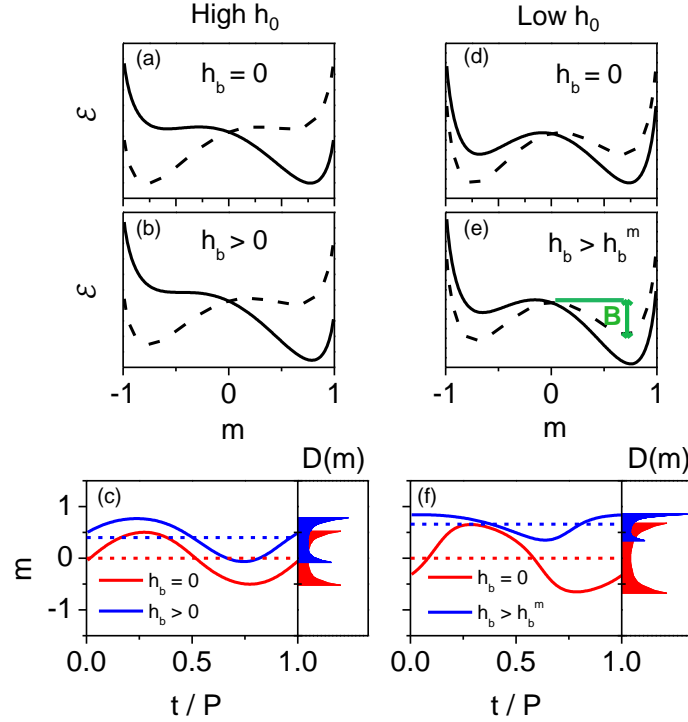
153

Figure 5.8 (a) and (d) Energy landscape for $(h_0 + h_b)$ (solid curve) and $(-h_0 + h_b)$ (dashed curve) applied fields, for large and small h_0 respectively, with $h_b = 0$. (b) and (e) Same as (a) and (d) with $h_b > 0$. (c) and (f) Steady state m *vs.* t dependence. Red curves show the $h_b = 0$ case, and blue curves the $h_b > 0$ case. The horizontal dotted lines indicate the Q values for each respective $m(t)$ curve. The panels to the right represent the distribution of the magnetization $D(m)$, *i.e.*, the probability to find the dynamic system at a magnetization value m.

When a small positive $h_b < h_b^m$ is additionally applied, $m(t)$ curves shift vertically with their shape being primarily unperturbed (not shown in the figure). However, in the low h_0 case, $\mathcal{E}$ is more substantially modified by h_b. Figures 5.8 (b) and 5.8 (e) show, in the high and low h_0 cases respectively, $\mathcal{E}$ under an applied field $+h_0 + h_b$ (solid curve) and $-h_0 + h_b$ (dashed curve). The metastable energy barrier B sketched in Fig. 5.8 (e) is affected, *i.e.*, the one that separates the metastable $m > 0$ from the stable $m < 0$ states when $h = -h_0 + h_b$. At $h_b = h_b^m$, B becomes so high that, for a given P, the system does not have time to get to the $m < 0$ state during the negative half-cycle of the field (assuming it was initialized in the $m > 0$ state). The system remains effectively trapped in the metastable $m > 0$ state, thus leading to a significant of the $m(t)$ curve, as can be observed in the blue curve of Fig. 5.8 (f). This leads to an anomalously sharp metamagnetic increase in Q and to the corresponding large value of χ^D. The panel on the right hand side of Fig. 5.8 (f) shows the $D(m)$ probability to find the system at a given magnetization value m for the $h_b = 0$ (red) and $h_b > h_b^m$ (blue) cases and it shows that for low h_0, the shape of $D(m)$ is greatly affected by $h_b > h_b^m$. On the other hand, $\mathcal{E}$ is not very much affected in the high

154

h_0 case, as may be seen by comparing Figs. 5.8 (a) ($h_b = 0$) and 5.8 (b) ($h_b > 0$). The $m > 0$ state is now favored leading to a vertical shift of $m(t)$, but the fairly sinusoidal shape is conserved[47], as is visible in the blue curve of Fig. 5.8 (c). The panel on the right hand side of Fig. 5.8 (c) shows that both $D(m)$ distributions have a similar shape, and they only show a vertical shift with h_b. This argument thus explains why metamagnetic tendencies are stronger for low h_0. It also explains why, for a given h_0 value, the metamagnetic onsets occur at larger h_b^m values for larger P: the slower the field (larger P), the more time the system has to escape the metastable state of antiparallel m vs. h, so that a larger h_b is necessary to give rise to the metastable trapping. This is in agreement with the sideband shape found in Figs. 5.4 and 5.6. In addition, one can also understand why, for a fixed P/P_c ratio, increasing h_0 leads to an increase in h_b^m: the higher h_0 is, the larger h_b needs to be to induce a noticeable change in $\mathcal{E}$, and thus create the possibility for metastable trapping.

Figures 5.8 (c) and (f) seem to point that a stronger non-sinusoidal shape of $m(t)$ is related to larger metamagnetic tendencies. In order to analyze this in greater detail, a Fourier analysis was performed. The coefficients of the Fourier series

$$c_n = \frac{1}{P} \int_0^P e^{-i\frac{2\pi n}{P}t} m(t)dt \tag{5.21}$$

were calculated for $m(t)$ curves for different P and h_b values, and for two h_0 cases. n in Eq. (5.21) stands for the order of the harmonics. Figure 5.9 shows $|c_2|^2$, the square of the amplitude of the $n = 2$ harmonic, as a function of P and h_b for $h_0 = 0.375$ in (a) and for $h_0 = 0.125$ in (b) using the same color scale. Clearly, $|c_2|^2$ is much lower for the $h_0 = 0.375$ case. Higher order harmonics are also very small. For $h_0 = 0.125$, the $|c_2|^2(P, h_b)$ diagram resembles that of $\chi^D(P, h_b)$ in Fig. 5.6 (f), with the maxima of $|c_2|^2$ occurring at the points where the χ^D onset arises. This relates the Fourier spectrum of the time-dependent magnetization to the occurrence of susceptibility sidebands and verifies the qualitative picture observed in Figs. 5.8 (c) and (d).

[47] Eventually, at a sufficiently high $h_b > 0$, even in the high h_0 case the magnetization could remain trapped in the metastable state, but at that juncture the Q induced by h_b will be already that large that the change in the susceptibility will not be as dramatic as in the low h_0 case and will occur at much larger h_b values.
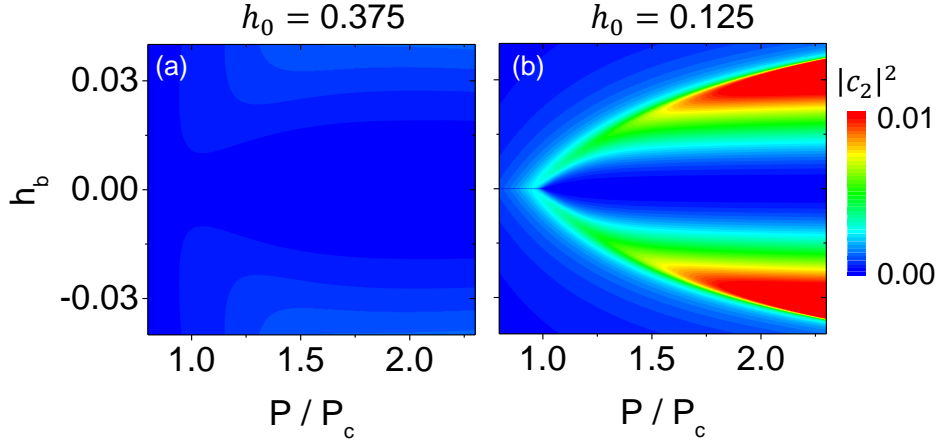
Figure 5.9 Squared amplitude of the second order Fourier harmonic of $m(t)$ *vs.* P and h_b, for $h_0 = 0.375$ in (a) and for $h_0 = 0.125$ in (b).

The presence of metamagnetic anomalies in the DPM phase of the KIM and their non-universal, h_0-dependent character constitutes a key difference with respect to the equilibrium Ising model. As already discussed in conjunction with Fig. 5.7, when h_0 is high, the susceptibility in the DPT for $P > P_c$ has the same qualitative behavior as that of the TPT in a rather extended region in the vicinity of the DPT critical point. Nevertheless, for low h_0, the P-region in which the DPT and the TPT susceptibilities behave in the same manner shrinks very significantly. This reduction of the region in which the equivalency between DPT and TPT holds does not only occur in the DPM phase; it also affects the DFM phase and has a crucial impact on the determination of critical exponents.

In order to determine the β_D critical exponent defined in Eq. (5.13) for the MFA calculated data, $Q(P, h_b = 0)$ datasets were fitted using $Q = A p^{\beta_D} \Theta_H(P_c - P)$, where $p = \frac{P_c - P}{P_c}$ and Θ_H is the Heaviside function. Datasets with the same number of data points but in different ranges of p between $-|p_{max}| \leq p \leq |p_{max}|$ were fitted and the corresponding β_D extracted. The difference of the fitted β_D with the expected one for the MFA (Gallardo2012), *i.e.*, $\beta_D = \frac{1}{2}$, is shown as a function of half the size of p_{max} in Fig. 5.10. For the lowest analyzed h_0 the fitted critical exponent only converges to the expected value for $|p_{max}| < 10^{-3}$, while for higher h_0, $\beta_D = \frac{1}{2}$ for $|p_{max}| = 10^{-2}$.

This observation becomes very relevant when addressing the experimental quantification of critical exponents. To date, experiments on DPTs have only been conducted in the high P, low h_0 regime, which is the exact same regime for which the size of the critical region is severely reduced.

Hence, the determination of DPT critical exponents from experimental data has not yet been possible. On the other hand, MFA calculations for sufficiently high h_0, as shown in Fig. 5.6 (i), demonstrate that metamagnetic tendencies can become extremely small and that qualitative agreement with the TPT behavior can be recovered. However, all the experimental data presented here and in [32] show relevant metamagnetic tendencies, because the experimentally accessible low h_0 regime is the one in which metamagnetic tendencies are most pronounced.
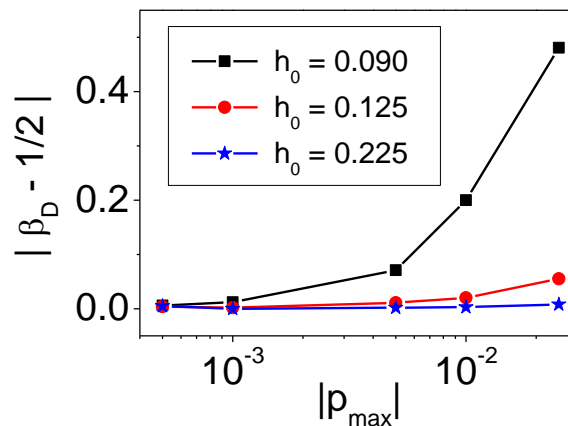

Figure 5.10 Deviation from the expected MFA β^D critical exponent for $Q(P)$ datasets fitted in different $-|p_{max}| \leq p \leq |p_{max}|$ ranges as a function of $|p_{max}|$, for different values of h_0. Extracted from [32].

5.5   Conclusions and outlook

The dynamic response of a ferromagnetic Ising-like system to an external oscillating magnetic field has been studied by means of magneto-optical Kerr effect experiments and numerical calculations based on the mean-field approximation. Upon varying the period of the driving field a dynamic phase transition (DPT) is observed, and the phase space near the critical point has been characterized. After reviewing many of the similarities between DPTs and thermodynamic phase transitions (TPTs), major discrepancies between the DPTs and TPTs are described.

Experiments were made to measure the dynamic order parameter as a function of the period of the oscillating field and the strength of a constant bias field. In the vicinity of the critical point metamagnetic fluctuations were observed in the dynamically disordered phase at finite bias field values. The experimentally observed metamagnetic tendencies were reproduced by numerical calculations based on the kinetic Ising model. Importantly, this behavior has no counterpart in the conventional equilibrium Ising model and, moreover, highly depends on the amplitude of the oscillating external field H_0 driving the DPT, which determines the speed of the critical dynamics.

For fast critical dynamics corresponding to high H_0 values, metamagnetic tendencies are weaker and occur at higher values of the bias field than for the high P_c/τ, low H_0, regime. Metamagnetic tendencies are explained in terms of an interplay between the energetics and the kinetics of the system in conjunction with Fig. 5.8.

In turn, the strength of these metamagnetic tendencies is related to the size of the critical region, *i.e.*, the region of the phase diagram where critical exponents can be reliably extracted. In the slow dynamics case, which is actually the regime in which most experiments are performed, the critical region is drastically reduced, thus hindering the experimental extraction of critical exponents.

The conclusions drawn here could be translated to fields other than magnetism; indeed, the response of a system to an external time-dependent driving force lies at the core of numerous phenomena in our everyday life [33], such as the activity of our brains [34] or the interaction of complex biological systems [35], where spatiotemporal patterns are formed. Just as the equilibrium Ising model, which was originally devised for the study of ferromagnetism, is now extensively used in the field of statistical mechanics in a wide range of disciplines [36], its dynamic counterpart, the kinetic Ising model (KIM), can be applied to many areas [37, 38], although the experiments presented here are limited to the ferromagnetism case and the calculations have been interpreted within the framework of magnetism.

References

[1] T. Tomé and M. J de Oliveira, Phys. Rev. A **41**, 4251 (1990).
[2] M. Rao, H. R. Krishnamurthy, and R. Pandit, Phys. Rev. B **42**, 856 (1990).
[3] M. Rao, H. R. Krishnamurthy, and R. Pandit, J. Appl. Phys. **67**, 5451 (1990).
[4] W.S. Lo, R.A. Pelcovits, Phys. Rev. A **42**, 7471 (1990).
[5] S. Sengupta, Y. Marathe, and S. Puri, Phys Rev. B **45**, 7828 (1992).
[6] Y. L. He and G. C. Wang, Phys. Rev. Lett. **70**, 2336 (1993).
[7] Q. Jiang, H. N. Yang, and G. C. Wang, Phys. Rev. B **52**, 14911 (1995).
[8] M. Acharyya, B.K. Chakrabarti, Phys. Rev. B **52**, 6550 (1995).
[9] M. Acharyya, Phys. Rev. E **56**, 1234 (1997).
[10] M. Acharyya, Phys. Rev. E **56**, 2407 (1997).
[11] S. W. Sides, P. A. Rikvold, and M. A. Novotny, Phys. Rev. Lett. **81**, 834 (1998).
[12] B.K. Chakrabarti and M. Acharyya, Rev. Mod. Phys. **71**, 847 (1999).
[13] P. Riego, P. Vavassori, and A. Berger, Physica B **549**, 13 (2018).
[14] R. J. Glauber, J. Math. Phys. **4**, 294 (1963).
[15] O. Idigoras, P. Vavassori, and A. Berger, Physica B **407**, 1377 (2012).
[16] G. Berkolaiko and M. Grinfeld, Phys. Rev. E **76**, 061110 (2007).
[17] M. F. Zimmer, Phys. Rev. E **47**, 3950 (1993).
[18] G. M. Buendía, P. A. Rikvold, Phys. Rev. E **78**, 051108 (2008).

[19] R. A. Gallardo, O. Idigoras, P. Landeros, A. Berger, Phys. Rev. E **86**, 051101 (2012).

[20] J. -S. Suen, J. L. Erskine, Phys. Rev. Lett. **78**, 3567 (1997).

[21] D. T. Robb, Y. H. Xu, O. Hellwig, J. McCord, A. Berger, M. A. Novotny, P. A. Rikvold, Phys. Rev. B **78**, 134422 (2008).

[22] A. Berger, O. Idigoras, P. Vavassori, Phys. Rev. Lett. **111**, 190602 (2013).

[23] J. F. F. Mendes and J. S. Lage, J. Stat. Phys. **64**, 653 (1991).

[24] N. Goldenfeld, *Lectures on phase transitions and the renormalization group* (Addison-Wesley, 1992).

[25] S.W. Sides, P.A. Rikvold, and M.A. Novotny, Phys. Rev. E **59,** 2710 (1999).

[26] G. Korniss, C.J. White, P.A. Rikvold, and M.A. Novotny, Phys. Rev. E **63**, 016120 (2000).

[27] H. Fujisaka, H. Tutu, and P.A. Rikvold, Phys. Rev. E **63**, 036109 (2001).

[28] H. Park, M. Pleimling, Phys. Rev. E **87**, 032145 (2013).

[29] G. Grinstein, C. Jayaprakash, and Y. He, Phys. Rev. Lett. **55**, 2527 (1985).

[30] D. T. Robb, P. A. Rikvold, A. Berger, and M. A. Novotny, Phys. Rev. E **76**, 021124 (2007).

[31] D. T. Robb and A. Ostrander, Phys. Rev. E **89**, 022114 (2014).

[32] P. Riego, P. Vavassori, and A. Berger, Phys. Rev. Lett. **118**, 117202 (2017).

[33] M.C. Cross, P.C. Hohenberg, Rev. Mod. Phys. **65**, 851 (1993).

[34] G. Schöner, J.A.S. Kelso, Science **239**, 1513 (1988).

[35] I. Shmulevich, S.A. Kauffman, M. Aldana, Proc. Natl. Acad. Sci. USA **102**, 13439 (2005).

[36] D. Stauffer, Am. J. Phys. **76**, 470 (2008).

[37] Glenn H. Fredrickson and Hans C. Andersen, Phys. Rev. Lett. **53**, 1244 (1984).

[38] K. Binder, Z. Phys. **267**, 313 (1974).

Chapter 6

Conclusions and outlook

Despite the variety of topics covered in the thesis, ranging from spintronics to ferromagnetic/non-magnetic interfaces and dynamical behavior of ferromagnets, some general conclusions can be drawn related to the entirety of the work.

The common characterization technique for all the phenomena has been the magneto-optical Kerr effect (MOKE). In particular, a specific technique based upon it, namely the generalized magneto-optical ellipsometry (GME) has been utilized extensively. For the purpose of adapting GME to the experiments performed in this thesis, instrumental advances, as well as modifications of the measurement and analysis routine have been performed. On one hand, the GME setup has been adapted to include the possibility to invert the magnetic state of the sample by means of an electric current *via* the spin Hall effect (SHE). On the other hand, this is the first work where three-dimensional vector magnetometry is demonstrated with GME. In order to do so, measurements around two non-equivalent crossing point of the polarizers (*s-p* as well as *p-s*) have been performed to be able separate longitudinal and polar MOKE unambiguously, which otherwise have the same symmetry around the individual crossing points of the polarizers. Related to this aspect, the procedure for the data analysis has been optimized.

Furthermore, GME has been proved to be a very versatile and robust methodology, enabling a very precise separation of MOKE-related signals from purely optical or spurious signals. This capability has enabled to identify that the GME signals detected in a current-driven high spin-orbit coupling metal, such as Pt or W, are primarily not related to the SHE-induced spin accumulation at the surface, but to experimental inaccuracies and purely optical reflectivity changes arising from Joule heating. In any case, the separation of magneto-optical and non-magneto-optical signals by GME is a general feature that can be widely utilized to improve the sensitivity of MOKE experiments, in particular in systems where MOKE is expected to be very small and comparable to potential non-MOKE-related false signals that can be synchronous with the magnetic field, current, or any other modulation used for the experiment, all of which can give rise to a signal component that could otherwise be erroneously interpreted to stem from MOKE.

Despite the excellent sensitivity achieved thanks to GME, it was not possible to detect MOKE signals related to the SHE in metals [1], although it was possible to establish upper limits for the expected Kerr rotation for each of the studied materials. Such limits are orders of magnitude smaller than the previously reported Kerr rotation values [2], which probably arise due to a misinterpretation of spurious false signals as MOKE signals. Following this 2016 GME experimental work [1], the required resolution to detect SHE-induced MOKE signals in metals appears to have been subsequently achieved in a non-ellipsometric MOKE setup thanks to current modulation and lock-in detection [3]. This suggests a possible way to decrease the noise level and illustrates a pathway to further improve the sensitivity of the GME setup utilized in this thesis, where the current was applied to the sample in a quasi-DC mode. The combination of GME with lock-in detection could further improve the resolution limit of this technique and lead to the detection of small SHE-induced spin accumulations *via* MOKE in an unambiguous way, given GME's ability to eradicate false positives.

A further outlook for the utilization of GME to study phenomena relevant for spintronics is the detection of spin transfer torques in bilayers of ferromagnets and non-ferromagnets by means of three-dimensional vector magnetometry. In these systems, a current applied along the non-magnetic material generates a spin current that creates a torque in the ferromagnetic layer, producing a change in its magnetization. This phenomenon has been already detected using MOKE [4] and should be easily detectable with the GME setup utilized in this thesis without the need for further improvement of its sensitivity, as the changes in magnetization occur in a ferromagnet, where the number of spin polarized electrons is large if compared to the spins accumulated at non-magnetic interfaces due to the SHE.

The other important feature of GME, namely the ability to perform three-dimensional vector magnetometry, has also been exploited. Most relevantly, GME can separate the MOKE effects related to the three components of the magnetization in a self-calibrated way, with a self-correction of possible misalignments. This occurs because the components of the magnetization giving rise to different MOKE effects, which can be separated by the symmetries with respect to the angles of the polarizer and the analyzer in GME, are defined with respect to the plane of the sample and the plane of incidence, which are given by the experiment itself and therefore, one can rule out that this signal stems from a misalignment of the setup. This is in contrast with what occurs in other kinds of magnetometry methods, where, especially when one

162

of the components of the magnetization is small, it is difficult to separate effects that come from a misalignment of the sample in the setup from actual magnetization orientation changes. Again, it should be stressed that to carry out three-dimensional vector magnetometry that unambiguously separates longitudinal and polar MOKE, this thesis demonstrates that measurements around two non-equivalent crossing points of the polarizers need to be performed.

This capability of GME has been crucial for the characterization of the samples studied in Chapter 4. From the fabrication perspective, such samples are also worth further consideration, given that they result from an innovative fabrication methodology developed in this thesis. Specifically, a method to deposit films with a spatial gradient of thickness along the length of the substrate has been established. This has been achieved by means of sputter deposition, in particular, by modifying the tilt of the sputtering gun so that a different density of atoms is deposited in different positions on the substrate. In this thesis, Ru wedge-like layers have been deposited on top of yet another non-trivial layer sequence, namely, a heteroepitaxial growth sequence that allows one to obtain hexagonal closed packed Co films with in-plane uniaxial anisotropy. Such Co layers, in the absence of a Ru overcoat, display a well-defined reversal path upon the application of an in-plane magnetic field that is easily described by a macrospin, which rotates in the plane of the sample, and thus constitutes an excellent testbed to investigate the effects of the Ru overcoat.

In combination with the capabilities of GME, these carefully designed samples with Ru wedge-type overcoats have led to the observation of polar MOKE signals in remanence that are absent in samples without Ru. Not only this, otherwise nominally identical samples, but for which the Ru overcoat is homogeneous in thickness instead of being deposited in an oblique fashion leading to the wedge shape, do not show any polar MOKE. The presence of the Co/Ru interface with a tilted deposition of Ru therefore proves to be crucial for the out-of-plane tilt of the magnetization. A hypothesis to explain this phenomenon is formulated: the tilted deposition of Ru leads to an inhomogeneous distribution of Ru atoms on the Co surface that mediate a periodically modulated Dzyaloshinskii-Moriya interaction (DMI) between the Co spins, while in the case of the homogeneous Ru overcoat the DMI is homogeneous. Based upon a spin model that incorporates the local variation of DMI, the experimental results have been qualitatively reproduced, including their dependence on the magnetic field strength and on the orientation of the crystallographic easy axis with respect to the applied field. Therefore, the spatially modulated

DMI is a plausible explanation for the observation of a net rotation of the magnetization. This observation could open a pathway to the design of spin textures *via* the deposition of inhomogeneous overcoats on top of ferromagnetic materials.

However, it would be important to determine the atomistic microscopic structure of the Co/Ru interface and to elucidate what the difference is between the overcoats with the tilted deposition and the homogeneous ones. In addition, the knowledge of the atomic positions of the Co and Ru atoms would allow one to determine the DMI vectors between Co spins based on symmetry considerations [5]. Plus, it would be interesting to further characterize these samples magnetically, *e.g.*, by means of Brillouin light scattering, a technique that probes spin waves, which are known to be affected by DMI in a specific manner [6]. Interestingly, the observed polar MOKE effect seems to be not uncommon, given that it has also been detected for Co/Pt interfaces, and again only when the Pt overcoats are deposited in a tilted fashion and not when their deposition is homogeneous. Possible reasons for the effect not having been reported in literature so far are multiple, *e.g.*, oblique depositions of overcoats being a fairly uncommon approach, but probably more importantly, the utilized magnetometry techniques may not have allowed to perform three-dimensional vector magnetometry in a self-calibrated way.

The investigation of the dynamic phase transition (DPT) of a Co film with in-plane uniaxial anisotropy subjected to an oscillating magnetic field has also led to interesting conclusions. For the first time, non-equivalencies between conventional thermodynamic phase transitions (TPTs) and DPTs in bulk systems have been observed and analyzed [7, 8] by means of a combination of MOKE measurements and model calculations. Metamagnetic tendencies have been observed in the dynamically disordered phase of the DPT with no analogue in the TPT, especially in the cases where the amplitude h_0 of the oscillating field driving the DPT is low. Also for low h_0 a shrinking of the critical regime of the DPT is observed, which hinders the experimental extraction of critical exponents. These facts evidence that h_0 is a crucial parameter determining the degree of similitude between DPTs and TPTs.

It is important to mention that all experiments and calculations of the DPT have been performed at the same ratio of temperature T to Curie temperature T_C, given that they were done on Co films at room temperature. However, it would be interesting to experimentally study the dependence of the DPT features on the very important T/T_C parameter. This can either be done by modifying

the temperature at which the experiment is performed or the T_C of the material, *e.g.*, by alloying it. One could also envision to perform experiments with the field applied along crystallographic directions different from the easy axis of anisotropic samples, as this could reveal new features of the DPT.

References

[1] P. Riego, S. Vélez, J. M. Gomez-Perez, J. A. Arregi, L. E. Hueso, F. Casanova, A. Berger, Appl. Phys. Lett. **109**, 172402 (2016).

[2] O. M. J. van't Erve, A. T. Hanbicki, K. M. McCreary, C. H. Li, and B. T. Jonker, Appl. Phys. Lett. **104**, 172402 (2014).

[3] C. Stamm, C. Murer, M. Berritta, J. Feng, M. Gabureac, P. M. Oppeneer, and P. Gambardella, Phys. Rev. Lett. **119**, 087203 (2017).

[4] M. Montazeri, P. Upadhyaya, M. C. Onbasli, G. Yu, K. L. Wong, M. Lang, M., Y. Fan, X. Li, P. K. Amiri, R. N. Schwartz ,C. A. Ross, and K. L. Wang, Nat. Comm. **6**, 8958 (2015).

[5] P. Lévy and A. Fert, Phys. Rev. B **23**, 4667 (1981).

[6] Cortés-Ortuño and P. Landeros, J. Phys. Condens. Matter **25**, 156001 (2013).

[7] P. Riego, P. Vavassori, and A. Berger, Phys. Rev. Lett. **118**, 117202 (2017).

[8] P. Riego, P. Vavassori, and A. Berger, Physica B **549**, 13 (2018).

Appendix I

Formula for Kerr rotation in crossed polarizers setup

Consider a crossed polarizers MOKE setup.

The Jones matrix for a polarizer is:

$$\overline{\overline{P}}_i(\theta_i) = \begin{pmatrix} \cos^2\theta_i & \sin\theta_i\cos\theta_i \\ \sin\theta_i\cos\theta_i & \sin^2\theta_i \end{pmatrix} \quad (A.I.1)$$

where θ_i is the angle between s polarization direction and the polarizer's axis.

The reflection matrix of the samples, assuming only longitudinal MOKE is:

$$\overline{\overline{R}} = r_p \begin{pmatrix} \tilde{r}_s & \tilde{\alpha} \\ -\tilde{\alpha} & 1 \end{pmatrix} \quad (A.I.2)$$

where $\tilde{\alpha}$ is the complex Kerr angle $\tilde{\alpha} = \theta_K + i\epsilon_K$. θ_K is the Kerr rotation and ϵ_K is the Kerr ellipticity.

Assuming an incidence with p polarization (*i.e.*, the first polarizer is aligned with p polarization):

$$\overline{\overline{P}}_1 = \begin{pmatrix} 0 & 0 \\ 0 & 1 \end{pmatrix} \quad (A.I.3)$$

The electric field after reflection is:

$$E_R = \overline{\overline{R}}\,\overline{\overline{P}}_1\,E_{in} = r_p \begin{pmatrix} \tilde{r}_s & \tilde{\alpha} \\ -\tilde{\alpha} & 1 \end{pmatrix}\begin{pmatrix} 0 & 0 \\ 0 & 1 \end{pmatrix}\begin{pmatrix} E_{in}^s \\ E_{in}^p \end{pmatrix} = r_p E_{in}^p \begin{pmatrix} \tilde{r}_s & \tilde{\alpha} \\ -\tilde{\alpha} & 1 \end{pmatrix}\begin{pmatrix} 0 \\ 1 \end{pmatrix} = r_p E_{in}^p \begin{pmatrix} \tilde{\alpha} \\ 1 \end{pmatrix} \quad (A.I.4)$$

The second polarizer is aligned close to being s-polarized. Actually, an small angle Δ away from extinction:

$$\overline{\overline{P}}_2(\theta_2) = \begin{pmatrix} \cos^2\theta_2 & \sin\theta_2\cos\theta_2 \\ \sin\theta_2\cos\theta_2 & \sin^2\theta_2 \end{pmatrix}\xrightarrow{\sin\theta_2\ll 1}\begin{pmatrix} 1 & \theta_2 \\ \theta_2 & 0 \end{pmatrix} \quad (A.I.5)$$

Thus, the electric field at the detector is

$$r_p E_{in}^p \begin{pmatrix} 1 & \theta_2 \\ \theta_2 & 0 \end{pmatrix}\begin{pmatrix} \tilde{\alpha} \\ 1 \end{pmatrix} = r_p E_{in}^p \begin{pmatrix} \tilde{\alpha} + \theta_2 \\ \tilde{\alpha}\theta_2 \end{pmatrix} \quad (A.I.6)$$

Leading to an intensity at the detector:

$$I_D = |r_p E_{in}^p|^2 (\tilde{\alpha}^* + \theta_2 \quad \tilde{\alpha}^* \theta_2) \begin{pmatrix} \tilde{\alpha} + \theta_2 \\ \tilde{\alpha} \theta_2 \end{pmatrix}$$

$$= |r_p E_{in}^p|^2 \left(|\tilde{\alpha}|^2 + \tilde{\alpha}^* \theta_2 + \tilde{\alpha} \theta_2 + \theta_2^2 + |\tilde{\alpha}|^2 \theta_2^2 \right) \text{ (A.I.7)}$$

Neglect terms of order $|\tilde{\alpha}|^2$, because MOKE is a small effect:

$$I_D = |r_p E_{in}^p|^2 \left(2\theta_2 \text{Re}(\tilde{\alpha}) + \theta_2^2 \right) = \theta_2 |r_p E_{in}^p|^2 (2\theta_K + \theta_2) \text{ (A.I.8)}$$

In order to calculate the normalized change of intensity upon magnetization reversal

$$\frac{\delta I}{I} = 2 \frac{I_D(\tilde{\alpha}) - I_D(-\tilde{\alpha})}{I_D(\tilde{\alpha}) + I_D(-\tilde{\alpha})} \text{ (A.I.9)}$$

one has to calculate

$$I_D(\tilde{\alpha}) + I_D(-\tilde{\alpha}) = \theta_2 |r_p E_{in}^p|^2 (2\theta_K + \theta_2 - 2\theta_K + \theta_2) = 2\theta_2^2 |r_p E_{in}^p|^2 \text{(A.I.10.a)}$$

$$I_D(\tilde{\alpha}) - I_D(-\tilde{\alpha}) = \theta_2 |r_p E_{in}^p|^2 (2\theta_K + \theta_2 + 2\theta_K - \theta_2) = 4\theta_2 \theta_K |r_p E_{in}^p|^2 \text{(A.I.10.b)}$$

Leading to

$$\frac{\delta I}{I} = 2 \frac{4\theta_2 \theta_K |r_p E_{in}^p|^2}{2\theta_2^2 |r_p E_{in}^p|^2} = \frac{4\theta_K}{\theta_2} \text{ (A.I.11)}$$

Therefore,

$$\theta_K = \frac{\theta_2}{4} \frac{\delta I}{I} \text{ (A.I.12)}$$

Appendix II

Derivation of generalized magneto-optical ellipsometry formula

Consider the Jones matrix of a polarizer $\bar{\bar{P}}_i$ whose polarizing axis forms an angle θ_i with the s polarization axis

$$\bar{\bar{P}}_i(\theta_i) = \begin{pmatrix} \cos^2 \theta_i & \sin \theta_i \cos \theta_i \\ \sin \theta_i \cos \theta_i & \sin^2 \theta_i \end{pmatrix} \quad (A.\,II.\,1)$$

and the reflection matrix of an optically anisotropic sample with first order magneto-optical effects:

$$\bar{\bar{R}} = r_p \begin{pmatrix} \tilde{r}_s & \tilde{\alpha} + \tilde{\gamma} \\ -\tilde{\alpha} + \tilde{\gamma} & 1 + \tilde{\beta} \end{pmatrix} \quad (A.\,II.\,2)$$

Consider also an arbitrary fully polarized electric field of the incident light

$$E_I = \begin{pmatrix} a \\ b \end{pmatrix} \quad (A.\,II.\,3)$$

After passing through a first polarizer P_1, being reflected on the sample, and passing through a second polarizer P_2 the electric field is affected

$$E_F = \bar{\bar{P}}_2 \, \bar{\bar{R}} \, \bar{\bar{P}}_1 \, E_I \quad (A.\,II.\,4)$$

Let us calculate the effect of P_1, the sample, and P_2:

$$\bar{\bar{P}}_2 \, \bar{\bar{R}} \, \bar{\bar{P}}_1 = r_p \begin{pmatrix} A & B \\ C & D \end{pmatrix} \quad (A.\,II.\,5)$$

$$A = F \cos \theta_1 \cos \theta_2 \quad (A.\,II.\,6.\,a)$$
$$B = F \sin \theta_1 \cos \theta_2 \quad (A.\,II.\,6.\,b)$$
$$C = F \cos \theta_1 \sin \theta_2 \quad (A.\,II.\,6.\,c)$$
$$D = F \sin \theta_1 \sin \theta_2 \quad (A.\,II.\,6.\,d)$$

with

$$F = \tilde{r}_s \cos \theta_1 \cos \theta_2 + (\tilde{\alpha} + \tilde{\gamma}) \sin \theta_1 \cos \theta_2 + (-\tilde{\alpha} + \tilde{\gamma}) \cos \theta_1 \sin \theta_2$$
$$+ \left(1 + \tilde{\beta}\right) \sin \theta_1 \sin \theta_2 \quad (A.\,II.\,7)$$

In the GME setup, a detector is placed after P_2, which will read an intensity

$$I_F = E_F^* \, E_F = r_p^2 (A^* a^* + B^* b^* \quad C^* a^* + D^* b^*) \begin{pmatrix} Aa + Bb \\ Ca + Db \end{pmatrix} = r_p^2 G |F|^2 \quad \text{(A. II. 8)}$$

with

$$G = |a|^2 \cos^2 \theta_1 + |b|^2 \sin^2 \theta_1 + (a^* b + a b^*) \cos \theta_1 \sin \theta_1 \quad \text{(A. II. 9)}$$

However, there could be a detected intensity coming from noise sources not related to the effects that are to be detected such that

$$I_D = I_F + \widetilde{I_0} \quad \text{(A. II. 10)}$$

where the noise is defined as $\widetilde{I_0}$.

The normalized change of intensity upon magnetization reversal, considering that

$$\tilde{\alpha}(-\boldsymbol{M}) = -\tilde{\alpha}(\boldsymbol{M}) \quad \text{(A. II. 11. a)}$$

$$\tilde{\beta}(-\boldsymbol{M}) = -\tilde{\beta}(\boldsymbol{M}) \quad \text{(A. II. 11. b)}$$

$$\tilde{\gamma}(-\boldsymbol{M}) = -\tilde{\gamma}(\boldsymbol{M}) \quad \text{(A. II. 11. c)}$$

reads

$$\frac{\delta I}{I} = \frac{I_D(\boldsymbol{M}) - I_D(-\boldsymbol{M})}{\frac{1}{2}\left(I_D(\boldsymbol{M}) + I_D(-\boldsymbol{M})\right)} = 2 \frac{r_p^2 G \left(|F(\tilde{\alpha}, \tilde{\beta}, \tilde{\gamma})|^2 - |F(-\tilde{\alpha}, -\tilde{\beta}, -\tilde{\gamma})|^2 \right)}{r_p^2 G \left(|F(\tilde{\alpha}, \tilde{\beta}, \tilde{\gamma})|^2 + |F(-\tilde{\alpha}, -\tilde{\beta}, -\tilde{\gamma})|^2 \right) + 2\widetilde{I_0}} \quad \text{(A. II. 12)}$$

Developing $|F(\tilde{\alpha}, \tilde{\beta}, \tilde{\gamma})|^2$

$$\begin{aligned}
|F(\tilde{\alpha}, \tilde{\beta}, \tilde{\gamma})|^2 = {}& |\tilde{r}_s|^2 \cos^2 \theta_1 \cos^2 \theta_2 + \tilde{r}_s^* (\tilde{\alpha} + \tilde{\gamma}) \cos \theta_1 \sin \theta_1 \cos^2 \theta_2 \\
& + \tilde{r}_s^* (-\tilde{\alpha} + \tilde{\gamma}) \cos^2 \theta_1 \cos \theta_2 \sin \theta_2 + \tilde{r}_s^* (1 + \tilde{\beta}) \cos \theta_1 \sin \theta_1 \cos \theta_2 \sin \theta_2 \\
& + |\tilde{\alpha} + \tilde{\gamma}|^2 \sin^2 \theta_1 \cos^2 \theta_2 + \tilde{r}_s (\tilde{\alpha}^* + \tilde{\gamma}^*) \cos \theta_1 \sin \theta_1 \cos^2 \theta_2 \\
& + (\tilde{\alpha}^* + \tilde{\gamma}^*)(-\tilde{\alpha} + \tilde{\gamma}) \cos \theta_1 \sin \theta_1 \cos \theta_2 \sin \theta_2 \\
& + (\tilde{\alpha}^* + \tilde{\gamma}^*)(1 + \tilde{\beta}) \sin^2 \theta_1 \cos \theta_2 \sin \theta_2 + |-\tilde{\alpha} + \tilde{\gamma}|^2 \cos^2 \theta_1 \sin^2 \theta_2 \\
& + \tilde{r}_s (-\tilde{\alpha}^* + \tilde{\gamma}^*) \cos^2 \theta_1 \cos \theta_2 \sin \theta_2 \\
& + (-\tilde{\alpha}^* + \tilde{\gamma}^*)(\tilde{\alpha} + \tilde{\gamma}) \cos \theta_1 \sin \theta_1 \cos \theta_2 \sin \theta_2 \\
& + (-\tilde{\alpha}^* + \tilde{\gamma}^*)(1 + \tilde{\beta}) \cos \theta_1 \sin \theta_1 \sin^2 \theta_2 + |1 + \tilde{\beta}|^2 \sin^2 \theta_1 \sin^2 \theta_2 \\
& + \tilde{r}_s (1 + \tilde{\beta}^*) \cos \theta_1 \sin \theta_1 \cos \theta_2 \sin \theta_2 \\
& + (\tilde{\alpha} + \tilde{\gamma})(1 + \tilde{\beta}^*) \sin^2 \theta_1 \cos \theta_2 \sin \theta_2 \\
& + (-\tilde{\alpha} + \tilde{\gamma})(1 + \tilde{\beta}^*) \cos \theta_1 \sin \theta_1 \sin^2 \theta_2 \quad \text{(A. II. 13)}
\end{aligned}$$

Given that $\tilde{\alpha}, \tilde{\beta}, \tilde{\gamma} \ll \tilde{r}_s$, second order terms in $\tilde{\alpha}, \tilde{\beta}$, and $\tilde{\gamma}$ are neglected in the following,

$$\left|F(\tilde{\alpha}, \tilde{\beta}, \tilde{\gamma})\right|^2 - \left|F(-\tilde{\alpha}, -\tilde{\beta}, -\tilde{\gamma})\right|^2$$

$$= 2\,\tilde{r}_s^*(\tilde{\alpha} + \tilde{\gamma})\cos\theta_1 \sin\theta_1 \cos^2\theta_2 + 2\,\tilde{r}_s^*(-\tilde{\alpha} + \tilde{\gamma})\cos^2\theta_1 \cos\theta_2 \sin\theta_2$$

$$+ 2\,\tilde{r}_s^*\tilde{\beta}\cos\theta_1 \sin\theta_1 \cos\theta_2 \sin\theta_2 + 2\,\tilde{r}_s(\tilde{\alpha}^* + \tilde{\gamma}^*)\cos\theta_1 \sin\theta_1 \cos^2\theta_2$$

$$+ 2(\tilde{\alpha}^* + \tilde{\gamma}^*)\sin^2\theta_1 \cos\theta_2 \sin\theta_2 + 2\,\tilde{r}_s(-\tilde{\alpha}^* + \tilde{\gamma}^*)\cos^2\theta_1 \cos\theta_2 \sin\theta_2$$

$$+ 2(-\tilde{\alpha}^* + \tilde{\gamma}^*)\cos\theta_1 \sin\theta_1 \sin^2\theta_2 + 2\,\tilde{r}_s\tilde{\beta}^*\cos\theta_1 \sin\theta_1 \cos\theta_2 \sin\theta_2$$

$$+ 2(\tilde{\alpha} + \tilde{\gamma})\sin^2\theta_1 \cos\theta_2 \sin\theta_2 + 2(-\tilde{\alpha} + \tilde{\gamma})\cos\theta_1 \sin\theta_1 \sin^2\theta_2$$

$$+ 4\mathrm{Re}(\tilde{\beta})\sin^2\theta_1 \sin^2\theta_2 \quad \text{(A. II. 14)}$$

where

$$\left|1 + \tilde{\beta}\right|^2 - \left|1 - \tilde{\beta}\right|^2 = \left(1 + \mathrm{Re}(\tilde{\beta})\right)^2 + \left(\mathrm{Im}(\tilde{\beta})\right)^2 - \left(1 - \mathrm{Re}(\tilde{\beta})\right)^2 - \left(\mathrm{Im}(\tilde{\beta})\right)^2$$

$$= 4\mathrm{Re}(\tilde{\beta}) \quad \text{(A. II. 15)}$$

has been considered, and

$$\frac{1}{2}\left(|F(\alpha, \beta, \gamma)|^2 + |F(-\alpha, -\beta, -\gamma)|^2\right)$$

$$= |\tilde{r}_s|^2 \cos^2\theta_1 \cos^2\theta_2 + \tilde{r}_s^* \cos\theta_1 \sin\theta_1 \cos\theta_2 \sin\theta_2 + \sin^2\theta_1 \sin^2\theta_2$$

$$+ \tilde{r}_s \cos\theta_1 \sin\theta_1 \cos\theta_2 \sin\theta_2 \quad \text{(A. II. 16)}$$

where

$$\left|1 + \tilde{\beta}\right|^2 + \left|1 - \tilde{\beta}\right|^2 = \left(1 + \mathrm{Re}(\tilde{\beta})\right)^2 + \left(\mathrm{Im}(\tilde{\beta})\right)^2 + \left(1 - \mathrm{Re}(\tilde{\beta})\right)^2 + \left(\mathrm{Im}(\tilde{\beta})\right)^2$$

$$= 2 + 2\left|\tilde{\beta}\right|^2 \quad \text{(A. II. 17)}$$

Has been considered and the second term $2\left|\tilde{\beta}\right|^2$ was neglected.

Based on (A. II. 12), this leads to

$$\frac{\delta I}{I} = 4\,\frac{B_1 f_1 + B_2 f_2 + B_3 f_3 + B_4 f_4 + B_5 f_5 + B_6 f_6}{f_3 + B_7 f_7 + 2B_8 f_4 + \dfrac{2\tilde{I}_0}{r_p^2 G}} \quad \text{(A. II. 18)}$$

with

$$f_{1,5}\,(\theta_1, \theta_2) = \sin^2(\theta_1)\sin(\theta_2)\cos(\theta_2) \mp \sin^2(\theta_2)\sin(\theta_1)\cos(\theta_1) \quad \text{(A. II. 19. a)}$$

$$f_{2,6}\,(\theta_1, \theta_2) = \cos^2(\tilde{\theta}_2)\sin(\tilde{\theta}_1)\cos(\tilde{\theta}_1) \mp \cos^2(\tilde{\theta}_1)\sin(\tilde{\theta}_2)\cos(\tilde{\theta}_2) \quad \text{(A. II. 19. b)}$$

$$f_3\,(\theta_1, \theta_2) = \sin^2(\theta_1)\sin^2(\theta_2) \quad \text{(A. II. 19. c)}$$

$$f_4\,(\theta_1,\theta_2) = \sin(\theta_1)\cos(\theta_1)\sin(\theta_2)\cos(\theta_2)\ \ (\text{A. II. 19. d})$$

$$f_7\,(\theta_1,\theta_2) = \cos^2(\theta_1)\cos^2(\theta_2)\ \ (\text{A. II. 19. e})$$

and

$$B_1 = \text{Re}(\tilde{\alpha})\ \ (\text{A. II. 20. a}) \quad B_2 = \text{Re}(\tilde{r}_s\tilde{\alpha}^*)\ \ (\text{A. II. 20. b})$$

$$B_3 = \text{Re}(\tilde{\beta})\ \ (\text{A. II. 20. c}) \quad B_4 = \text{Re}(\tilde{r}_s\tilde{\beta}^*)\ \ (\text{A. II. 20. d})$$

$$B_5 = \text{Re}(\tilde{\gamma})\ \ (\text{A. II. 20. e}) \quad B_6 = \text{Re}(\tilde{r}_s\tilde{\gamma}^*)\ \ (\text{A. II. 20. f})$$

$$B_7 = |\tilde{r}_s|^2\ \ (\text{A. II. 20. g}) \quad B_8 = \text{Re}(\tilde{r}_s)\ \ (\text{A. II. 20. h})$$

The noise term in the denominator contains G, which depends on the orientation of the first polarizer θ_1. However, this can be avoided by forcing the light that enters the first polarizer to be circularly polarized. This can be achieved by placing a properly aligned quarter-wave plate between the light source, which is a laser that provides linearly polarized light, and the first polarizer. Thus E_I would have

$$a = \frac{1}{\sqrt{2}}, \quad b = \frac{i}{\sqrt{2}} \quad (\text{A. II. 21})$$

and therefore, $G = \frac{1}{2}$, leading to

$$\frac{\delta I}{I} = 4\,\frac{B_1 f_1 + B_2 f_2 + B_3 f_3 + B_4 f_4 + B_5 f_5 + B_6 f_6}{f_3 + B_7 f_7 + 2B_8 f_4 + I_0}\ \ (\text{A. II. 22})$$

With $I_0 = 4\frac{\tilde{I}_0}{r_p^2}$ being independent of the setting of the polarizers.

Another source of error could be the misalignment of the polarizers. To account for such, two additional fitting parameters are considered, namely offsets for θ_1 and θ_2, $\Delta\theta_1$ and $\Delta\theta_2$ respectively, so in the $f_i, i = 1, 2, \dots, 8$ functions in Eqs. (A.II.19 a -e) θ_1 needs to be replaced by $\theta_1 - \Delta\theta_1$ and θ_2 by $\theta_2 - \Delta\theta_2$.

Appendix III

Fits and calculations of the macrospin model

A method to minimize the free energy of the macrospin model is given here.

The free energy of the model is given by Eq. (4.2):

$$\frac{\mathcal{F}}{V} = -\mu_0 H M_s \cos(\Phi_M) - \widetilde{K}_1 \cos^2(\Phi_0 - \Phi_M) - \widetilde{K}_2 \cos^4(\Phi_0 - \Phi_M) \quad (A.\,III.\,1)$$

As a reminder, Φ_M is the angle between the magnetization and the applied field axis, Φ_0 is the angle between the EA and the field axis, $\widetilde{K}_1$ and $\widetilde{K}_2$ are MCA constants, M_s is the saturation magnetization and H is the strength of the applied field. The minimization of $\mathcal{F}/V$ is achieved if the magnetization vector, which is contained in the plane of the sample and whose length is constant, is aligned with the effective field $\boldsymbol{H}^{eff}$ acting on it.

The magnetization vector is decomposed in two components, along the EA and perpendicular to it (*i.e.*, along the in-plane hard axis, HA):

$$M_{EA} = M_s m_{EA} = M_s \cos \Phi_M \quad (A.\,III.\,2.\,a)$$

$$M_{HA} = M_s m_{HA} = M_s \sin \Phi_M \quad (A.\,III.\,2.\,b)$$

and the components of $\boldsymbol{H}^{eff}$ along the EA and the HA are:

$$H_{EA}^{eff} = H \cos \Phi_0 + 2\widetilde{H}_{K_1} m_{EA} + 4\widetilde{H}_{K_2} m_{EA}^3 \quad (A.\,III.\,3.\,a)$$

$$H_{HA}^{eff} = H \sin \Phi_0 \quad (A.\,III.\,3.\,b)$$

where $\widetilde{H}_{K_1} = \frac{\widetilde{K}_1}{\mu_0 M_s}$ and $\widetilde{H}_{K_2} = \frac{\widetilde{K}_2}{\mu_0 M_s}$. So, the effective field along the EA is different from the projection of the external field because MCA is also acting, trying to align the magnetization along the EA.

For the magnetization $\boldsymbol{M}$ to be parallel to $\boldsymbol{H}^{eff}$ respecting $m_{EA}^2 + m_{HA}^2 = 1$ one has that

$$m_{EA} = \frac{H_{EA}^{eff}}{H^{eff}} \quad (A.\,III.\,4.\,a)$$

$$m_{HA} = \frac{H_{HA}^{eff}}{H^{eff}} \quad (A.\,III.\,4.\,b)$$

where

$$H^{eff} = \sqrt{\left(H_{EA}^{eff}\right)^2 + \left(H_{HA}^{eff}\right)^2} \quad \text{(A. III. 5)}$$

Equations (A.III.4.a) and (A.III.4.b) need to be solved self-consistently, since the effective field depends on the magnetization components. As a starting condition, the magnetization is aligned with the field.

When self-consistency is achieved, the field-projected magnetization is calculated as

$$M_H = M_s(m_{EA} \cos \Phi_0 + m_{HA} \sin \Phi_0) \quad \text{(A. III. 6)}$$

For a given set of $M_s, \widetilde{K}_1$, and $\widetilde{K}_2$, the corresponding M_H can be calculated for different values of H and Φ_0.

Conversely, one can take experimentally measured data of M_H for many values H and Φ_0 and consistently fit it to Eq. (A.III.5) to obtain the $M_s, \widetilde{K}_1$, and $\widetilde{K}_2$ of the sample. This procedure is followed to extract $M_s, \widetilde{K}_1$, and $\widetilde{K}_2$ from VSM datasets $M_H(\Phi_0, H)$.

List of publications

Work related to this thesis has also resulted in the following publications:

- P. Riego, P. Vavassori, and A. Berger, *Towards an understanding of dynamic phase transitions*, Physica B (Amsterdam) **549**, 13-23 (2018).
- P. Riego, P. Vavassori, and A. Berger, *Metamagnetic anomalies near dynamic phase transitions*, Phys. Rev. Lett. **118**, 117202 (2017).
- P. Riego, S. Vélez, J. M. Gomez-Perez, J. A. Arregi, L. E. Hueso, F. Casanova, and A. Berger, *Absence of detectable current-induced magneto-optical Kerr effects in Pt, Ta and W,* Appl. Phys. Lett. **109**, 172402 (2016).

Other publications:

- P. Riego and A. Berger, *Nonuniversal surface behavior of dynamic phase transitions*, Phys. Rev. E **91**, 062141 (2015).
- B. J. Kirby, H. F. Belliveau, D. D. Belyea, P. A. Kienzle, A. J. Grutter, P. Riego, A. Berger, and Casey W. Miller, *Spatial evolution of the ferromagnetic phase transition in an exchange graded film*, Phys. Rev. Lett. **116**, 047203 (2016).
- J. Arregi, P. Riego, and A. Berger, *What is the longitudinal magneto-optical Kerr effect?*, J. Phys. D: Appl. Phys. **50** 03LT01 (2017).
- P. Riego, S. Tomita, K. Murakami, T. Kodama , N. Hosoito, H. Yanagi, and A. Berger, *Enhanced magneto-optical Kerr effects in Py/Ag/Bi trilayers*, J. Phys. D: Appl. Phys. **50** 19LT01 (2017).
- L. Fallarino, B. J. Kirby, M. Pancaldi, P. Riego, A. L. Balk, C. W. Miller, P. Vavassori, and A. Berger, *Magnetic properties of epitaxial CoCr films with depth-dependent exchange coupling profiles*, Phys. Rev. B. **95**, 134445 (2017).
- E. Oblak, P. Riego, L. Fallarino, A. Martínez-de-Guerenu, F. Arizti, and A. Berger, *Ultrasensitive transverse magneto-optical Kerr effect measurements by means of effective polarization change detection*, J. Phys. D: Appl. Phys. **50** 23LT01 (2017).
- L. Fallarino, P. Riego, B. J. Kirby, C. W. Miller, and A. Berger, *Modulation of magnetic properties at the nanometer scale in continuously graded ferromagnets*, Materials **11**(2) 251 (2018).
- B. J. Kirby, L. Fallarino, P. Riego, B. B. Maranville, C. W. Miller, and A. Berger, *Nanoscale magnetic localization in exchange strength modulated ferromagnets,* Phys. Rev. B **98**, 064404 (2018).
- S. Tomita, T. Suwa, P. Riego, A. Berger, N. Hosoito, and H. Yanagi, *Enhanced magneto-optical activities of modulated Fe-Pt multilayer metamaterials*, Phys. Rev. Applied **11**, 064010 (2019).
- E. Y. Vedmedenko, J. A. Arregi, P. Riego, A. Berger, *Interlayer Dzyaloshinskii-Moriya interactions*, accepted in Phys. Rev. Lett. (May 2019) (arXiv:1803.10570).

Acknowledgements

I never believed in much, but I believed in you.

Neil Young

The time has come to close this stage in life, and I have to thank many people that have accompanied me through it.

First, I want to thank my supervisor Andreas Berger, an excellent scientist and a great advisor. Thank you for your help and guidance in this process, I have learned a lot from you. Needless to say, I admire your scientific rigor and vision. It has been great working with you.

Second, I thank Txema Pitarke for accepting to be my co-supervisor and for giving me the opportunity to work at CIC nanoGUNE, with the invaluable access to top-notch facilities that this implies.

To my colleagues in the Nanomagnetism group, not only for the work together, but especially for the nice atmosphere. I want to start by thanking the former members of the group, and in particular Lorenzo and Jon Ander, for teaching me so much, for sharing with me their knowledge and experience, and for being always ready to answer my doubts and concerns, even long after they left nanoGUNE. Mila esker! Thanks Cesar for your help with the whole process of sample fabrication, and especially for those HF moments. To Paolo, Matteo, Nicolò, Ramon, Eva, Sara, thank you for being always ready to answer my doubts or give a helping hand in the lab. Aitor, Alberto, Eleftheria, Eneko, Naëmi, Matteo, Mikel, Mario… it has been a pleasure to be part of the same team. Thank you all!

I also want to thank the rest of the incredible people at nanoGUNE. To many of them for their great help with the work-related stuff: Juanma, Saül, Edurne (eskerrik asko danagatik, Edur!), but, most importantly, because it is always great to have nice people around at the workplace in a

period with so many ups and downs as the PhD. Thanks to all of those who have made me feel at ease by sharing with me moments of often small, but sometimes big talk.

I have been really lucky to have the chance to visit different groups during my thesis and I am very grateful for that. I would like to thank Prof. Stéphane Mangin, Prof. Neil Mathur, and Prof. Ulrich Nowak for allowing me to work in their groups in Nancy, Cambridge and Konstanz, respectively. These experiences have helped me to grow as a scientist, but also as a person, as I have learned lots of things and met great people. Thanks Mohammed Salah, David, and Simone for your great support and patience during my stay in your groups.

I would also like to acknowledge Dr. Satoshi Tomita for our joint collaboration, as well as Dr. Brian J. Kirby and Dr. Dirk Sander for reading this thesis and giving their feedback for the international doctoral mention. Thank you for having taken the time to do so.

Gracias a la gente que consigue que apague el piloto automático, a los que veo a menudo y a los que, por desgracia, veo menos de lo que me gustaría. Por las excursiones, vacaciones, cafés, cervezas, risas, planes frustrados, recomendaciones musicales, consejos varios, conversaciones sobre el pasado, el presente y el futuro, pero, sobre todo, por el lujo que son vuestro tiempo y compañía.

Un enorme *gracias* a mi familia, por estar siempre ahí. A mi madre, de quien he aprendido a elegir las batallas adecuadas. A mi padre, una mente curiosa que me ha enseñado a cuestionarlo todo y que, por supuesto, y que así siga siendo, me cuestiona todo. Y finalmente, gracias, Jon, por haber estado a mi lado todo este tiempo. Ayudándome, motivándome y haciéndome mejor y más feliz poco a poco. Todavía tienes trabajo para rato.

Nothing to add.